A Structural and Magnetic Study of Ammonium Iron Halides

Deborah Aitken Porter

A Thesis Submitted fo the Degree of
Doctor of Philosophy

University of Edinburgh
Department of Chemistry
1998

"Le superflu, chose très nécessaire."

Voltaire

A Structural and Magnetic Study of Ammonium Iron Halides

Abstract

Some ABX_3 materials, in which A is a monovalent cation, B a divalent cation and X a monovalent anion, are known to exhibit the hexagonal perovskite structure; these have a chain-like structure produced by face sharing BX_6 octahedra that lie parallel to the crystal *c* axis. For materials in which B is a first row transition metal, this structural anisotropy leads to pseudo-one dimensional magnetic behaviour; the interchain exchange is several orders of magnitude larger than the intrachain exchange.

This thesis discusses the investigation of the crystal structure and crystallographic and magnetic phase transitions in the hexagonal perovskites, ammonium iron chloride and bromide; specifically to consider the effect of the non-spherical ammonium ion on both the structure and the magnetic properties. Powder samples have been studied between 420 and 4.2 K using high resolution synchrotron X-ray diffraction, and between 470 and 1.5 K using neutron diffraction. The rotation of the ammonium ion within the structure was studied via quasi-elastic neutron diffraction. Single crystals of both materials were obtained and studied using SQUID magnetometry and X-ray diffraction (between room temperature and 10 K).

Ammonium iron chloride is found to undergo a structural phase transition at 181.0(2) K where the symmetry is lowered as the $FeCl_3$ chains twist slightly. A second structural phase transition is observed at 19.5(2) K; in this case the unit cell is found to double in the *a* direction with respect to the primitive cell. Quasi-elastic neutron scattering measurements show NH_4FeCl_3 exhibits quantum tunnelling in its low temperature phase, proving the NH_4 motion is frozen at that temperature. Neutron diffraction reveals antiferromagnetic reflections corresponding to a helical magnetic array below 3.7(2) K; susceptibility data also show a transition at this temperature.

Ammonium iron bromide undergoes a structural phase transition at 270(10) K which correspond to the $FeBr_3$ chains simultaneously twisting and slipping. At 90(10) K a second phase transition occurs where once again the unit cell is seen to expand with respect to the primitive cell. Antiferromagnetic reflections are observed in the neutron data at 5.0(2) K and 2.8(2) K, these also corresponds to transitions observed in the susceptibility measurements.

The complex magnetic susceptibility and the low-temperature ordered magnetic structures of these materials is discussed in relation to small distortions in the exchange geometry, and the ligand field environment.

Acknowledgements

Firstly and most importantly I would like to thank Andrew for being so enthusiastic, motivated, motivating(?), inspirational, patient, understanding, supportive and clever. And of course none of this would have been possible without Dick, I am eternally grateful for all his help and expertise.

I am also grateful to Simon Parsons for single crystal work carried out in Edinburgh and to Judith Howard, Roy Copley, Andeas Goeta and Dima Yufit for the single crystal work in Durham. The work at the ESRF was facilitated by local contacts Andy Fitch and Eric Dooryhee and could not have proceeded at all without the beautiful glove box and the kind help of M. Harald Müller. I am also grateful for the company of Simon Carling and Andrew Montieth for company during some of the experiments. Neutron scattering experiments involved Clemens Ritter, Alan Hewat (D2B) and David Martin (IRIS).

I'd like to say thanks to mum and dad for being so supportive. A huge debt of gratitude is due to the entire Harrison group; Andrew, Gavin, Bin-bing, Gareth, Clare, Douglas and especially Carolyn, thank you all for holding me up, keeping me going, coffee breaks, big nights out, camping trips, munro bagging and holidays!!! Thanks to Kathy for solidarity and yoga, and to Lucy for teaching me to be tough, to Vanessa, for endless support during this last year and for helping with the candles and a special thanks to Helen and Bronagh for being there forever.

There are lots of people in the department of chemistry in Edinburgh who have helped me (cope) over the last four years, but I'd like to particulary mention Stuart for all his help mending the vac. line and Stuart (the glassblower) for creating the vac line and for emergency salvaging of many a badly made ampoule!.

Last and most certainly not least, thanks to Lee. I can't even describe how much you've changed my life!!!!! Thanks for everything - I promise I've learned from this experience.....

Courses and Conferences

Courses Attended

27/2/95 - 2/3/95	Neutron Training Course at Rutherford Appleton Laboratory
6/4/97 - 14/4/97	BCA Sixth Intensive Course in X-ray Structure Analysis at The University of Durham
23/6/97 - 31/6/97	EPSRC Graduate School at Brunel University

Conferences

12/6/95 - 14/6/95	Departmental Conference at Firbush Point Field Centre	(talk)
18/12/95 - 19/12/95	Polar Solids Meeting at the University of Bristol	
23/5/96	Scottish Materials Conference at the University of Aberdeen	
10/6/96 - 12/6/96	Departmental Conference at Firbush Point Field Centre	(poster)
18/9/96 - 20/9/96	Neutron Users Meeting at the Rutherford Appleton Laboratory	(poster)
18/12/96 - 19/12/96	Polar Solids Meeting at the University of Sussex	(poster)
9/6/97 - 11/6/97	Departmental Conference at Firbush Point Field Centre	(talk)
18/8/97 - 21/8/97	International Conference on Neutron Scattering at the University of Toronto, Canada	(poster)
22/8/97	Workshop on Advanced Neutron Powder Diffraction Instrumentation and Data Analysis Techniques at the University of Toronto	

External Experiments

11/2/96 - 14/2/96	D1B and D2B at the Institut Laue-Langevin, Grenoble
20/1/97 - 25/1/97	Diffractometer BM16 at the ESRF, Grenoble
6/11/97 - 13/11/97	Diffractometer BM16 at the ESRF, Grenoble
14/11/97 - 17/11/97	D2B at the Institut Laue-Langevin, Grenoble
30/3/98 - 2/4/98	IRIS at the Rutherford Appleton Laboratory, Didcot, Oxon.

Published Papers

D. A. Porter, A. Harrison, A. V. Powell and C. Ritter - ILL experimental report, expt. no. 5-31-828 (1996)

D. A. Porter, A. Harrison, D. Visser, R. C. B. Copley, A. E. Goeta, J. A. K. Howard and K. S. Knight, Physica B **241-243** 385 (1998)

Contents

1. Introduction

1.1. The quest for model magnetic materials

Since magnetic phenomena were first observed they have been of profound interest both fundamentally, and as a technological tool [1]. The fact that magnetism is a macroscopically observable property has meant that theoretical study was begun long before the development of a sophisticated microscopic picture of matter, using quantum mechanical principles. Early attempts to understand magnetic materials were responsible for the superstition that mariners should not eat onions or garlic, these being substances that were believed to rob the lodestones, used in navigation, of their sense of North and South, and it took Gilbert's careful observations and theories in the sixteenth century [2] to disprove this idea - though the seafaring superstition lingered for considerably longer. In the next century a link was found between electricity and magnetism – though this time nautical observation proved to be the source of enlightenment, with electrical storms at sea being held responsible for the reversal of the polarisation of lodestone compass needles – and the fluid theories for electricity, current at the time, were applied to magnetic phenomena. It took the passage of another two centuries before magnetism was linked to phenomena at atomic or molecular lengthscales, and finally the development of quantum theory at the start of this century before the relation between bulk and microscopic, electronic behaviour was put on a firm footing. However, there are many aspects of solid-state magnetism that remain unclear and it is still a major challenge to be able to relate the magnetic properties of real materials to their structure and chemical composition. This is part of a more general problem in understanding how the bulk properties of real, many-electron systems, relate to their microscopic properties. The study of

magnetism has an important role to play in this process because many macroscopic measurements provide a direct link to the microscopic electronic character of the material, and provide incisive tests of theory. Chemists and physicists have complementary roles in the development of this field; chemists design and synthesise materials which have potentially interesting magnetic behaviour and physicists perform detailed measurements on their magnetic properties and attempt to rationalise their observations. This approach operates most successfully when the chemist and physicist work together and appreciate both the aims, predictions and limitations of the fundamental physics, as well as the limitations of the samples; either in terms of the extent to which they mimic model magnetic systems, or are influenced by imperfections such as impurities and disorder.

There are two fundamental types of magnetism which describe the behaviour of a material containing magnetic atoms or molecules. The first of these, *diamagnetism*, arises from all the paired electrons on all atoms in the material. The great majority of materials are diamagnetic and even materials containing unpaired electrons have a diamagnetic response arising from the paired electrons. This response can be quantified by measurement of the susceptibility, χ; the definition and measurement of χ are outlined in greater detail in chapter 2, but at this stage we can consider the *sign* of χ. Diamagnets are repelled by an applied magnetic field and are said to exhibit negative susceptibilities. The second type, *paramagnetism*, is observed in atoms containing unpaired electrons, where the atom has an overall magnetic moment (μ), which is sometimes called the *spin* because it results from the spin (S) and orbital (L) angular momentum of the electron (this is discussed more fully in section 2.1). Paramagnets are *attracted* by an applied field and are considered to have positive susceptibilities.

In many materials the bulk magnetic properties arise from the behaviour of isolated magnetic atoms, and their response to an applied magnetic field can be rationalised quite simply considering the Boltzmann distribution over the Zeeman-split spin states (Section 2.4). This is reasonable in many cases, such as organic free radicals or dilute rare earth salts, where the moments are well separated on discrete molecules or ions. However, in many materials, the magnetic atoms or molecules cannot be regarded as isolated and the interaction between them frequently complicates the energy levels of the system and the effect becomes *cooperative* (Section 2.5). In metals the conduction electrons are delocalised throughout the material and convey information about spin polarisation over a very long range; this is called the RKKY model. In insulating solids, the more discrete bonding means that the magnetic moment is largely localised on the metal atoms and information about relative polarisations of neighbouring moments is conveyed through mixture of the relevant valence orbitals by covalent interactions. This form of interaction is generically called 'exchange' because its origin lies in the differences in quantum mechanical exchange energy between different spin states, and it is very short range in insulators.

There are several malleable factors available to the chemist in the development of a model magnet; firstly the *size* of the magnetic moment can be chosen by controlling the angular momentum, J, of the magnetic ion. The number of unpaired electrons and the immediate chemical environment of the magnetic ion determines the ligand field, and therefore the splitting and occupation of the valence orbitals. The combination of the spin and orbital momentum can be selected by varying the oxidation state and the ligand field environment of a particular transition element; e.g. V^{4+} with valence configuration $3d^1$ corresponds to spin = ½ while for Mn^{2+} with valence configuration $3d^5$ and a high-spin state in an octahedral ligand field, spin = 5/2. The *second* control factor is also a consequence of the nature of the magnetic ion and its site in the

crystal, that is the anisotropy of its angular momentum. A moment may be isotropic in space, with no preference for the *x*, *y* or *z* direction, or it may have a very distinct anisotropy and only possess significant components within a plane or a particular axis, giving 2 or 1 spin degrees of freedom respectively; e.g. Mn^{2+} ions generally have a ^6A ground state and no spatial anisotropy, while Co^{2+} ions in an octahedral ligand field have a ^2E ground state, which generally gives a strong anisotropy such that the moment is mainly along one axis. The third factor that may be manipulated is the nature of the exchange between spins. By suitable choice of the geometry and composition of bridging ligands between magnetic atoms, it may be possible to engineer interactions of particular sign (ferro- or antiferromagnetic) and strength. Furthermore, the short-range nature of such interactions in insulators means that it may be possible to produce a magnetic lattice where exchange is strong only in certain directions, thus controlling the *lattice dimensionality*. Within a particular lattice dimensionality the geometry of the magnetic lattice may also vary. For example in a planar system, the magnetic ions may be arranged in a square or triangular array or more complex arrays such as a Kagomé network (Figure 1.15, p26).

The various factors that control the bulk magnetic properties may be summarised in the Hamiltonian for the interaction of nearest neighbours (*i,j*) in a lattice, given in Equation 1.1.

$$H = -2J\sum_{i>j}\left[aS_i^zS_j^z + b\left(S_i^xS_j^x + S_i^yS_j^y\right)\right] \qquad (1.1)$$

where *J* is the exchange constant and describes the magnitude and sign of the exchange interaction and the weighting of *a* and *b* may be varied to produce different exchange dimensionalities; the isotropic case, in which a = b is known as Heisenberg exchange, while the extreme anisotropic cases $a = 0$ or $b = 0$ are known as the XY or

Ising models respectively. There may also be a lattice dimensionality that depends on the atomic packing, which in turn dictates the magnetic exchange pathways, and this is reflected in the Hamiltonian in terms of various values for J_{ij}, depending on the relative disposition of ions *i* and *j*. Some examples of real materials in which the various terms in the Hamiltonian have been manipulated to give special cases are given below.

The structure of Cs_3CoCl_5, shown in Figure 1.1, contains isolated $CoCl_4^{2-}$ units, with additional Cs and Cl ions. The spin of ½ on each Co^{2+} ion experiences a strong single-ion anistropy that produces a very anisotropic moment, with significant components only in one direction; each Co^{2+} ion is equivalent and is coupled antiferromagnetically to each of six nearest neighbours so this material provides a good example of a cubic Ising antiferromagnet [3-7].

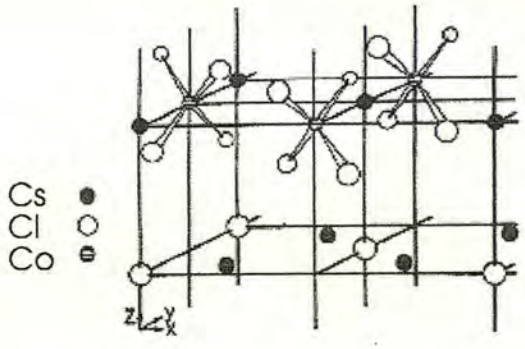

Figure 1.1. The crystal structure of Cs_3CoCl_5. The magnetic ions are arranged in a simple cubic environment and behave collectively as a 3D Ising system.

$Cu(NH_3)_4SO_4.H_2O$ was the first substance to be recognised as having one-dimensional (1-D) magnetic properties and its structure is shown in Figure 1.2 [8]. The superexchange interaction between the S =1/2 spins on Cu^{2+} *via* the oxygen ion is significantly more favourable than that *via* the two NH_3 groups; thus the system

behaves as an assembly of nearly isolated magnetic chains (orientated along the *c*-axis) with a ratio of interchain exchange to intrachain of around 5×10^{-3} [9-12].

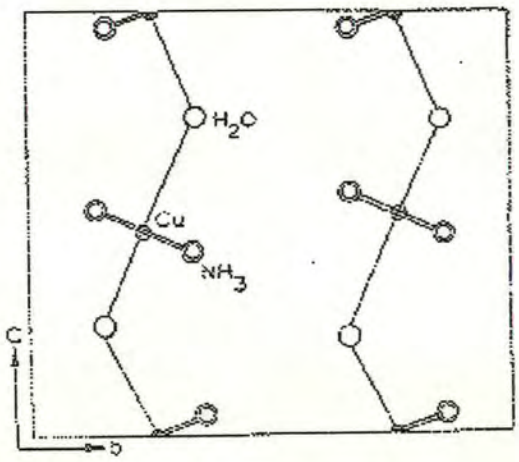

Figure 1.2. The projection of the unit cell of $Cu(NH_3)_4SO_4.H_2O$ on the bc plane.

$(C_3H_7NH_3)_2CuCl_4$ behaves as a model two-dimensional (2-D) magnet, and the origin of this can be appreciated by considering the structural anisotropy depicted in Figure 1.3 which displays layers of Cu^{2+} ions separated by two layers of non-magnetic propyl ammonium groups [13,14]. If the alkyl group in this structure is varied, the separation between the Cu^{2+} layers is seen to change correspondingly, without a change in structure type. As a result of this trend the properties of the range of materials $(C_nH_{n+1}NH_3)_2CuCl_4$ (n = 0, 1, 2, 3 .....) have been studied, allowing extrapolation to an ideal 2- D system [15,16].

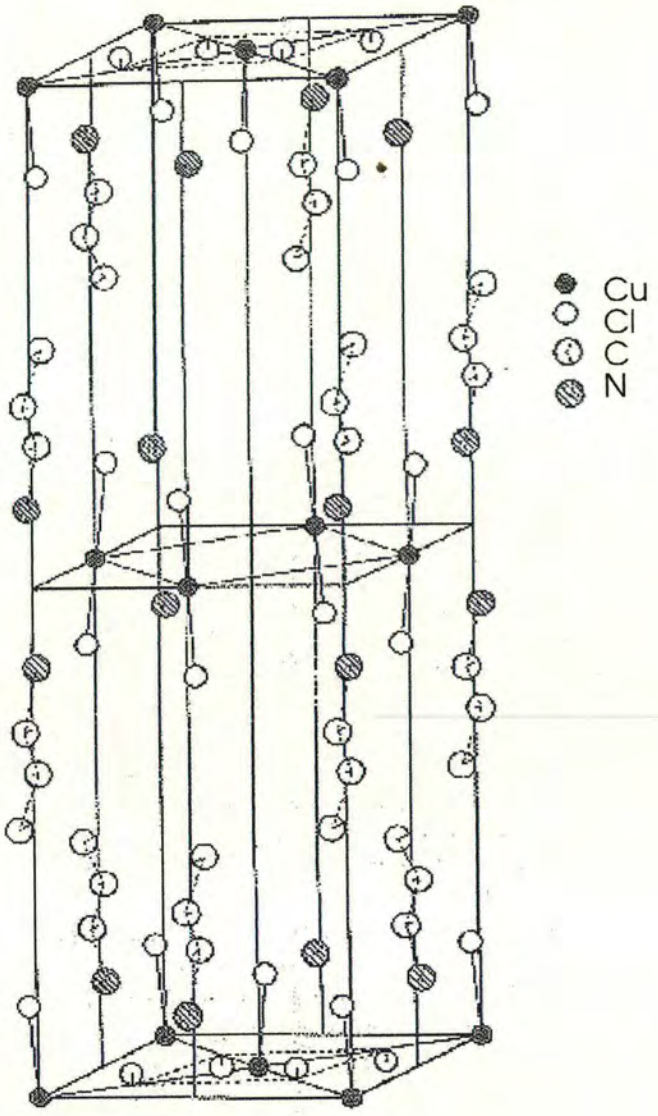

Figure 1.3. The crystal structure of $(C_3H_7NH_3)_2CuCl_4$. Part of the propyl ammonium groups and H atoms have been omitted for the sake of clarity [13]

1.2. Phase transitions and critical phenomena

The nature of an ordered phase provides some insight into the microscopic character of a material and a link with the terms in the Hamiltonian. Further information about

a magnetic system may be gained by examining the nature of any transitions between phases, e.g. to an ordered or disordered magnetic phase. Magnetism is also a useful method by which to study the nature of phase transitions in their own right. The study of phase transitions is a cross disciplinary subject with links to almost all the physical and life sciences, with tremendous technological implications.

One of the most familiar examples of a phase transition is between the gas and liquid states of a fluid, and this may be influenced by controlling some external parameter such as pressure, P, or temperature, T. Thus the state of the system is defined in terms of variables such as P, T and density, ρ, and we may conveniently summarise the response the of system to the various influences as a phase diagram, drawing out the boundaries between phases in terms of factors such as P and V. In the case of the gas-liquid transition on warming at constant pressure, the free energy G of the system passes discontinuously from one phase to the other and the transition is said to be first order; other thermodynamic variables such as entropy or density will also undergo a discontinuous transition at this point. However, as one moves along the phase boundary to higher temperatures, the difference in density between the gaseous and liquid phases becomes smaller until at a particular point called the critical point, the difference disappears. Beyond this point there is no distinction between the liquid and gas phases. This form of phase transition is analogous to the behaviour of an exchange-coupled antiferromagnet on cooling. At relatively high temperatures there is little correlation between moments, but this increases until at a critical temperature, long-range order sets in. Close to and below this point, called the Néel temperature (T_N), a considerable proportion of the moments are still not correlated, and we can define an order parameter, <p>, that describes the degree of the order in terms of the percentage of moments that are correlated according to the fashion expected for the perfectly aligned antiferromagnet, which is called the sublattice magnetisation. This is

analogous to the difference in density between gas and liquid phases in the gas-liquid transition. Some thermodynamic properties of the system may now vary in a non-discontinuous fashion as the critical point is approached; for example <p> for an antiferromagnet in zero applied magnetic field may vary with T as T approaches T_N as $((T_N-T)/T_N)^{\beta}$, where β is the critical exponent for the magnetisation. In Table 1.1 we give an number of examples of phase transitions that may show critical phenomena.

Table 1.1 Some phase transitions and associated order parameters [17].

Transition	Order Parameter <p>	Free Choice in <p>	Thermodynamic conjugate of <p>
liquid-gas	density difference $\rho - \rho_c$	liquid or gas	Chemical potential μ
Ferromagnet-paramagnet	magnetisation M	if n equivalent 'easy axes' 2n choices	Magnetic field H (along easy axes)
Antiferromagnet-paramagnet	sublattice magnetisation	if n 'easy axes' 2n choices	not physical
Superconductor-normal metal	Δ (complex gap parameter)	phase of Δ	not physical
Superfluid-normal fluid	<Ψ>(condensate wave function)	phase of <Ψ>	not physical
Ferroelectric-unpolarised	lattice polarisation		electric field
phase separation in alloy	concentration	2 choices	difference of chemical potentials

What is remarkable is that the critical properties for very different physical systems may be very similar – that is the dependence of the relevant order parameter on some thermodynamic variable such as temperature will behave not only according the same functional form as the sublattice magnetisation does for a antiferromagnetic-paramagnetic phase transition, but that the critical exponent β may also adopt the same value. It has been found that for systems such as an antiferromagnet in which

the bulk properties depend on the collective and cooperative behaviour of the constituent parts, the critical properties may only depend on the dimensionality of the interactions (for example the dimensionality of the network of the most significant exchange interactions), the dimensionality of the order parameter (the number of components of spin involved in the exchange interaction) and whether the forces involved are short or long range [18-20]. This is the Theory of Universality [20], and one of its consequences is that the study of one type of phase transition can enhance our understanding of an unrelated type of physical transformation. Thus, the study of structural distortions and structural and magnetic phase transitions can yield information about the nature of phase changes in general. As discussed above, the dimensionality of magnetic interactions in insulators can be controlled relatively easily, so model magnets are particularly interesting in this context.

1.3. Low dimensional systems

The design and study of magnetic materials is important in developing the understanding of fundamental magnetic interactions, and also of more general electronic behaviour. It is also important in developing theories of cooperative phenomena, through the study of phase transitions in materials designed to have specific spin or lattice dimensionality; which may then be related to transitions in quite different physical systems, but linked through the principle of Universality. There is therefore a strong incentive to design, synthesise and study model materials with specific variable-dimensional properties. Frequently the properties of low dimensional materials are more readily treated by exact theory. Ising first proposed a theory for the ordering of a one dimensional antiferromagnet in 1925, finding that an infinitely long 1-D system only undergoes long-range order at absolute zero [21]; the classic work of Onsager in 1944 produced an exact solution of the thermodynamic properties

of the 2D Ising model in zero field [22]. Experimentally it is difficult to produce a truly one or two-dimensional material on which to test the theory, but chemists may manipulate the crystal structure of a material to optimise structural anisotropy to produce chainar or layered materials whose properties resemble idealised 1-D or 2-D magnets. We have already seen the structure of $Cu(NH_3)_4SO_4.H_2O$, the first system found to exhibit linear chain or 1-D magnetism (Figure 1.2); the susceptibility and specific heat data were found to contain broad maxima at low temperatures rather than the sharp cusp expected for a 3-D magnet near any long-range ordering transition, confirming the belief that at a given finite temperature, low-dimensional magnets are more susceptible to disruption by thermal fluctuations than 3-D magnets. Since then many more 1-D and 2-D magnets have been synthesised, and theoretical developments have progressed in parallel. The degree of sophistication of the materials produced has become greater as the models required for study have become more complex [23], and as chemists have become more skilled at manipulating magnetic architecture.

This thesis concerns a class of material, namely hexagonal perovskites of general formula ABX_3, where A is usually a univalent cation, B is usually a divalent cation, and X is usually a halide ion, $CsNiCl_3$ being a good example of a material with this structure and composition. Such materials have provided a rich source of 1-D model magnets for decades [23]. More recently, they have also been recognised as model systems for the study of more subtle co-operative phenomena that depend on small changes in the nature of the exchange between the magnetic chains in the material [24,25]. We will first consider the structure of these materials, and then their magnetic properties.

1.4. ABX_3 structures

Ionic materials of general composition ABX_3, where A and B are cations and X is an anion, have been found to exhibit a large range of structure types, the most important of which are the calcites, aragonites, ilmenites, perovskites, hexagonal structures and the pyroxenes [26]. These differences in structure are dictated by the radius ratios of the constituent ions; varying the pressure and temperature of these materials can provide a wide range of structural phase transitions. This can allow manipulation of many structural possibilities and therefore, in the case where B is magnetic, such as a first-row transition metal ion, this affords a large number of potential model magnetic materials and phase transitions in general.

The ideal perovskite structure can be described as cubic close-packed structure in which the A and X ions are stacked in cubic-close packed layers along the cubic (111) direction, the B cations then reside in 1/4 of the octahedral holes. The structure is shown in Figure 1.4, this can also be represented as an array of corner sharing BX_6 octahedra, as illustrated in Figure 1.5.

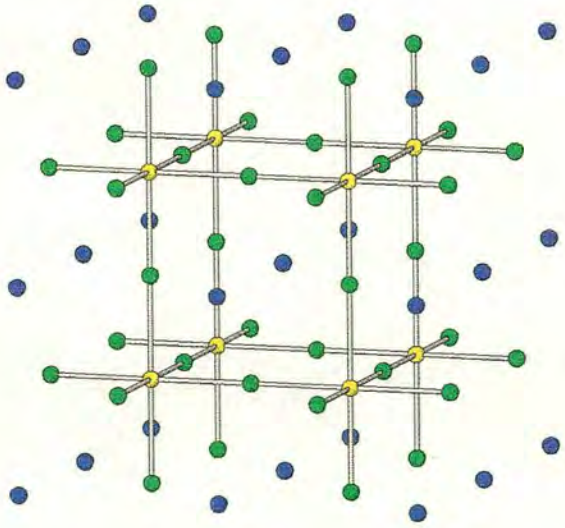

Figure 1.4. The perovskite cubic close packed structure as exhibited by ABX_3 materials; A(blue), B(yellow) and X(green).

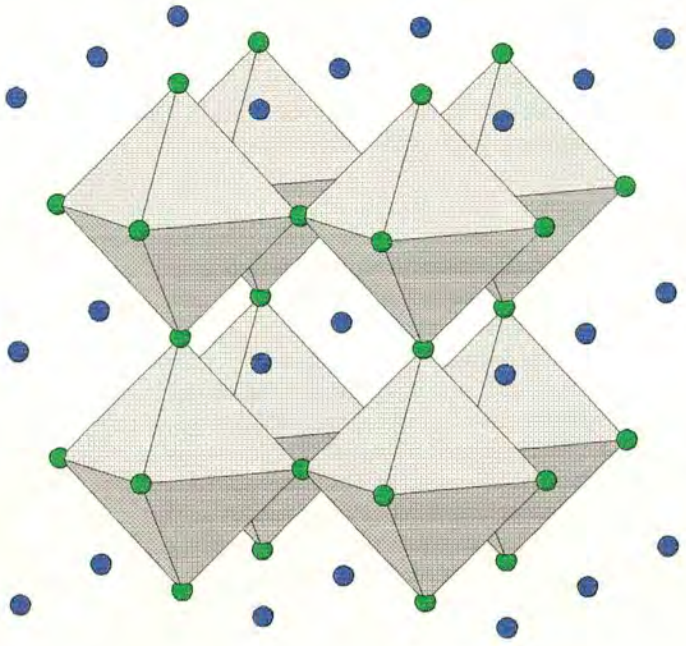

Figure 1.5. The cubic perovskite structure can also be represented by an arrangement of BX_6 octahedra in cubic perovskite.

In cubic perovskite materials it is interesting to observe the dependence of physical properties on structure - most notable perhaps are the industrially exploitable characteristics such as ferroelectricity and co-operative magnetism, and more recently in the development of high capacitance dielectric materials and highly magnetoresistant materials [27]. The structure, and therefore the electro-magnetic behaviour, is critically sensitive to not only the nature of the atoms but also to the temperature and pressure of the system. Distortions in this structure are may be described by relative tilting of the octahedra, the various structures and structural distortions of the cubic perovskites have been well explored and are now reasonably well understood [28].

The relative size of the ions is critically important in deciding which structure is adopted by an ABX_3 compound. When the B cation is small relative to X then cubic perovskite structure distorts away from cubic close-packed (ccp) to a hexagonal hexagonal close-packed (hcp) system. In the hexagonal system, the octahedra fold together to form face-sharing chains. The hexagonal perovskite structure is shown in Figure 1.6. This can again be represented by BX_6 octahedra; in this case the octahedra are face-sharing and can be seen to form chains with respect to the *c*-axis; this is illustrated in Figure 1.7.

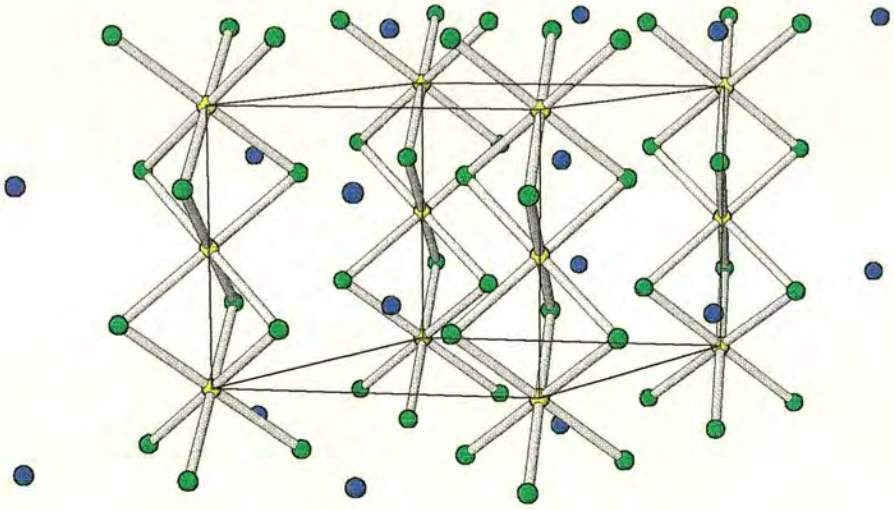

Figure 1.6. The hexagonal perovskite ABX_3 structure; A(blue), B(yellow) and X(green). In the hexagonal perovskite structure the smaller size of the B cation causes the AX_3 layers to become hexagonal close-packed.

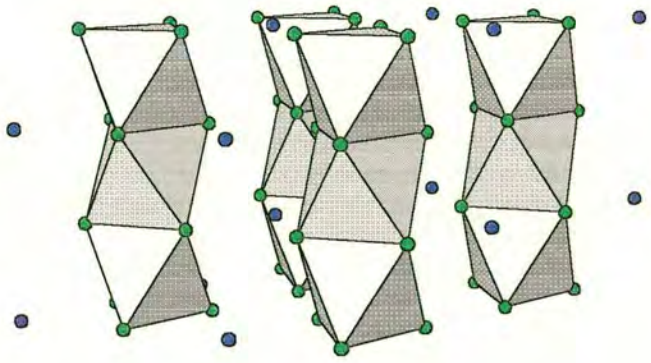

Figure 1.7. The hexagonal perovskite structure can be represented by face sharing BX_6 octahedra, separated by A cations.

Intermediate structures are also known where some percentage of octahedra share faces or edges. These hexagonal structures can all be derived by the close-packing of AX_3 layers along the *c*-axis, with the B cations filling 1/4 of the octahedral holes. If the AX_3 layers are stacked with a cubic-close packing the ideal perovskite structure is obtained. If the layers are hexagonal close-packed then the $BaNiO_3$, or hexagonal perovskite structure is obtained. If the packing is part cubic and part hexagonal close packed then many structures are possible; a few of those observed are shown in Table 1.2 [29], *c* corresponds to the repeat distance in the *c*-direction.

Table 1.2. Close-packed stacking of the AX_3 layers in ABX_3 materials can produce hexagonal perovskite, cubic perovskite and several intermediate structures [29].

Projection of octahedral network on the (110) plane of the hex. cell	Structure Type	Number of Layers	Percent Face Sharing	Stacking sequence of close-packed AX_3 Layers
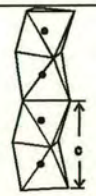	[$BaNiO_3$]	2	100%	ABAB (hhh...)
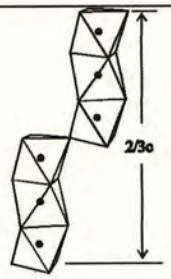	[$BaRuO_3$]	9	67%	ABCBCACAB (chh...)
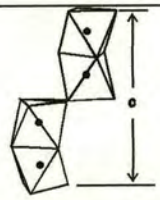	[High-$BaMnO_3$]	4	50%	ABAC (chch...)
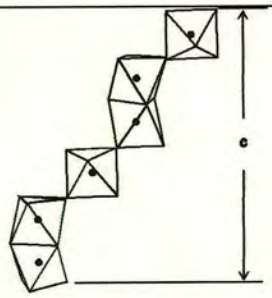	[hex-$BaTiO_3$]	6	33%	ABCACB (cch...)
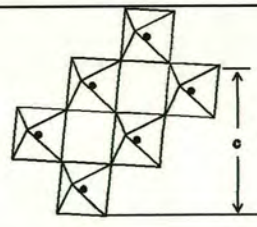	[perovskite]	3	0%	ABC (ccc...)

The materials of interest in this project are those which possess the ideal hexagonal perovskite structure, *i.e.* those whose structures are described by BX_3 chains separated by A cations. Specifically, those in which A is a monovalent cation, B is a divalent first row transition element and X is a halogen (usually Cl or Br, as the flouride compounds generally adopt the cubic perovskite structure and the iodides with ABX_3 formula are often not found [30]). The structure is also found to be sensitive to the size and shape of the A cation. Another avenue of modification available, therefore, is to have a non spherical A spacer ion, e.g. ammonium (NH_4^+) and tetra-methyl ammonium (NMe_4^+), between the BX_6 octahedral chains thus changing the site symmetry of the A cation position.

Many materials of this type have been studied, Tables 1.3 and 1.4 show a summary of the crystallographic space groups obtained for a range of chloride and bromide compounds where A is Rb, Cs, NH_4 and NMe_4 [31]. Those materials which adopt the hexagonal perovskite structure can usually be described by the space group $P6_3/mmc$ and the hexagonal unit cell can be described as a x a x c, where a is the separation between the BX_3 chains and c includes two B-B distances along the chain axis; this unit cell is shown in Figure 1.8.

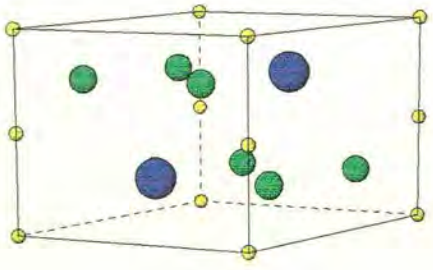

Figure 1.8. Hexagonal perovskite ABX_3 a x a x c unit cell with $P6_3/mmc$ symmetry. Blue = A^+, Yellow = B^{2+} and Green = X^-

Table 1.3. Structures adopted by the $ABCl_3$ materials; all hexagonal cells are *a* x *a* x *c* unless otherwise indicated. (Ionic radii, r_i, taken from R. D. Shannon [32])

$B^{2+} \rightarrow$ $A^{+} \downarrow$	r_i / nm	Rb	Cs	NH_4	NMe_4
r_i / nm		0.149	0.170	0.150	-
Mg	0.072	-	$P6_3/mmc$ [33]	cubic[34]	-
Ti	0.086	$P6_3/mmc$[34]	Hexagonal [34]	-	-
V	0.079	$P6_3/mmc$ [35]	$P6_3/mmc$ [36]	Hexagonal [34]	$P6_3$ mc [36]
Cr	0.073 low spin 0.080 high spin	$P6_3/mmc$ ↓ C2/m ->C2 ($\sqrt{3}$a x a x c) [37,38,39]	$P6_3/mmc$ ↓ C2/m [37,38]	Distorted NH_4CdCl_3 structure [34]	$P6_3/m$ [40,41]
Mn	0.067 ls	$P6_3/mmc$ [42]	R3-m [43]	Cubic Pm3m ↓ orthorhombic Pbnm [44,34]	$P6_3/mmc$ ↓ $P6_3/m$ ↓ P21/m [45,46,47]
Fe	0.061 ls 0.078 hs	$P6_3/mmc$ [48]	$P6_3/mmc$ [48]	$P6_3/mc$ [49]	P31 c [50]
Co	0.065 ls 0.0745 hs	$P6_3/mmc$ [51]	$P6_3/mmc$ ↓ $P6_3/mcm$ ($\sqrt{3}$a x $\sqrt{3}$a x c) [52,53]	$P6_3/mmc$ [41]	
Ni	0.069	$P6_3/mmc$[54]	$P6_3/mmc$ [55]	$P6_3/mmc$ [42]	$P6_3/m$ ↓ $P2_1/a$ (2a x a x c) [56,45]
Cu	0.073	orthorhombic NH_4CdCl_3 structure [34]	$P6_3/mmc$ Jahn-Teller distortion [57]	$P2_1/c$ [42,58]	$P6_3/mmc$ ↓ C2/m ↓ $P2_1$ [59]
Cd	0.095	Pnam [42]	$P6_3/mmc$ [42]	Pmnb [60]	$P6_3/mmc$ ↓ $P6_3/m$ ↓ $P2_1/m$ [45,61]

Table 1.4. Structures adopted by the $ABBr_3$ materials; all hexagonal cells are *a* x *a* x *c* unless otherwise indicated. (Ionic radii, r_i, taken from R. D. Shannon [32])

$B^{2+} \rightarrow$ $A^{+} \downarrow$	r_i / nm	Rb	Cs	NH_4	NMe_4
r_i / nm		0.149	0.170	0.150	-
Mg	0.072	$P6_3/mmc$ ↓ $P6_3mc$ ↓ incommensurate structure [34]	$P6_3/mmc$ [34]	hexagonal [34]	-
Ti	0.086	-	-	-	-
V	0.079	-	-	-	-
Cr	0.073 l s 0.080 h s	$P6_3/mmc$ [37]	$P6_3/mmc$ [37]	$P2_1/c$ [34]	$P6_3$ [40,41]
Mn	0.067 ls	$P6_3/mmc$ ↓ $P6_3mc$[34]	$P6_3/mmc$ [62]	Pmnb [63]	$P6_3/mmc$ ↓ $P6_3/m$ ↓ $P6_3$ [64]
Fe	0.061 ls 0.078 hs	$P6_3/mmc$ ↓ $P6_3mc$[65] $P6_3$ cm [66] ($\sqrt{3}a$ x $\sqrt{3}a$ x c)	$P6_3/mmc$ [67]	$P6_3$ [68]	-
Co	0.065 ls 0.0745 hs	$P6_3/mmc$ [34]	$P6_3/mmc$ [69]	hexagonal [34]	-
Ni	0.069	$P6_3/mmc$ [54]	$P6_3/mmc$ [61]	hexagonal [34]	$P6_3$ [61]
Cu	0.073	$P6_3/mmc$ [37]	$P6_3/mmc$ [37]	$P2_1/c$ [34]	-
Cd	0.095	Pmnb [70]	$P6_3/mmc$ [34]	Pmnb [71]	$P6_3/m$ [72]

The factors influencing which structure is adopted by a particular compound involve a delicate balance of ionic and covalent interactions, and precise theoretical predictions are not yet good enough to allow the prediction of the structure type of a new material. The behaviour of a series of compounds can be summarised in an empirical way in what is called a structural field map. The structural field maps for the $ABCl_3$ and $ABBr_3$ compounds are shown in Figures 1.9 and 1.10 respectively [34].

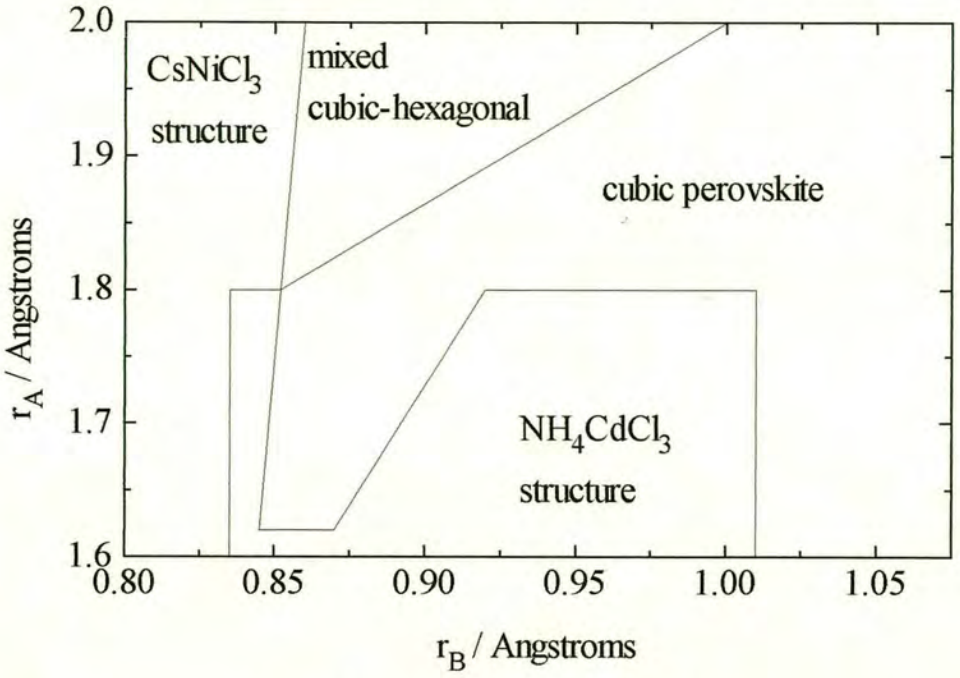

Figure 1.9. Structural field map for $ABCl_3$ materials [34].

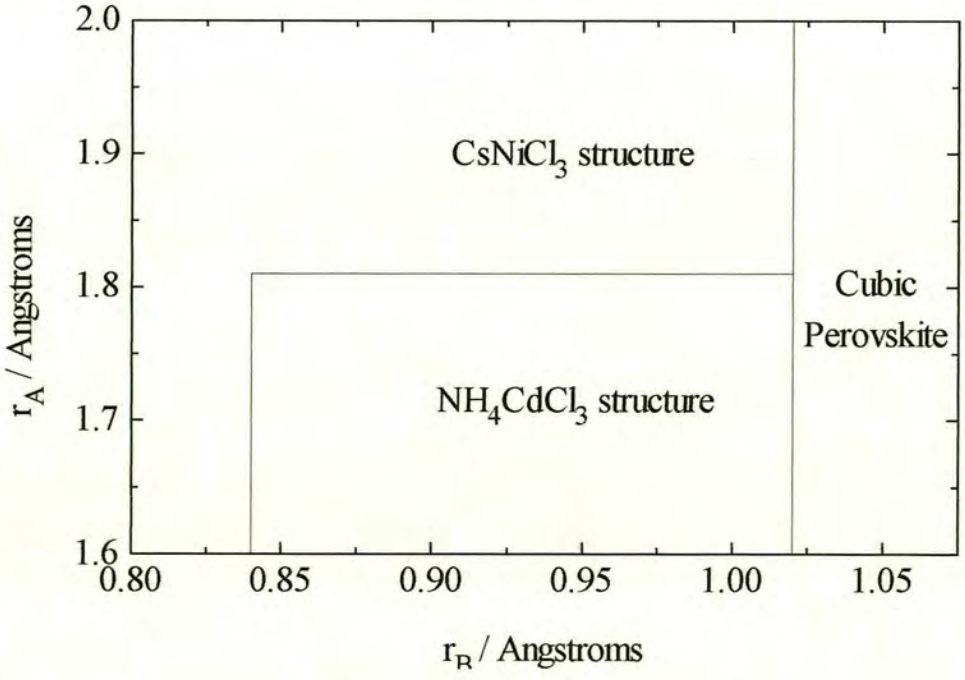

Figure 1.10. Structural field map for $ABBr_3$ materials [34].

Some materials listed in Tables 1.3 and 1.4 can be seen to distort to lower symmetry as the temperature is decreases; their symmetries are shown with the room temperature structure at the top and the succeeding lower temperature structures indicated with arrows. Some of these lower-symmetry phases involve very small distortions, reflecting the fact that distortions may be driven by relatively weak interactions.

There are several possibilities for distortion in the hexagonal perovskites. If the structure is considered from the perspective shown in Figure 1.11, *i.e.* looking along the *c*-axis, the unit cell can change in a few important ways, some possibilities are shown Figure 1.12. The distortions can be considered largely in terms of twisting and slipping of BX_3 chains.

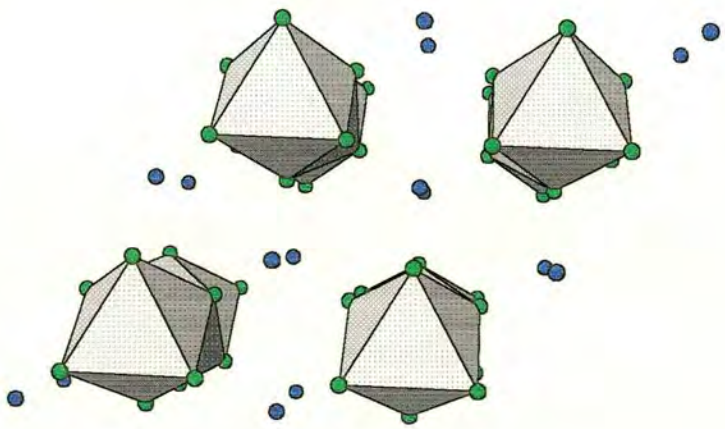

Figure 1.11. The hexagonal perovskite structure viewed along the *c*-axis. This is referred to as the *a b* or basal plane.

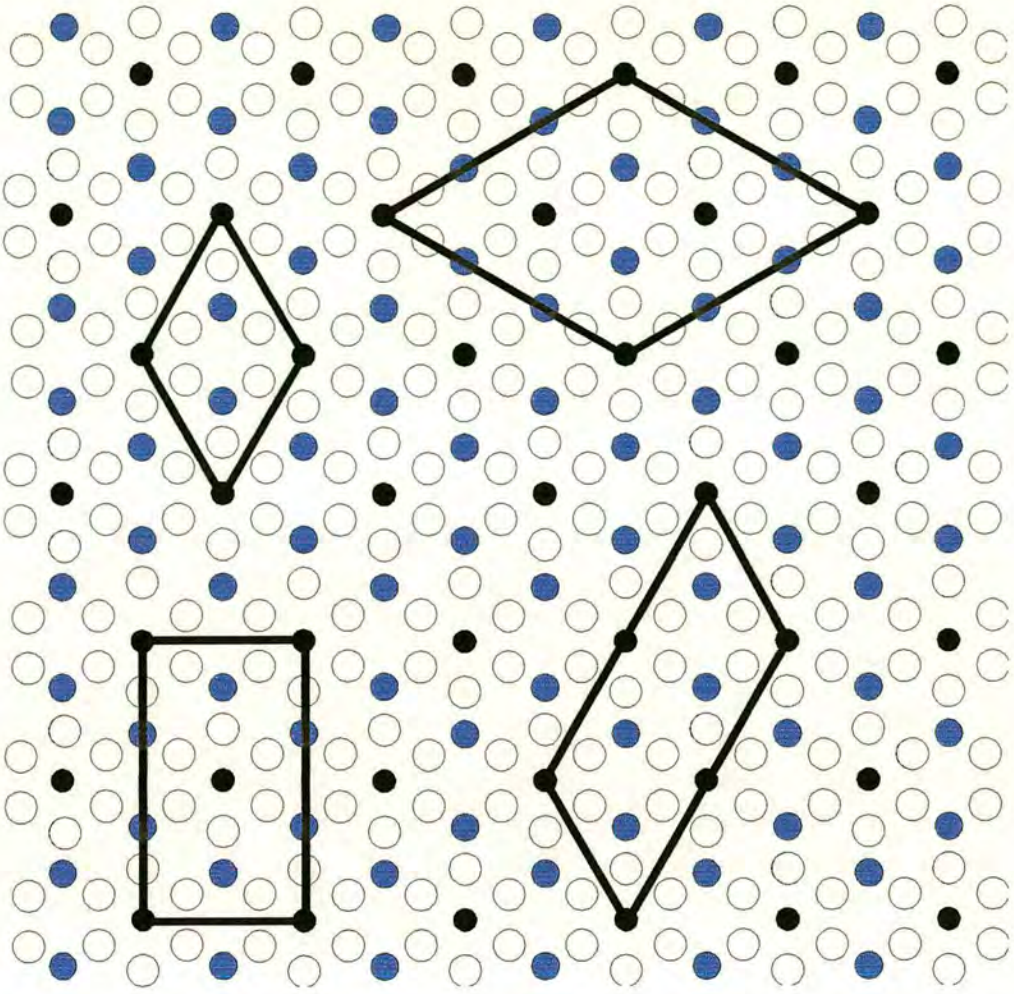

Figure 1.12. Some unit cell possibilities, shown in the *a b* plane, clockwise from top left - hexagonal *a x a x c*, hexagonal $\sqrt{3}a$ *x* $\sqrt{3}a$ *x c*, monoclinic *2a x a x c* and orthorhombic $\sqrt{3}a$ *x a x c*. Blue circles represent A, B -Black and X - white.

1.5. Cooperative magnetism in hexagonal perovskites

In the hexagonal perovskite structure BX_6 octahedra fold together to share faces, forming essentially infinite, BX_3 chains along the *c* axis; this is shown in Figure 1.13. This structural anisotropy has an important consequence if the B cation is magnetic; the magnetic exchange is likely to be more significant along the chains than between

the chains. As the separation between the chains is increased the magnetic behaviour should tend towards that of an ideal 1-D magnetic system. However, the interchain exchange in hexagonal perovskites can not be ignored, and even in compounds in which the A cation is particularly large such as the tetramethylammonium salts NMe_4MnCl_3, three-dimensional magnetic long-range order sets in at low temperatures [23]. Hexagonal perovskite materials are therefore described as *pseudo*-1-D.

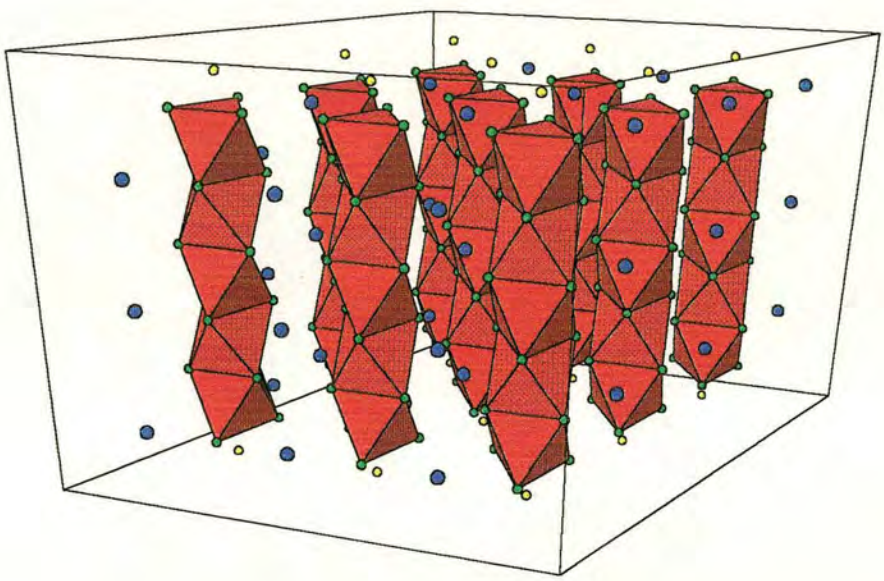

Figure 1.13. In the hexagonal perovskite structure, BX_6 octahedra share faces to form infinite chains in the *c*-direction with A^+ cations (A^+ is shown in blue, B^{2+} is yellow and X^- is green). When B is a magnetic ion the material may behave as a pseudo-one dimensional magnet.

Magnetic exchange between ions results from fundamental atomic and quantum mechanical factors, principally coulombic repulsion between electrons, the Pauli

Exclusion Principle and Hund's rule of maximum multiplicity. Although exchange can occur directly, between magnetic ions with significant orbital overlap in insulating materials, more often the pathway is largely via intervening diamagnetic ions. This mechanism is known as 'superexchange' and was first postulated by Kramers in 1934 [73]. In an insulator magnetic cations, separated by distance r, may interact *via* several exchange mechanisms [74], resulting in a net exchange interaction J with a particular sign and strength. The various common contributions to the exchange mechanism are outlined briefly in Table 1.5. In general, the terms that provide an antiferromagnetic interaction are more common and stronger than the terms that lead to ferromagnetic exchange, and the great majority of exchange-coupled insulators are coupled antiferromagnetically. The strength and sign of the exchange constant, J, is dictated by three major factors: (a) the nature of the magnetic ions (M) (i.e. the orbital geometry and occupancy), (b) the geometry of the exchange pathway and (c) the nature of the diamagnetic bridging ion (X). We shall consider a particular case below that illustrates some of these factors. For given metal ions coupling through comparable bridges of the same geometry, range of the superexchange interaction falls off rapidly with distance r, typically varying as r^{-9} to r^{-12} - in comparison with the relatively long range of magnetic dipole-dipole interactions which decrease as r^{-3}.

Table 1.5. Mechanisms of exchange in insulating magnets

Mechanism	Description
Direct	via B – orbitals on X and M are orthogonal => FM
Kinetic	'virtual' transfer of e^- from X into corresponding orbital on neighbouring X, always AFM
Spin polarisation	transfer of an e^- from B to an empty M orbital =>FM
Correlation	2 e^- transferred from X to 2 half filled orbitals on B – simultaneous bond formation =>AFM

If a magnetic material is cooled to sufficiently long temperatures a co-operative transition may occur to an ordered magnetic state. The configuration adopted by the moments depends primarily on the sign of the exchange of an ion with its neighbours, and on the topology of the lattice for the exchange pathways. Thus, for moments that lie at the vertices of a square lattice and couple through nearest-neighbour antiferromagnetic exchange, it is possible to arrange the moments so that each is antiferromagnetically coupled to all of its neighbours. However, there are cases where the lattice topology prevents this. Consider the element of a triangular lattice depicted in Figure 1.14(a) in which the spins are free to rotate in the plane of the paper and are coupled antiferromagnetically.

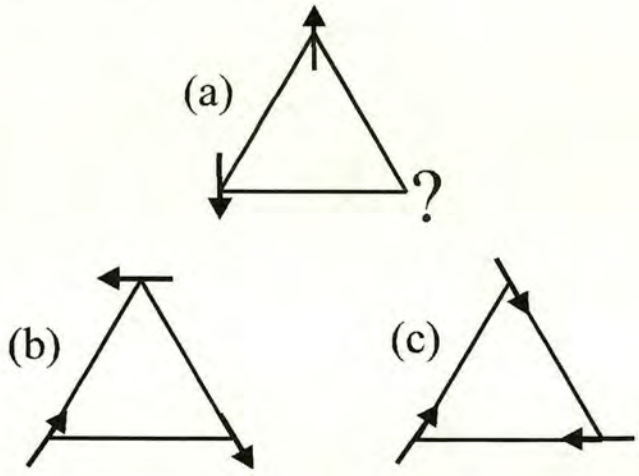

Figure 1.14. Magnetic moments on a triangular antiferromagnet are geometrically frustrated, (a) three adjacent moments cannot all align antiparallel to each other (b) and (c) two degenerate 120° compromise arrangements

It is possible to place any pair of moments in the antiparallel arrangements of 1.14(a), but not a third so that all pairs are *simultaneously* antiparallel. This is a case of geometric *frustration* [75] for nearest-neighbour exchange, this will afflict any antiferromagnet with an odd number of bonds in a closed loop in the lattice. The

compromise situation, with the lowest exchange energy, is shown in Figure 1.14(b). It should be noted that this canted antiferromagnet (c), has a handedness or chirality which introduces another degree of freedom or degeneracy which has been postulated [76] to change the Universality Class of the magnet.

There are other ways in which frustrated lattices may be constructed - in some cases leading to greater degeneracy and the formation of fluctuating ground states. The Kagome lattice depicted in Figure 1.15(b) is such a case. The lattice is constructed from triangles, but now they are connected through their vertices. For the regular triangular lattice, adjacent triangles share edges, and the configurations of spins in one triangle fixes that in neighbouring triangles unambiguously; this is not so for the Kagome lattice, and many spin states are allowed that produce the minimum energy 120° array in each elemental triangle [77-81] Figure 1.15(b) and 1.15(c) show two such spin states.

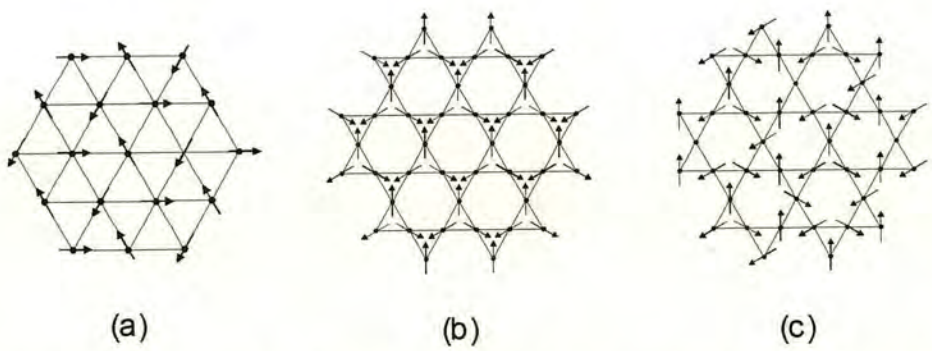

Figure 1.15. Spin arrays for antiferromagnetically coupled XY moments on (a) triangular lattice and (b) a Kagome lattice; (c) depicts an alternative spin state to (b) with the same energy.

ABX_3 compounds which exhibit the hexagonal perovskite structure provide examples of a stacked triangular lattice; two dimensional triangular layers of B atoms sit directly

above one another along the *c*-axis, coupled in this direction with exchange *J* which is usually antiferromagnetic. In all known cases, the magnetic exchange interactions in the *a b* plane are also antiferromagnetic, with exchange constant *J'*. *J* propagates through a single B-X-B bridge (Figure 1.16) rather than the lengthier B-X-X-B bridges (Figure 1.17) which link the chains in the *a b* plane, and in general the ratio *J*/*J'* ranges from greater than 100 to approximately 10.

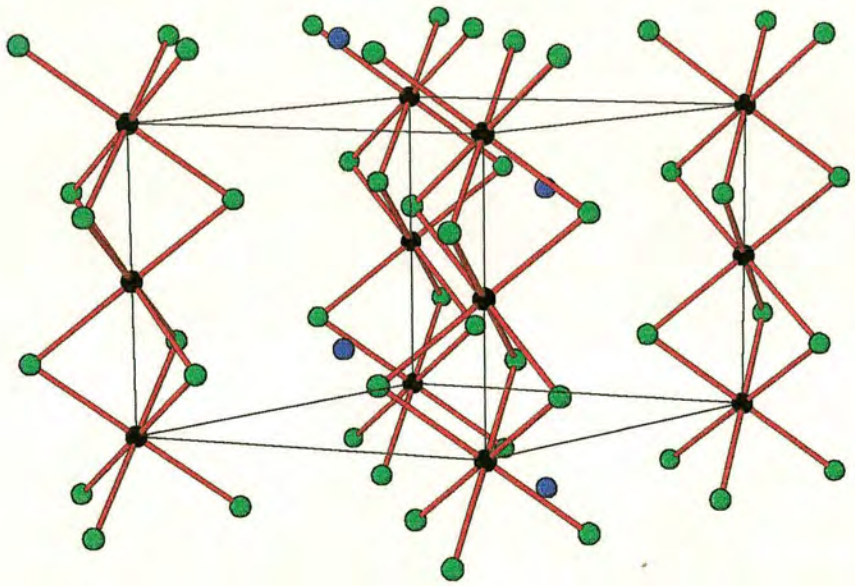

Figure 1.16. Magnetic B cations (shown in black) are coupled along the *c*-direction by superexchange, which acts through the neighbouring X anions (green), with exchange constant *J*. Exchange pathways are shown in red.

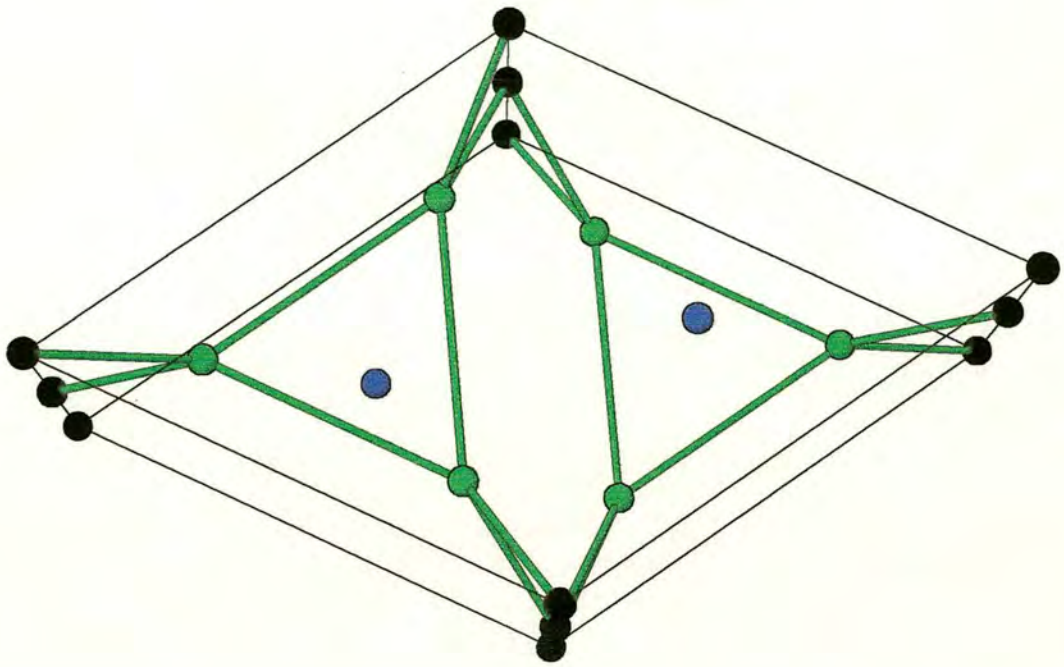

Figure 1.17. Interchain magnetic exchange pathways in ABX_3 hexagonal perovskites (shown in green), with exchange constant *J'*, between the B cation (black) chains occurs *via* two intervening X anions (green). In this diagram the structure is oriented with the *c*-axis pointing out of the page.

1.6. $AFeX_3$ Materials

In ABX_3 hexagonal perovskites where B = Fe^{2+} the magnetic behaviour is particularly rich, and two observations highlight the delicate balance between structure and magnetism. The first of these involves the nature of magnetic exchange within the

FeX_3 chains. In ABX_3 materials in general, the intrachain magnetic exchange occurs *via* a super-exchange interaction involving the exchange pathway along X - B - X, (see Figure 1.16 above) where the bond angle is somewhat smaller than 90°. The sign and strength of this exchange depends on the balance between a ferro- and an antiferomagnetic term. If there is an orthogonal link in the exchange bridge - for example if the pathway for exchange involves the p_x and p_y orbitals on the halide ion - ferromagnetic exchange is predicted by Hund's first rule; alternatively, if there is clearly an admixture of orbitals in the bridge - for example if σ-bonding orbitals on the iron atoms interact significantly with s-symmetry orbitals on the halogen atom, or with the p_x and p_y orbitals with a bridging angle significantly different from 90°, then antiferromagnetic contributions will occur, in accordance with the Pauli exclusion principle (PEP). In the $AFeX_3$ materials studied to date (where A = Rb and Cs) the X-Fe-X angle is found to be very close to the point where the two competing factors, dictating the interchain exchange, cross over: $AFeCl_3$ is found to order ferromagnetically along the chains, but the slightly larger Br^- ion causes the B-X-B bridging angle to become more acute and the resulting exchange is antiferromagnetic [33,82-83]. In all cases none of the bridging angles involved in the B - X -X - B interchain superexchange pathway are close to being orthogonal, and *J'* is always anti-ferromagnetic.

The second observation highlighting the balance between structure and magnetism in $AFeX_3$ compounds concerns a competition between the influence of the ligand-field and the exchange interactions on the size of the magnetic moment on the Fe^{2+} ions. For reasons that will be considered in greater detail in the next Chapter, the effect of the ligand field and spin-orbit coupling on the ^5D free-ion term of Fe^{2+} in hexagonal perovskites is to produce a singlet ground state, with a low-lying excited doublet. If the ions were isolated, these materials would be expected to be diamagnetic at

temperatures where there was negligible population of the excited state. However, a magnetic moment may be induced either through the application of an external magnetic field, Zeeman-splitting the excited state and mixing it into the ground state, or through magnetic exchange, which has a similar effect. There is a fine balance between these two influences: the rubidium salts in $RbFeX_3$ (where X is Cl or Br) possess a magnetic moment down to the lowest measured temperature of the order of 1K, while in the cesium salts, $CsFeX_3$ (where X is Cl or Br), the larger Cs^+ ion causes the separation between the FeX_3 chains to increase, the subsequent interchain exchange is then too weak to induce long range ordering.

1.7. Aims of this project

The very delicate balance of forces in $AFeX_3$ salts with the hexagonal perovskite structure makes them a good subject for the study of structure - magnetism correlations. This project is concerned with the study of the changes in magnetic properties afforded if A is a non-spherical cation such as NH_4^+. The effects likely to be important here involve the temperature dependence of the motion of the NH_4^+ group and hydrogen bonding as its orientation freezes out. In practice the most incisive technique for elucidating magnetic structure is neutron scattering, which requires us to work with compounds in which H is replaced by D, so we also considered the effect of ND_4^+ substitution on the structure. NH_4FeCl_3 and NH_4FeBr_3 have been made previously, and preliminary studies show them to have the hexagonal perovskite structure [84,68]. NH_4FeF_3 has the cubic perovskite structure and attempts to make $AFeI_3$ to date have only yielded incongruently melting mixtures [30]. We also planned to prepare materials with yet larger and low-symmetry A cations, attempting to substitute various alkyl ammonium ions in this position. It was anticipated that these various types of substitution might lead to distorted crystal

structures, which in turn might have networks of exchange interactions that are of lower symmetry than in the undistorted compounds. This in turn might upset the balance of forces in the frustrated *a b* plane, leading to more complex spin structures. This is a field of considerable current interest, as part of a more general problem in materials with degenerate or fluctuating magnetic ground states, and there is a significant amount of theoretical work devoted to predicting the behaviour of distorted triangular lattices [25,24,85-92]. There are, however, relatively few model systems to test such theoretical work, and one of the aims of this thesis was to investigate the suitability of $A'BX_3$ compounds, in which A' is chosen to drive a particular type of deformation.

A second strand to this work was an investigation of the influence of doping $RbFeX_3$ compounds with Cs analogues to investigate the way in which such substitution broke up the magnetic long-range order. It may be anticipated that for low concentrations of Cs^+ ions, local distortions in the vicinity of a Cs ion disrupt the exchange field and lower the value of local moments. This effect can be reversed in the pure compounds by the application of an external magnetic field, so one might expect a similar response in the doped materials. In effect, an applied magnetic field might reverse the effect of doping and make the material homogenous once more. Preliminary measurements on doped $RbFeCl_3$ support this hypothesis: neutron scattering measurements [93] on samples of $Rb_{1-x}C_xFeCl_3$ with x = 0.05 - 0.44 reveal a destruction of long-range magnetic order for the smallest amounts of dopant, producing at most short-range correlations at temperatures down to almost 50% of T_N for the pure compound, and the observation of broad, magnetic Bragg peaks at low temperatures. However, on application of a magnetic field of up to 5T, these Bragg peaks sharpened considerably, and although true long-range order was not

quite restored (the peaks remained resolution limited) the field had clearly reversed much of the disorder induced by doping.

1.8. Thesis Summary

The main aim of this work is a detailed study of the nuclear and magnetic structure of the hexagonal perovskites NH_4FeX_3 (X = Cl, Br) in any structural and magnetic phases, in order to provide a comprehensive understanding of the relation between the structure and magnetism although the ultimate aim is to unify treatment of the two in the final discussion. An account of more detailed magnetic models to treat the particular case of $AFeX_3$ magnetic materials in given in Chapter 2. Chapter 3 provides an introduction to the rudiments of diffraction and a short description of the diffractometers used during this project. The results obtained from X-ray and neutron diffraction experiments on NH_4FeCl_3 are discussed in chapter 5 and a quasi-elastic study carried out on this material is described in Chapter 6. Chapter 7 describes the results obtained from diffraction experiments on NH_4FeBr_3 and Chapter 8 contains magnetic susceptibility measurements taken on both NH_4FeCl_3 and NH_4FeBr_3 and on Cs doped $RbFeBr_3$ materials. Finally the main points and results are summarised in Chapter 9.

2. Magnetism

2.1. Introduction

A successful theory of the magnetic behaviour of a material should provide a link between the various experimentally observed magnetic properties, and a microscopic description of the constituent atoms and the nature of their interactions. This Chapter will first outline how the bulk magnetic susceptibility of the material may be measured, this being the most readily accessible probe of magnetic properties for most experimentalists. The chapter will then discuss how the susceptibility may be related to the magnetic Hamiltonian, starting with a simple (Curie) model for magnetism. The Curie model is then developed as the various assumptions on which it rests are stripped away, these being inadequate for a low-dimensional exchange-coupled magnet with significant ligand field effects. Later Chapters will describe the principles and practice of elastic neutron scattering measurements, which provide a more incisive probe of microscopic magnetic properties.

2.2. Measurement of Magnetic Susceptibility

If a material is placed in a magnetic field $\boldsymbol{B}_0$ it may be polarised to a degree $\boldsymbol{M}$ per unit volume so that the total field $\boldsymbol{B}$ in the material is given by:

$$\boldsymbol{B} = \boldsymbol{B}_0 + \mu_0 \boldsymbol{M} = \mu_0(\boldsymbol{H}+\boldsymbol{M}) \qquad (2.1)$$

Where μ_0 is the permeability of free space and has the value $4\pi \times 10^{-7}$ Hm^{-1}. $\boldsymbol{B}$ is also called the magnetic induction and has units of Tesla, while $\boldsymbol{H}$, somewhat confusingly,

is called either the magnetic field or the magnetic force, and is measured in A m^{-1}. $\boldsymbol{M}$ is called the magnetisation of the sample per unit volume and has the same units as $\boldsymbol{H}$. The volume magnetic susceptibility χ is the ratio of the magnetisation to the magnetic field that induces it:

$$\chi = \boldsymbol{M}/\boldsymbol{B}_0 = \boldsymbol{M}/(\mu_0 \boldsymbol{H}) \qquad (2.2)$$

χ defined in this manner has units of $JT^{-2}m^{-3}$. However, it is more common for chemists to express susceptibilities in terms of moles of sample. Furthermore, there is widespread disregard for SI units in magnetism [94,95,96], and it is still common to use cgs units for which μ_0 is defined as 1 and is dimensionless; the susceptibility is then expressed in units of emu cm^{-3}, where 1 emu ('electromagnetic unit') = 1 cm^3, and the conversion factor between SI units and cgs units is given by 1 $JT^{-2}m^{-3} = 10^{-7}$ emu cm^{-3}. This conversion will need to be used when the data collected by experimental and theoretical workers is refered to.

There are many ways in which the bulk susceptibility may be measured, but they may be divided into a few broad categories: some methods measure some force of interaction between the sample and an applied magnetic field; some methods measure use electromagnetic methods, relating induction or current generated in a pick-up coil to the magnetic induction of the sample. The most direct methods of measuring magnetic susceptibility are force techniques using a Faraday or Gouy balance, which measure the force exerted on a sample when it placed in a strong magnetic field in terms of a change in the weight of the sample. Traditionally, this method uses a very sensitive balance for the measurement and provided a very direct means of measurement that is both conceptually straightforward, and relatively free of any artefacts. The technique has been adapted recently to incorporate advances in force measurement using very sensitive capacitance measurements and in this modified form

now provides one of the most sensitive magnetometry techniques. An alternative approach exploits the fact that the magnetisation of the sample produces a magnetic field that may induce a small current in conducting coil if the coil and magnetisation move relative to each other; alternatively, an alternating current passed through the coil may produce an alternating magnetic field that interacts with the sample. Thus, the magnetisation of the sample may be probed in terms of the current induced in a small pick-up coil moved relative to a magnetically polarised sample, or in terms of the complex magnetic inductance of the system. The former is the basis of some SQUID (Superconducting QUantum Interference Device) magnetometers, while the latter is the basis of the A.C. inductance bridge.

In this work a SQUID magnetometer was used to collect the susceptibility data, and the principle of operation is illustrated schematically in Figure 2.1. At the heart of the SQUID magnetometer is a pair of Josephson junctions, each of which comprises a thin insulating barrier between two pieces of superconducting material. Classically, this barrier would cause the entire device to be an insulator. However, superconductivity is a very non-classical phenomenon; the charge carriers in such a material are quasi particles composed of a bound pair of electrons, which move through the material in a phase-coherent manner. Such particles are able to tunnel through the insulating boundary if it is sufficiently thin, and they do so in a manner that is very sensitive to their phase on either side of the boundary. This gives rise to a tunnelling current that is very sensitive to changes in this phase, which in turn may be influenced through an external magnetic field. In the commonly used configuration shown in Figure 2.1, two such junctions are linked, so that net current flowing through this portion of the circuit is the result of the interference between the two halves of the ring. This interference is then amplified and converted to a voltage directly proportional to the applied magnetic field. Therefore, the Josephson junction

acts as a very sensitive flux amplifier; this has been exploited in instruments to pick up small changes in magnetic flux as consequence of neural activity, and spatial deviations in the earth's flux for mineral prospecting [97]. It is also routinely applied in laboratory measurements of the magnetisation of magnetic materials, as is the case in the work presented here.

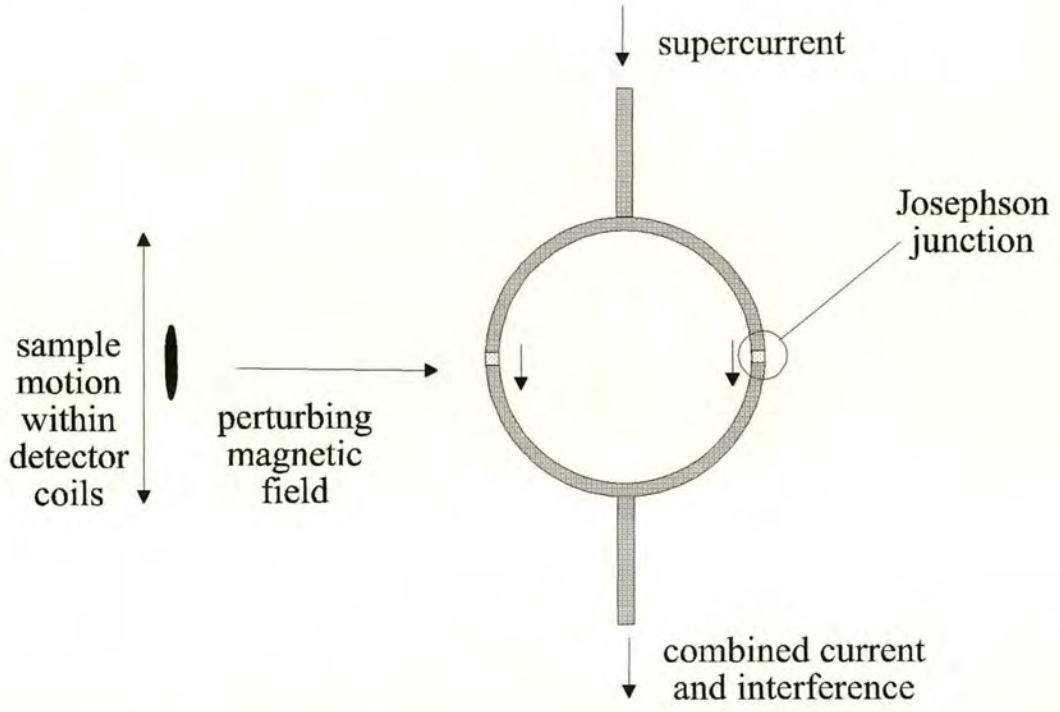

Figure 2.1: Measurement of magnetisation through changes in tunnelling current in a SQUID magnetometer.

2.3. Microscopic origin of magnetic susceptibility

Let us first consider the relatively simple case of a magnet composed of isolated atoms with spin and orbital momentum quantum numbers S and L respectively, and let

us assume that Russell Saunders coupling applies, *i.e.* S and L, directly to total angular moment quantum number J. The moment μ_J associated with J is then given by:

$$\mu_j = g\beta\sqrt{J(J+1)} \tag{2.3}$$

β is the Bohr magneton, defined as

$$\beta = |e|\, h/4\pi mc \cong 9.274 \text{x} 10^{-24}\, JT^{-1} \tag{2.4}$$

where e and m are the charge and mass of the electron respectively, and c is the speed of light. g is the Landé factor, which in the case of Russell-Saunders coupling is given by:

$$g = \frac{3J(J+1)+S(S+1)-L(L+1)}{2J(J+1)} \tag{2.5}$$

In many cases, and in particular in the present case where the magnetic ion is a first-row transition metal, the expression (2.3) for μ_J does not hold because the ligand field perturbs J through L; it is then necessary to consider the contributions from s and l of the individual ligand-field split states explicitly. This point shall be returned to later. However, for the moment it will be assumed that this expression for μ_J, is applicable in considering the effective of temperature and coupling between magnetic centres on the magnetic susceptibility.

2.4. Susceptibility of isolated magnetic ions: the Curie Law

Suppose a magnetic field $\boldsymbol{B_0}$ is applied to the isolated magnetic ion that was discussed discussed in the previous section; the ground state will then be Zeeman split to give $2J+1$ m_j states whose energies E_{mj} are given by:

$$E_{mj} = -m_j g \beta H \tag{2.6}$$

Each m_J state has a different projection of the moment along the field direction, μ_{mJ}, given by:

$$\mu_{mJ} = m_j g \beta \tag{2.7}$$

The net magnetic polarisation, $< \mu_{mJ} >$, is then given simply by the Boltzmann average over all the m_j states:

$$< \mu_{mJ} >= \frac{\sum_{mj=-J}^{J} \mu_{mj} \, exp(-E_{mj} / kT)}{\sum_{mj=-J}^{J} exp(-E_{mj} / kT)} \tag{2.8}$$

Under certain conditions this simplifies: if the splitting between the Zeeman levels is small relative to kT, this expression simplifies to produce

$$< \mu_{mJ} >= \frac{g^2 \beta^2 J(J+1)}{3kT} \tag{2.9}$$

so for one mole of ions, the molar magnetisation $M = N_A < \mu_{mJ} >$ and the molar susceptibility χ_m is then given by:

$$\chi_m = M/B_0 = C/T \tag{2.10}$$

where $C = \dfrac{N_A g^2 \mu_B^2 J(J+1)}{3k}$; this result is known as the Curie Law.

2.5. Susceptibility of coupled magnetic ions: the Curie-Weiss Law

The Curie Law is only valid if there is just one thermally accessible set of m_J states derived from a single J state for which J is a good quantum number, and if there is no appreciable magnetic coupling between ions. Where coupling between magnetic ions cannot be neglected, it is found experimentally that a different expression may describe the magnetic susceptibility reasonably well any magnetic ordering transition, and this is given by the Curie-Weiss Law:

$$\chi = C/(T-\theta) \tag{2.11}$$

where θ parameterises the sign and strength of the coupling: it is negative for antiferromagnets and positive for ferromagnets. θ can be extracted from experimental data by plotting $1/\chi$ against T and measuring the intercept with the temperature axis; the Curie constant C is defined in exactly the same way as for the Curie Law while θ may be related to the mean exchange field that a particular ion experiences. This will depend on the correlation between a moment and its neighbours. An explicit treatment of this term was first proposed by Weiss and was based on the assumption that as a material approached the ferromagnetic transition temperature, the spins interact via a molecular field, which originates from all other

particles in the structure and is proportional to the observed magnetisation and no interatomic interactions are involved [98]. Thus, each moment experiences an additional internal field $\boldsymbol{H_m}$ which is proportional to the magnetisation of the sample, i.e:

$$\boldsymbol{H_m} = \lambda \boldsymbol{M} \qquad (2.12)$$

where λ is the Weiss field constant. If this term is addded to the magnetisation of the sample in 2.1, and then calculate the new form of the susceptibility from Equation 2.10, it can be shown that

$$\chi_m = M/B_0 = C/(T-\lambda C) \qquad (2.13)$$

When $B_0 = 0$, and $T = T_c$, $M \neq 0$, so $\lambda C = T_c$. A similar treatment may be applied to an antiferromagnet, dividing the material into sublatttices for each spin polarisation. For a two-sublattice antiferromagnet with field constant λ defined as for the ferromagnet (2.12) this yields the Curie-Weiss expression (2.11) with $\theta = \lambda C/2$.

Molecular field theory provides a reasonable starting point for rationalising susceptibilities well above any magnetic ordering transition, but as the magnet approaches the critical region on cooling towards a phase transition short-range correlations become significant. Thus, although molecular field theory predicts that the magnetic contribution to the heat capacity associated with a magnetic ordering transition will only be finite at and below the transition temperature, in practice there is a considerable tail to the heat capacity above this temperature. This is particularly important in lower dimensions; for example, in any chain-like antiferromagnet three-dimensional long-range order will only occur at temperatures of the order of the

interchain exchange field. Therefore, the build-up of correlations within the chains will usually occur at significantly higher temperatures, over a range of temperatures, and is manifested in the experimental heat capacity and magnetic susceptibility as a broad maximum rather than the sharp features seen in the critical region of 3-D magnets. In special cases, exact, analytic expressions based on a solution of the appropriate Hamiltonian have been derived for thermodynamic properties of low-dimensional magnets. For 1-D magnets for example, there are explicit expressions for S = ½ Ising chain, but not for the Heisenberg case, though there is an expression for a 1-D Heisenberg linear chain with large spin S, which may be scaled to smaller values, and this is:

$$\chi_m = \frac{N_A g^2 \mu_B^2 S(S+1)}{3k} \cdot \frac{1-u}{1+u} \qquad (2.14)$$

where $u = (T/T_0)\text{-coth}(T_0/T)$ and $T_0 = 2JS(S+1)/k$. [99-101]. This expression will be used later in the treatment of the susceptibility of NH_4FeX_3 and ND_4FeX_3 (X = Cl, Br).

2.6. Magnetic behaviour of orbitally unquenched chainar materials

The magnetic materials that are considered in this thesis do not conform to the conditions required for the simple molecular field theory, embodied in Equation (2.11), to be a good approximation; most significantly, the moment on Fe^{2+} possesses a significant unquenched orbital component that gives rise to ligand-field states and a successful expression for the magnetic susceptibility must take account of the population of these states. Below an approach is detailed such that this perturbation may be treated explicitly. It will also be considered how the mean field approximation may be modified to describe short-range magnetic correlations that alter the exchange

field experienced by a particular spin, taking account of the fact that the orientation of a moment on a particular site will influence the orientation of neighbouring moments. The $AFeX_3$ hexagonal perovskites will be used as a point of reference in developing these models because much of the original developmental work was performed on $RbFeBr_3$ and $RbFeCl_3$ [82-83,102-106].

The cubic component of the ligand field in $RbFeX_3$ (X = Cl, Br) acts on the free-ion ^5D ground term of the $3d^6$ ion Fe^{2+} to produce a lower orbital triplet ($^5T_2$) and an upper orbital doublet (^5E) at an energy of 10Dq (approximately 6500 cm^{-1} in these materials,[107]). The magnitude of this separation allows us to ignore the ^5E state in treating the temperature dependent magnetic behaviour to a first approximation. The $^5T_2$ level is further perturbed by spin-orbit coupling, λ, and the trigonal component of the ligand field, Δ, so that the Hamiltonian H that embodies the electronic character of these materials for the purposes of deducing the magnetic behaviour may be written:

$$H_i = \Delta(L_z^2 - 2) + \lambda L.S \qquad 2.15$$

Where the z direction is parallel to the crystal c axis. The orbital triplet has a threefold degeneracy and may be treated in a similar fashion to an orbital P state with orbital angular momentum $L' = 1$. The correspondence between the matrix elements in the $^5T_2$ and P states is that the values of L are -1 times those of L', and the values of L_z^2 are 3 times those of $L_z'^2$. Therefore Equation (2.15) can now be written as:

$$H_i = \Delta'(L_z'^2 - 2/3) + |\lambda| L.S \qquad 2.16$$

where $\Delta' = 3\Delta$. When $\Delta/\lambda = 0$, the ground state for this Hamiltonian is $J = 1$, and the next state $J = 2$ is at an energy of the order of 150 cm^{-1} in $RbFeX_3$ (X = Cl, Br). As

Δ/λ is increased, the degeneracy of each J state is lifted, so for example the m_J states of the ground $J = 1$ state are split into a ground singlet, $|m_J = 0>$, and an excited doublet, $|m_J = \pm 1>$. For values of Δ/λ appropriate to $RbFeX_3$ (X = Cl, Br), the separation between these three lowest states, and the next state, derived primarily from the J =2 state is sufficiently large for us to ignore any thermal population of the upper state at temperatures below approximately 100 K, and it is then possible as well as convenient to use an effective $S = 1$ Hamiltonian to describe the magnetic properties. If a term for the exchange with neighbouring spins j is also introduced, then the Hamiltonian for the ion i becomes:

$$H_i = DS_{iz}^2 - \sum_j 2\{J^{\perp}(S_{ix}S_{jx} + S_{iy}S_{jy}) + J^{\parallel}(S_{iz}S_{jz})\} \qquad 2.17$$

where $J^{\parallel}$ and $J^{\perp}$ are the components of the exchange parallel and perpendicular to the z direction, D represents the trigonal distortion, and the sum of the second part of this expression is taken over all neighbours j with which there is significant exchange. It should be noted that if the aim is to relate properties predicted on the basis of *this* Hamiltonian to real, measurable properties, then the various real m_L and m_J contributions to the singlet and doublet states must be accounted for. This point will be returned to when the data is treated.

The various ligand-field and spin-orbit perturbation to the free ion terms are summarised schematically in Figure 2.2.

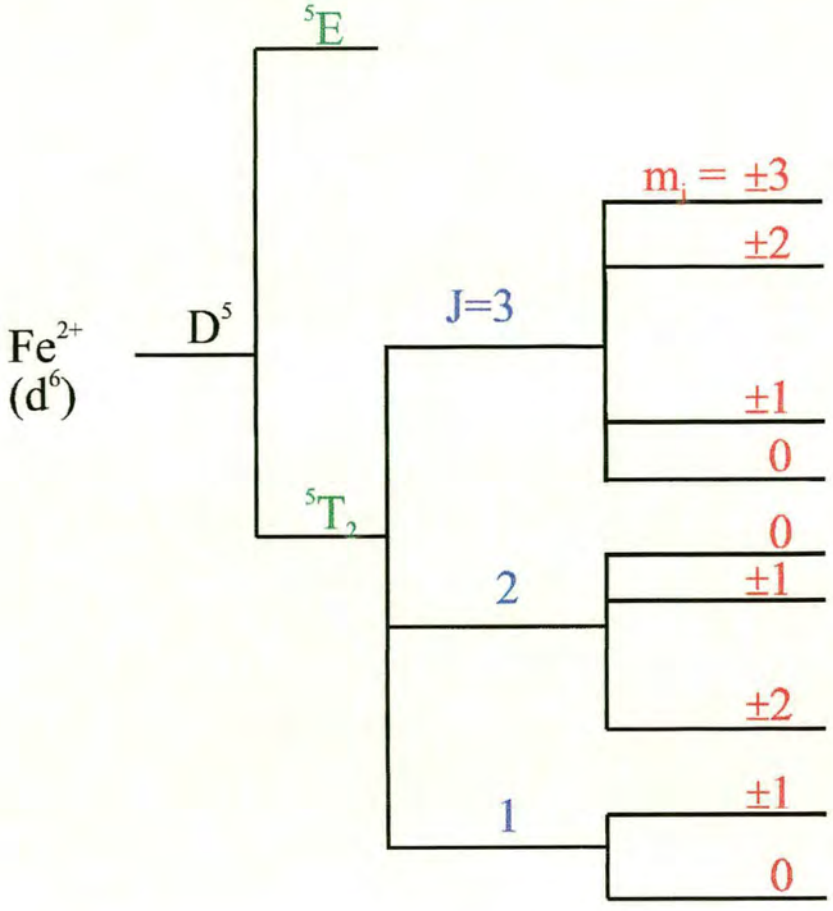

Figure 2.2. Energy level diagram for $AFeX_3$ compounds with the hexagonal perovskite structure.

In the absence of exchange, these $AFeX_3$ materials would be expected to have singlet ground states and therefore show no magnetic moment to a first approximation. The effect of exchange is to mix the excited doublet into the ground state, and if it is sufficiently large, will produce an induced moment. Thus, when A = Rb, the ground state does have a moment, while for the Cs salts, with larger unit cells and smaller exchange constants, the exchange interaction is not sufficiently large to induce a moment and these compounds behave as singlet ground state magnets. A moment may also be induced in this kind of material by applying an external magnetic field; in

the case of the Cs salts, a moment may be induced through the application of a field of the order of 5 T [108]. The sensitivity of the moment in these materials to the exchange field, and therefore to the orientation of neighbouring moments, requires us to consider the effect of magnetic correlations in a more sophisticated manner than is provided by mean-field theory.

2.6.1. The Correlated Effective Field Approximation

In the molecular field approximation, the many-body problem summarised in the Hamiltonian 2.17 can be reduced to a single-ion problem by substituting the moment S_j on the neighbouring atom $_j$ by the expectation value $< S_j >$:

$$S_i.S_j \rightarrow S_i. < S_j > + S_j. < S_i > \qquad (2.18)$$

However, one might expect that the orientation of the moment on atom *i* has an influence on that of its neighbours i.e. there will be some correlation between *i* and *j* that produces a deviation from the thermal average. This effect was first treated explicitly in this context by Lines and co-workers who developed what was called a Correlated Effective Field (CEF) theory [109, 110]. Nearest-neighbour magnetic correlations are accounted for by a correlation parameter, α:

$$S_i.S_j \rightarrow S_i. (< S_j > + \alpha (S_i. - < S_i >) + S_j. (< S_i > + \alpha (S_j. - < S_j >) \qquad 2.19$$

So, for a magnet with predominantly ferromagnetic exchange, α will be a positive number ranging from 0 to 1, and increasing as the degree of correlation between neighbouring moments increases, and for an antiferromagnet it will range from 0 to – 1, becoming more negative as the neighbours become more correlated. In general, α

may have x, y and z components, and for the materials considered here, which have axial symmetry, we need to consider α^{γ}, where $\gamma =$ || and $\perp$.

This now presents the problem of calculating α^{γ}. The solution to this problem is to use a result from the fluctuation dissipation theorem, which relates the fluctuations in a many-body system to the systematic response to some external force. The particular form of this theory that is used to calculate α^{γ} relates the mean spin-spin correlation function to the average of the susceptibility taken over all energies ω and wavevectors q of magnetic fluctuations:

$$C^{\gamma} = \frac{1}{N}\sum_{q}\frac{1}{\pi}\int_{-\infty}^{\infty} d\omega \coth\left(\frac{\beta\omega}{2}\right) Im\,\chi^{\gamma}(q,\omega+i\eta) \qquad 2.20$$

$$\text{as}\ \eta \to 0$$

where $\gamma =$ || and $\perp$, χ^{γ} is the complex susceptibility, $\beta = 1/(k_B T)$ and N is the number of magnetic ions. C^{γ} ($\gamma =$ || or $\perp$) are defined as follows:

$$C^{\perp} = \langle\{S_i^{+}, S_j^{-}\}\rangle \qquad 2.21(a)$$

$$C^{\parallel} = \langle\{S_{iz}, S_{jz}\}\rangle \qquad 2.21(b)$$

Where $\langle\ldots\rangle$ denotes a thermal average and $\{\ldots\}$ signifies an anti-commutator.

It may be shown that in the paramagnetic phase of these materials, the mean exchange field which are proportional to $\langle S_i\rangle$, $\langle S_j\rangle$, becomes zero and the Hamiltonian H_i simplifies to:

$$H_i = ES_{iz}^2 \qquad 2.22$$

where E is the effective-ion anisotropy, corrected to take account of anisotropic exchange:

$$E = D + 2(\alpha^{\perp} J^{\perp} - \alpha^{\parallel} J^{\parallel}) \qquad 2.23$$

The susceptibilities $\chi^{\gamma}(q,\omega)$ [111] may then be shown to be:

$$\chi^{\perp}(q,\omega) = \frac{\phi^{\perp}(\omega)}{1-(J_q^{\perp} - \alpha^{\perp} J_0^{\perp})\phi^{\perp}(\omega)} \qquad 2.24(a)$$

$$\chi^{\parallel}(q,\omega) = \frac{\phi^{\parallel}(\omega)}{1-(J_q^{\parallel} - \alpha^{\parallel} J_0^{\parallel})\phi^{\parallel}(\omega)} \qquad 2.24(b)$$

where J_q^{γ} is the Fourier transform of the exchange interaction, J_0^{γ} is the value of J_q^{γ} for $q = 0$, and $\phi^{\gamma}(\omega)$ are the single-ion susceptibilities, that is the susceptibility of the isolated (uncoupled) magnetic ions, and are given by:

$$\phi^{\perp}(\omega) = \frac{-4E\rho}{(\omega^2 - E^2)} \qquad 2.25(a)$$

$$\phi^{//}(\omega) = 2\beta\rho'(\omega = 0); 0(\omega \neq 0) \qquad 2.25(b)$$

where ρ and ρ' are given by:

$$\rho = \frac{(e^{\beta E} - 1)}{(e^{\beta E} + 2)} \qquad 2.26(a)$$

$$\rho' = \frac{1}{(e^{\beta E} + 2)} \qquad 2.26(b)$$

To determine α^{γ} for a given set of values of J^{γ} and D at a particular temperature, one could guess an initial value for α^{γ}, calculate the difference between the left and right hand side of Equation 2.20 for the separate cases of $\gamma =$ || and $\perp$, then refine α^{γ} to minimise this difference. The practical procedure for this is described in Chapter 8. It was found that at low temperatures, as the magnet approached an ordering transition, two solutions were found for α^{γ} which gave a non-physical prediction of two magnetic transitions when only one is observed [105]; this could be rectified, whilst also simplifying the calculation, by setting $\alpha^{||} = \alpha^{\perp} = \alpha$, and calculating α from 2.20 using the transverse susceptibility ($g^{\gamma} = \perp$). This is the approach that shall be used in this work. Note that the molecular field approximation is readily obtained simply by fixing $\alpha = 0$ in the expressions 2.24(a) and (b) for the susceptibility. Note too that these expressions are appropriate for single ions of spin $S = 1$; in defining the effective $S = 1$ for the shown in Hamiltonian 2.17. It can also be noted that real components of the spin are related to the contributions of the various m_L and m_S states that arise from action of Δ' and λ' on the $L' = 1$ and $S = 2$ momentum components of the $^5T_2$ state, and these give rise to anisotropic g values which have been tabulated as a function of Δ'/λ'. In relating the susceptibility calculated from 2.24(a)(b) to one mole of real ions, we must multiply by the factor $N_A g^{\gamma 2} \mu_B{}^2$, where μ_B is the Bohr magneton. It is not always possible to produce a single crystal of a material for oriented susceptibility measurements, in which case a powder average χ is taken; this is related simply to the components parallel and perpendicular to the c axis as follows:

$$\chi = \frac{\chi^{//} + 2\chi^{\perp}}{3} \qquad 2.27$$

2.7. Summary

In this Chapter a theory has been described for the bulk magnetic susceptibility of a material in which strong ligand-field and spin-orbit coupling produce an induced moment magnet. This magnet has a singlet ground state and an excited doublet state such that the moment of the ground state is very sensitive to the balance between the exchange field and the ligand field. For such materials it is necessary to treat nearest-neighbour spin correlations in a more sophisticated fashion than molecular field theory, and we have described how theorists have attempted to build this into the expression for the susceptibility using the Correlated Effective Field Approximation.

3. Structural Techniques

3.1. Introduction

The nuclear and magnetic structural characterisation of the materials discussed in this thesis was carried out using a variety of diffractometers with different, complementary, characteristics. The fundamental principles of diffraction, the machines used and the methods of data collection and manipulation are outlined in this chapter.

3.2. Principles of Diffraction

The most important method for the structure determination of crystalline materials involves analysing the diffraction of radiation or particles scattered by a regular array of atoms. This exploits the fact that radiation which has a wavelength comparable with inter-atomic spacing is diffracted by crystalline materials. The most straight forward description of diffraction is based on the understanding that radiation incident on a regularly repeating set of identical planes will produce peaks of intensity as a function of incident angle, due to constructive and destructive interference, in the reflected radiation. When the difference between the path lengths of two incident rays of radiation, reflected from the same set of atomic planes with Miller indices *hkl*, is equal to an integral number of wavelengths, constructive interference is observed. This description is expressed using Bragg's Law:

$$n\lambda = 2d \sin\theta \qquad (3.1)$$

where λ is the wavelength of incident radiation, θ is the angle of incidence and d is the separation of the atomic *hkl* planes. The rather simplified picture of an incident beam impacting with the atoms and being reflected back at the mirrored angle can be

replaced by a more thorough treatment. This treatment considers the electronic excitation induced by the X-ray radiation interacting with the electrons associated with each individual atom, and the subsequent energy emission. Both treatments arrive at the Bragg's equation. For a more complete description of the theory of diffraction and its practical consequences the reader is referred to one of the many excellent texts available [112-114].

Firstly, let us consider the diffracted beam from a set of atomic *hkl* planes. The diffracted beam has both amplitude and phase, these are quantified as the *structure factor*, $F(hkl)$, which is a summation of the effect of all atoms in the unit cell contributing to the reflection. The structure factor is given by:

$$F(hkl) = \sum_j N_j f_j \exp\left[2\pi i\left(hx_j + ky_j + lz_j\right)\right]\exp\left[-M_j\right] \qquad (3.2)$$

where x_j, y_j and z_j describe the position of the jth atom in the unit cell, N_j is the site occupancy divided by the site multiplicity for the jth atom site and f_j is the scattering factor of the jth atom; M_j is given by:

$$M_j = 8\pi^2 \overline{u_s^2} \sin^2\theta/\lambda^2 \qquad (3.3)$$

where $\overline{u_s^2}$ is the root-mean-square thermal (and random static) displacement of the jth atom parallel to the diffraction vector.

The structure factor may also be expressed as:

$$F(hkl) = \left|F(hkl)\right| e^{i\alpha(hkl)} \qquad (3.4)$$

where $|F(hkl)|$ represents the amplitude and $\alpha(hkl)$ represents the phase. The intensity of the scattered radiation is proportional to $|F(hkl)|^2$ and, therefore, the phase information is lost in all diffraction studies. This 'phase problem' is the central problem in crystallography. The solution of a single crystal diffraction data set involves derivation of $\alpha(hkl)$ either from 'trial structures' e.g. the Patterson method or by purely analytical techniques such as direct methods [112-114].

Although single crystal diffraction studies are the best technique to extract the most possible information about the structure, it is not always possible to grow a suitable single crystal for a single crystal diffraction experiment. In such cases, where the sample is crystalline but the crystallites are small, a powder diffraction experiment can be used. In a powder diffraction experiment, where the point source is non-divergent and powder sample is randomly oriented, the incident beam is still diffracted by the sample according to the Bragg condition. All orientational information is lost, however, due to the random arrangement of the crystallites. As a direct result of this fact all the possible orientations of a crystallite, simultaneously diffract within the powder sample during a powder diffraction experiment. The diffraction pattern that results is a *cone* of reflected intensity with half angle 2θ. These are generally referred to as Debye-Scherrer cones after the developers of the original detection technique.

3.3. Different forms of incident radiation: X-rays, neutrons and electrons

As stated in the previous section, to obtain a diffraction pattern the incident radiation must be of a wavelength which is comparable to d, the separation of the planes of

atoms. Therefore, the options available to the crystallographer are X-rays, electrons and thermal neutrons, and each of these interact in different ways with the materials; electrons and X-rays are scattered by the electrons, but neutrons pass through the electron cloud and interact directly with the nucleus, *via* the strong nuclear force. The three methods are most applicable in different cases, and the most suitable method must be selected for each system; very often a comparison between two methods is required to extract the maximum information.

One major difference between X-ray and neutron diffraction can be appreciated by examination of Equation 3.2 which shows that the structure factor is dependant on the atomic scattering factor, f_j. X-ray radiation is scattered by electrons and the scattering factor for an atom is the ratio of the amplitude of the wave scattered by the atom to that scattered by a single electron. Therefore, the scattering factors of the atoms in X-ray diffraction is dependant on the number of electrons and increases in a linear fashion with increasing atomic number, Z, of the atom. In neutron diffraction the incident neutrons are scattered by the *nuclei* of the atoms, in this case the atomic (nuclear) scattering factors only vary by a factor of two or three in comparison with the variation of X-ray scattering amplitudes; these vary almost a hundred fold over the Periodic Table. In the context of neutron scattering f_j is called the *scattering length*, b_j, (see Section 3.3.2). As a consequence of this weakly Z dependent scattering behaviour, neutron diffraction can be very useful for detecting light atoms in the presence of heavy ones, distinguishing between atoms with similar atomic numbers and even between different isotopes of the same element.

As explained above the nature of the incident radiation is very important in the correct selection of an experiment and to the interpretation of the results. This Section outlines the radiation sources chosen in this project.

3.3.1. X-ray diffraction

X-ray diffraction is usually the method of first choice. This is because it is generally the cheapest and most widely available, gives the highest resolution data and is the most intense, thus requiring smaller samples.

3.3.1.1. Conventional X-ray sources

Conventional single crystal and powder X-ray diffractometers make use of X-rays which are emitted when a metal source is bombarded with high energy electrons. The source is often a sealed evacuated tube containing a metal anode target (usually copper or molybdenum) which emits X-rays; the required wavelength (1.542Å for Cu K_α and 0.711 Å for Mo K_α) is then selected using a monochromator. Higher intensity radiation can be achieved if this set-up is modified slightly to include a rotating anode source; this involves a rotating metal target.

3.3.1.2. Synchrotron radiation

An alternative method of producing X-rays, which can produce very high resolution, high intensity data, is the use of synchrotron radiation. A synchrotron is a charged particle accelerator in which electrons (or other ions) are accelerated to very high (relativistic) velocities. The particles are restrained to a circular orbit by the use of an increasing magnetic field and acceleration is achieved by radio frequency electric fields whose frequency is increased as the particles speed up. X-ray radiation is emitted tangentially from the accelerator ring, see Figure 3.1.

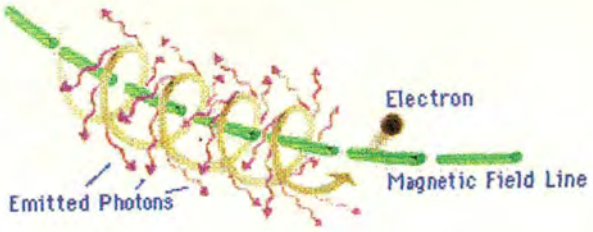

Figure 3.1. A representation of the process of X-ray emission from the the confines of a circular orbit [115].

Synchrotrons have been an intrinsic part of the development of high resolution diffraction techniques in recent years. The emitted X-ray radiation can be used directly, as at the Synchrotron Radiation Source (SRS) Daresbury, U.K, and the European Synchrotron Research Facility (ESRF) in Grenoble, see Figure 3.2 [115]. Alternatively, a high velocity proton beam can be drawn from the ring and directed at a target to produce a pulse of neutrons, allowing time of flight (TOF) studies, which is the case at the ISIS Facility at the Rutherford Appleton Laboratory, Didcot. The X-rays obtained from synchrotrons have several advantages over laboratory X-rays; the very bright (high flux) beam and high vertical collimation allow the construction of diffractometers with very high resolution, and the tunability of the energy of the radiation allows the anomalous scattering to be used in powder structure determination.

Anomalous scattering is observed when an incident X-ray excites an atom and is delayed slightly, thus causing a very small phase shift. The synchrotron radiation can be tuned to collect diffraction data close to and far from the absorption edge of any anomalous scatterers present. These data can be used to give extra information in some non-centrosymmetric crystal structures and to determine the absolute configuration of a structure containing only one enantiomorph.

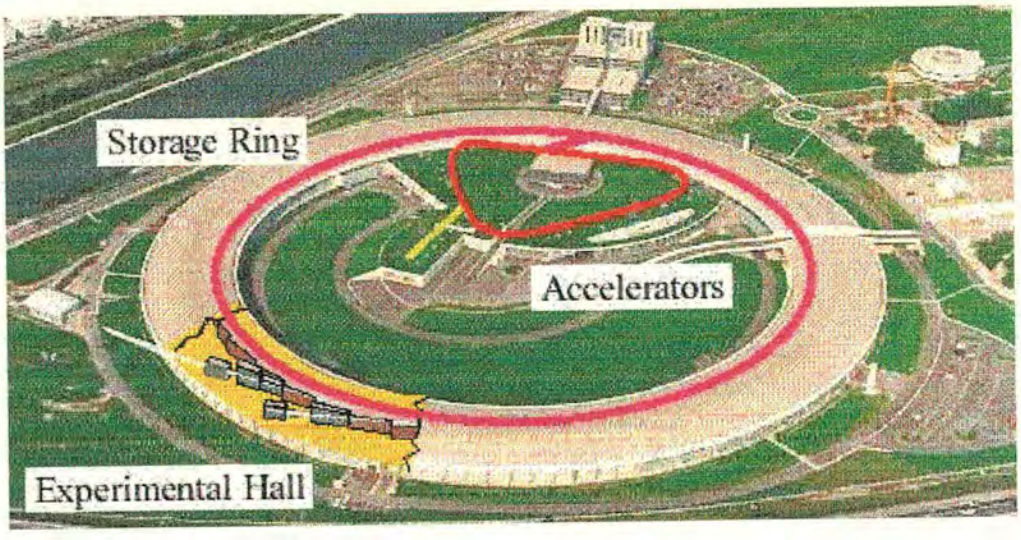

Figure 3.2. A photograph of the European Research Facility (ESRF) in Grenoble, note the size of the storage ring which is several km in circumference [115].

The very high resolution attained in these diffractometers can, however, cause problems in profile refinement as features of the sample such as strain, preferred orientation and particle size become significant and can complicate the peak shape. The diffraction community is only just beginning to come to terms with the problems raised by such high quality data, as this may highlight the shortfalls of some approximations used in the data processing. Some of the problems regarding the observed peak shapes and the accurate modelling of the peak shapes is addressed later in this Chapter, see Section 3.4.1.

3.3.2. Neutron Diffraction

Neutron diffraction differs from X-ray diffraction in several fundamental ways. Firstly, the neutrons may be scattered by the nucleus of the atom, while X-rays are scattered by the electrons. This has two effects: (a) the observed centres of the atoms are sometimes distorted slightly from the nuclear centres in X-ray diffraction, as the

centres of electron density may be displaced by bonding; (b) the scattering from X-rays is proportional to the number of electrons and hence on atomic number but neutron scattering is proportional to a much more complicated nuclear interaction. A neutron interacting with a nucleus may be scattered or absorbed; the scattering length, b, of a nucleus is a complex representation of these two effects where elastic scattering corresponds to the real part and absorption to the imaginary part. The scattering cross-Section, σ_s, of a nucleus describes the proportion of neutrons scattered per second and the absorption cross-Section describes the proportion absorbed:

$$\sigma_s = 4\pi b^2 \tag{3.5}$$

When the scattering produces constructive interference ,Bragg reflections are observed; this is known as *coherent* scattering, σ_c, and is proportional to the average scattering length, $\bar{b}$:

$$\sigma_c = 4\pi\left|\bar{b}\right|^2 \tag{3.6}$$

The value of $\bar{b}$ may vary from site to site giving rise to *incoherent* scattering, σ_i, which is proportional to the mean square deviation in $\bar{b}$:

$$\sigma_i = 4\pi\left(\left|b\right|^2 - \left|\bar{b}\right|^2\right) \tag{3.7}$$

One particularly significant consequence of the complex mechanism of interaction between *nucleii* and neutrons is that the magnitude of the interaction of a neutron with different isotopes of the same element may vary widely; a prime example of this

being the difference between hydrogen and deuterium. Their scattering lengths and coherent, incoherent and absorption cross-Sections are compared in Table 3.1. This has several implications experimentally. Firstly, it is desirable to replace H with D in a material to be studied using neutron diffraction because the large coherent scattering cross section of D allows deuterium positions to be calculated even in the presence of a heavy metal and secondly the large incoherent scattering cross section of H causes a vastly increased background [116-117]. Also, the large incoherent scattering of H is very useful in quasi-elastic studies (see Chapter 6).

Table 3.1: A comparison of the neutron scattering behaviour of hydrogen and deuterium [116,117]. b is the scattering length, σ_c is the coherent scattering cross-section, σ_i is the incoherent scattering cross-section, σ_a is the absorption cross-section.

	b / (x 10^{-15} m)	σ_c / (x 10^{-28} m^2)	σ_i / (x 10^{-28} m^2)	σ_a / (x 10^{-28} m^2)
H	-3.7423	1.7599	79.91	0.3326
D	6.674	5.597	2.04	5.19 x 10^{-4}

Another major advantage of neutron scattering over other forms of diffraction originates from the fact that the neutron has a magnetic moment, μ_n, which is given by:

$$\mu_n = -\gamma \mu_N \sigma \tag{3.8}$$

where γ (= 1.913) is gyromagnetic ratio of the neutron, μ_N (= 5.05082 x 10^{-27} JT^{-1}) is the nuclear magneton and σ is a Pauli spin operator for a particle with $S = ½$.

Magnetic scattering occurs when the magnetic moment of the neutron interacts with local magnetic fields such as those produced by the spin and orbital angular momenta of an unpaired valence electron. As a result of this interaction neutron diffraction patterns from magnetic materials, taken below their magnetic long-rang ordering temperatures, show reflections induced by the magnetic structure. In a ferromagnetic structure the magnetic unit cell is exactly coincident with the structural unit cell and extra intensity is observed on some existing reflections below the ordering temperature. In an antiferromagnetic material the magnetic cell is often expanded with respect to the structural unit cell and new reflections may be observed at high d-spacings.

3.3.2.1. Nuclear Reactors as Neutron Sources

A continuous beam of neutrons can be produced from a low power 10-100 MW uranium-fuelled nuclear reactor; neutrons are produced over a range of energies (1-10 MeV) simultaneously and then passed through a moderator to slow them to thermal velocities ($v \approx 4$ km s^{-1}, $\lambda \approx 1$ Å). The wavelength can be selected by choice of moderator, e.g. D_2O at 300 K produces neutrons with mean wavelengths of about 1 Å, which is good for most elastic and inelastic diffraction purposes, while liquid H_2 at 25 K produces 'cold' neutrons with mean wavelengths close to 4 Å. The neutron beam used for diffraction is selected out using a monochromator, though it will still have a distribution of energies within the selected beam. These energies are distributed according to a Gaussian distribution, which can be seen by examining the peak shape of each reflection in the diffraction pattern (see Section 3.4.1). Once the diffraction patterns have been recorded the diffraction the analysis is identical as for diffraction using X-rays, differing only in the information gained from the nature of the neutron's magnetic moment and scattering ratios.

3.3.2.2. Spallation Sources

An alternative method of neutron production is by using *spallation* source. In a spallation source a heavy metal target (typically U or Ta) is hit by timed pulses from an accelerated proton beam produced by a synchrotron. Each pulse causes neutrons to be ejected from the target atoms with a wide range of energies and hence wavelengths, so that for a given pulse, these neutrons reach the sample at different times. The diffracted neutrons are collected as a function of their time of flight which may then be related to wavelength. Spallation sources can be used to look at phenomena that conventional, continuous wave neutrons produce from nuclear reactors would find difficult. A particular strength of the spallation technique is that a single detector at a single position can collect data over a wide rang of d-spacings; this is useful if the experimental geometry is restricted, *e.g.* when the sample is studied in a pressure cell. The ISIS facility at the Rutherford Appleton Laboratory (RAL) is an example of a spallation source.

3.4. Powder Pattern Refinement and the Rietveld Method

In an ideal world a perfect single crystal of any new material would be selected and analysed by single crystal diffraction. In this case it is usually mounted on a 4-circle device which allows positioning of the crystal in any chosen orientation. The crystal is aligned so that the reflections can be correctly assigned with respect to the crystal axes. The incident X-ray beam interacts with the sample and the diffracted sphere of radiation is collected over a period of time by moving the crystal and the detector. Normal procedures are complicated when the crystal is air sensitive and when structures are required at very low temperatures; both of these problems are important for the compounds considered in this thesis.

The difficulty in obtaining good single crystals of many materials has provided the motivation for significant advances in *powder* diffraction. The random orientations of the crystallites in a powder sample condenses the three dimensional information from the sample into one dimension. Consequently reflections which originate from *hkl* planes with the same d-spacings but different relative directions, *e.g.* 002 and $00\bar{2}$, and would be spatially resolved in a single crystal experiment, are completely coincident in a powder pattern and it is impossible to distinguish these by analysis. A problem also arises when reflections with *similar* d-spacings overlap causing broadened or asymmetric peaks. It is now necessary to find a way to resolve such profiles into contributions from individual sets of reflections and apportion the integrated intensity of the complex line shape into components from those reflections. As the resolution of powder diffraction techniques has increased, so too has the quality and quantity of information which can be extracted. This advance has been motivated by the immense difficulty in producing single crystals of many interesting materials. Increasing the resolution of the data by increasing the wavelength of incident radiation can sharpen the peaks but cannot always resolve them completely. Rietveld refinement was developed primarily to deal with this problem [118,119].

In 1966 H. M. Rietveld produced the first algorithm which assigned the integrated intensities of peaks in a powder profile to a set of contributing reflections [120]. This development was facilitated by the growing capabilities of the computers available at that time. The original programs were designed to analyse powder neutron data by exploiting the apparent Gaussian peak shape in the reflections observed in this type of data. The peak shape is governed by the instrumental resolution and the nature of the crystallites; in the case of neutron diffraction at a reactor source it was observed that the shape could be approximated using the

Gaussian function. The contribution to the intensity at a given angle θ_i due to a reflection centred at θ_{hkl} is given by the Gaussian function as:

$$I(\theta_i) = \sqrt{\frac{4\ln 2}{H_{hkl}\pi}} \exp\left(\frac{-4\ln 2(2\theta_i - 2\theta_{hkl})^2}{H_{hkl}^2}\right) \qquad (3.9)$$

where H_{hkl} is the full-width at half-maximum (FWHM) of the Bragg reflection with Miller indices *hkl*, .The H_{hkl} values depends on the mosaic spread of both the crystals used in the monochromator and the crystallites in the sample.

As more powerful computers became available the program was extended to allow the refinement of peak profile [118,121]. The angular dependance of H_{hkl} of a Gaussian diffraction peak can be described by the expression:

$$H_{hkl}^2 = U\tan^2\theta_{hkl} + V\tan\theta_{hkl} + W \qquad (3.10)$$

where U, V and W are the halfwidth parameters, which may varied in the refinement, and $2\theta_{hkl}$ is the calculated position of the centre of the Bragg peak [122]. The refinement process utilises a non-linear least-squares fitting program and was originally designed to refine powder neutron data; it has now been expanded to cater for X-ray data by including a suitable peak profile [123]. From this humble beginning the Rietveld method has grown in popularity and is now used routinely as a powerful tool in structural refinement. Several texts are available to explain in detail the complexities of Rietveld refinement [e.g. 119]. A brief introduction to the method and a description of non-standard features used in this project are given here.

3.4.1. Peak profiling

A vital part of refining a structure from powder diffraction data is obtaining a good estimate of the peak shape. As described above, the underlying shape of a powder neutron diffraction peak is usually Gaussian, but more often a more complex function is needed to correctly model the line shape for higher resolution data, particularly for X-ray measurement. The peak model shown above, in equation 3.10, works well for medium to low resolution neutron powder diffractometers, but X-ray sources produce non-Gaussian, non-symmetric diffraction profiles; these could however be fitted using a convolution of the Gaussian, G, (Eq 3.9) and Lorentzian, L, (Eq 3.11) expressions

$$I(\theta_i) = \frac{2}{H_{hkl}\pi} 1 \Big/ \left[1 + \frac{4(2\theta_i - 2\theta_{hkl})^2}{H_{hkl}^2} \right] \qquad (3.11)$$

this is given by the pseudo-Voigt, pV, function (Eq 3.12),

$$I(\theta_i) = \eta L + (1 - \eta) G \qquad (3.12)$$

where the weighting factor, η, can be refined as a linear function of 2θ, i.e.

$$\eta = NA + NB(2\theta) \qquad (3.13)$$

where NA and NB are the refinable variables.

A further complication is observed when using high resolution instruments; the profile may be sufficiently narrow to reveal broadening due to intrinsic sample features, such as microstrain and small crystallite size and these may make up a

significant portion of the peak width; this usually results in anisotropic line shapes. Low angle (high d-spacing) peaks are always asymmetric as a result of the finite aperture height (neutron scattering) and width (synchrotron diffraction) of the detector, this effect is known as *axial divergence* [124,125]. In Figure 3.3 the origin of the axial divergence effect is illustrated; 2H is the width/height of the detector slit.

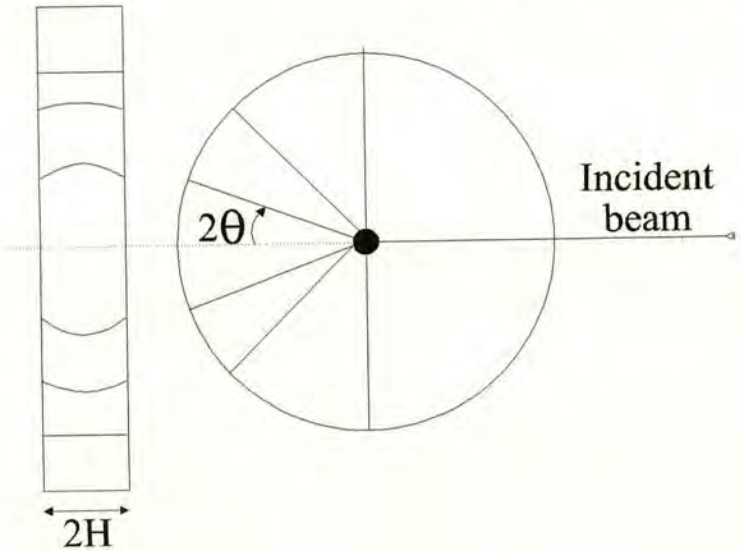

Figure 3.3. The above schematic shows how the diffraction cones intersecting with the detector cylinder, gives rise to a variation in ellipticity as shown on Debye-Scherrer film (left).

The effect is also exacerbated by the finite width or height (the parameter 2H in Figure 3.4 is either described as the width or height of the sample depending if the diffractometer is an X-ray diffractometer or a neutron diffractometer) of the sample as this causes the ellipses to broaden, see Figure 3.4.

In Figure 3.4 the detector slit lies on the surface of a cylinder and the diffracted cones intersect with this cylinder to form ellipses. The ellipticity is maximum at 90° and decreases as 2θ tends toward 0° or 180°, this can be observed using a Debye-Scherrer camera.

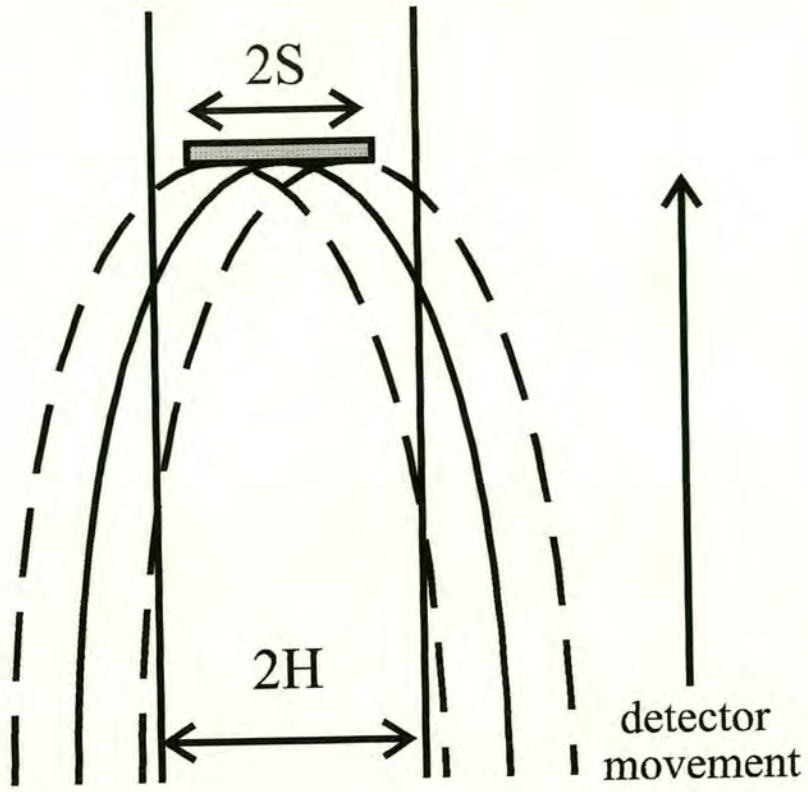

Figure 3.4. This shows broadening of ellipse (from solid to dotted line) caused by sample size; 2H is the height of the detector slit and 2S the height of the sample [124,125].

At low angles the portion of the cone which intersects with the diffractometer slit is significantly curved and extra intensity is observed, by the detector, on the side of the slit closest to the centre of the ellipse. Originally all peaks were fitted using a Gaussian function and were soon modified to include multiple Gaussian contributions which could account for peak asymmetry [123]. In high resolution studies the effect of axial divergence is significant and must be properly accounted for if maximum information is to be extracted from the data. An asymmetry correction involving the parameters H and S described above, along with the distance between the sample and detector, L, has been developed and axial divergence may now be effectively modelled [124,125]. This was done in this work by using the Le

Bail method [126] option in GSAS (see Section 3.4.3), this procedure calculates the peak shape while the observed structure factors are extracted from the refinement; this means that a realistic starting value for the parameters used in the asymmetry correction can be obtained before the structural parameters are refined. Other factors contributing to anisotropic peak broadening such as microstrain, and crystallite shape cannot be adequately modelled at the moment [127] for data obtained using the highest resolution instruments presently available. e.g. Data collected on BM16 at the European Synchrotron Research Facility- see Section 3.5.15.

3.4.2. Quantifying the quality of the fit

When refining data from powder diffraction studies many parameters may be refined simultaneously. These parameters include those that define the background, peak shape, structure, lattice, thermal and absorption, and the effectiveness of the calculated profile. This effectiveness of the fit is quantified by the R-factors, these are R_p, the *pattern* R-factor, and R_{wp}, the *weighted-profile* R-factor (For details of the weighting scheme see the GSAS manual, ref 128):

$$R_p = \sum_i \frac{\left|Y_{obs}^i - Y_{calc}^i\right|}{\sum_i Y_{obs}^i} \tag{3.14}$$

$$R_{wp} = \sqrt{\frac{\sum_i w_i \left(Y_{obs}^i - Y_{calc}^i\right)^2}{\sum_i w_i \left(Y_{obs}^i\right)^2}} \tag{3.15}$$

where Y_{obs}^i and Y_{calc}^i are the observed and calculated intensities of each data point. This summation is calculated over the entire diffraction pattern and the points are

weighted by w. As Y^i_{obs} and Y^i_{calc} tend to become equivalent the R-factors are minimised. The *expected* R-factor, R_{exp}, is dependant on the number of observables, N_{obs}, variables, N_{var}, and constraints, N_{cons}, applied in the refinement:

$$R_{\exp} = \frac{\sqrt{N_{obs} - N_{\text{var}} + N_{cons}}}{\sqrt{\sum_i w_i \left(Y^i_{obs}\right)^2}} \tag{3.16}$$

The overall quality of the fit is expressed as χ^2 and is calculated as follows:

$$\chi^2 = \frac{\sum_i w_i \left(Y^i_{obs} - Y^i_{calc}\right)^2}{N_{obs} - N_{\text{var}} + N_{cons}} \tag{3.17}$$

where χ^2 is also known as the 'goodness of fit' parameter.

Refinement is continued until the value of χ^2 and the R-factors is minimised and the calculated profile is seen to fit all the observed reflections as well as possible.

3.4.3. The Generalised Structural Analysis System (GSAS)

At present there are many programs available the refinement of powder data using the Rietveld method (for a list of such programs the reader is referred to the web site maintained by the IUCR [129]). There are currently many different program suites available; most of these are distributed free in the same manner as the original program containing Rietveld's original code. The program selected for this work is GSAS (Generalised Structure Analysis System), it is one the most widely used of those available, and can be easily be obtained from the GSAS web site [130].

3.5. Diffractometers

This section gives an account of the various diffractometers used in this project, describes their operation, their individual features and the details of the experiments carried out using them.

3.5.1. X-ray diffractometers

3.5.1.1. Phillips powder X-ray diffractometer

A Phillips powder X-ray diffractometer with aCuK_{α} radiation source and Xpert system optically-encoded goniometer, operating in flat-plate sample geometry was used for initial characterisation of samples. The data could only be obtained at room temperature and were not of sufficient resolution to allow satisfactory structure refinement. Furthermore, the sample holder available was not sufficiently air-tight to protect the samples from contact with air and the samples hydrated during study.

3.5.1.2. Siemens 4-circle single crystal diffractometer

A single crystal of NH_4FeCl_3 was measured using a Siemens 4-circle diffractometer with a Molybdenum sealed source (50 kV, 35 mA) at the University of Edinburgh. This diffractometer can record high resolution data in a temperature range of 373 to 80 K using a nitrogen cooled Oxford Cryostream. The data were refined using SHELXL93 [131].

3.5.1.3. **Fddd** *high intensity single crystal diffractometer*

In the world today there are a small number of custom-built diffractometers which are beginning to allow data collection at very low temperatures. The only such

machine in the UK capable of allowing ultra low temperatures for data collection is the 'Fddd' high-intensity single crystal diffractometer in Durham (Figure 3.5) [132].

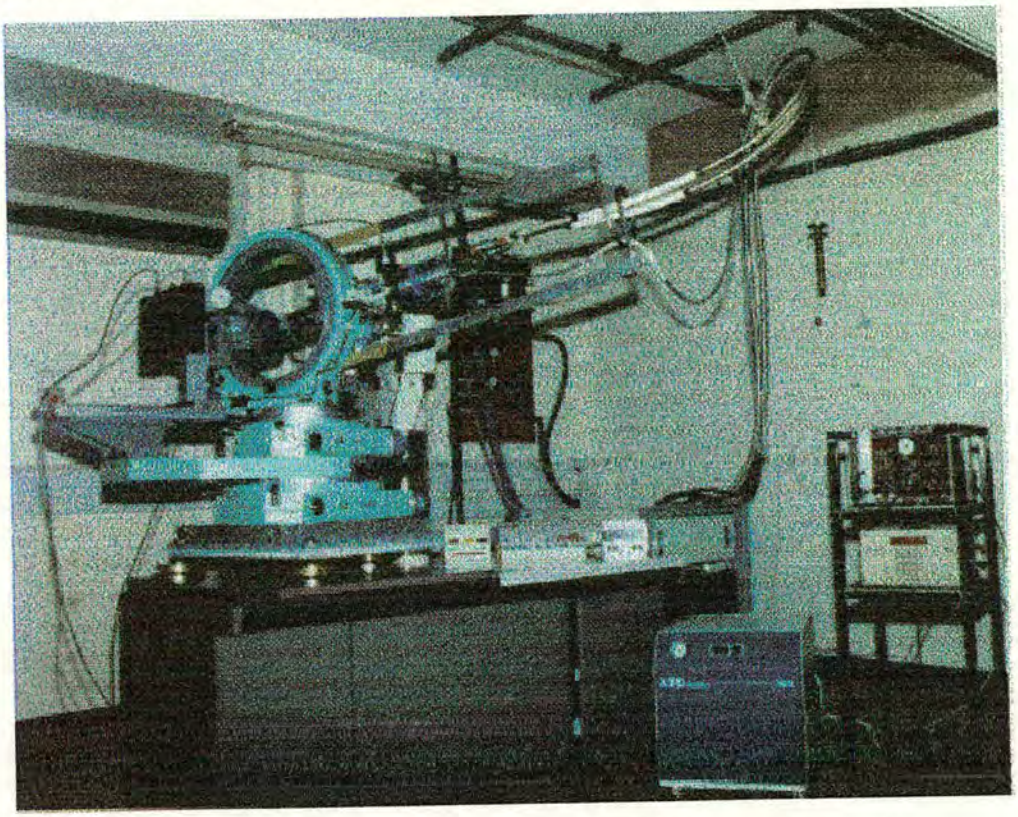

Figure 3.5.The Fddd high intensity single crystal diffractometer at the chemistry department at Durham university.

The Fddd diffractometer shown in Figure 3.5 is a four circle diffractometer with a rotating anode source and cryostat which allows sample cooling down to 9K using a closed-cycle two-stage helium refrigeration system. The generator is a Siemens Molybdenum rotating anode which produces higher fluxes than the conventional sealed tube sources used previously in this type of machine. This high flux allows small samples to be studied and measuring time is reduced. Low temperature structural transition work was one of the main driving forces behind its creation. The results obtained using this diffractometer are presented in Section 5.2.2.

3.5.1.4. Siemens SMART diffractomer

The Siemens SMART diffractomer utilises a CCD-based area detector and is fitted with a sealed Molybdenum sealed source (50 kV, 35 mA) and a nitrogen cooled Oxford Cryostream. The data were processed using the Siemens Saint software[133] and refined using SHELXL93. The big advantage gained by using the area detector lies in the ability to simultaneously collect large number of reflections in a selected region of the Ewald sphere. It is, therefore, a very efficient method of data collection. In addition, the use of such a detector is particularly suited to the detection of a set of weak reflections. This factor may be particularly important in the detection of the weak superlattice reflections observed in the study of structural phase transitions, considered in this project (especially if the position of the reflections is unknown), where the structure distorts from a simple unit cell to more complex expanded cell.

3.5.1.5. High resolution powder diffractometer, BM16 at ESRF, Grenoble

BM16 is a high resolution powder diffractomer located on beamline 15 of the synchrotron ring at the European Synchrotron Radiation Facility (ESRF); it is currently the world's highest resolution powder diffractometer. It was designed to allow collection of high angle and high resolution data. The high resolution of the beam is obtained using the vertical collimation mirror, which is positioned in front of the double crystal monochromator (see Figure 3.6), a 2θ resolution with an optimal instrumental contribution to the peak width of 0.006° can be achieved. In these studies the standard configuration of the beam line was adopted, in which the crystals are aligned so as to utilise the Si(111) plane (for even higher resolution the Si(311) reflection is used).

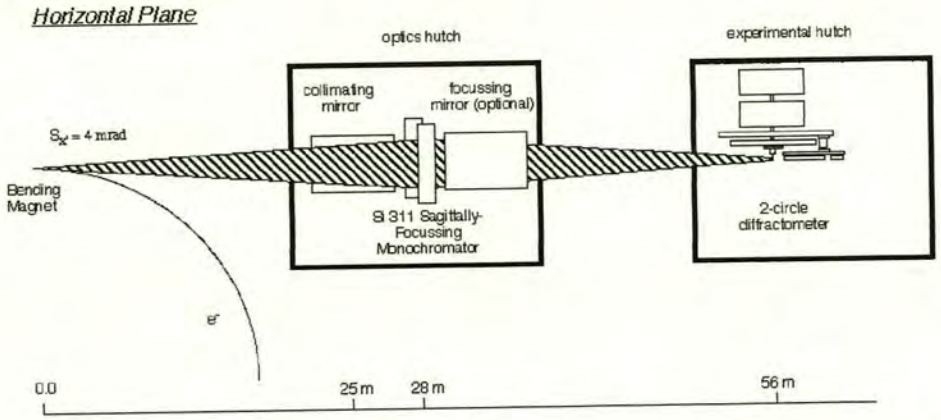

Figure 3.6. A schematic diagram of diffractometer and associated optics on beam line BM16 [134].

The powder samples are loaded into 0.6mm, low molecular weight borosilicate glass capillaries (these were obtained from Hilgenberg). These capillaries were fixed onto a goniometer head and set spinning to produce a powder average. Obtaining a good powder average over all crystallites in a synchrotron experiment is complicated by the parallel geometry of the beam - only a restricted number of crystallites are at a correct orientation to diffract, so grinding the sample well and rotating it during data collection greatly improves the response. Data are collected on this machine in a continuous scanning mode to eliminate the dead time of a conventional step scan. After data collection the counts from all nine detectors are summed, binned and normalised. This process makes the data equivalent to a normalised step scan and allowing analysis by standard programs.

3.5.2. Neutron Diffractometers

3.5.2.1. Powder neutron diffractometer, D2B at ILL, Grenoble

Diffractometer D2B at ILL is a high-resolution two-axis machine. The data are collected using a multidetector consisting of 64 ^{3}He counting tubes spaced at 2.5°

intervals. A complete diffraction pattern may, therefore, be collected in 100 steps of 0.025°; this takes about 30 minutes then the scan may be repeated to improve statistics. This diffractometer is now routinely used to produce high quality data on nuclear and magnetic structures to allow subsequent refinement. The optimum flux is obtained when the wavelength of 1.594 Å is utilised by selecting the (335) reflection of Ge. A schematic diagram of the diffractometer is given in Figure 3.7.

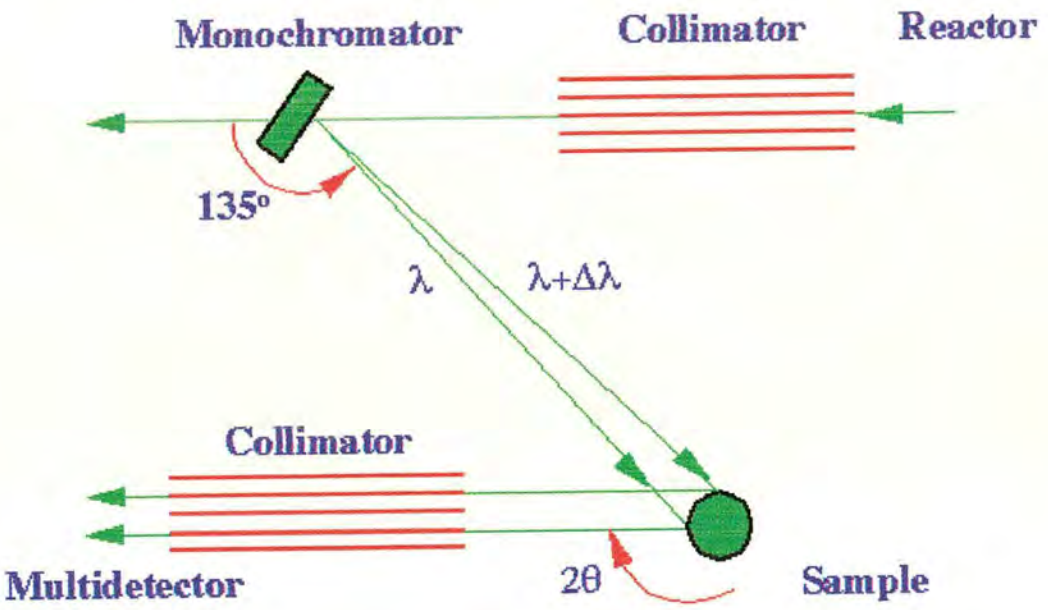

Figure 3.7. Schematic diagram of diffractometer D2B showing the progress of neutrons through the instrument, from the reactor to the multidetector [135]

A temperature range of 1.5 - 525 K was accessible using an ILL cryofurnace . The results of experiments carried out using this diffractometer are discussed in Chapters 5 and 7.

3.5.2.2. High flux powder neutron diffractometer, D1B at ILL, Grenoble

D1B is a two-axis spectrometer with very high neutron flux, (6.5 x10^6 n $cm^{-2}s^{-1}$ at λ=2.52 Å) at relatively large d-spacings. A high spatial resolution at small angles

(FWHM of 0.2°) can be achieved, allowing clear observation of magnetic reflections, and the high flux means that diffraction patterns can be obtained within minutes so that by incrementally changing temperature, structural and magnetic phase transitions can be studied as they occur. The full available temperature range (1.5-300 K, provided by a standard ILL 'Orange' cryostat) may be scanned in 3-5 hours.

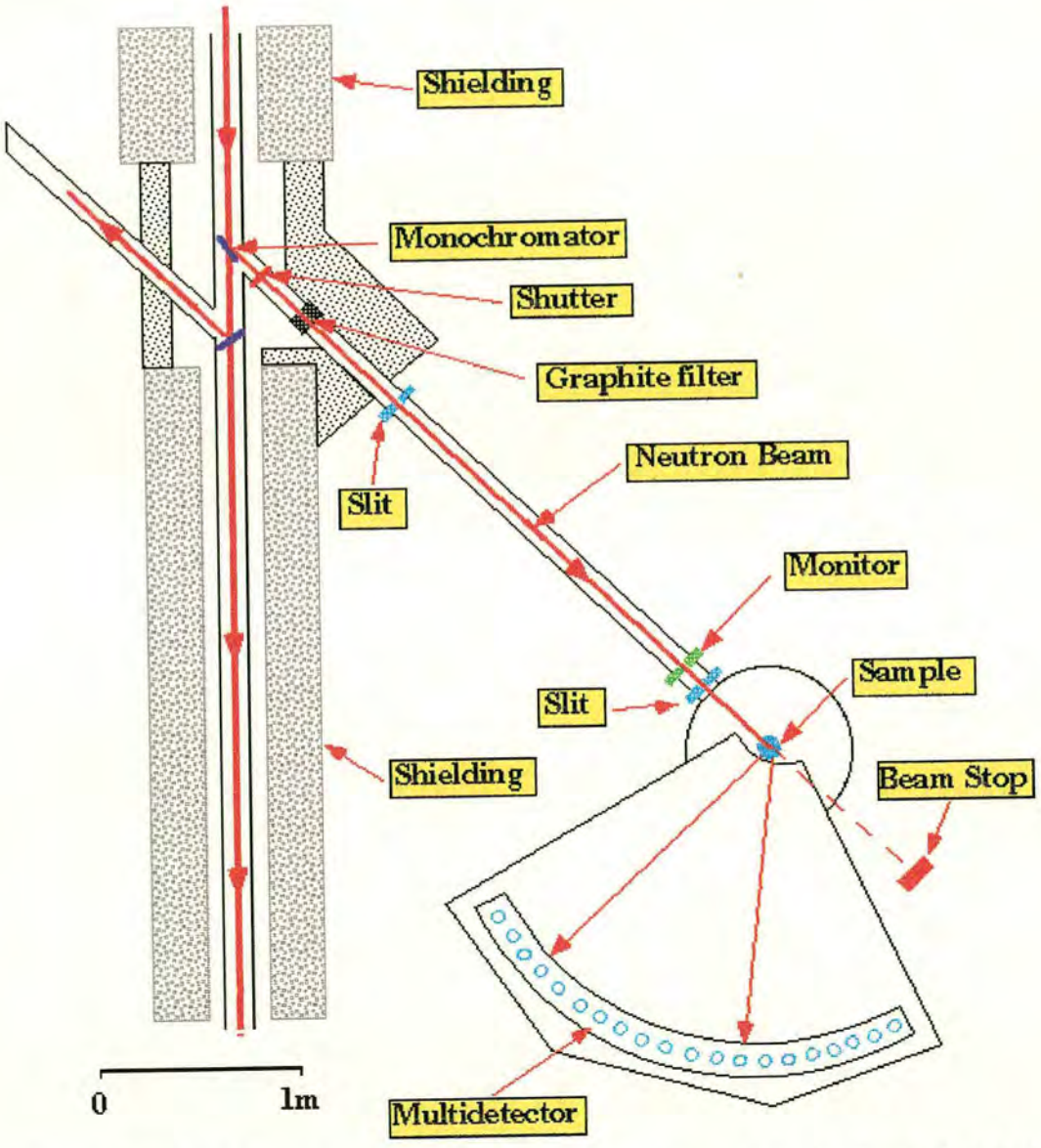

Figure 3.8. A schematic of the Diffractometer setup on line D1B at ILL [136].

The layout of the diffractometer is given in Figure 3.8; the large ^{3}He/Xe position sensitive detector comprises 400 multi-electrode cells and covers an 80° 2θ range which allows the entire pattern to be collected simultaneously.

3.5.2.3. High resolution quasielastic and inelastic scattering spectrometer and powder neutron diffractometer, IRIS at RAL

The IRIS Diffractometer at the ISIS Facility, Rutherford Appleton Laboratory was used to obtain information about the rotation of the ammonium groups in the materials studied here, as described in Chapter 6. IRIS is a high resolution quasielastic and inelastic scattering spectrometer but can also be used as a large d-spacing diffractometer, Figure 3.9. Diffraction data were collected on a sample of ND_4FeCl_3 and a quasi-elastic study of both NH_4FeCl_3 and ND_4FeCl_3 was also undertaken.

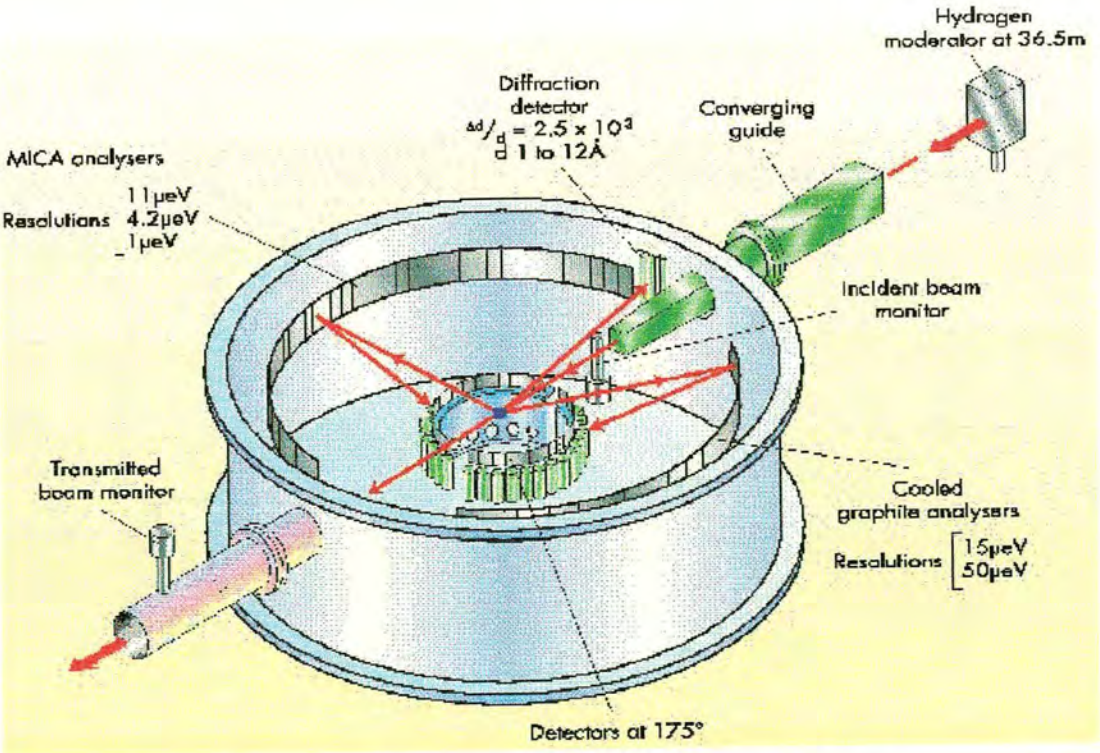

Figure 3.9. A schematic of the IRIS Diffractometer at RAL [137]

Before the quasi-elastic experiment could begin the amount of sample required to give optimum results had to be calculated. For good statistics the sample is required to transmit 85 -95% of the beam (this minimises any problems with multiple scattering). The attenuation of the transmitted beam may be calculated from:

$$I = I_0 e^{-n\sigma t} \tag{3.22}$$

where I_o is incident intensity, I is transmitted intensity, n is number of scattering atoms per unit volume, σ is the 'average' scattering cross-section for the atoms in the sample and t is the sample thickness. Data were recorded over a range of temperatures and the resolution of the elastic line was altered by selecting more than one analyser reflection. The results of this experiment are described and discussed in chapter 6.

3.6. Summary

Diffraction is a powerful method for the determination of crystal, molecular and magnetic structures. By careful consideration of incident radiation, sample preparation and diffractometer design, a wide range of phenomena may be investigated. This chapter has outlined the methods selected in this project to study the small structural distortions observed in the ammonium iron halides as they are cooled, the long range magnetically ordered structures, and the dynamical behaviour of the ammonium group within the solid structure; the results of these experiments are discussed in chapters 5, 6 and 7.

4. Sample Preparation

4.1. Introduction

In principle, ammonium iron halides are relatively straightforward to make. Compounds, with formula NH_4FeX_3, are formed by grinding together stoichiometric amounts of NH_4X and FeX_2 powders and heating *i.e.*

$$NH_4X + FeX_2 \xrightarrow{heat} NH_4FeX_3$$

However there are two major complications; firstly, both reactants and products, especially the bromide, are extremely air sensitive. Consequently great care must be taken to ensure the starting materials are completely dry and all handling must take place in a protected environment. The second complication is that at the temperature at which melting occurs, the ammonium salts evaporate under ambient pressure, so the reagents must be sealed into strong inert vessels during the preparation. This involves placing the reactants into sealed, Pyrex ampoules and heating to ~873 K. Under these conditions the vapour pressure of the NH_4X salts (NH_4Cl b.p. = 793 K, NH_4Br b.p. = 815 K at atmospheric pressure) is high, often causing explosion.

4.2. Ammonium Halides

NH_4Cl and NH_4Br were obtained from Aldrich (99.5%). These were then transferred into silica sublimation tubes and sublimed under a vacuum of $1x10^{-4}$ Torr at 373 - 423 K for around six hours. This was to remove impurities, especially any water. The sublimation tube was then transferred to an argon glove box (scrubbed using molecular sieve and a proprietary patented O_2 catalyst (Saffron) to give <100 PPM

H_20) and the pure, dry, white crystalline powder scraped out and stored in sealed bottles in the glove box.

4.3. Iron Chloride

$FeCl_2$ was prepared by dehydration of $FeCl_2.4H_2O$ (Aldrich 99%). The green crystals of $FeCl_2.4H_2O$ were packed into a silica boat and then placed in an isolated silica tube which incorporated an HCl (BDH, 99.9%) gas flow, see figure 4.1.

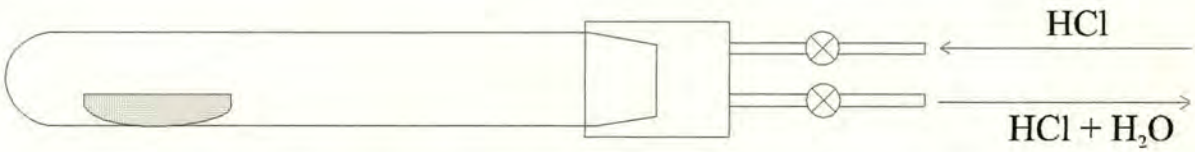

Figure 4.1. Apparatus used for the dehydration of $FeCl_2.4H_2O$

The tube was then inserted into a Carbolyte tube furnace and heated to ~ 873 K. The water was driven off, first condensing at the cooler end of the tube and then draining away. The process was stopped after around five hours, when the water evolution ceased. $FeCl_2$ formed as an ingot of brown material in the boat with large, pink, translucent flakes surrounding it. This purified material was then transferred to a sublimation tube and sublimed under a vacuum of $1x10^{-4}$ Torr at ~ 723 K to remove excess HCl and any residual water. The pure $FeCl_2$ obtained was a ring of pinkish powder which was also scraped out and stored in a sealed bottle in the argon glove box.

4.4. Iron Bromide

$FeBr_2$ was made by flowing HBr (BDH - 99.9%) gas over iron powder (Aldrich 97%) at ~ 873 K, using the apparatus shown above in Figure 4.1. The pure $FeBr_2$

was an ingot of yellowish brown material in the boat and large golden yellow flakes on the inside of the tube. This was again sublimed under vacuum of $1x10^{-4}$ Torr at ~ 723 K, to remove any excess HBr and metallic iron. The yellow powder obtained was scraped off and stored in the glove box. $FeBr_2$ (99.95%) was also obtained direct from Cerac, as a brown powder; this was found to be of poor purity, leaving a substantial amount of black, iron oxide deposits on sublimation, but as described below satisfactory results could be obtained using this reagent.

4.5. Ammonium Iron Halides

Stoichiometric amounts of NH_4X and FeX_2 (X = Cl and Br) were ground together using an agate pestle and mortar in the argon glove box. The mixture was then loaded into a Pyrex tube with a constriction, and sealed by a tap to protect the contents form moisture on removal from the glove box (Figure 4.2).

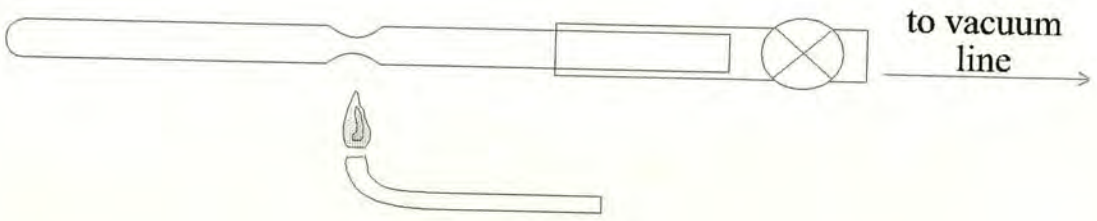

Figure 4.2. Reactants are placed into Pyrex tube and sealed under vacuum

The tube was attached to a vacuum line and carefully sealed into ampoules using a methane flame torch (hot flame) at $1x10^{-4}$ Torr. All possible precautions were taken to avoid water contaminating the samples as the products are highly hygroscopic and deliquesce in minutes, if handled openly on the bench. The ampoules containing the reactant mixtures were heated to 846 K in the Carbolite furnace (this temperature is just below the melting point of Pyrex), the samples were left at this temperature for

12-16 hours and then cooled slowly. The ampoules were carefully blown from thick Pyrex (2 mm wall thickness) and small diameter (14 mm O.D.) to limit the risk of explosion, as the pressure from the ammonium halides rises on heating. Despite these precautions several ampoules did explode but damage to the furnaces was minimised by placing the ampoules inside a steel pipe and placing fire bricks at either end to minimise explosion damage to the fume cupboard. The furnace was tilted slightly to allow the material to flow into a polycrystalline chunk. The cool ampoules were then removed and reheated to allow the product to flow to the other end of the ampoule leaving any residue behind on the walls of the tube. Samples made using commercial $FeBr_2$ left a black residue which was not observed in those synthesised with 'home made' reactants. The final material obtained in all cases were found to contain little or no impurity, (see section 4.8, characterisation). The final product was a small striated polycrystalline block with needle crystals observable on the surface and on the walls of the glass. These ampoules were scored with a glass knife and cracked open in the glove box, and single crystals prised from the block using a scalpel. Crystals were separated and selected for single crystal work, while powder samples were collected by again choosing good crystals and grinding them. Ideally, large single crystals would have been pulled for single crystal neutron work, using a Bridgman furnace but unfortunately this was not possible due to the large risk of explosion and potential damage to expensive apparatus.

4.6. Substituted Ammonium Iron Halides

Several attempts were made to synthesise substituted iron halides with highly asymmetric A cations, *e.g.* $CH_3NH_3FeX_3$ and $(CH_3)_2NH_2FeX_3$, by heating the substituted ammonium halides (obtained from Aldrich (99%) and dried under vacuum at ambient temperature, as sublimation at a slightly elevated temperature caused breakdown). Unfortunately, most attempts ended in ampoule explosion,

incomplete reaction or breakdown of substituted materials to produce elemental carbon and no satisfactory results were obtained.

4.7. Cs doped $RbFeBr_3$

A sample of $RbFeBr_3$ and 4 samples of $Rb_{1-x}Cs_xFeBr_3$ with x = 0.05, 010, 0.15 and 0.20 were prepared in a similar manner to the ammonium iron halides, less care needed to be taken in treating these materials as there are no volatile components. In this case RbBr and CsBr were supplied by Aldrich (99.7% and 99.9% purity respectively), and $FeBr_2$ was prepared as before.

4.8. Characterisation

After preparation it was possible to identify the materials *via* flat plate powder x-ray diffraction (see Section 3.5.1). However the extreme air sensitivity of the samples prevented impurity-free data as the sample holder was not sufficiently air tight. The outcome of this problem was that the sealed ampoules which were taken to ILL and ISIS contained samples which had not been explicitly characterised. It was assumed that as the sealed samples had been prepared in exactly the same way, and looked exactly the same as samples which had been analysed, that they were indeed pure. Some problems were experienced with impurities however, particularly in the very high resolution powder synchrotron work.

5. Structural Results - NH_4FeCl_3

5.1. Introduction

Diffraction is the most incisive method of determining the crystal structure of a material (Section 3.2). In this project, ammonium iron chloride samples were studied using both X-ray and neutron diffraction. Very high resolution single crystal and synchrotron X-ray studies were required to observe the structural distortions, which are very small. Neutron diffraction data was essential to the complete understanding of the phase diagram, to obtain the magnetic structures and the hydrogen positions and to elucidate potential hydrogen bonding in the low temperature structures. The diffraction results, refinements and nuclear and magnetic structural conclusions reached on ammonium iron chloride are described in this Chapter.

The ammonium iron chloride samples were made as outlined in Section 4.1.4. Single crystal and powder X-ray experiments and powder neutron experiments were performed, as described below, to give the fullest possible picture of the structure of the materials at all temperatures. It should be noted that the way in which the experiments was conducted was dependent on the availability of both suitable samples *and* instrumental time. Thus, although the Durham Fddd diffractometer would be the instrument of choice for most of the *structural* measurement, suitable single crystals were not initially available. The experiments are presented here in a logical, technique based way.

5.2. Single crystal X-ray diffraction

5.2.1. Siemens 4-circle diffractometer

X-ray diffraction data were collected on a single crystal of NH_4FeCl_3 using a Siemens 4-circle diffractometer (Section 3.6.2). Data were collected at 220 K and 120 K and both data sets were found to index on the primitive a x a x c cell. The data were refined using SHELXL93 [131] to give space group $P6_3/mmc$ (#194) at 220 K with unit cell dimensions of a = 6.9988(3) Å, c = 6.0202(4) Å and atom positions as shown in Table 5.1; errors are shown for all variable parameters. 2771 reflections were collected, 166 unique, $R1$ = 1.42 % (155 data).

Table 5.1. Details of the NH_4FeCl_3 structure at 220 K.

Atom	Site	*X*	*Y*	*z*	*U(eq)*
Fe	2 *a*	0	0	1	23(1)
Cl	6 *h*	-0.1624(1)	-0.3249(1)	0.75	29(1)
N	2 *d*	0.3333	-0.3333	0.75	37(1)
H(1)	4 *f*	0.3333	-0.3333	0.6087(39)	55
H(2)	12 *k*	0.4015(20)	-0.1971(39)	0.7832(73)	55
H(3)	12 *k*	0.2649(20)	-0.2649(20)	0.7827(73)	55

At 120 K the material was found to lose a mirror plane parallel to the c-axis (at x, y, 1/4) and a glide plane parallel to the c-axis and become space group $P6_3/m$ (#176), as illustrated in Figure 5.1. The 120 K structure refined in space group $P6_3/m$ (twinned) and had unit cell dimensions of a = 6.9875(3), c = 6.0022(7) and the atom positions are shown in Table 5.2. 2961 reflections were collected, 269 of which were unique and $R1$ = 0.96 % (256 data).

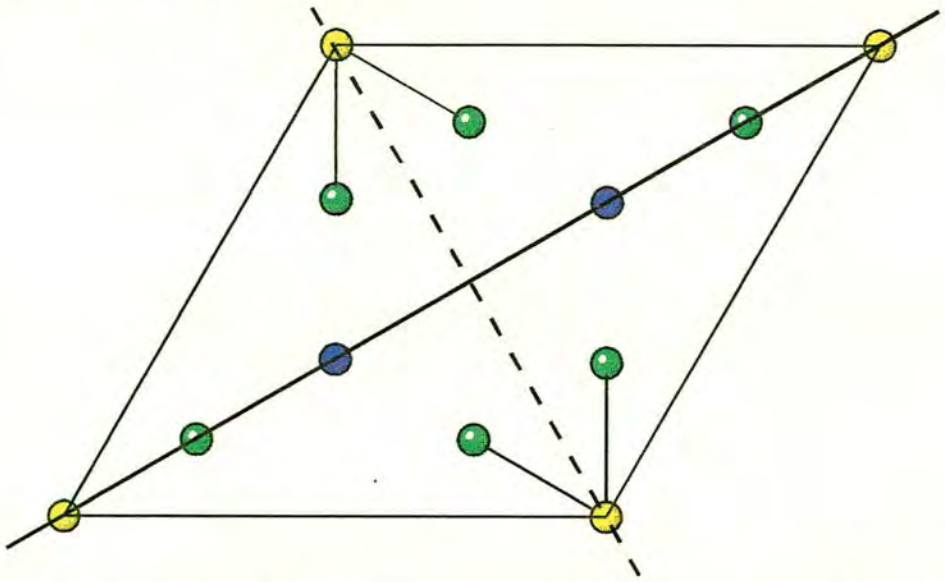

Figure 5.1. Twisting of the $FeCl_3$ chains causes the loss of the mirror plane (solid line) and the glide plane (dashed line) parallel to the *c*-axis.

This reduction in symmetry can be attributed to a twisting of the $FeCl_3$ chains and the structure is twinned as the chains have equal probability of twisting clockwise and anticlockwise, which is shown in Figure 5.2 (H atoms are omitted).

Table 5.2. Details of the NH_4FeCl_3 structure at 120 K.

Atom	Site	*X*	*Y*	*z*	*U(eq)*
Fe	2*b*	0	1	1	14(1)
Cl	6*h*	-0.1435(1)	0.6752(1)	0.75	17(1)
N	2*d*	0.3333	0.6667	0.75	26(1)
H(1)	4*f*	0.3333	0.6667	0.8989(26)	81(15)
H(2)	12*i*	0.2100(25)	0.6591(37)	0.7047(20)	51(7)

The H positions are not accurately found and the N-H bond lengths are 0.851 Å (220 K) and 0.894 Å (120 K) which are much shorter than the accepted value of 1.053 Å [138]. This is because X-ray diffraction locates centres of electron density (Section

3.3.2), also the NH_4 group is probably undergoing significant thermal motion at this temperature which further complicates the location of the H atoms.

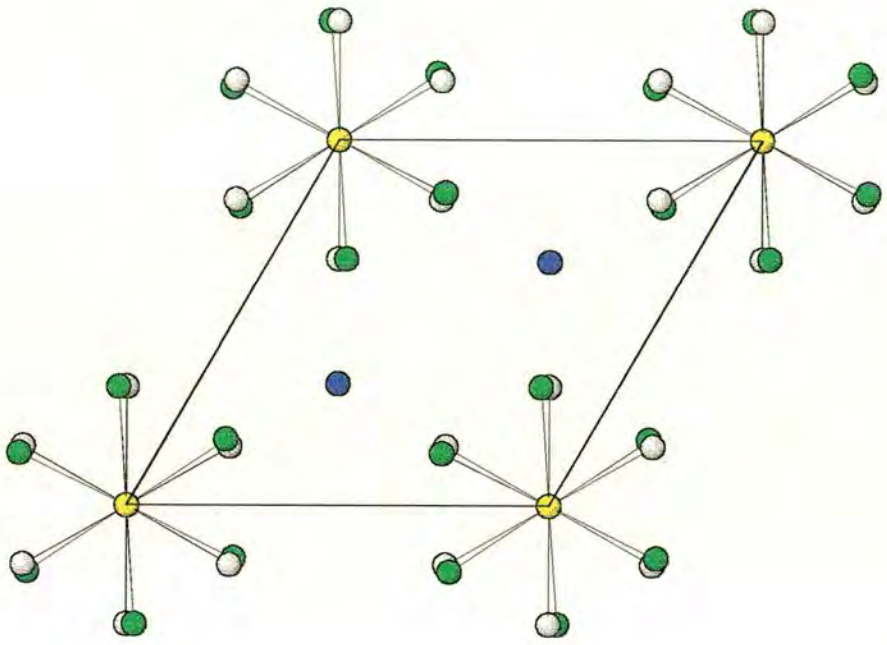

Figure 5.2. *a* x *a* x *c* primitive unit cell depicting the positions of Cl atoms at 220 K (white) and 120 K(green), the twisting here is anticlockwise (Yellow circles represent Fe and blue circles represent N).

This diffractometer is equipped with an N_2-cooled Cryostream cryostat and is capable of collecting data over a temperature range of 80 K to 373 K. NH_4FeCl_3 is expected to have a structural transition below 80 K and so any lower temperature structures could not be studied using this machine. To obtain the low temperature crystal and molecular structure, more specialised equipment was required. Two possibilities using X-ray radiation were available; the first of these was the custom-

built Fddd single crystal diffractometer at the Chemistry Department, Durham University, which can collect data at temperatures as low as 9 K (see Section 3.6.3). The X-ray flux of this rotating anode source diffractometer is around five to ten times higher than the Seimens 4-circle diffractometer; the intensity of the collected data will therefore be higher and this may prove to be important in the detection of these very small distortions. The second option was to study the material using very high resolution powder X-ray diffraction which could be done using diffractometer BM16 on the synchrotron source at the ESRF, Grenoble. Here, high quality data can be collected to very low temperatures (4.2 K) in relatively short periods of time (see 3.6.4). Both of these avenues were explored and the results are given below.

5.2.2. Measurements using the Fddd diffractometer

A single, needle-shaped crystal of NH_4FeCl_3 was studied on the Durham Fddd diffractometer (Section 3.6.3). The sample was mounted using low-temperature epoxy glue (Oxford Instruments, TRZ0004, suitable to at least 4 K) onto a 0.3 mm graphite rod and immediately transferred into a Schlenk tube, under nitrogen, for 24 hours, to allow the glue to set. The crystal was aligned and data collected at 291 K, 120 K, 30 K and 10 K. At all temperatures the structure could be modelled in space group $P6_3$ (#173), lattice parameters and goodness of fit parameters are shown in Table 5.3. Full listing of parameters obtained in these refinements is given in Appendix 1.

The unit cell at 291 K corresponds to a primitive a x a x c cell as expected and the data set gave the best refinement in space group $P6_3$, without any hydrogen atoms included, and the final atom positions are very close to those obtained in the 220 K data (collected in Edinburgh and refined in $P6_3/mmc$) as shown above (*c.f.* Tables 5.1 and 5.4).

Table 5.3: Lattice parameters and goodness of fit details.

Space Group	Temperature / K	*a* / Å	*c* / Å	*R*1	Reflections / Unique (refined)
$P6_3$	291	7.025(1)	6.043(1)	1.54%	304 (278)
$P6_3$	120	6.994(2)	6.010(1)	1.35%	294 (285)
$P6_3$	30	6.988(1)	6.007(1)	1.64%	294 (285)
$P6_3$	10	13.973(2)	6.008(1)	2.3%	781 (555)

A structural phase transition was observed at 181 K, below which the (-3 -3 -1) reflection started to show a steep increase in intensity, this is illustrated in Figure 5.3.

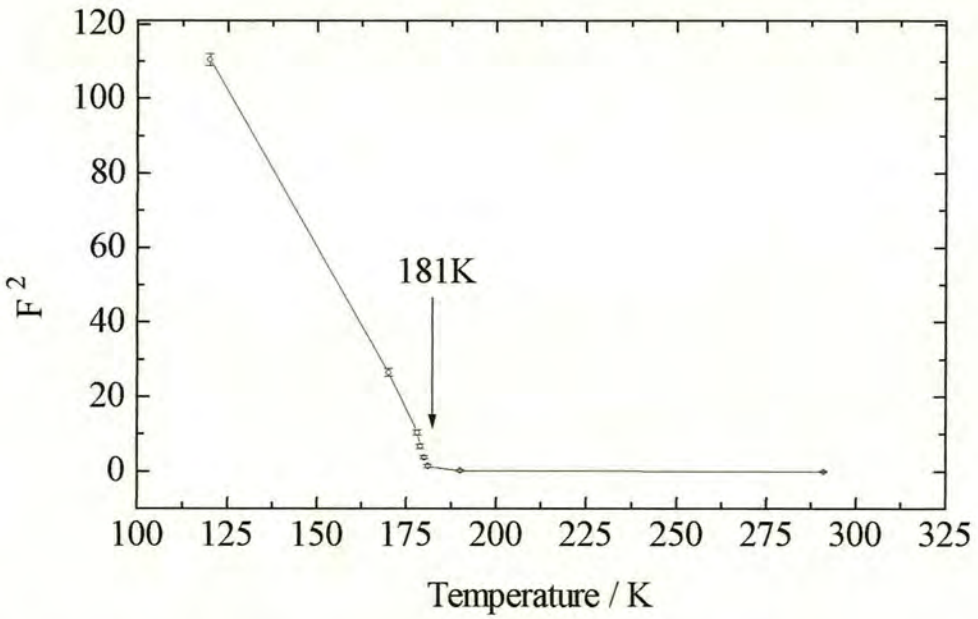

Figure 5.3. A F^2 *vs.* temperature plot of the (-3 -3 -1) reflection in NH_4FeCl_3 showing a sharp increase at the transition temperature 181 K.

The data sets collected below this transition at 120 K and 30 K also refined best in space group $P6_3$ and the lack of intensity in the (-3 -3 -1) reflection above 181 K is

consistent with the loss of the mirror plane and glide plane both parallel to the *c*-axis and mutually perpendicular, as described above in the data collected in Edinburgh. The models at 120 K and 30 K included a 43% twin component for which *a* and *b* are swapped and *c* is reversed; this corresponds to the equal probability of chains twisting in opposite directions (see Figure 5.2 above). The refined atom positions from the 120 K are shown in Table 5.5; once again these agree well with the refinement of the 120 K data set collected in Edinburgh (Table 5.2).

A second structural phase transition was observed at 19.5 K; reflections which can be indexed as (-1/2 0 -4), (1/2 0 -4) and (0 1/2 -4) were seen to appear at this temperature. This indicates a unit cell in which both of the lattice constants for the basal plane are doubled relative to those observed at higher temperatures, *i.e.* giving a $2a \times 2a \times c$ cell. *Monoclinic* $2a \times a \times c$ cells are found as low temperatures phases of a number of other ABX_3 hexagonal perovskites [139] (Section 1.4) while this $2a \times 2a \times c$ cell, with space group $P6_3$ (at 10 K $a = 13.973(2)$ Å and $c = 6.008(1)$ Å), has not been previously observed, to the best of our knowledge. The distortion here involves a slipping of the $FeCl_3$ chains relative to one another in the *c*-direction and this is illustrated in Figure 5.4 and Table 5.6. The $FeCl_6$ octahedral units are also significantly distorted, producing three slightly different magnetic bridging angles. Table 5.7 provides a comparison of in-chain Fe-Cl-Fe bridging angle at different temperatures. This angle is very important in determining the nature of the magnetic exchange (Section 1.5).

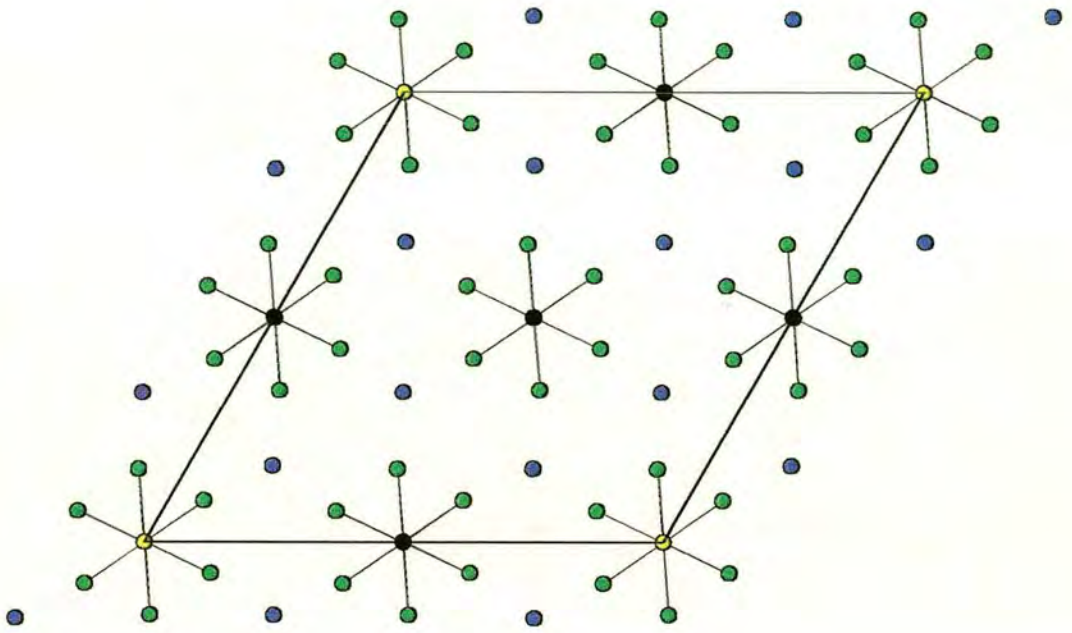

Figure 5.4. The 2*a* x 2*a* x *c* unit cell found at 10 K for NH_4FeCl_3 using the Fddd diffractometer. The red circles represent one subset of iron atoms which are shifted along the *c*-axis (into the page) relative to the second, black, subset.

The parameters obtained from the refinements of data collected on the NH_4FeCl_3 needle are shown in Tables 5.4, 5.5 and 5.6; further data including all important bond lengths and angles are listed in Appendix A.

Table 5.4: Atom positions obtained from data collected on Fddd on NH_4FeCl_3 at 291 K, space group $P6_3$, a = 7.025(1), c = 6.043(1).

Atom	*x*	*y*	*Z*	*U(eq)*
Fe	0	0	0	31(1)
Cl	-0.1621(1)	-0.3241(1)	0.2492(8)	38(1)
N	0.33333	-0.33333	0.2503(81)	51(1)

Table 5.5: Atom positions obtained from data collected on Fddd on NH_4FeCl_3 at 120 K, space group $P6_3$, a = 6.994(1), c = 6.010(1)

Atom	*x*	*y*	*Z*	*U(eq)*
Fe (120K)	0	0	0.0008(4)	16(1)
Cl	-0.1429(1)	-0.3248(1)	0.2493(7)	19(1)
N	0.33333	-0.33333	0.2432(61)	28(2)

Table 5.6: Atom positions obtained from data collected on Fddd on NH_4FeCl_3 at 10 K, space group $P6_3$, a = 13.973(2), c = 6.008(1)

Atom	*x*	*y*	*z*	*U(eq)*
Fe (1)	0	0	-0.0256(3)	4(1)
Cl (1)	0.0695(2)	0.1621(2)	0.2235(2)	5(1)
Fe (2)	0.0010(1)	0.5005(1)	-0.0036(3)	7(1)
Cl (2)	-0.1624(2)	0.4076(2)	0.2452(2)	10(1)
Cl (3)	0.0692(2)	0.6623(2)	0.2467(3)	8(1)
Cl (4)	0.0926(2)	0.4301(2)	0.2485(3)	8(1)
N (1)	0.3333	0.6667	0.1933(19)	50(5)
N (2)	-0.1697(6)	0.1627(6)	0.2678(10)	7(1)

Table 5.7. The intrachain bridging angles in NH_4FeCl_3 at 10 K.

Data	Temperature / K	Fe-Cl-Fe angle
Durham	291	74.92(1)°
Edinburgh	220	74.78(1)°
Edinburgh	120	74.60(1)°
Durham	120	74.61(1)
Durham	10K	74.70(1)°, 74.60(1)° and 74.54(1)°

In summary, the results obtained at 291 K and 120 K compare well with the 220 K and 120 K refinements obtained in Edinburgh. The structural transition observed, in which the $FeCl_3$ chains were found to twist relative to one another, was found to occur at 181 K in this experiment. There is a transition to a further low temperature structure at 19.5 K, where the unit cell volume is increased by a factor of 2 or larger. This second transition may either be driven by structural packing factors (as for the 181 K transition) or by hydrogen bonding induced as NH_4 groups stop rotating and adopt fixed positions; a similar transition is *not* observed in $RbFeCl_3$, which suggests this distortion may indeed be influenced by hydrogen bonding. Neutron diffraction data may provide the location of the H positions (see Section 5.3.1) and a quasi-elastic study was carried out to investigate the motion of the NH_4^+ group (see Chapter 6).

5.3. Powder X-ray diffraction using synchrotron radiation

Data were also collected using diffractometer BM16 at the European Synchrotron Research Facility (ESRF), Grenoble (Section 3.6.4). Synchrotron radiation proves an effective way of obtaining very high resolution powder diffraction data over a wide range of temperatures (Section 3.3.1.1). The samples were loaded into 0.6 mm

diameter borosilicate capillaries inside an argon glove box. Great care had to be taken when handling the delicate capillaries as these could easily break, causing at best a loss of sample and at worst a puncture in the gloves. The capillaries were then heat-sealed inside the glove box. If the seals were good the powder should be completely protected. However, the sealing was also very difficult to accomplish inside the restricted environment of the glove box and some seals may have been imperfect. In one case the sample imploded in the cryostat under vacuum, this demonstrated the high sensitivity of the machine as it was still possible to collect diffraction patterns on the tiny amount of powder left on the walls of the broken capillary! The data sets collected in these experiments are summarised in Tables 5.8 and 5.89. In some cases the high flux of the instrument also revealed traces of an impurity, shown to be $FeCl_2$.

Table 5.8. Summary of powder X-ray synchrotron data sets collected on NH_4FeCl_3.

Temperature/K	$FeCl_2$ impurity
423	n
300	y
291	n
30	n
4	n

Table 5.9. Summary of powder X-ray synchrotron data sets collected on ND_4FeCl_3.

Temperature/K	$FeCl_2$ impurity
300	y
291	n
200	y
160	y
30	y
4.2	y

5.3.1. GSAS refinement data collected on BM16

All data have been analysed using Rietveld refinement (Section 3.4), using the program suite GSAS [130]. All refinement plots and parameter details are given in Appendix A.

As discussed in Section 3.4, the overlap of reflections in powder data means that the maximum information can only be extracted if the peak shape is properly modelled and as the resolution of powder data continues to improve, efficiently modelling the line shape is becoming increasingly problematic. The first difficulty with the BM16 peak shape is that it contains a significant asymmetry due to axial divergence (Section 3.4.1). The effect of axial divergence is most apparent at high d-spacing; thus in the refinement of data for NH_4FeCl_3 the (010) reflection, which is present close to 6 Å, is significantly asymmetric (Figure 5.5). One solution is to leave the highest d-spacing peaks out of the refinement and then refine them separately. The peak shape can, however, be modelled in GSAS, using a Lorentzian peak shape incorporating the asymmetry correction of Finger *et al.* [124,125]. The Le Bail extraction method [126] option in GSAS was used here to model individual peaks

while the observed structure factors were extracted. For each refinement the (010) reflection was individually modelled to obtain values of S/L and H/L (where 2S = sample width, 2H = detector width, L= radius, these are illustrated in Section 3.4.1). These values were then inserted as starting values in the refinement of the entire powder data set; this method is reported to be the most effective to date [140]. The peak asymmetries were modelled much more successfully using this modification (see Figure 5.6)

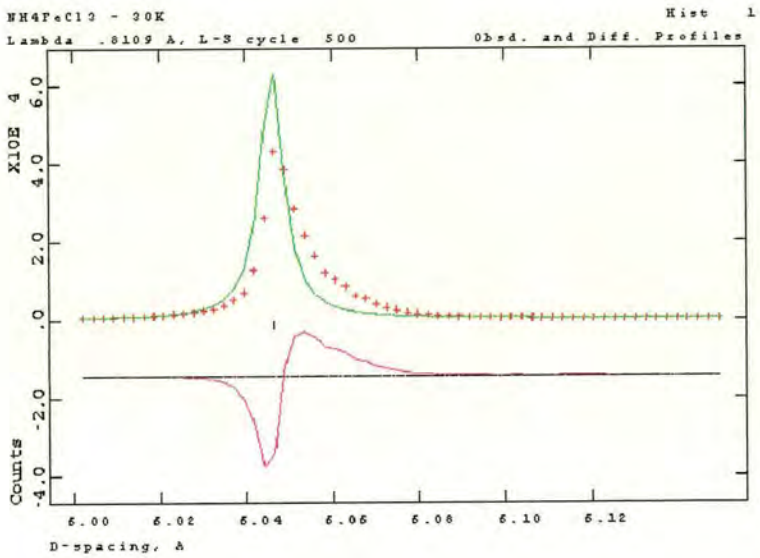

Figure 5.5. Data and fit showing that axial divergence causes asymmetric broadening at large d-spacing (reflection is modelled using a Lorentzian function).

The starting values of S/L and H/L are obtained from the diffractometer layout; the width of the beam (i.e. 2S) is 5.8 mm and the horizontal size of the detector slits (i.e. 2H) is 15 mm and the distance between the sample and the detector slits was 784 mm. i.e. S/L = 0.0031 and H/L = 0.0096. The final values of S/L and H/L obtained in the refinements differed from these values, although the diffraction optics were the same in each case, see Table 5.10. The differences between the values obtained in

each case would seem to suggest that refinement is necessary as there is apparently clearly a dependence not only on the chemical nature of the sample concerned but also on the properties of an individual sample, *e.g.* crystallite size.

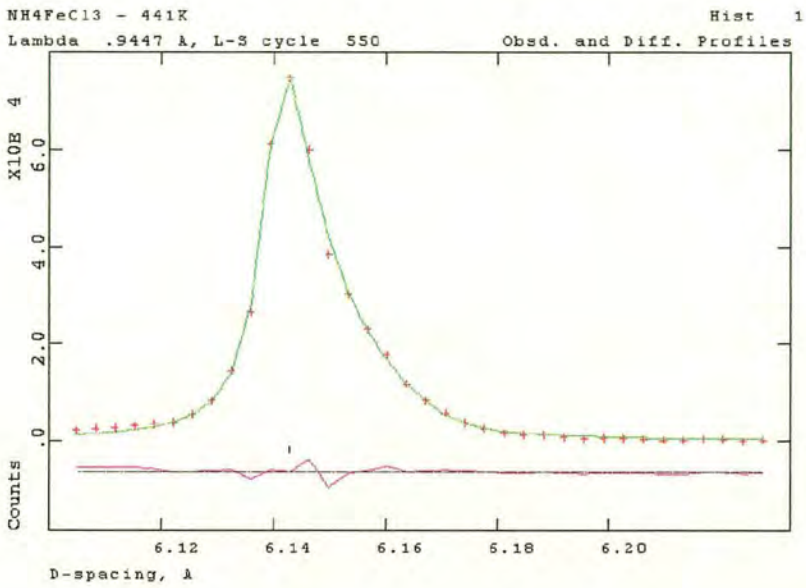

Figure 5.6. The effect of axial divergence can be modelled well using the asymmetry correction of Finger *et al* [124].

Table 5.10: Refined values obtained for the asymmetry parameters S/L and H/L

Sample	Temperature / K	S/L	H/L	Wavelength / Å
NH_4FeCl_3	423	0.0077(1)	0.0083(1)	0.944680
NH_4FeCl_3	300	0.0033(1)	0.0071(1)	0.653133
NH_4FeCl_3	291	0.0074(1)	0.0086(1)	0.944680
NH_4FeCl_3	30	0.0039(1)	0.0090(1)	0.810855
ND_4FeCl_3	300	0.0033(1)	0.0071(1)	0.653133
ND_4FeCl_3	291	0.0077(1)	0.0085(1)	0.944680
ND_4FeCl_3	200	0.0033(1)	0.0071(1)	0.653133
ND_4FeCl_3	160	0.0033(1)	0.0071(1)	0.653133
ND_4FeCl_3	30	0.0033(1)	0.0071(1)	0.653133

The refinements were carried out as follows. Starting values of lattice parameters, atom positions and approximate peak shape were inserted into the input file (a Lorentzian peak shape function allowing anisotropic broadening along the (001) axis was chosen). Lattice parameters and the zero angle of the instrument were then refined. A background function appropriate to this kind of experiment was chosen - a six member power series (function # 6 in GSAS), which describes the effect of diffuse scattering from the sample and holder and air scattering over the full range of d-spacing, was selected and refined in each case. The atom positions, and isotropic thermal parameters were then varied.

The data could be refined fairly successfully (Tables 5.11 and 5.12, page 103), although there were still a few problems with peak shapes. In some data sets the peak shape observed was also degraded by the poor alignment of the capillary, which appeared to be poorly aligned with respect to its axis of rotation on the mount. This resulted in the capillary moving very slightly in and out of the beam and the resulting peaks had a slightly stepped shape. In addition, the (*hk*0) reflections are seen to be significantly narrower than those with $l \neq 0$. GSAS does contains a function which attempts to model this and works quite well on some reflections, *e.g.* those shown in Figure 5.7. The physical origin of this effect is the presence of stacking faults, introducing anisotropic disorder to the lattice. This model then also significantly broadens the (00*l*) reflections which are not observed to broaden in this data. This, therefore, is not an ideal solution; modelling this type of feature is becoming a widespread problem as more and more high resolution data is collected.

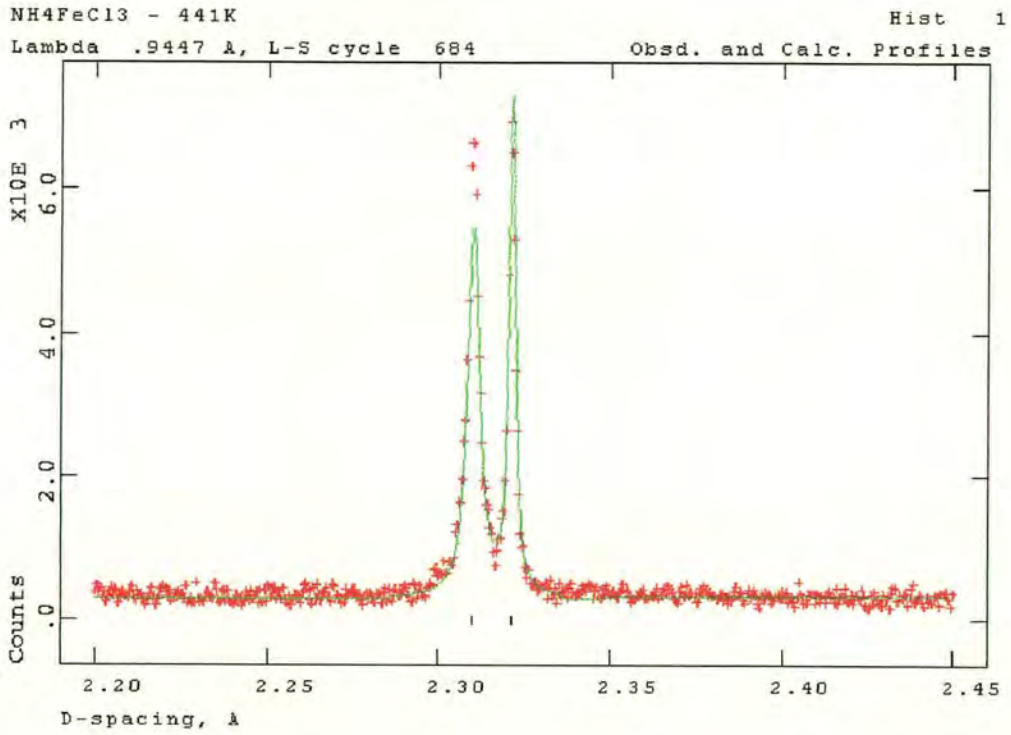

Figure 5.7. Anisotropic broadening of different reflections; in this diffraction pattern of ND_4FeCl_3 at 423 K, the reflection on the left (112) is seen to be significantly broader than the one on the right (210).

There is currently no software available to satisfactorily fit the data, but this may be remedied in the fairly near future as many groups are currently working on the problem [127]. Consequently, lattice parameters are reliably obtained for all temperatures (see Table 5.11 and 5.12) and the atom positions are very close to those found in the single crystal X-ray data above and the neutron refinements (Section 5.3.1) at the corresponding temperatures (see below). The data above the 181 K transition could not be modelled with symmetry lower than $P6_3/mmc$ and no improvement was seen in the refinement if the numbers obtained from the refinements of Fddd data are used. The high resolution of the data is a problem in refinement but can be seen to clearly show new reflections relating to the very small

structural distortions observed here. For example, the onset of the (111) reflection between 200K and 160K was very clear in the ND_4FeCl_3 data as shown in Figure 5.8. This is in good agreement with the data for NH_4FeCl_3 obtained in Durham. The (113) reflection is also evident below 200K (Figure 5.9); the appearance of these reflections (i.e. the (*hhl*) where $l \neq 2n$) is expected when the glide and mirror plane parallel to the *c*-axis are lost from a structure with $P6_3/mmc$ symmetry. These are consistent with a phase transition at 181K, produced by the twisting of the $FeCl_3$ chains and subsequent loss of symmetry.

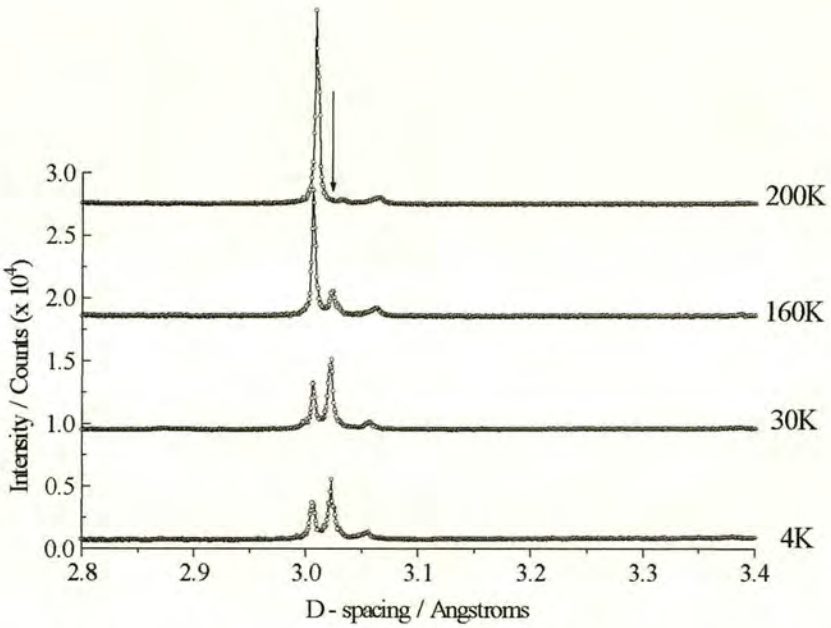

Figure 5.8. Onset and growth of the (111) reflection on cooling ND_4FeCl_3

Limited beam time meant that hydrogenated and deuterated samples were not both run at all temperatures but at least one temperature was obtained above and below each structural transition temperature. An impurity phase ($FeCl_2$) was observed in one of the deuterated samples.

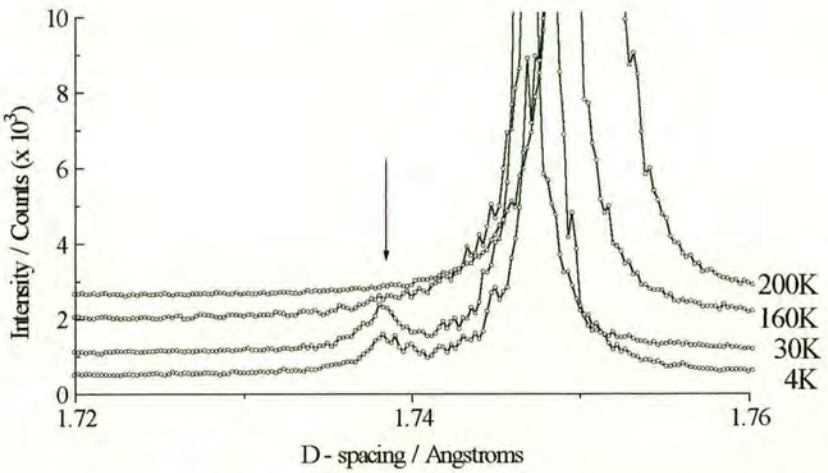

Figure 5.9. Onset of the (113) reflection in ND_4FeCl_3 observed in BM16 data

Limited beam time meant that hydrogenated and deuterated samples were not both run at all temperatures but at least one temperature was obtained above and below each structural transition temperature. An impurity phase ($FeCl_2$) was observed in one of the deuterated samples. This is indicated above in Tables 5.8 and 5.9. The impurity peaks were very small and were excluded from the data sets prior to further analysis, the resulting GSAS refinements were stable but the poor quality of the samples was reflected in the goodness of fit parameters (Table 5.9). At and above room temperature the structure was refined successfully with a $P6_3/mmc$ hexagonal perovskite structure with chloride ions in special positions on mirror planes.

5.3.2. Low temperature structure of NH_4FeCl_3

Superlattice reflections are observed to appear in data collected on a sample of NH_4FeCl_3 (see Figure 5.10) between 30 K and 4.2 K. The new peaks index as the

(014) and (114) reflections of this $2a$ x $2a$ x c lattice. These are the (0 1/2 4) and (1/2 1/2 4) reflections with respect to the primitive a x a x c lattice, the same as observed in the Fddd data taken at 10 K. No extra peaks were observed, however, when the data collected on ND_4FeCl_3 at 30 K and 4.2 K were compared, Figure 5.11.

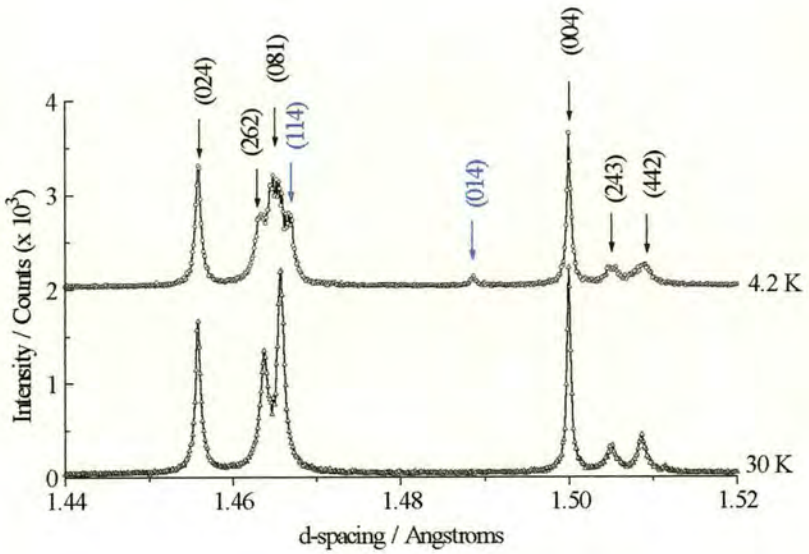

Figure 5.10. Appearance of superlattice reflections in NH_4FeCl_3 data taken at 4.2 K; these are shown in blue.

Understanding the effect, if any, of substitution of H by D to the hydrogen bonding and consequently to the nature of the transition, observed at 19.5 K above, is further complicated by the nature of the samples. The diffraction pattern of the NH_4FeCl_3 sample at 4.2 K is of far greater quality than the ND_4FeCl_3, at the same temperature, indicating that the sample quality is much higher. The very high quality of the NH_4FeCl_3 data presented in Figure 5.10 is apparent in the sharpness of its peaks when compared to the ND_4FeCl_3 data shown in Figure 5.11.

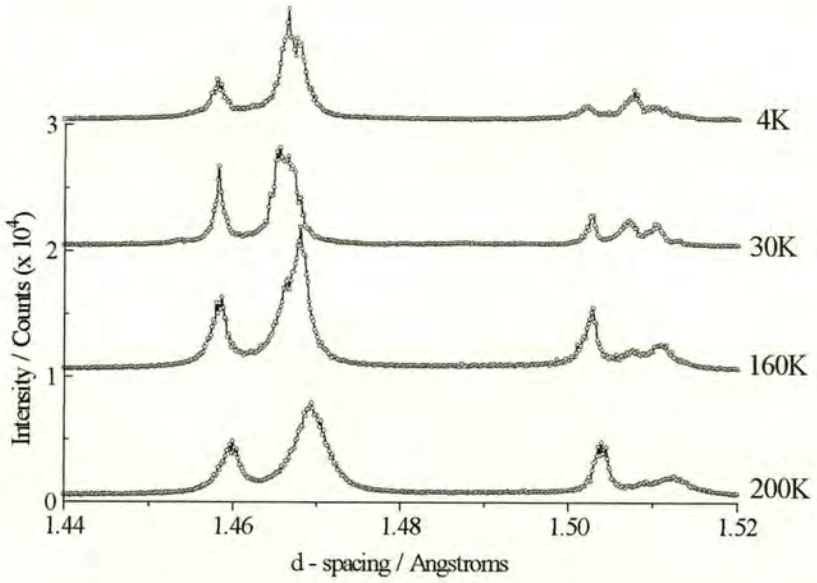

Figure 5.11. There appears to be no evidence of any superlattice reflections at 4.2 K in ND_4FeCl_3 data recorded using BM16.

An attempt was made to refine the 4.2 K NH_4FeCl_3 data (see Figure 5.12) using the atom positions and lattice parameters obtained in the refinement of the Fddd single crystal 10 K NH_4FeCl_3 data set as a starting point. All parameters were refined as described to give a reasonably good fit ($\chi^2 = 10.5$ and $R_{wp} = 0.29$) and some intensity was calculated in the (014) superlattice reflection, this intensity appears to be due to a slight distortion of the BX_6 octahedra and produce a buckling along the *c*-axis, where the Cl atoms are no longer positioned on the (x,y,1/4) mirror planes as observed in the Fddd 10 K NH_4FeCl_3 refinement. However the refinement became unstable if the atom positions were allowed to vary in a completely unconstrained manner and had to be coaxed into optimal positions manually.

There were some discrepancies in the indexing of these data on the hexagonal $P6_3$ $2a$ x $2a$ x c unit cell. Figures 5.12 and 5.13 show selected regions of the diffraction pattern with further distortion of reflections relative to those observed at 30 K, this distortion could not be indexed on this cell. This may indicate a further distortion of the structure involving a loss of hexagonal symmetry. There was no evidence of these addition reflections in the 10 K Fddd data. This may perhaps be attributed to the fact that the BM16 data was collected at the lower temperature of 4.2 K. There is, therefore, a possibility that a third structural distortion is occurring between these two temperatures and this could perhaps be investigated in the future by a low temperature heat capacity experiment.

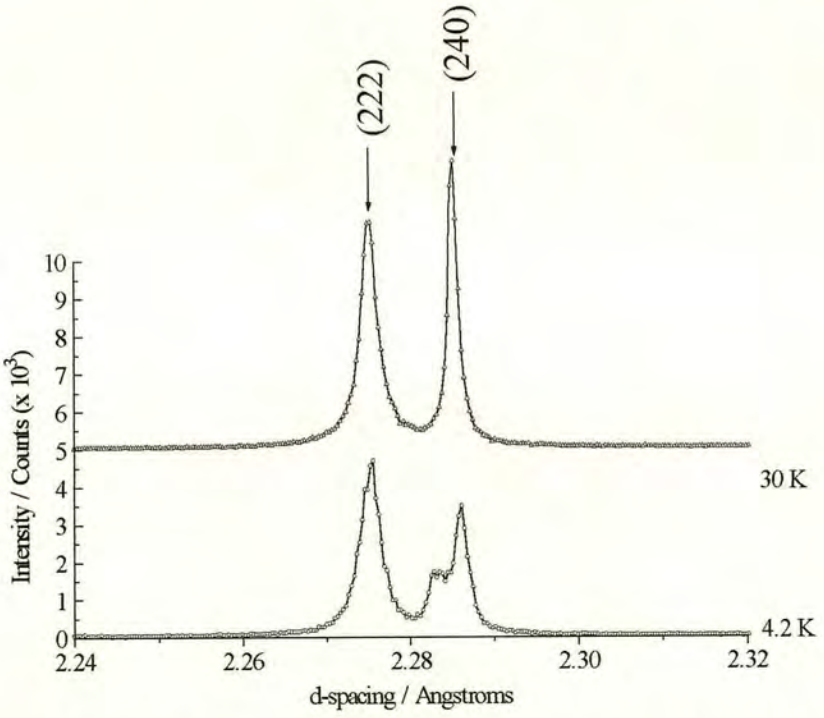

Figure 5.12. An additional reflection is seen to appear in the 4.2 K data collected on NH_4FeCl_3 compared to those collected at 30 K, this cannot be indexed on the hexagonal $2a$ x $2a$ x c unit cell. Miller indices shown here refer to the expanded cell.

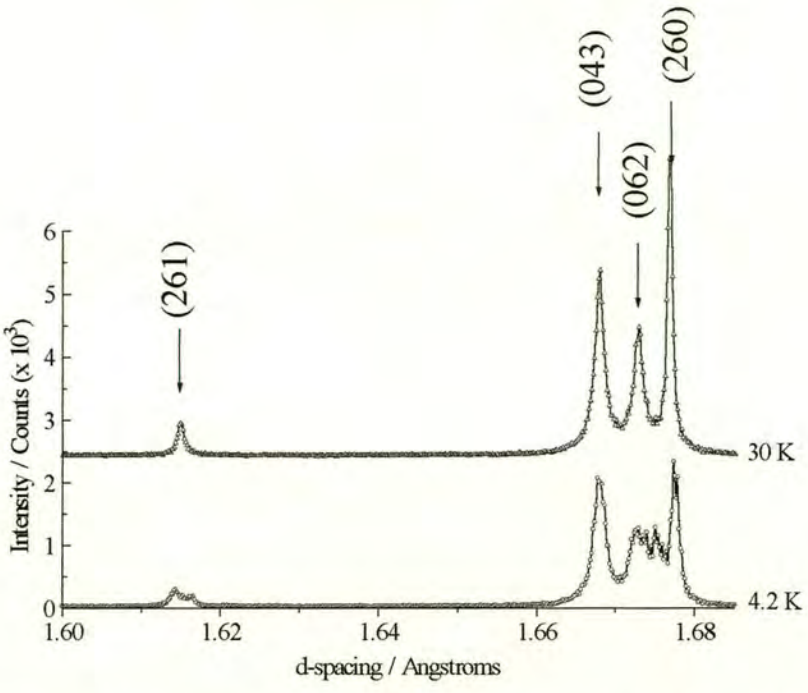

Figure 5.13. Addition reflections are seen to appear in the 4.2 K data collected on NH_4FeCl_3 compared to those collected at 30 K, these cannot be indexed on the hexagonal 2*a* x 2*a* x *c* unit cell

The reflections in this data may be well enough resolved to allow solution *via* an auto indexing package. The peak positions were identified by hand using MicroCal Origin, and processed using the auto indexing program Treor 90 [141]. This indicated an orthorhombic unit cell with lattice parameters a = 13.972(1), b = 12.084(1) and c = 6.000(1) (i.e. $2a$ x $\sqrt{3}a$ x c) and a unit cell volume of 1013.01(1)Å^3.

Table 5.11: Lattice parameters and goodness of fit values obtained from NH4FeCl3 refinements of BM16 data.

Temperature / K	Space Group	a / Å	c / Å	χ^2	R_{wp}
423	$P6_3/mmc$	7.09107(7)	6.08946(11)	1.737	0.2118
300	$P6_3/mmc$	7.02398(3)	6.03843(3)	14.07	0.1601
291	$P6_3/mmc$	7.01923(8)	6.03602(14)	2.731	0.1911
30	$P6_3/m$	6.98179(1)	6.00031(2)	4.271	0.1731

Table 5.12: Lattice parameters and goodness of fit values obtained from ND4FeCl3 refinements of BM16 data.

Temperature / K	Space Group	a / Å	c / Å	χ^2	R_{wp}
300	$P6_3/mmc$	7.02496(4)	6.03810(6)	29.83	0.1605
291	$P6_3/mmc$	7.01927(6)	6.03673(13)	2.713	0.1851
200	$P6_3/mmc$	6.99858(6)	6.01481(9)	47.56	0.1523
160	$P6_3/m$	6.99059(4)	6.00921(6)	63.95	0.1613
30	$P6_3/m$	6.98487(5)	6.00911(6)	69.05	0.1973

5.3.3. Summary

Single crystal X-ray and synchrotron studies have shown a transition involving a twisting of $FeCl_6$ chains at 181 K in NH_4FeCl_3 and one between 160 and 200 K in ND_4FeCl_3. A second transition at 19.5K has been observed in NH_4FeCl_3 to a new $2a$ x $2a$ x c hexagonal unit cell. Synchrotron data taken at 4.2 K may suggest a further distortion to a $2a$ x $2a$ x c monoclinic cell or a $2a$ x $\sqrt{3}a$ x c orthorhombic cell on further cooling. At this stage it seems entirely possible that hydrogen bonding may be a significant factor, evidence of the presence of a transition at around 19.5 K in

the deuterated compound may facilitate solution of this problem, this is considered using neutron diffraction measurements.

5.4. Neutron Diffraction

Neutron diffraction plays a vital role in elucidating the structural and magnetic properties of solids. Many other techniques, such as X-ray diffraction, solid state NMR, magnetometry, are more widely available and, generally, less expensive., but neutron diffraction is the most direct and powerful way of studying, for example, long range magnetic order and hydrogen atom positions. Neutron scattering data should complement the X-ray work, outlined above, as the hydrogen positions may be of importance below the second structural phase transition at 19.5 K. It is possible that the rotation of the ammonium group freezes out completely and that hydrogen bonding may be influencing the structure. Furthermore, neutron diffraction may reveal the nature of any magnetic long-range order at low temperatures. A good understanding of the magnetic structure is pivotal in any future analysis of the local magnetic exchange in the material. If the low temperature structure involves chain slipping this may affect the symmetry of the interchain magnetic exchange, as this interaction is very sensitive to very small changes in lengths and angles in the Fe-Cl-Cl-Fe pathway between the chains.

Ideally, one would conduct further neutron studies using a single crystal; unfortunately this was not an option as it is difficult to grow sufficiently large crystals (Section 4.5). The single crystals made were approximately 4×10^{-3} mm^3, which is large enough for X-ray work but neutron diffraction requires crystals of the order of at least 100 mm^3. A powder neutron study was, therefore, the best available option.

5.4.1. Crystal Structure Refinement

Neutron scattering experiments have been previously carried out on both NH_4FeCl_3 using diffractometers D1B and HRPD at RAL [142,143]. The data collected on these occasions was incomplete, not fully analysed and contained impurities so no useful conclusions were reached. Neutron diffraction data were collected using diffractometers D2B and D1B at the ILL, Grenoble (Sections 3.6.5 and 3.6.6) and IRIS at the RAL (Chapter 6).

5.4.1.1. Diffraction measurements taken using the IRIS spectrometer

IRIS is a high resolution inelastic neutron scattering spectrometer at the ISIS Facility. (Chapter 6). It can also be used as high-resolution, long-wavelength diffractometer [137a]. Diffraction data were collected on a sample of ND_4FeCl_3 at two temperatures and with different instrumental configurations as outlined in Table 5.13.

Table 5.13. Summary of conditions for data collection on the IRIS spectrometer

Current / μA	Temperature/K	d-spacing range / Å
27.1	4.2	2.20-3.80
38.1	4.2	3.40-5.10
63.1	4.2	4.60-6.40
156.1	4.2	5.90-7.40
100.1	4.2	7.00-8.70
129.5	4.2	8.30-9.90
126.1	4.2	9.60-11.00
50.7	4.2 -> 1.9	9.60-11.00
90.6	1.9	9.60-11.00
43.2	1.9	4.60-6.40

The data were then processed using the program ADD which sums the response from all the detectors and outputs a file with a single intensity for each step in two theta [144].

5.4.1.2. Rietveld refinement of D2B data for ND_4FeCl_3

Data were collected on a 4 g powder sample of ND_4FeCl_3 loaded into an 8 mm diameter vanadium can; the sample was loaded in an argon glove box, and indium wire was placed in a channel around the top of the can; a steel cap was then screwed down onto the wire, compressing it to make a gas-tight seal to prevent the material being exposed to air. Diffraction patterns were collected on diffractometer D2B, and are summarised in Table 5.14. These patterns were refined using GSAS and the refinement plots and important bond length and angle data are included in Appendix B

Table 5.14. D2B data collected on ND_4FeCl_3

Temperature / K	Space group	a / Å	c / Å	χ^2	R_{wp}
473	$P6_3/mmc$	7.08532(10)	6.08450(17)	2.740	0.0510
363	$P6_3/mmc$	7.04914(10)	6.05726(15)	3.159	0.0487
300	$P6_3/mmc$	7.02607(6)	6.04126(12)	5.205	0.0520
200	$P6_3/mmc$	6.99887(10)	6.02349(13)	3.399	0.0510
160	$P6_3/m$	6.99388(11)	6.01579(13)	3.593	0.0528

The refinements were carried out as follows. The starting positions of the lattice parameters and the atom positions were taken from the X-ray refinements and inserted onto the input file. The instrumental zero point and lattice parameters were then allowed to refine. A cosine-Fourier background function with eight parameters

was utilised in each case. The peak shape was modelled using a pseudo-Voigt function. Finally, all the atom positions and anisotropic thermal parameters were varied. The input file was also adjusted to contain a description of the ND_4 group as a rigid body disordered over two positions, up and down with respect to the *c*-axis (Figure 5.14).

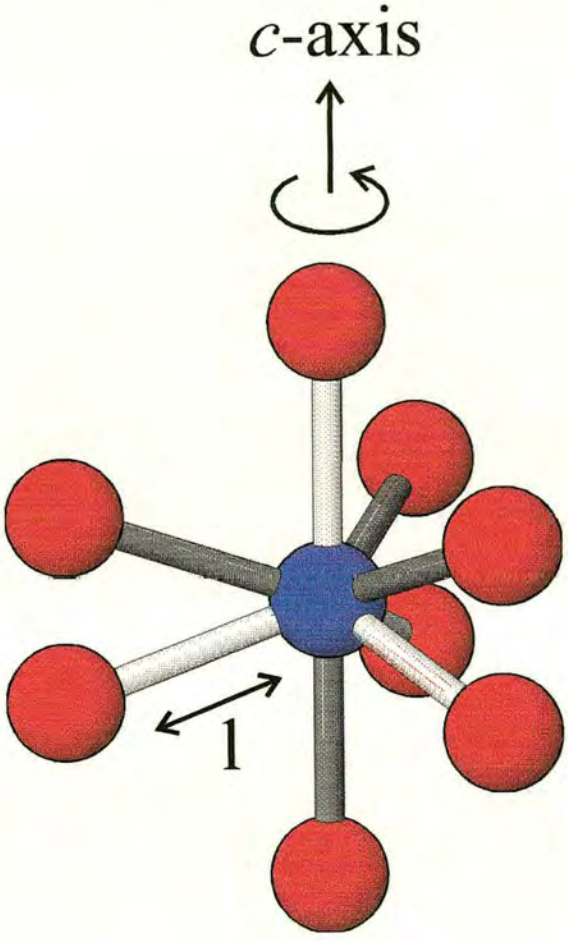

Figure 5.14. The ammonium group is modelled with equal probability of pointing up or down along the *c*-axis. Refinement within the hexagonal unit cell allows rotation with respect to the *c*-axis and the bond length, *l*, can vary.

The NH_4 group is modelled as a rigid body with relative fractional co-ordinates (*i.e.* where the N-H bond length is defined as 1) as given in Table 5.15, these were calculated using the ideal tetrahedral angle of 109.47°.

Table 5.15: Relative atom positions for a tetrahedral NH_4 unit in units of the N-H bond length

Atom	*x*	*y*	*z*
N	0	0	0
D	0	0	1
D	-0.9480900	0	-1/3
D	0.5132002	0.7698000	-1/3

The structure of this rigid body was then allowed to vary by changing the defining N-H bond length and the rotation of the unit with respect to the unit cell. In the primitive hexagonal unit cell the only symmetry-allowed rotation has an axis parallel to the *c*-axis. The N-H bond length could be refined; resulting in a gradual elongation of the bond from 0.9 Å at high temperatures and tending towards 1.05 Å (the accepted N-H bond length[145]) as the sample was cooled; this is probably due to the more accurate positional determination of the D atoms as the rotation slows. Figures 5.15 and 5.16 show the unit cell of ND_4FeCl_3 as modelled by powder neutron data taken at 473 K and illustrates the very significant structural disorder or motion revealed by the large values of the anisotropic thermal parameters.

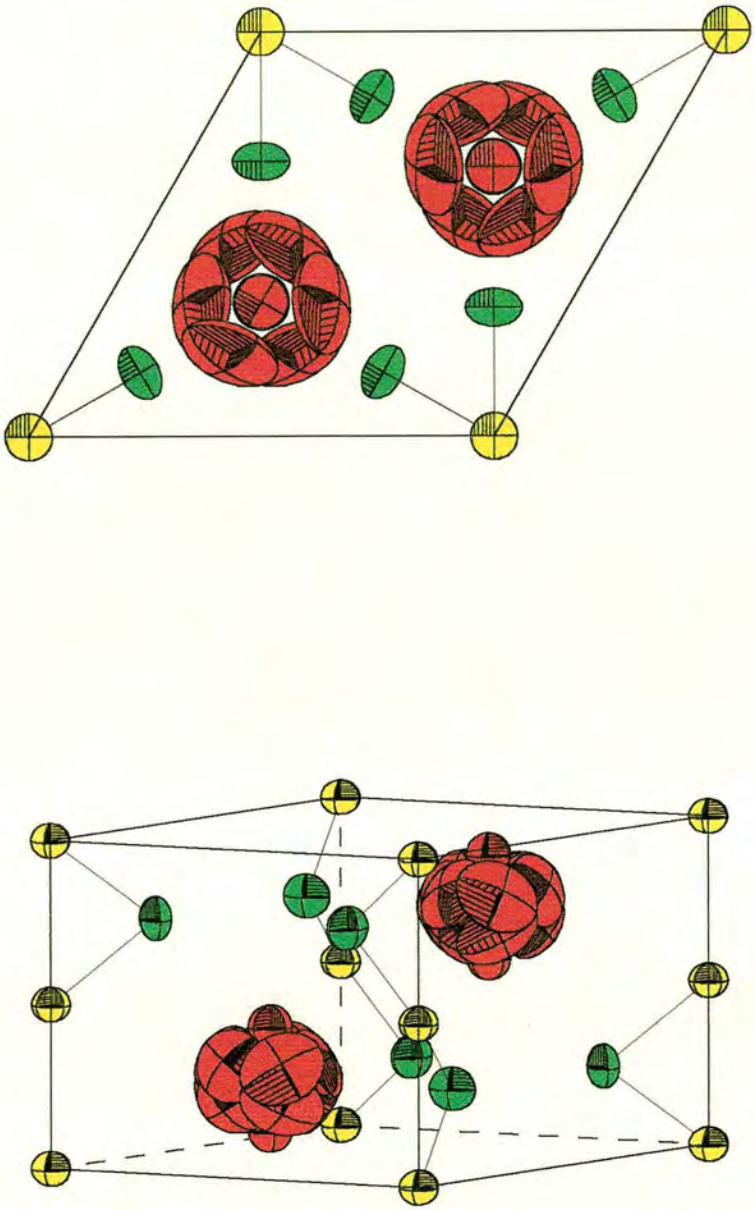

Figure 5.15. Refined unit cell of ND_4FeCl_3 at 473 K, showing structural disorder, represented by thermal ellipsoids, particularly of the D atoms (depicted here as red ellipses, the yellow ellipses represent Fe and the Cl = green the (blue) N atoms are almost completely obscured by the D atoms).

The atom positions and anisotropic thermal parameters obtained in these refinements appear to show a decrease in the motion of the NH_4 group as the sample is cooled, as illustrated in Figure 5.16. In these diagrams it is apparent that the Cl atoms are not very well modelled at 200 K and 160 K. This is probably due to a degree of disorder as these temperatures are relatively close to the transition, this was identified to occur in ND_4FeCl_3 between 160 and 200 K in the BM16 data. Also, although consistent results were obtained when the thermal parameter were allowed to vary anisotropically, the refinement eventually became unstable if the peak shape parameters were allowed to refine simultaneously.

The Fe-Cl bond lengths and Fe-Cl-Fe bridging angles are listed in Table 5.16.

Table 5.16. Fe-Cl bond angles and bond lengths obtained from refinements of D2B data for ND_4FeCl_3

Temperature / K	Fe - Cl Bond Length / Å	Fe - Cl - Fe Angle / °
473	2.4800(10)	75.67
363	2.4756(10)	75.42
290	2.4741(10)	75.24
200	2.4808(10)	74.75
160	2.4817(10)	74.60

(a)363 K

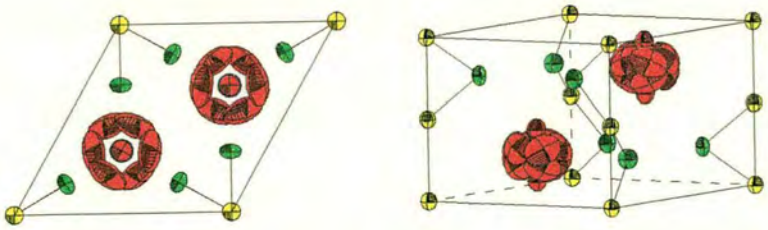

(b) 290 K

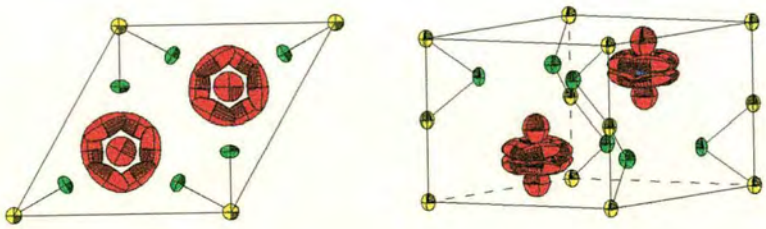

(d) 200 K

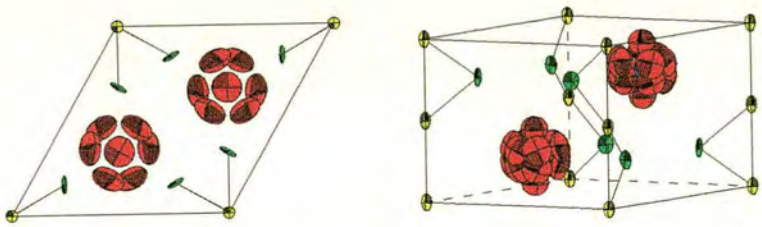

(e) 160 K

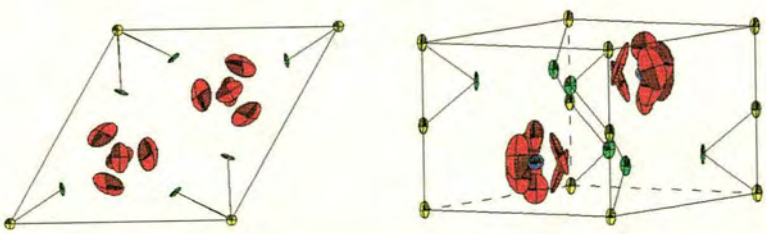

Figure 5.16. Representations of the anisotropic thermal parameters obtained in the refinements of data taken on D2B ND_4FeCl_3 suggesting a decrease in thermal motion of the ND_4 unit as sample is cooled (a) 363, (b)290, (c)200 and (d)160 K.

5.4.1.3. Low temperature structure of ND_4FeCl_3

A data set was collected on a sample of ND_4FeCl_3 on D2B at 1.5 K. Extra reflections are observed relative to the 160 K D2B data set (which was the lowest temperature at which data were previously collected) and can be indexed on a $2a$ x $2a$ x c hexagonal unit cell with $P6_3$ symmetry, as shown in Figure 5.17. This may suggest that the transition observed in the X-rays at 19.5 K is also observable in this neutron data. At this temperature the reflections may also be resulting from an ordered *magnetic* structure.

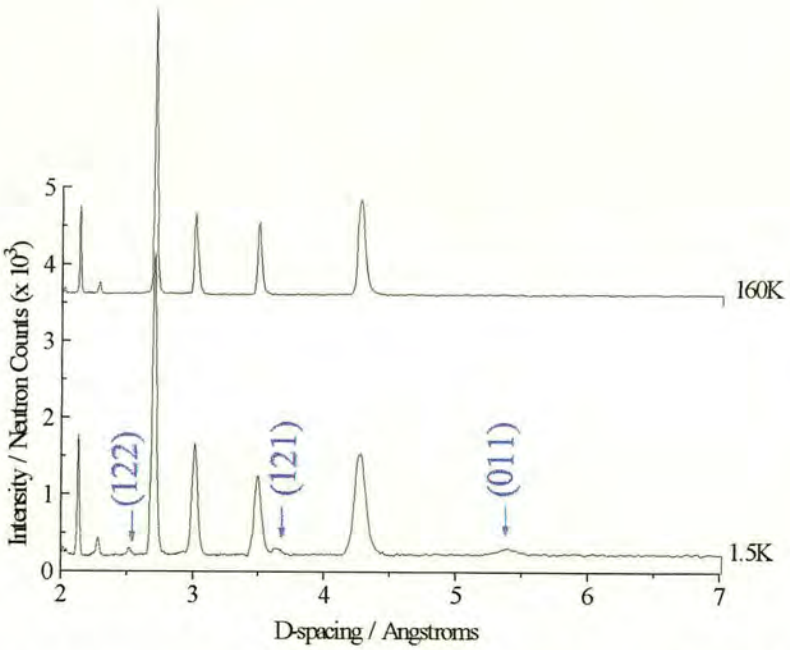

Figure 5.17. New reflections appear in D2B ND_4FeCl_3 data at 1.5 K. These index on a $2a$ x $2a$ x c hexagonal unit cell

However, comparison with data collected on diffractometer D1B indicates that these reflections are also present at 6 K (Figure 5.18). This is *above* the magnetic long range ordering temperature deduced from susceptibility data (Chapter 8) so we attribute this feature to a structural transition.

The same superlattice reflections were also observed in the low temperature neutron diffraction data (4.2K) on ND_4FeCl_3 collected on a sample of ND_4FeCl_3 at 4.2 K using spectrometer IRIS at RAL. At this point it is useful to compare the relative resolution of the powder diffractometers involved in this study, see Figure 5.19.

It is very clear from Figure 5.19 that the resolution of the BM16 data is far superior to those taken using the other instruments. The IRIS data is of much higher resolution than that obtained from the other neutron diffractometers; however, no additional superlattice reflections are observed at this temperature (4.2 K) that cannot be indexed on a $2a$ x $2a$ x c cell.

The transition from the primitive a x a x c cell to the expanded cell was earlier seen to occur in NH_4FeCl_3 at 19.5 K (Section 5.2.2). If a similar transition is occurring in the deuterated samples, the superlattice reflections observed in the neutron data should appear at ~19.5 K. D1B data had been taken for ND_4FeCl_3 prior to this work [143], but not refined because of high levels of impurity; however, it may be used for purposes of monitoring the appearance of superlattice reflections [141]. Figure 5.20 shows the diffraction patterns recorded over a temperature range of ~13 - 30 K; the superlattice reflections can be seen clearly seen to evolve in this region. The sum of intensity in the region of the (121) reflection was calculated and is shown in Figure 5.21, it can be seen here that the reflection appears between 22.5 and 21 K. A more accurate study, by single crystal X-ray diffraction, or a low temperature heat capacity experiment, is required to obtain the temperature of this transition more precisely.

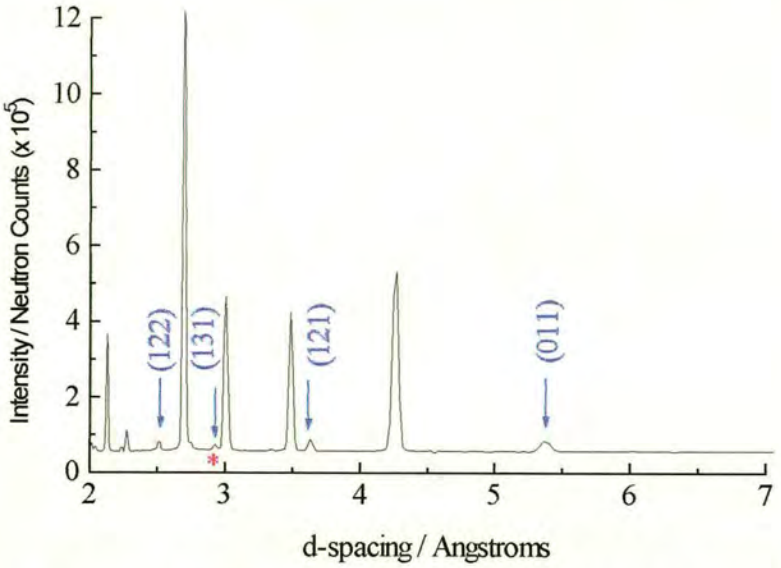

Figure 5.18. D1B data collected on a sample of ND_4FeCl_3 at 6 K. The reflections shown above in Figure 5.17 are again observed.

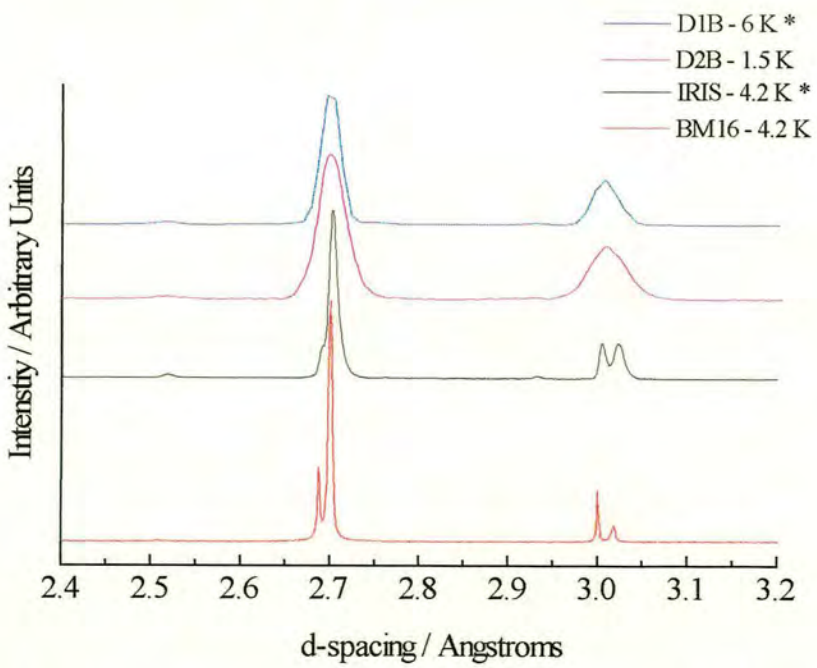

Figure 5.19. Comparison of the resolution of the powder diffractometers used in this study. D1B, D2B and IRIS data were all taken using the same sample of ND_4FeCl_3, the BM16 data was recorded on a sample of NH_4FeCl_3.

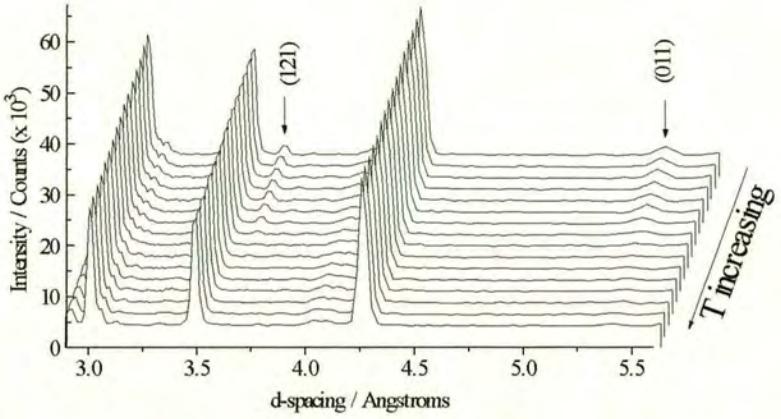

Figure 5.20. Superlattice reflections appearing in data taken for a sample of ND_4FeCl_3 on diffractometer D1B data in the region of 20 K.

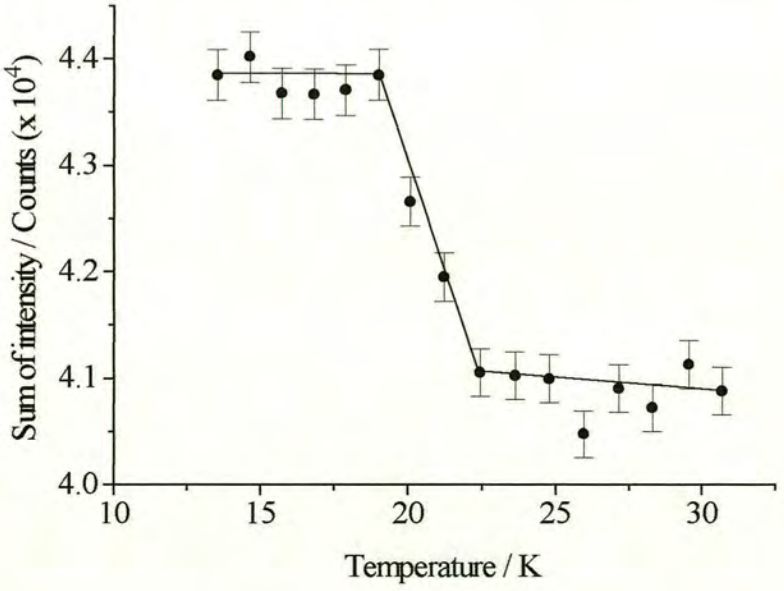

Figure 5.21. Variation with temperature in the sum of intensity in the (121) reflection observed in ND_4FeCl_3 on D1B. The line through the data is merely a guide to the eye.

The data set for ND_4FeCl_3 at 1.5 K could be refined using a $P6_3$ $2a$ x $2a$ x c unit cell. In this space group, two of the NH_4^+ groups are on special positions on the 6_3 screw axis and cannot tilt, and the others refine to tilted positions. However, the refinement tends towards reducing intensity in the superlattice reflections. It is very difficult to retain intensity in these reflections, because their intensities are *much* smaller than those of the remaining reflections, this is a problem as there is not any significant driving force in the refinement to maintain this intensity (Figure 5.22).

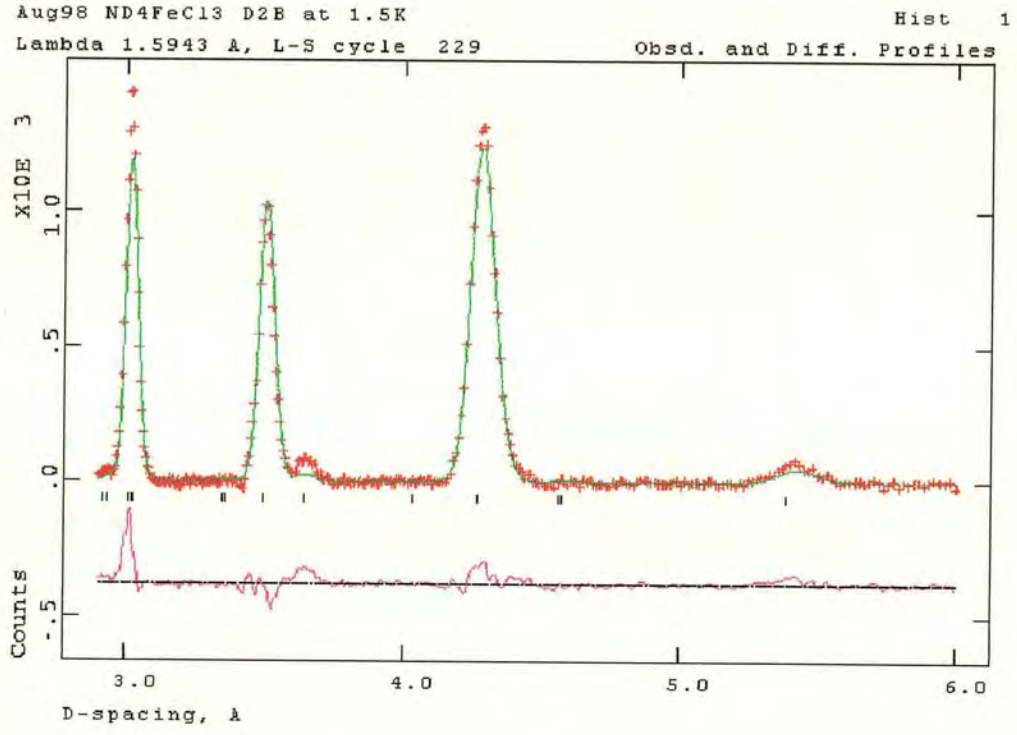

Figure 5.22. Refinement of the powder profile of ND_4FeCl_3 at 1.5 K can be seen to produce intensity in the low temperature superlattice reflections but this is not stable.

5.4.2. Long -range magnetic ordering

Data collected on IRIS showed additional reflections below 4.2 K, consistent with the onset of magnetic long range order. The emergence of reflections at 5.1, 10.3 and 11.0Å is very clear between 4.2 and 1.9K, as shown in Figures 5.23 and 5.24.

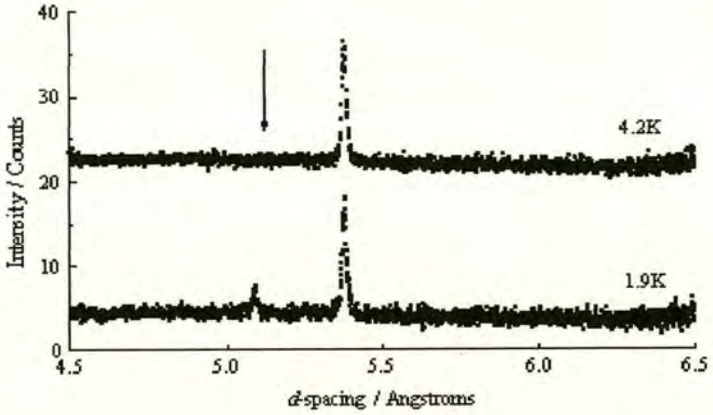

Figure 5.23. New reflection appearing between 4.2 and 1.9 K at 5.1 Å in data taken on ND_4FeCl_3 on IRIS.

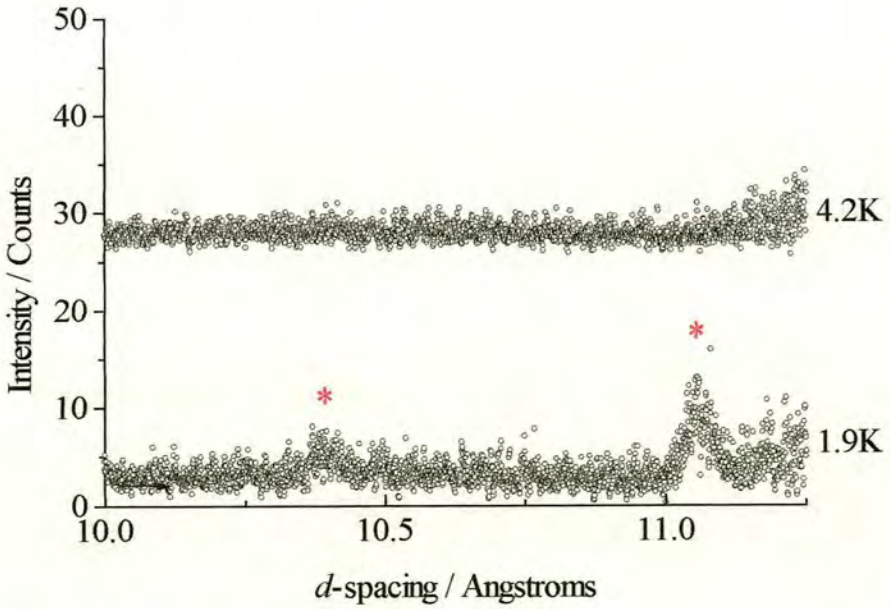

Figure 5.24. The appearance of additional magnetic reflections at 10.3 and 11.0Å are observed in ND_4FeCl_3 between 4.2 and 1.9K

Data subsequently collected on diffractometer D1B at ILL on a powder sample of ND_4FeCl_3 also showed these additional reflections. Several scans were taken at 5 minute intervals over the temperature range 1.5 – 20 K; and are displayed in Figure 5.25. Two new reflections can clearly be seen to emerge at 10.3 and 11.0 Å. Once again the sum of intensity counts in the region of the reflections can be calculated to determine the approximate ordering temperature. In this case the reflections are overlapping and the region incorporating both reflections was summed (Figure 5.26). The 3-D long rang magnetic ordering transition is seen to occur at 3.7(2) K; this is consistent with a magnetic transition observed in the magnetic susceptibility data (Chapter 8). It is not possible to determine, from these data, whether or not these two reflections are emerging at exactly the same temperatures.

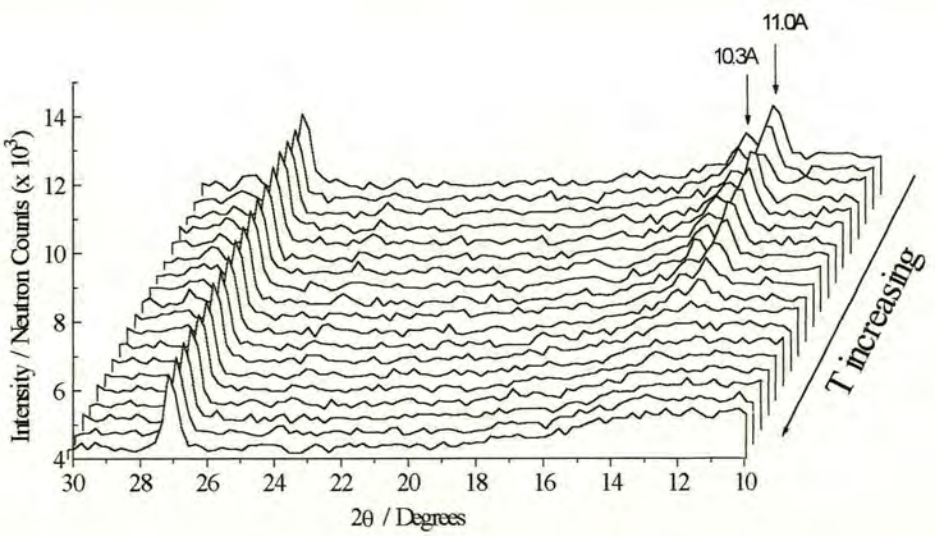

Figure 5.25. Emergence of magnetic reflections at 10.3Å and 11.0Å in data taken on D1B on a sample of ND_4FeCl_3.

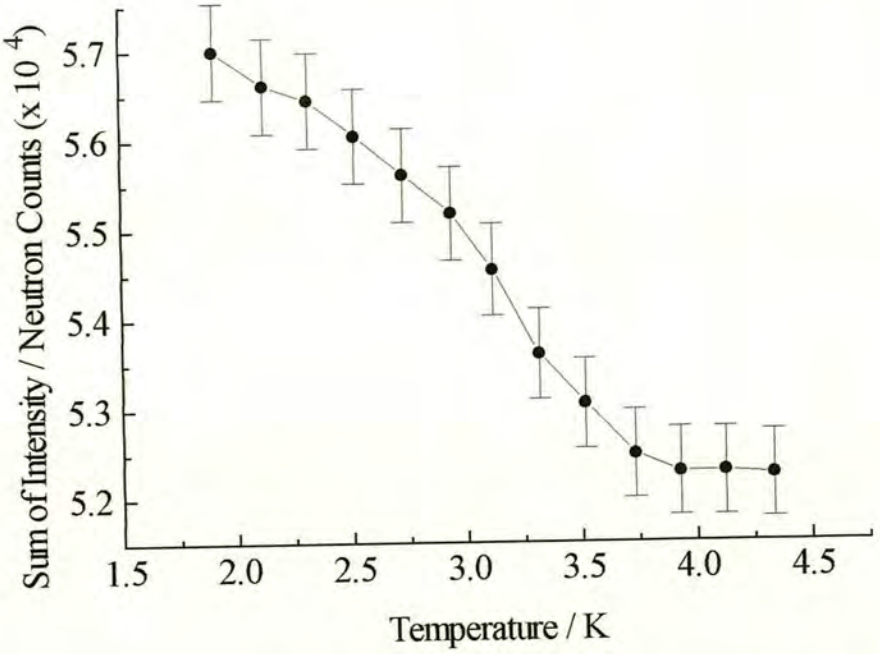

Figure 5.26. Area underneath both magnetic peaks observed in ND_4FeCl_3 on D1B

These reflections appear close to the position in which the (1/3 1/3 0) reflection would occur (~10.48 Å); the appearance of a the (1/3 1/3 0) reflection would indicate a unit cell expanded by a factor of $\sqrt{3}$ along both the *a* and *b* directions, with no expansion in the c-direction, thus indicating a regular triangular antiferromagnetic array in the basal plane with ferromagnetic correlations along the *c*-axis. The appearance of these two reflections slightly displaced from 10.48 Å is consistent with the incommensurate magnetic phase model proposed by Wada *et al* for $RbFeCl_3$ [147]. In this model the incommensurate structure arises from a competition between nearest neighbour antiferromagnetic exchange, *J'*, favouring a triangular antiferromagnetic array, and a dipole-dipole interaction, favouring the spin structure depicted in Figure 5.27. This latter interaction becomes significant when the inchain exchange is ferromagnetic, so that the whole chain acts as a giant magnetic dipole.

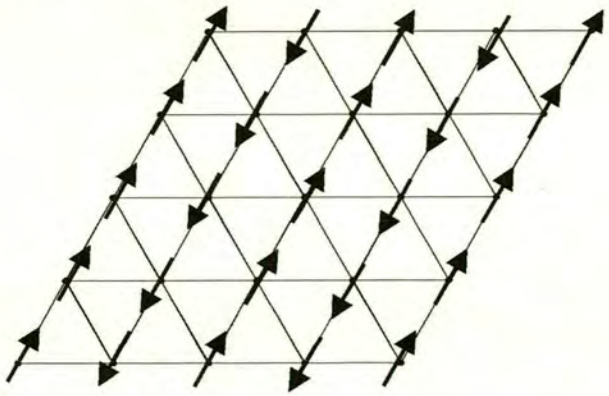

Figure 5.27. Antiferromagnetic alignment favoured by a triangular system with a large dipole moment.

These two arrays correspond to ordering vectors at the K and M points of the reciprocal lattice respectively (Figure 5.28) [148].

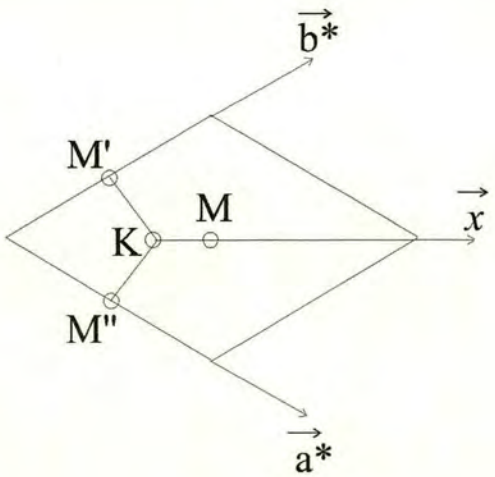

Figure 5.28. The K and M points on the reciprocal lattice space of the $RbFeCl_3$ type. K corresponds to the (1/3 1/3 0) position and the M points correspond to the (1/2 1 0) positions

Competition between the two forces may lead to a variety of spin structure, with ordering vectors at the K point, or displaced from K toward the M points, depending on the temperature. Thus, any underlying distortion of the triangular exchange geometry in the *ab* plane of the distorted ND_4FeCl_3 or NH_4FeCl_3 may be masked by this significant additional perturbation. This is unfortunate in view of the fact that one of our aims here is to observe the influence of disturbing lattice geometry on a frustrated system, so we turn our attention to related materials in which the in-chain exchange is not ferromagnetic. Previous studies on other $AFeX_3$ compounds reveal that all the bromide materials investigated have antiferromagnetic exchange along the *c*-axis axis; their nuclear and magnetic structures are discussed in Chapter 7.

5.5. Summary

A single crystal X-ray diffraction study in the Department of Chemistry at the University of Edinburgh found NH_4FeCl_3 to have $P6_3/mmc$ symmetry and lattice parameters $a = 6.9988(3)$ Å and $c = 6.0202(4)$ Å at 220 K. On cooling to 120 K the mirror plane parallel to the *c*-axis and the c glide plane were lost due to a twisting of the $FeCl_3$ chains; the structure then had $P6_3/m$ symmetry and lattice parameters of $a = 6.9875(3)$ Å and $c = 6.0022(7)$ Å. A data set at lower temperatures could not be obtained on this instrument.

A single crystal X-ray study was performed using the Fddd diffractometer in the Department of Chemistry at the university of Durham. Data were collected at 291 K, 120 K, 30 K and 10 K and all data sets were modelled in space group $P6_3$ and the lattice parameters are shown in Table 5.17. The refinement results at 291 K and 120 K compared well with those obtained in Edinburgh and the previously observed structural transition was found to occur at 181 K. The 30 K data set indicated no

further transition at this temperature, but the 10 K data set indicated a unit cell expansion to a $P6_3$, $2a$ x $2a$ x c cell, this transition was found to occur at 19.5 K.

Table 5.17. Lattice positions obtained from refinement of the data collected on a single crystal of NH_4FeCl_3 using the Fddd diffractometer.

Temperature / K	a / Å	c / Å
291	7.025(1)	6.043(1)
120	6.994(2)	6.010(1)
30	6.988(1)	6.007(1)
10	13.973(2)	6.008(1)

High resolution powder synchrotron data were also recorded using diffractometer BM16 at the ESRF, Grenoble. The data were refined using the Rietveld refinement program, GSAS; this was difficult due to the complex peak shape of the diffraction pattern. However, reasonable refinement was achieved and the lattice parameters obtained are shown in Tables 5.18 and 5.19.

Table 5.18. Lattice positions obtained from Rietveld refinement of data collected on NH_4FeCl_3 on BM16.

Temperature / K	a / Å	c / Å	Volume / Å^3
423	7.09107(7)	6.08946(11)	265.175(7)
300	7.02398(3)	6.03843(3)	258.001(2)
291	7.01923(8)	6.03602(14)	257.549(7)
30	6.98197(1)	6.00031(2)	253.315(1)

Table 5.19. Lattice positions obtained from Rietveld refinement of data collected on ND_4FeCl_3 on BM16.

Temperature / K	a / Å	c / Å	Volume / Å^3
300	7.02496(4)	6.03810(6)	258.059(4)
291	7.01927(6)	6.03673(13)	257.574(7)
200	6.99858(6)	6.01481(9)	255.136(5)
160	6.99059(4)	6.00921(6)	254.317(4)
30	6.98487(5)	6.00911(6)	253.897(5)

Data obtained on a powder sample of NH_4FeCl_3 at 4.2 K on BM16 was fitted using the atom parameters and lattice positions from the 10 K data set taken on the Fddd in Durham. There were some reflections in this data set which could not be indexed on this $2a$ x $2a$ x c hexagonal cell. The data were auto indexed, this resulted in a $2a$ x $\sqrt{3}a$ x c orthorhombic cell. These reflections could also be indexed on monoclinic $2a$ x a x c and $2a$ x $2a$ x c and a $2a$ x $\sqrt{3}a$ x c orthorhombic cell. It is very difficult to decide, using these data, which of these best described the distortion. As the data were collected on the Fddd at 10 K and on BM16 at 4.2 K there is also a possibility that there is a further structural distortion between these two temperatures; low temperature heat capacity measurements would help to clarify this.

Neutron diffraction data were collected on diffractometers D1B and D2B at the ILL, Grenoble and on IRIS at the ISIS Facility, RAL. The samples used in these experiments were deuterated and allowed better determination of the D positions. The D2B data were refined using GSAS and the results were consistent with the transitions observed in the X-ray study. The lattice positions obtained at various temperatures are listed in Table 5.20.

Table 5.20. Lattice parameters obtained from GSAS refinement of data collected on ND_4FeCl_3 on D2B

Temperature / K	*a* / Å	*c* / Å	Volume / Å^3
473	7.08532(10)	6.08450(17)	264.530(8)
363	7.0491(10)	6.05726(15)	260.663(10)
290	7.02607(6)	6.04126(12)	258.276(5)
200	6.99887(10)	6.02349(13)	255.526(10)
160	6.99388(11)	6.01579(13)	254.835(10)

The unit cell volumes obtained in all refinements are shown in Figure 5.29, based on an *a* x *a* x *c* cell. The errors in the points shown here are very small with respect to the symbols used and so are omitted for clarity.

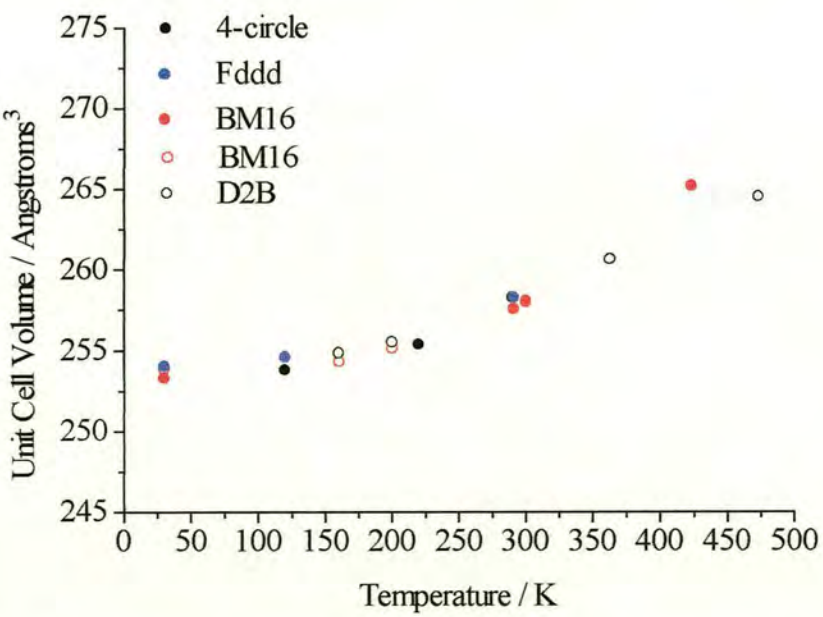

Figure 5.29. Unit cell volumes obtained using four different diffractometers, calculated for an *a* x *a* x *c* hexagonal unit cell. Open circles represent results obtained using deuterated samples.

The nature of the long-range magnetic order at low temperatures was also obtained as a result of the neutron diffraction experiments. Reflections were observed at 10.3 and 11.0 Å as the sample was cooled to below ~22.5 K. These are close to 10.4Å, which corresponds to (1/3 1/3 0) indexed on the primitive unit cell, which would indicate an expansion of the unit cell in the *a* and *b* directions, consistent with a regular triangular antiferromagnetic array. The fact that two reflections are present and that their positions are close to, but not equal, to the (1/3 1/3 0) reflection, suggests the presence of an incommensurate magnetic structure due to competing dipole-dipole interactions, as previously observed in $RbFeCl_3$.

6. Quasi-Elastic Diffraction Results- NH_4FeCl_3

6.1. Introduction

The diffraction measurements of the structure of NH_4FeCl_3 and ND_4FeCl_3 suggest a significant degree of spatial disorder and perhaps even motion of the ammonium groups, depending on the temperatures. Orientation disorder and molecular motion is common in ammonium salts, and indeed in many other ionic materials containing molecular species [149]. In principle, this type of motion could be probed by solid-state NMR spectrometry, studying the nuclear spin relaxation time τ_1 as a function of temperature to pinpoint the freezing point, and estimate an activation energy. In practice, this is difficult for a material containing magnetic moments, as this provides another, very efficient relaxation mechanism for nuclear polarisation. An alternative technique, that also provides very detailed information about both the spatial character of molecular reorganisation is quasi-elastic neutron scattering [150]. High-resolution spectroscopy can be performed with neutrons on an energy scale typically ranging from μeV to meV, allowing the experimentalist to observe the transitions of the molecule between bound rotational energy states – or librational states – for molecules whose orientation order is frozen, and also to observe the motion of free rotors at higher temperature through the broadening in energy of the diffraction peaks.

In this Chapter a a quasi-elastic neutron scattering study of NH_4FeCl_3 to elucidate the motion of the NH_4^+ unit is described. Firstly, the principles of quasi-elastic scattering are briefly outlined, and then a description of the experiment using the IRIS spectrometer at the ISIS Facility, RAL is provided.

6.2. Molecular motion and quasi-elastic neutron scattering.

Let us first consider the behaviour of a molecular unit, such as NH_4^+, bound in a crystal lattice which provides a potential of a particular symmetry and strength. This potential is a consequence of various forms of electrostatic interaction between the multipole of the molecule and the surrounding ions, and also involving Van der Waals interactions and may be described in terms of an oscillating potential, as a function of rotation about a particular axis. For example, in the case of NH_4^+ rotating about a 3-fold axis, the potential could be visualised schematically as in Figure 6.1.

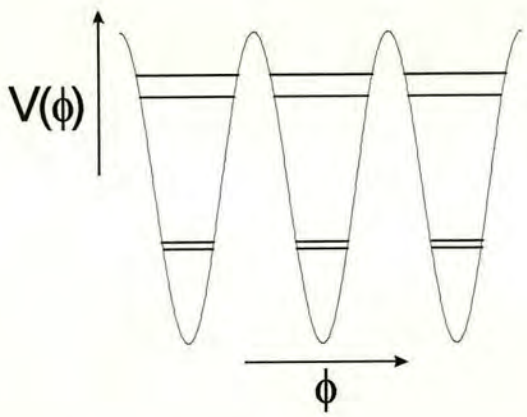

Figure 6.1. Potential for NH_4^+ as a function of angle of rotation ϕ about a three fold axis in the electrostatic potential provided by the host lattice. Quantum librational states are illustrated schematically, with a further splitting to represent the tunnelling states.

Within each well of the potential there are quantum states that represent the rocking motion or libration of the molecule. Separations between librational states is typically of the order of meV or tens of meV.

This classical picture of the possible orientations of a molecule in a potential well neglects an additional degeneracy that arises from nuclear spin, and restrictions on symmetry of the possible nuclear spin states. In the case of R, each H atom has a two-fold degeneracy associated with the spin I=1/2 on each nucleus. There are therefore $2^4 = 16$ possible orientations of these spins. These states may interact with one another to produce very small splittings in the energies of the librational states, of the order of μeV [151]; such states are called 'tunnelling states', and the precise scheme of the splitting is very sensitive to the symmetry and strength of the potential.

At high temperatures the molecule may have sufficient thermal energy to hop freely between these libration states, executing diffusional motion. This is manifested in a neutron scattering experiment by a very broad response in energy, centred at zero energy (*i.e.* centred on the elastic response at some value of the scattering vector) and with a half-width Γ that is inversely related to the diffusive half-life. This response is called *quasi-elastic*. In some cases – for example CH_4 or H_2 in certain condensed phases, the molecular motion is similar to that of a free rotor [152].

On cooling, the molecule will slow down and the quasi-elastic response becomes sharper; the temperature dependence of Γ may be treated with the Arrhenius expression to provide an estimate of the activation energy E_A for rotation diffusion, according to:

$$\Gamma = \Gamma_0 \exp(-E_A/kT) \qquad (6.1)$$

For example, for the temperature dependence of the quasi-elastic scattering from NH_4^+ in $(NH_4)_2SnCl_6$, E_A was found to be 590 +/- 30 K, and $\Gamma_0 = 4.5$+/-0.5 meV for measurements over the temperature range 70 to 300K [151].

The molecular motion will eventually slow to the point that the hopping between different orientations freezes out, and the quasi-elastic response may no longer be distinguished from the elastic response. It may then become possible to perform spectroscopy on the librational states. Thermal neutrons may be produced with energies comparable to such transitions – which are typically of the order of meV, so inelastic neutron scattering may provide a very good probe of the librational states of molecules – in particular when reorientation involves motion of hydrogen atoms for which the incoherent cross-section is very high. Thus, for $(NH_4)_2SnCl_6$, inelastic neutron scattering revealed librational transitions that allowed the energies of the first two excited librational states to be determined, at 13.4 +/- 0.5 and approximately 30 meV [151].

Very high resolution inelastic neutron scattering measurements may reveal transitions between tunnel states; once more, such transitions were observed in $(NH_4)_2SnCl_6$, with splittings from the elastic response of the order of 2 μeV [151]. In this case the 16-fold degenerate nuclear spin states split into 5A, 3T and 2E states, and transitions between a ground A state and an excited T state are observed, as well as between this T state and a higher E state. By modelling this spectrum in conjunction with information about the librational states, it was possible to refine a detailed model of the potential experienced by the NH_4^+ unit in this host.

Thus, in principle it is possible to use a combination of quasi-elastic and inelastic neutron scattering measurements to probe the potential experienced by a molecule in a crystal host through measurement of diffusive rotation, librational motion, and interference between ground nuclear spin states. We now consider how quasielastic measurements are performed in practice.

6.3. Quasi-elastic and high-resolution inelastic neutron scattering

In order to probe the energies of transitions between tunnel states by neutron spectroscopy, as well as resolve quasielastic scattering from the elastic incoherent scattering for relatively slow diffusion processes, it is necessary to be able to measure very small changes in neutron energy. For a conventional reactor source, this requires the selection of the longest wavelengths possible using a cold H_2 moderator, and very high resolution selection of neutron energy before and after scattering. For this kind of work the energy may either be selected using a crystal, selecting wavelength and therefore energy through the Bragg relation; alternatively, the energy may be selected through the velocity – either through the time of flight of a neutron at a pulsed source, or by means of a set of rotating choppers whose timing and length is set to allow a narrow band of neutrons of a mean velocity v to pass. For time-of-flight techniques, the mean energy E of neutrons of energy v is then given by:

$$E = \frac{1}{2} m_n v^2 \qquad (6.2)$$

where m_n is the neutron mass.

The particular instrument used in this work is shown schematically in Figure 6.2, which should also be compared with the more realistic representation of Figure 3.8. A pulse of cold neutrons from a hydrogen moderator M is focussed onto the sample S using a curved wave-guide to increase the neutron flux at the sample. Between the M and S there is are two rotating disk choppers made of neutron-absorbing materials which allow a relatively broad band of neutron velocities through; this is designed to eliminate frame overlap between pulsed, whereby fast events from one pulse catch

up with slow events from the previous pulse. The chopper also defines the energy window of the experiment. These particular neutrons may be scattered from S at an angle ϕ onto a bank of analyser crystals set radially about the sample. Finally, the detectors counts neutrons scattered through the angle 2θ at the analyser crystals. The whole instrument can be considered to be composed of two spectrometers – the primary one selecting the incoming neutron energy E_1, and the secondary one analysing the scattered energy E_2.

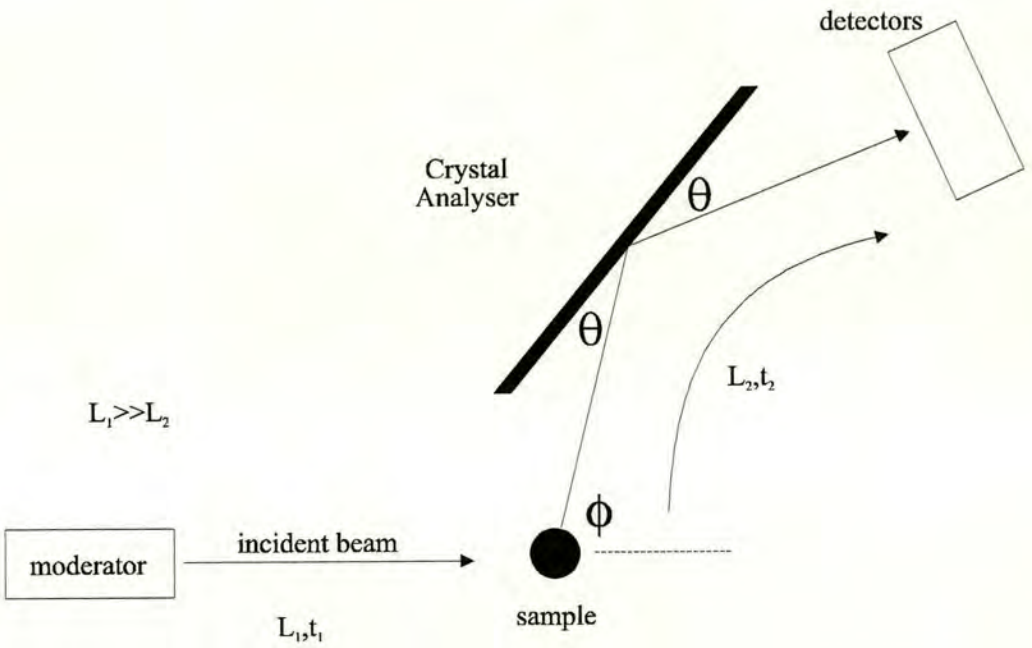

Figure 6.2. General layout of an inelastic neutron scattering spectrometer with indirect geometry; this should be compared with the more realistic representation of the IRIS spectrometer in Figure 3.9.

Let us consider how we can express E_2 in terms of the geometry and timing of the scattering. Suppose neutrons scattered by the sample take a time t_2 to traverse the distance L_2 between sample and analyser crystals. From 6.2, we may write E_2 as:

$$E_2 = \frac{m_n}{2}\left(\frac{L_2}{t_2}\right)^2 \tag{6.4}$$

and if we invoke the de Broglie relation for the momentum p of these neutrons

$$p = m_n v = h/\lambda \tag{6.5}$$

and use the Bragg relation for the scattering at the analyser, we find:

$$E_2 = \frac{1}{2m_n}\left(\frac{h}{2d_a \sin\theta}\right)^2 \tag{6.6}$$

where d_a is the d-spacing of the particular reflection for the analyser. Therefore, from 6.4 and 6.6 we find that the time t_2 is fixed for a given combination of θ, d_a and L_2, and given by:

$$t_2 = \frac{2m_n L_2 d_a \sin\theta}{h} \tag{6.7}$$

Now, since the timing of the pulse is set by the spallation source timing, and has a particular value t, we can also define the time t_1 taken to traverse the primary spectrometer, and the energy transfer for the scattering by the sample is given by:

$$\Delta E = E_1 - E_2 = \frac{1}{2}m_n\left[\left(\frac{L_1}{(t-t_2)}\right)^2 - \left(\frac{L_2}{t_2}\right)^2\right] \tag{6.8}$$

6.4. Quasi-elastic neutron scattering on the IRIS spectrometer

6.4.1. Sample preparation

Samples of NH_4FeCl_3 and ND_4FeCl_3 were studied on the IRIS spectrometer at the ISIS Facility, RAL. First the optimum sample thickness had to be calculated using relation {3.22) for the transmission ; the optimum thickness should be such that transmission is 85-90%, reducing the probably of multiple scattering of neutrons by the sample to an acceptable level for a sample of flat-plate geometry. Usually scattering from all atoms except hydrogen can be ignored, because it has the largest incoherent scattering by far (Table 3.1). The required sample thicknesses were calculated as 0.650 mm for NH_4FeCl_3 and 10.40 mm for ND_4FeCl_3, and this figure was then used to calculate the amount of sample required to fill a flat plate sample holder. A cylindrical sample geometry would be preferable since this would allow simultaneous investigation of the whole range of scattering vectors allowed by the instrument geometry, but it proved impossible to load such an air-sensitive sample into such a sample holder in the glove-box that was available.

A 1 mm deep aluminium holder 40 mm x 40 mm square, with a 0.5 mm layer of cadmium in the bottom was selected for the NH_4FeCl_3 sample and this required 1 g of sample. For the ND_4FeCl_3 sample a 40 mm x 40 mm x 5 mm holder was used - to fill this would have required more than the available 4 g of material, so wedges of cadmium film, layered and wrapped in aluminium tape, were placed vertically down the sides of the container leaving an aperture of approximately 40 mm (v) x 25 mm (h) for the powder.

6.4.2. Quasi-elastic measurements

A common problem in performing quasielastic neutron scattering experiments to look at molecular motion, is the determination of the appropriate energy scale of the problem. If the molecular motion is very fast, the quasielastic scattering may be very broad, and may only be detected at through measurements over a very wide energy range; alternatively, for slow motion, the contribution of the quasi-elastic scattering to the central, elastic peak in the spectrum may be very small and close to or smaller than the resolution of the experiment.

Reconnaisance measurements were initially performed on both samples, selecting different resolutions through choice of different sets of analyser crystals. The characteristics of the various analyser crystals that were used is given in Table 6.1.

Table 6.1 Resolution, energy window and relative reflectivity of the various analyser crystals (with specific take-off reflection noted): PG is pyrolytic graphite.

Crystal and reflection	Relative reflectivity	Resolution / μeV	Energy range / meV
PG(002)	1.0	15.2	-0.4 to 0.4
PG(004)	0.7	50.0	-3.5 to 4.0
Mica (002)	0.04	1.2	-0.02 to 0.02
Mica (004)	0.15	11.0	-0.4 to 0.4

The data was then processed using the program ICON which groups the data so that all scattering with the same scattering vector Q is summed, and then the data are expressed as function of energy transfer [153].

Table 6.2. Experimental conditions for each attempt to observe quasielastic scattering from NH_4FeCl_3 or ND_4FeCl_3, given in chronological order. The length for each measurement is expressed in terms of the integrated neutron flux impinging on the instrument, expressed in terms of beam current.

Sample	Current / μA	Temperature/K	Analyser
NH_4FeCl_3	250.1	150K	PG(002)
NH_4FeCl_3	300.1	150K	PG(004)
NH_4FeCl_3	500.1	5K	MI(004)
NH_4FeCl_3	500.1	5K	MI(004)
NH_4FeCl_3	500.1	50K	MI(004)
NH_4FeCl_3	344.5	50K	MI(002)
NH_4FeCl_3	277.6	5K	MI(002)
NH_4FeCl_3	500.1	15K	MI(004)
NH_4FeCl_3	500.1	25K	MI(004)
NH_4FeCl_3	500.1	200K	MI(004)
NH_4FeCl_3	200.1	300K	MI(004)
NH_4FeCl_3	210.2	300K	MI(004)
NH_4FeCl_3	316.1	300K	PG(002)
NH_4FeCl_3	321.1	300K	PG(004)
ND_4FeCl_3	256.4	300K	PG(004)
ND_4FeCl_3	300.5	300K	PG(002)
ND_4FeCl_3	85.6	300K	PG(004)

We saw no quasi-elastic broadening of the elastic peak beyond instrumental resolution for either sample at any temperature, with any analyser, presumably because we never managed to use the appropriate resolution for our material at the

particular temperatures. A summary of the various attempts to observe a quasi-elastic signal is given in Table 6.2 in terms of the various conditions for each experiment.

6.4.3. Quantum tunneling

Although we were unable to observe any quasi-elastic signal, we did observe a low-energy inelastic response at low temperatures in NH_4FeCl_3 which is likely to be due to quantum tunnelling. Thus at 4.2K, with the Mica(004) analyser, we observed satellite peaks at energies of approximately 10 and 18 μeV, which is comparable in energy to quantum tunnelling in other ammonium salts [150, 154]. These are displayed in Figure 6.3. We were unable to see this effect when the higher resolution Mica (002) analyser (ΔE = 1.2 μeV) was used, but this could be due to the much smaller flux and poor signal to noise ratio for practical counting times.

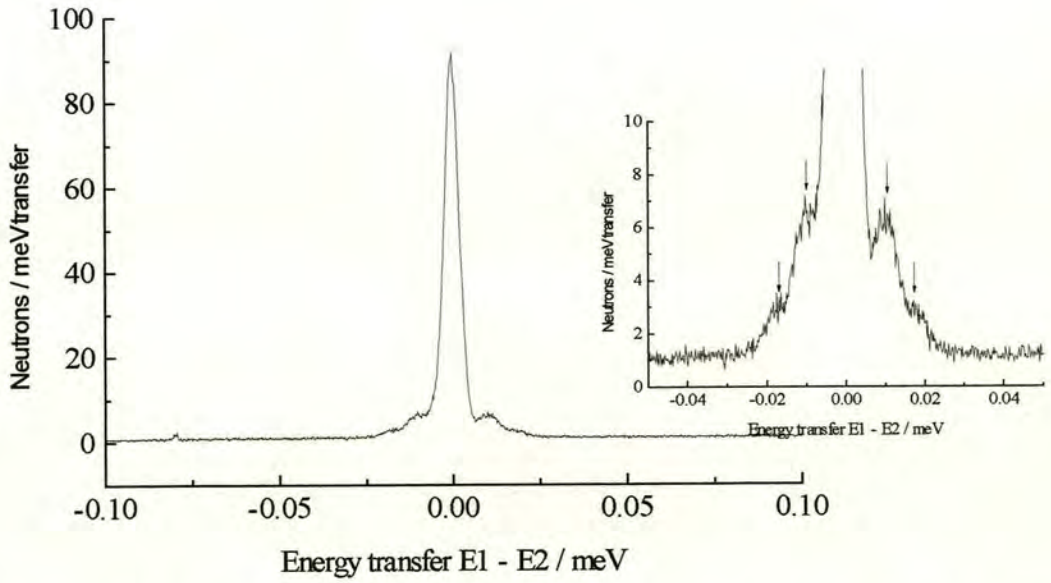

Figure 6.3. Inelastic response from ND_4FeCl_3 observed at 4.2K observed using Mica (004) analysers; the inset expands the central region to reveal secondary satellites.

Further measurements with the same experimental set-up showed that the satellite peaks were present at 15 K, but had disappeared by 25 K; the centres and widths of these peaks did not appear to change between 4.2 and 15K. The disappearance of the inelastic response is illustrated in Figure 6.4.

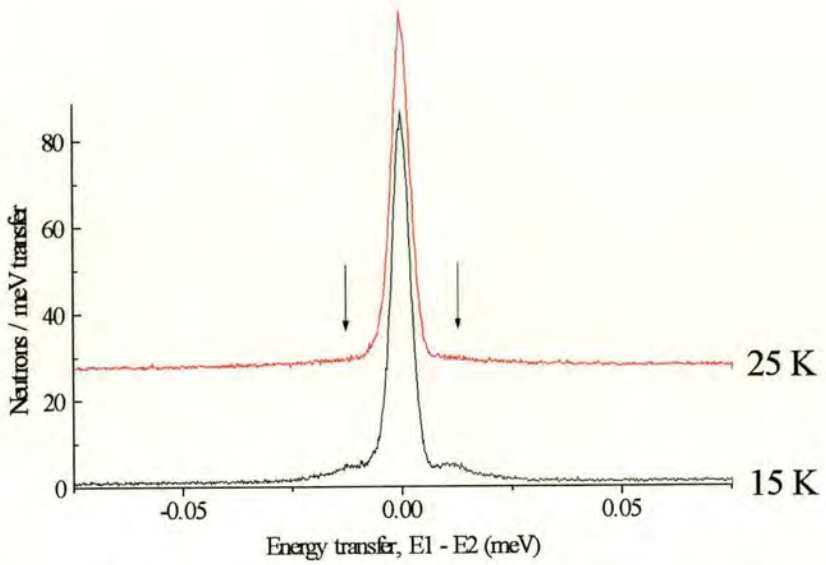

Figure 6.4. Inelastic response attributed to quantum tunnelling at low temperatures in NH_4FeCl_3 appear between 25 and 15 K.

In the case of $(NH_4)_2SnCl_6$ the transitions between tunnelling states fall in energy and intensity as the sample is warmed towards the temperature at which the onset of reorientation ordering occurs [151] as demonstrated through the onset of quasielastic broadening. It is therefore tempting to attribute the disappearance of the tunnelling peaks on warming to the onset of activated hopping between librational state, and perhaps even to suggest that this is related to the structural phase transition at 19.5K. However, a proper analysis really requires a better understanding of the potential in which the NH_4^+ unit rotates. It is not possible to assign the two transitions we

observed in the low temperature spectrum of NH_4FeCl_3 to any particular nuclear spin state without such a potential, and this awaits more detailed measurements and complementary modelling.

6.5. Conclusions

Quasi-elastic and inelastic neutron scattering measurements have been performed on NH_4FeCl_3 and ND_4FeCl_3 as a function of temperature and energy resolution using the spectrometer IRIS at the ISIS Facility. We failed to see any indication of quasi-elastic broadening of the elastic response under any conditions but we did find evidence of a quantum tunnelling transition between nuclear spin states at 15 K and below in NH_4FeCl_3. The disappearance of this feature between 15 and 25 K is compatible with the onset of hopping motion between librational states, and this in turn could be related to the structural phase transition at 19.5K.

With the benefit of hindsight, we might have chosen to focus our efforts to observe the emergence of the quasielastic response from the elastic response starting from temperatures close to and above 20K. We suspect that at the temperatures where we concentrated our search for this phenomenon, the quasielastic response is too broad to observe with the instrument we used.

There are relatively few examples of the observation of tunnelling states of this kind in ammonium salts so further work on this or related materials could be of interest to those modelling reorientations in molecular materials in general. Future work might involve more careful measurements of the spectrum of the low temperature excitations to try to observe other states, as well as complementary measurements of

the inelastic response from librational excitations that would help us to model the potential properly.

7. Structural Results - NH_4FeBr_3

7.1. Introduction

A deuterated powder sample of NH_4FeBr_3 has been previously studied [68], using diffractometer D1B; these data suggested that the system has a primitive hexagonal unit cell at room temperature and undergoes two structural phase transitions at 270(10) and 90(10) K. The data in the previous study were of low resolution and the sample contained impurities. The aim of the present study was to look in more detail at the structural transitions occurring in NH_4FeBr_3 and to fully characterise the structure in all three phases. This will be attempted by considering diffraction data collected using a wide range of diffractometers, and incorporating X-ray and neutron diffraction techniques. Familiarity with the material discussed in Chapter 5 is assumed, as the layout of this Chapter and the methods of data collection, manipulation and refinement are comparable. In this case, however, the powder measurements were obtained before a single crystal, suitable for diffraction, could be produced.

7.2. Powder X-ray diffraction using synchrotron radiation

Samples of NH_4FeBr_3 and ND_4FeBr_3 were made as described in Chapter 4. The samples were loaded into borosilicate capillaries as previously described for this instrument and data were collected on diffractometer BM16, at the ESRF, as summarised in Table 7.1. In some of these data there were problems with impurities, those marked ‡, in the Table, contained a large number of unidentifiable impurity peaks, possibly due to exposure to

moisture, and no satisfactory results were obtained from Rietveld refinement of these data sets. The remaining data sets were refined using GSAS, some of these also possessed trace amount of $FeBr_2$, presumably due to an imbalance in the stoichiometetry in the reaction mixture, in turn possibly due to a significant amount of ammonium bromide remaining in the gaseous state during reaction. In these cases the angular range containing suspected $FeBr_2$ reflections was excluded from the refinement.

Table 7.1. Summary of data sets collected for NH_4FeBr_3 on BM16. Deuterated samples are marked with an asterisk, and those with large amounts of impurity are marked with ‡.

Temperature / K	Impurity
423	y‡
291	y‡
291*	y
200*	y
120*	y
120	n
4.2*	n

7.2.1. Room temperature structure

The 291 K data set collected on a sample of ND_4FeBr_3 was modelled in space group $P6_3/mmc$. Several problems, similar to those discussed in relation to the data collected for NH_4FeCl_3 samples using this instrument, were encountered in fitting the peak shape. The asymmetry correction of Finger *et al* [124,125] was again successfully implemented

(Figure 7.1). In this case the values of S/L and H/L were 0.0076(1) and 0.0085(1) respectively.

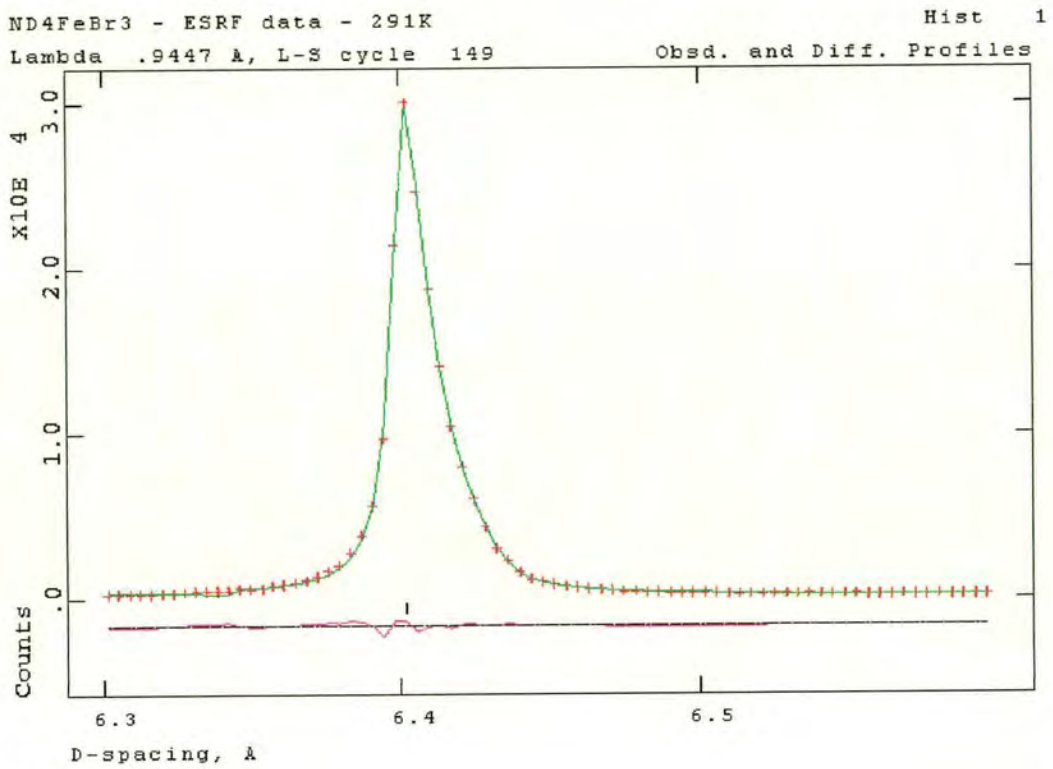

Figure 7.1: The peak with largest d-spacing is significantly asymmetric due to axial divergence; this can be successfully modelled using the correction of Finger *et al* [124,125].

The 291 K data set was refined in space group $P6_3/mmc$ using GSAS. The lattice parameters obtained were $a = 7.39275(5)$ Å and $c = 6.34144(15)$ Å. 11999 data points were used in the refinement and $\chi^2 = 7.896$, $R_{wp} = 0.1795$, the atom positions are shown in Table 7.2.

Table 7.2. Atom positions obtained from Rietveld refinement of 291 K data set collected on ND_4FeBr_3 using BM16. $P6_3/mmc$, a = 7.39275(5) and c = 6.34144(15) Å

Atom	Site	x	y	z
Fe	2 *a*	0	1	1
Br	6 *h*	0.163337(122)	-0.163337(122)	1/4
N	2 *d*	1/3	2/3	0.75

Anisotropic broadening was again found to cause a major problem in the fitting, a consequence of this was that the absorption of the bromine atoms could not be adequately modelled and the thermal parameters obtained are negative. The anisotropic broadening problem appears to be exactly the same as that found with the NH_4FeCl_3 refinements. The peak shape is Lorentzian and is allowed to broaden anisotropically with respect to the (001) direction. This causes the calculated peak shapes to be narrower when $l = 0$; this narrower peakshape is observed in the data, and predicts a broadening in the (00*l*) reflections, but this is *not* observed in the data (Figure 7.2).

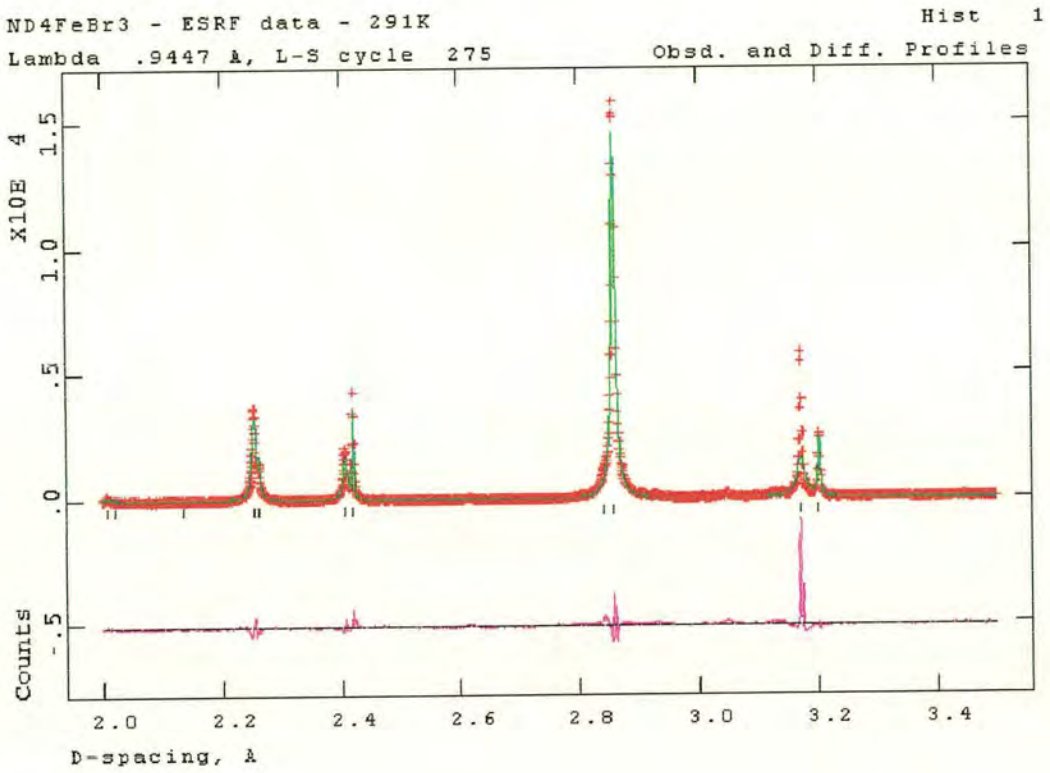

Figure 7.2. The anisotropic broadening of the (112) reflection, at 2.40 Å, and the (210) reflection, at 2.42 Å, peaks is modelled well, but the calculated peak shape (green) for the (002) reflection at 3.18 Å is much broader than observed peak shape (red), (*cf.* Figure 5.7).

7.2.2. Investigation of the structure below the first transition at 270(10) K

A structural distortion is observed by 200 K, which is consistent with previous observations [68]. Superlattice reflections are observed when data collected on ND_4FeBr_3 at 291 K are compared with a 200 K data set (Figure 7.3). The Miller indices corresponding to the primitive a x a x c hexagonal cell are shown. The two diffraction

patterns considered here were collected on two different samples; the impurity reflections in the 200 K data are due to $FeBr_2$ and those in the 291 K data are unidentified.

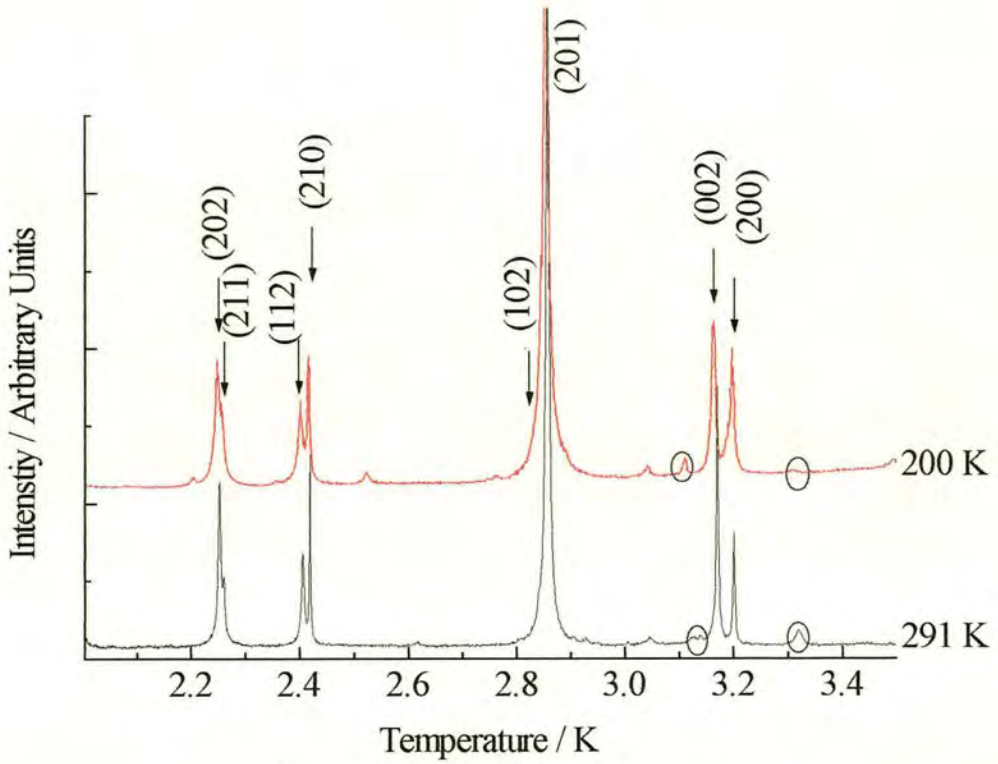

Figure 7.3. Superlattice peaks are seen to appear in ND_4FeBr_3 between 291 and 200 K. Impurity peaks are marked using circles

The data collected on NH_4FeBr_3 sample at 120 K also shows the presence of these superlattice reflections; this data set is of very high quality, no impurity peaks are present and the peaks are very sharply defined (Figure 7.4).

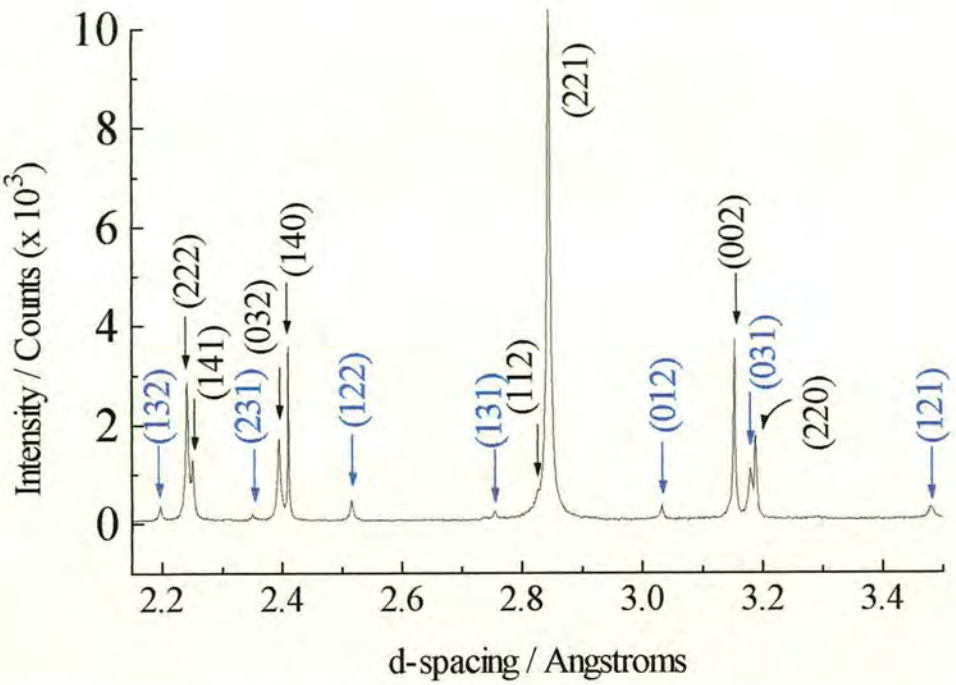

Figure 7.4: NH_4FeBr_3 data collected on BM16 at 120 K. This can be indexed on a $\sqrt{3}a$ x $\sqrt{3}a$ x c hexagonal unit cell; Miller indices in black are equivalent to those shown above for the primitive cell, those in blue label the superlattice reflections.

The reflections in the NH_4FeBr_3 120 K data set are sufficiently well resolved to allow attempted cell identification *via* an auto indexing package, in this case Treor 90 [141]. The peak positions were identified by hand using MicroCal Origin, and the auto-indexing procedure found a solution which accounted for all the observed reflections, the calculated and observed reflection listings are given in Appendix B. This indicated a hexagonal unit cell with lattice parameters a = 12.754(1) and c = 6.304(1) (i.e. $\sqrt{3}a$ x $\sqrt{3}a$ x c) and a unit cell volume of 888.16(1) Å^3. All observed reflections index on this cell.

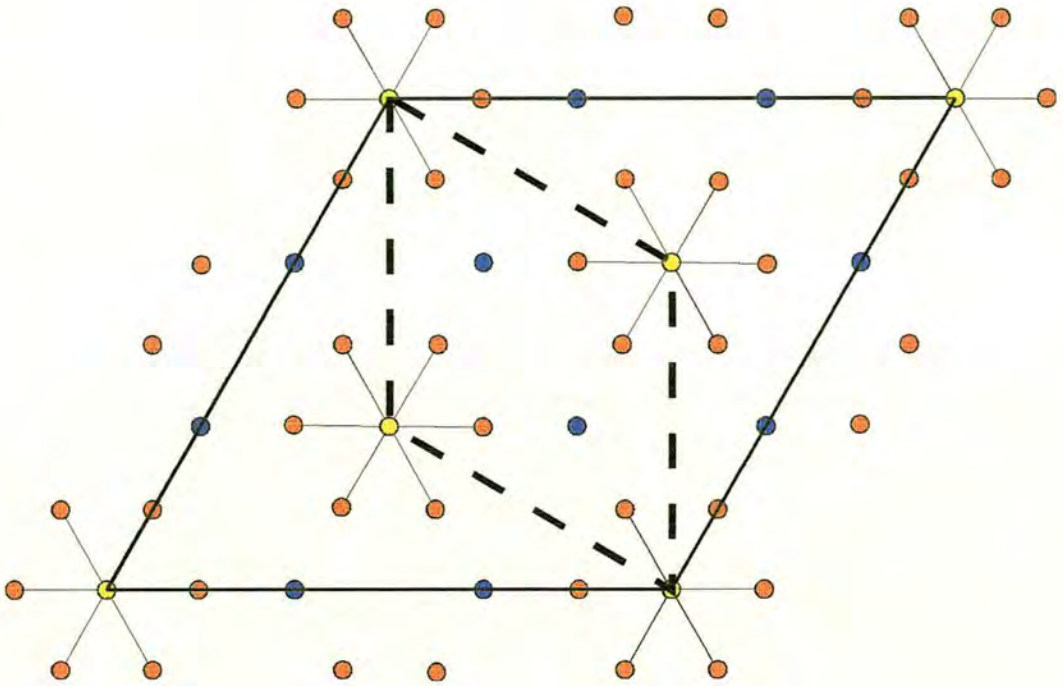

Figure 7.5: An expansion from the primitive *a* x *a* x *c* cell (shown as a dashed line) to the $\sqrt{3}a$ x $\sqrt{3}a$ x *c* hexagonal unit cell (shown as a solid black line) is observed in NH_4FeBr_3. The two chains of $FeBr_3$ chains inside the expanded cell become inequivalent, to those at the corners. Fe atoms are represented by yellow circles, N by blue and Br -by orange while H atoms are omitted for clarity.

$RbFeBr_3$ and $KNiCl_3$ (which are also hexagonal perovskite materals) both exhibit a phase transition from space group $P6_3/mmc$ to $P6_3$ cm with a unit cell expansion from *a* x *a* x *c* to $\sqrt{3}a$ x $\sqrt{3}a$ x *c*. This type of transition has recently been modelled [124. 125], starting from the hypothesis that the structural (and dynamical) behaviour of this type of material is determined by the relative radius ratio R_A/R_B. In the case of NH_4FeBr_3, however, a superlattice reflection which indexes as (031) on the $\sqrt{3}a$ x $\sqrt{3}a$ x *c* hexagonal unit cell is seen to emerge, this reflection is absent in a structure with $P6_3$ cm

symmetry. This reflection can be identified as the (111) reflection in the primitive lattice and arises from the loss of the *c*-glide plane and the parallel mirror plane; this can be identified as the same loss of symmetry observed in the $P6_3/mmc$ to $P6_3/m$ transition in NH_4FeCl_3 at 181 K. This reflection is allowed in space group $P6_3$ and the data were, therefore, refined in this space group. The position of the N atoms could not be varied in the refinement; these were left on the special positions which would be occupied if a mirror plane perpendicular to the *c*-axis, intersecting at 1/4, were still present.

The 120 K NH_4FeBr_3 data set was refined in space group $P6_3$ using GSAS. The lattice parameters obtained were a = 12.75279(7) Å and c = 6.30555(10) Å. 12711 data points were used in the refinement and χ^2 = 8.250, R_{wp} = 0.1792. The atom positions obtained are given in Table 7.3. The intensities of the superlattice reflections are modelled very well using this structure (Figure 7.6).

Table 7.3. Atom positions obtained from Rietveld refinement of 120 K data set collected on NH_4FeBr_3 using BM16. $P6_3$, a = 12.75279 (7) Å and c = 6.30555 (10) Å

Atom	Site	*x*	*y*	*Z*
N	6	1/3	2/3	0.75
Fe	2	0	0	0. 0317(99)
Fe	2	2/3	1/3	-0.0382(102)
Fe	2	1/3	2/3	-0.0404(100)
Br	6	0.1602(8)	-0.5107(10)	0.2150(97)
Br	6	0. 4936(10)	0.1794(7)	0.2177(97)
Br	6	0.1567(9)	-0.0167(11)	0.2913(97)

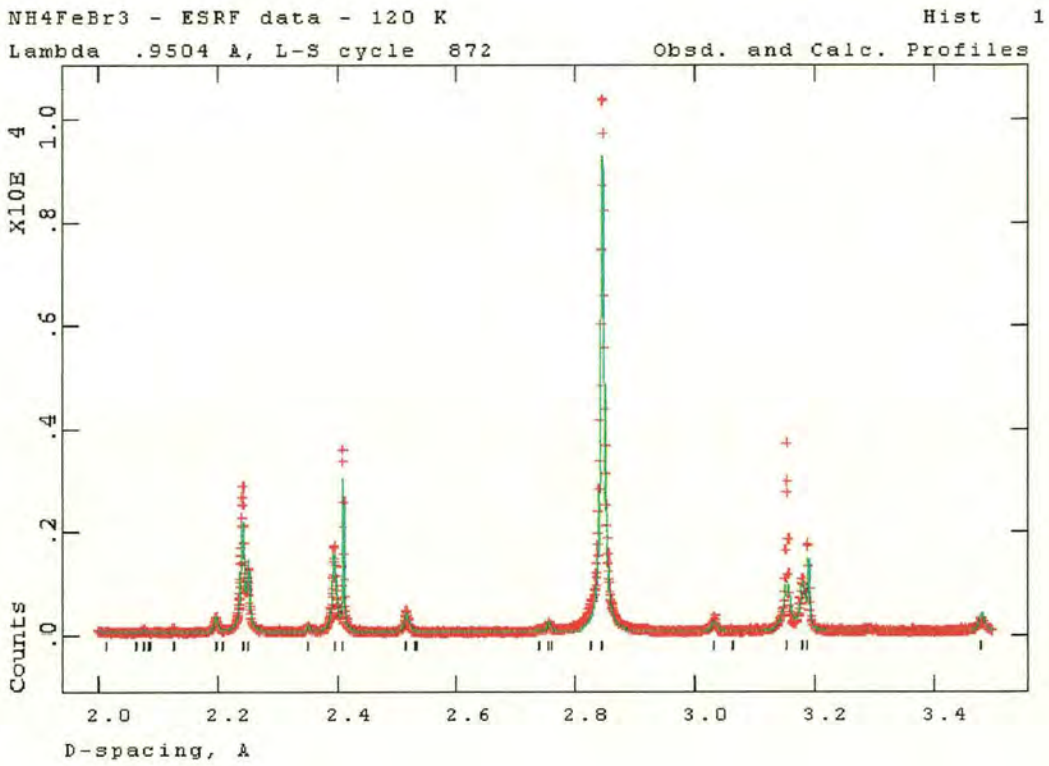

Figure 7.6. Rietveld refinement of data collected on NH_4FeBr_3 at 120 K. The superlattice reflections are well modelled.

The distortion observed here in NH_4FeBr_3 can be described in terms of relative slipping and twisting of the $FeBr_3$ chains. If the unit cell is viewed by looking down the *c*-axis (Figure 7.7a), the chains can be seen to twist while the slipping of the chains is illustrated by a view in the (110) direction. In this diagram the atom positions before and after the distortion are shown; the atom positions obtained from refinement of the 291 K data set for ND_4FeBr_3 (Table 7.2) in the primitive unit cell have been transformed to their equivalents in the expanded $\sqrt{3}a$ x $\sqrt{3}a$ x c unit cell to allow a direct comparison with those obtained from refinement of of the 120 K data set for NH_4FeBr_3 (Table 7.3).

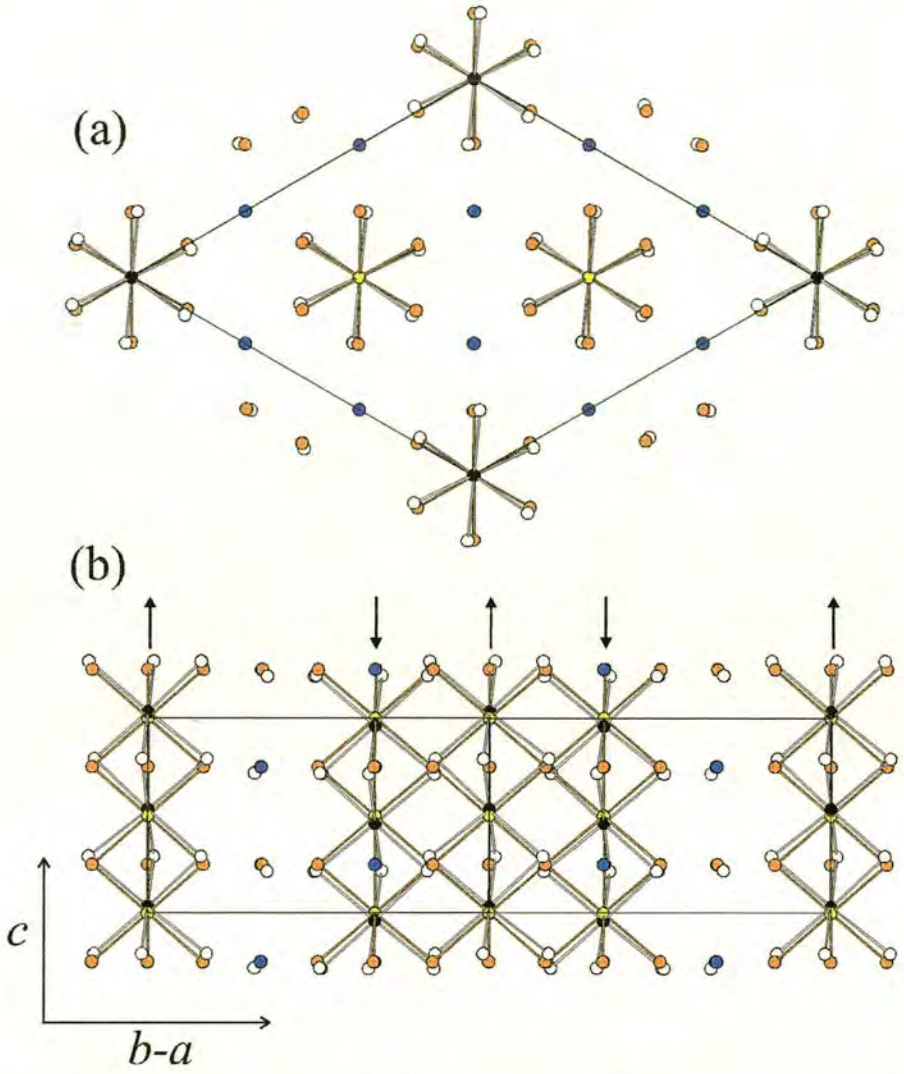

Figure 7.7. The structural distortion observed in NH_4FeBr_3 involves (a) twisting and (b) slipping of of $FeBr_3$ chains. The N, Fe and Br in the undistorted cell are blue, yellow and orange circles respectively, while the new positions of the Br and Fe atoms are represented by white and black circles respectively.

The two chains which are displayed at the two 120° corners of the cell shown in Figure 7.7, are superimposed and form the central chain in Figure 7.8. The two chains which are inside the $\sqrt{3}a$ x $\sqrt{3}a$ x c unit cell in Figure 7.7a are therefore seen to move into the

page (in Figure 7.7a, down in Figure 7.7b) and the four at the cell corners move out of the page (in Figure 7.7a, up in Figure 7.7b).

7.2.3. Investigation of the structure below the second transition at 90(10) K

A further transition is seen in NH_4FeBr_3 between 120 and 50 K (Figure 7.8), which is consistent with previous work [68].

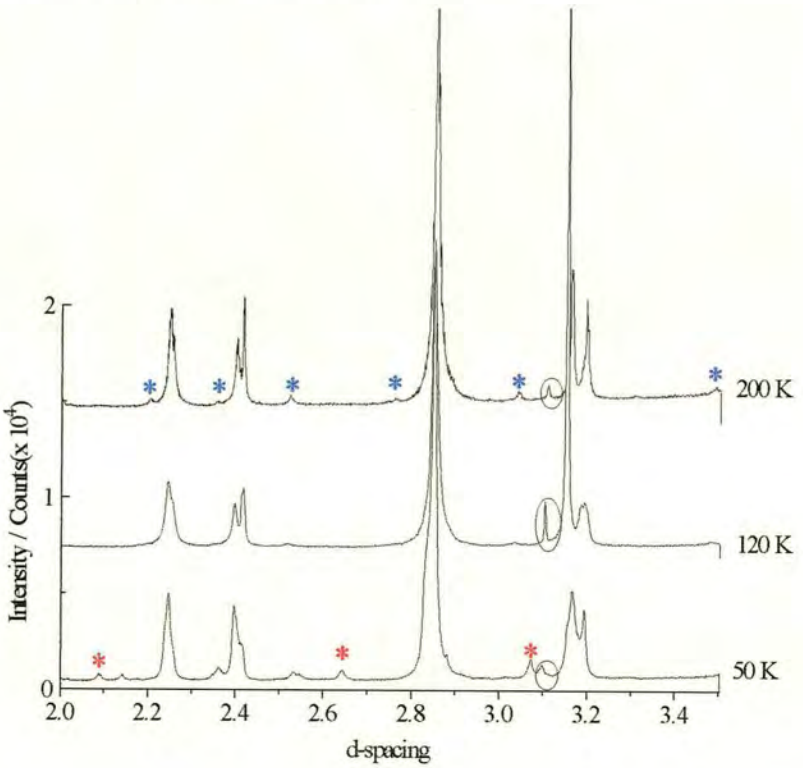

Figure 7.8: The structure of ND_4FeBr_3 is seen to distort further on cooling to 50 K. Blue asterisks represent the superlattice reflections of the $\sqrt{3}a$ x $\sqrt{3}a$ x c cell, red asterisks represent new reflections seen at 50 K and circles mark the position of the $FeBr_2$ impurity peaks.

An attempt was made to collect a series of diffraction patterns at 10 K intervals in the region of this second transition. Each run was short, approximately 30 minutes (c.f. 6 hours for other runs), and a monitor count of ~40000 was collected in each case. Unfortunately, the data quality is poor as the capillary broke under vacuum in the cryostat. The extremely high sensitivity of this diffractometer is perhaps illustrated by the fact that diffraction patterns were still recorded and it was not apparent until the sample was changed that the explosion had occurred, and the patterns had been collected on only the small quantity of sample left clinging to the inner walls of the broken capillary. Representative portions of the data sets obtained over the temperature range 105 K to 65 K are shown in Figure 7.10.

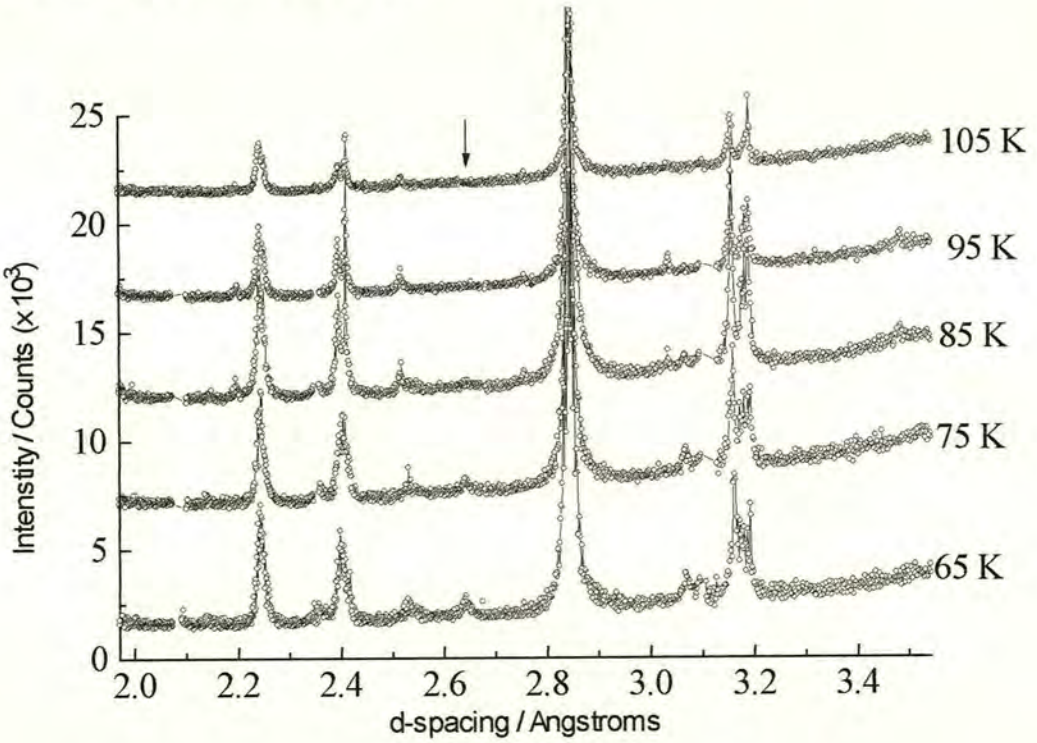

Figure 7.10: Data collected on ND_4FeBr_3 over the temperature range 65 - 105 K spanning the second structural transition. The new reflection at 2.64 Å (indicated by arrow) can be seen to appear between 85 and 95 K

The superlattice peak at 2.64 Å begins to appear in these data at 95 K. More accurate analysis is not possible due to the relatively low quality of these data.

If the higher quality full data sets collected are considered once again, one particularly significant difference between the data collected above and below this transition is the appearance of a new reflection close to the (010) reflection of the primitive cell, as illustrated in Figure 7.11.

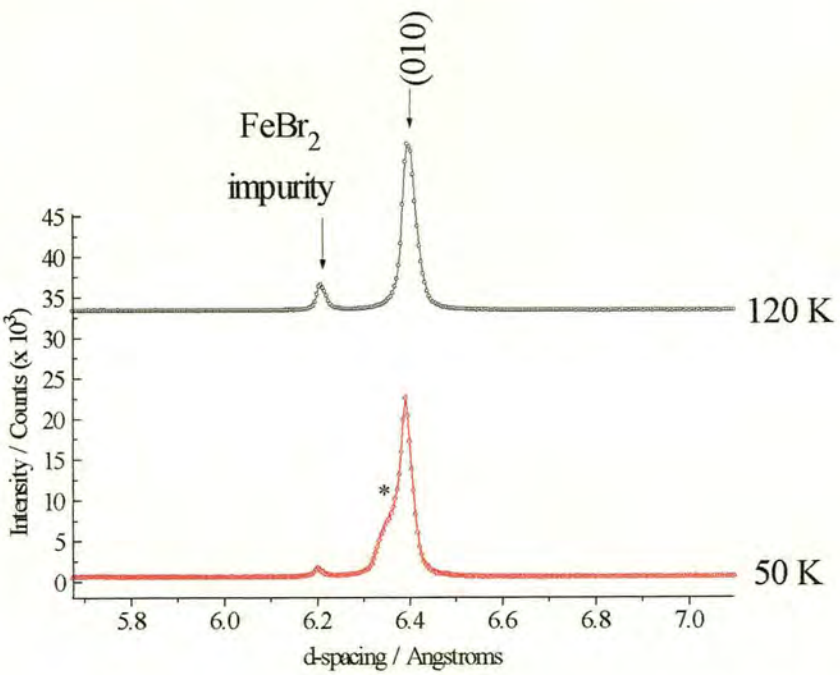

Figure 7.11: A new reflection, marked by an asterisk, appears at ~ 6.3Å on cooling ND_4FeBr_3 to 50 K.

A fresh attempt was made to take data on BM16 using better samples of NH_4FeBr_3 and ND_4FeBr_3, and these reveal this transition more clearly. This is shown in Figure 7.12, a data set collected on NH_4FeBr_3 at 120 K is compared to one collected on ND_4FeBr_3 at

4.2 K (there was not time to run both samples at both temperatures), there seems no reason to assume that these data sets are not directly comparable as the structural transitions of the deuterated and non-deuterated materials are likely to be similar and the temperatures considered here are not close to the known transition temperatures.

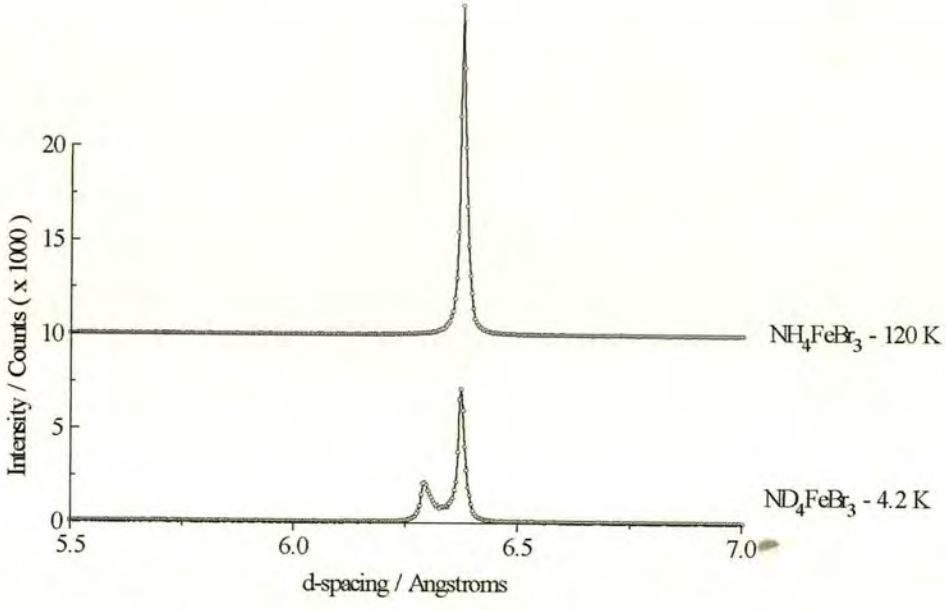

Figure 7.12: The new reflection is seen be appear at ~ 6.3Å at 50 K in ND_4FeBr_3 (Figure 7.11) is very clear at 4.2 K

The higher quality of data obtained in these two data sets, i.e. NH_4FeBr_3 at 120 K and ND_4FeBr_3 at 4.2 K, can also be used to compare the other superlattice reflections (Figure 7.13).

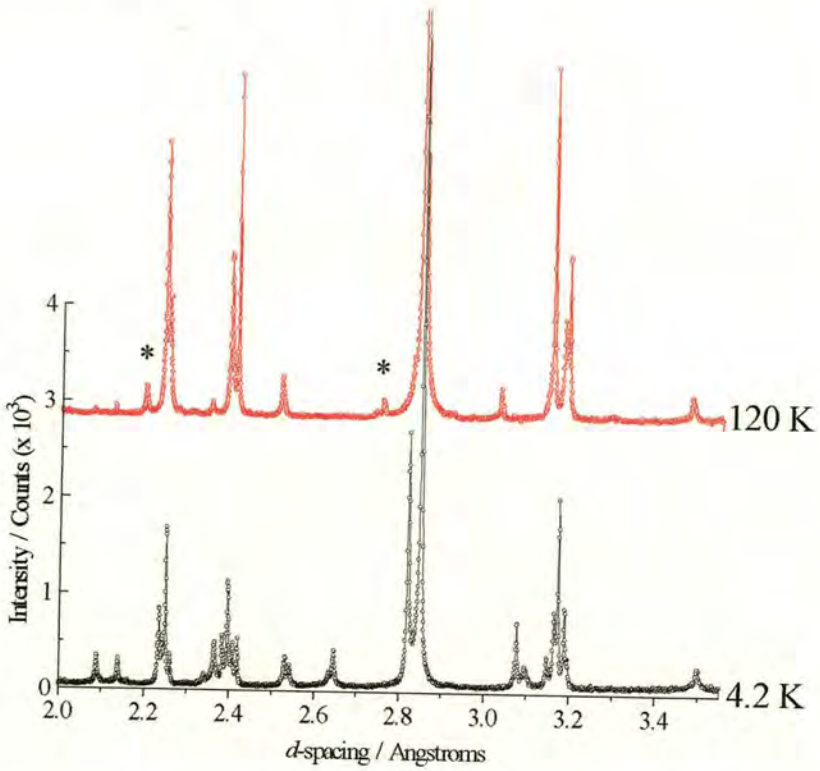

Figure 7.13: The (131) and (132) superlattice reflections of the $\sqrt{3}a$ x $\sqrt{3}a$ x c hexagonal unit cell (marked by asterisks) are seen to have disappeared in the lower temperature data.

The data set for ND_4FeBr_3 at 4.2 K was then autoindexed using Treor 90 [141]. The results indicated an orthorhombic unit cell with lattice parameters a = 12.588(1), b = 7.394(1) and c = 6.345(1) (*i.e.* a $\sqrt{3}a$ x a x c) and a unit cell volume of 590.62 (1)Å^3; the observed and calculated reflection list for this procedure is given in Appendix B. This appears inconsistent as it would suggest that the unit cell shrinks on cooling. This cell (with volume = $\sqrt{3}a^2c$) is smaller than the $\sqrt{3}a$ x $\sqrt{3}a$ x c cell (volume = $\left(3\sqrt{3}/2\right)a^2c$) found at higher temperature, it is therefore more likely that the real supercell is a multiple of $\sqrt{3}a$ x a x c with the a or b cell edge being multiplied by an integer.

7.3. Neutron Diffraction

7.3.1. Powder neutron diffraction using diffractometer D2B

7.3.1.1. Room temperature structure

Data were collected on a 4 g powder sample of ND_4FeBr_3 loaded into an 8 mm diameter vanadium can. A larger sample was available, but photographs taken of the non-diffracted beam, with the sample in place, revealed that the sample absorbed neutrons significantly when a12 mm diameter can was used. The sample was loaded in an argon glove box and indium wire was placed in a channel around the top of the can. On tightening the steel cap this wire was squashed and formed an airtight seal to prevent the material being exposed to air. Data were collected over a range of temperatures on this sample.

The data were refined using GSAS, a similar procedure was used as that described for the refinement of data collected on D2B for ND_4FeCl_3. The sample was found to contain a very small amount of ND_4Br impurity, the regions containing these reflections were removed from the refinement. At temperatures 470, 380 and 300K the data refined well in space group $P6_3/mmc$. The lattice parameters and goodness of fit parameters are shown in Table 7.4. The refinement plots and important bond lengths and angles is given in Appendix B. Figure 7.14 shown a sample region of the refinement of the data set collected at 470 K.

Table 7.4. Lattice parameters and goodness of fit parameters from refinements of ND_4FeBr_3 data collected on D2B.

Temp / K	Space Group	*a* / Å	*c* / Å	χ^2	R_{wp}
470	$P6_3/mmc$	7.46380(21)	6.39091(29)	2.037	0.0437
360	$P6_3/mmc$	7.43135(24)	6.36580(34)	3.019	0.0528
300	$P6_3/mmc$	7.39933(16)	6.34659(26)	4.345	0.0560

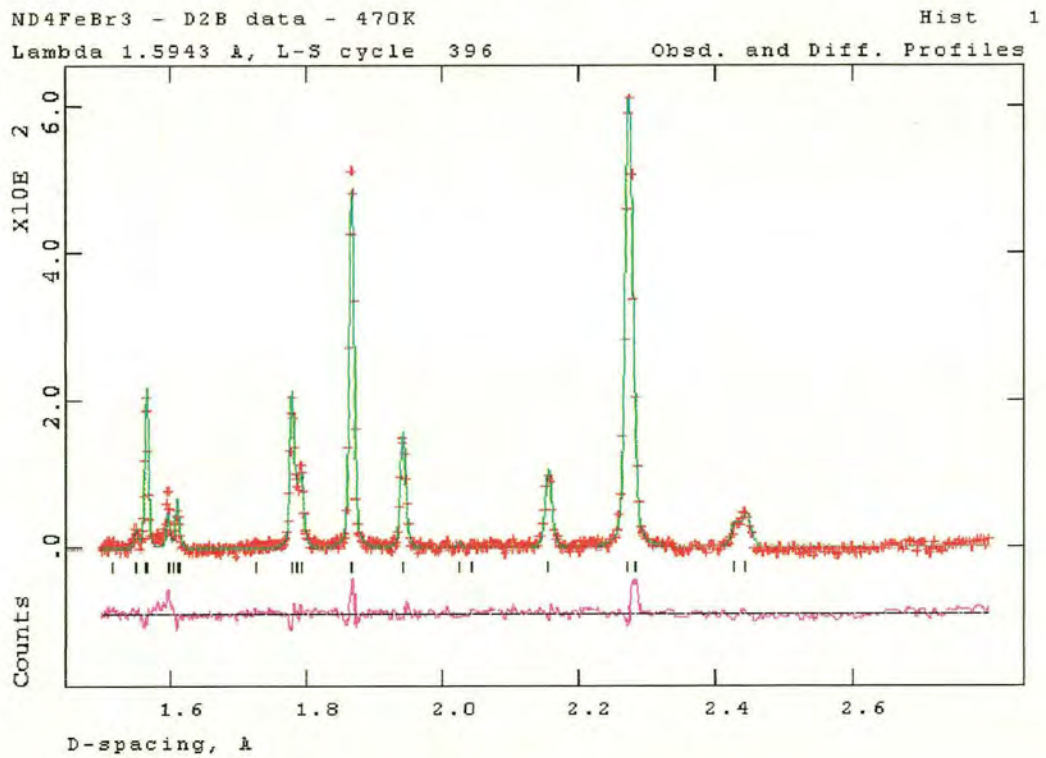

Figure 7.14. ND_4FeBr_3 data collected on D2B at 470 K and refined using GSAS.

The ND_4^+ unit was modelled as a constrained rigid body with an N-H bond length of 1.04Å and tetrahedral geometry, and the refinement of the tetrahedron allowed rotation with respect to the *z*-axis and the N-H bond length was allowed to vary, in the same way as described for the refinements of D2B data collected for ND_4FeCl_3 (Section 5.4.1.2). In this case the refinements were unstable if the thermal parameters were allowed to vary anisotropically; the isotropic thermal parameters found for ND_4FeBr_3 were significantly larger than those found for ND_4FeCl_3 at comparable temperatures. This may be because the cavity for the A cation is larger in the bromide salt, when compared to the analogous chloride, this is reasonable as the corresponding unit cell is larger. A consequence of this here is that the ND_4 unit should be more mobile. The isotropic thermal paramaters are illustrated in Figure 7.15.

7.3.1.2. Investigation of the structure after the first transition at 270(10) K

As expected, new reflections are seen to appear between 300 and 200 K; some of these are highlighted in Figure 7.16 and these can be successfully indexed on a $\sqrt{3}a \times \sqrt{3}a \times c$ hexagonal unit cell. Data sets collected at 200 K and 120 K were successfully refined using this unit cell and space group $P6_3$, the lattice parameters and goodness of fit parameters are given in Table 7.5. The refinement plots are given in Appendix B.

(a) 470 K

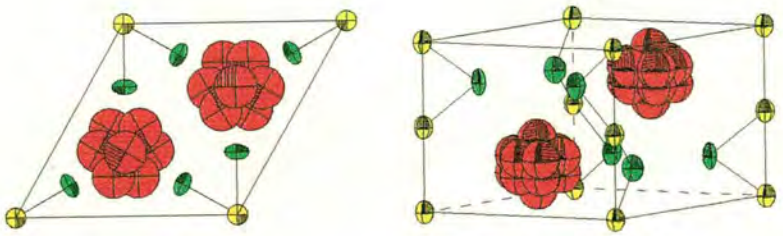

(b) 380 K

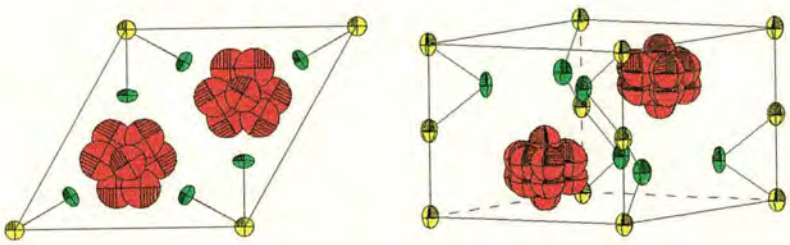

(c) 300 K

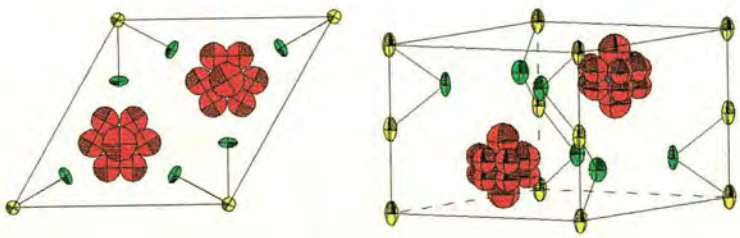

Figure 7.15. The isotropic thermal parameters obtained from refinement of ND_4FeBr_3 data illustrate the high degree of disorder in the D positions. (a) 470 K top, (b) 380 K and (c) 300 K. The D atoms are depicted here as red ellipses, the yellow ellipses represent Fe and green ellipses represent Br the (blue) N atoms are almost completely obscured by the D atoms.

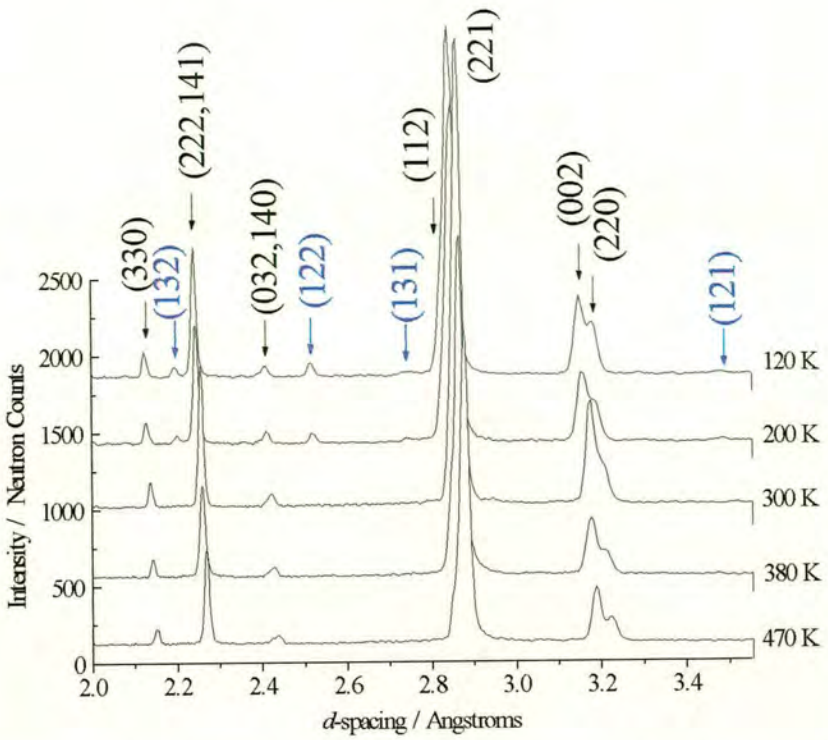

Figure 7.16. Superlattice reflections, indicated in blue, are seen to appear between 300 and 200 K in D2B data collected on ND_4FeBr_3. These index on a $\sqrt{3}a$ x $\sqrt{3}a$ x c hexagonal unit cell.

Table 7.5. Lattice parameters and goodness of fit parameters from refinements of ND_4FeBr_3 data collected on D2B.

Temp / K	Space Group	*a* / Å	*c* / Å	χ^2	R_{wp}
200	$P6_3$	12.78049(40)	6.32587(25)	3.438	0.0590
120	$P6_3$	12.76533(29)	6.31356(20)	4.763	0.0649

The refinements again included a rigid body model of the ND_4^+ unit. The superlattice reflections are well modelled, this is illustrated in Figure 7.17.

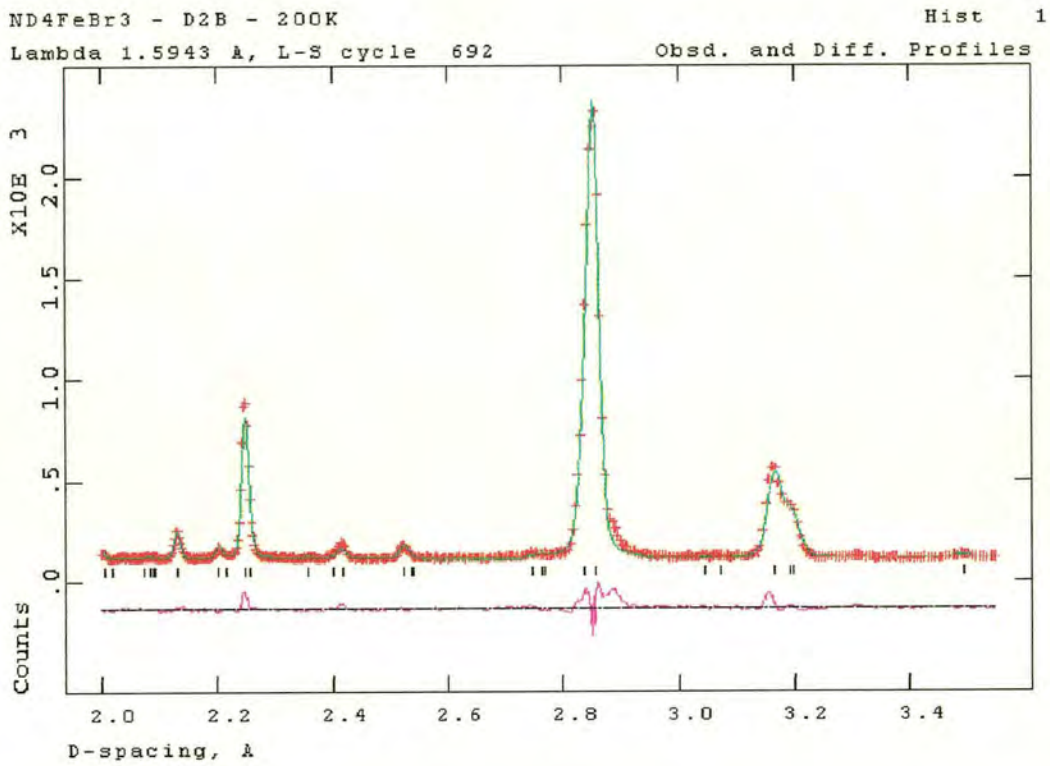

Figure 7.17. D2B data for ND_4FeBr_3 at 200 K, refined using GSAS, the superlattice peaks (*c.f.* Figure 5.16) are well modelled.

7.3.1.3. Investigation of the structure after the second transition at 90(10) K

Data collected on diffractometer D2B again clearly shows a structural transition between 120 and 50 K, which is shown in Figure 7.18. Once again the (131) and (132) reflections of the $\sqrt{3}a$ x $\sqrt{3}a$ x c hexagonal unit cell are lost after the transition.

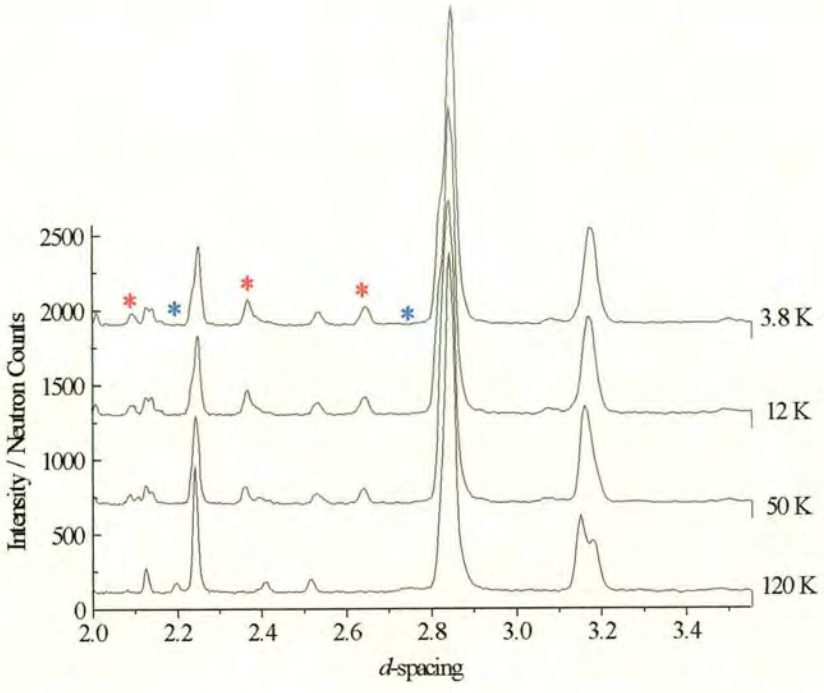

Figure 7.18. A structural transition is observed in ND_4FeBr_3 between 120 and 50 K. Blue asterisks mark reflections lost and red asterisks mark the new ones observed on cooling.

The data sets collected below the transition could once again be indexed on an $\sqrt{3}a$ x a x c orthorhombic unit cell. However, any cell smaller than this does not make chemical sense as the structure of this material above the transition temperature of 90(10) K involves a significant movement of the $FeBr_3$ chains relative to one another, a transition from a $\sqrt{3}a$ x $\sqrt{3}a$ x c hexagonal unit cell to this smaller orthorhombic cell would require this chain slipping to be undone.

The projection of the $\sqrt{3}a$ x $\sqrt{3}a$ x c hexagonal unit cell on the ab plane is shown in Figure 7.19, the expanded $\sqrt{3}a$ x $3a$ x c orthorhombic cell and the $2\sqrt{3}a$ x $2\sqrt{3}a$ x c cell are shown for comparison. A distortion from the hexagonal cell to one of these expanded cells is consistent with the loss of the (131) and (132) reflection indicated above; this would suggest the two $FeBr_3$ chains inside the $\sqrt{3}a$ x $\sqrt{3}a$ x c hexagonal cell becoming inequivalent, these are highlighted in red in Figure 7.19. Of these two the orthorhombic $\sqrt{3}a$ x $3a$ x c cell seems the more likely as the higher resolution BM16 data collected on ND_4FeBr_3 can also be indexed on this cell.

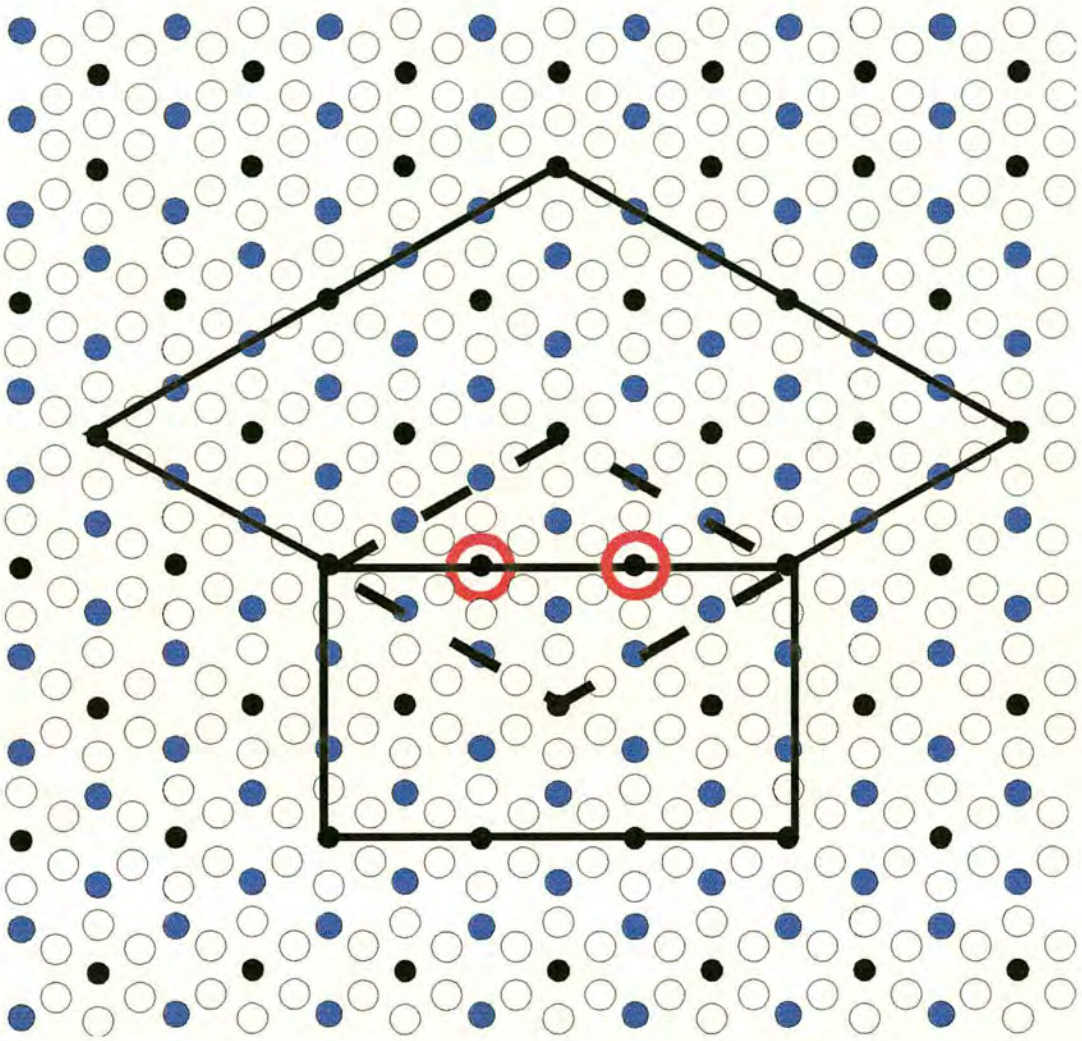

Figure 7.19. A comparison of the √3a x √3a x c hexagonal cell, the √3a x 3a x c orthorhombic cell and the 2√3a x 2√3a x c hexagonal cell. The loss of the (131) and (132) reflections of the √3a x √3a x c hexagonal cell is consistent with the two Fe (black) atoms, highlighted in red, becoming inequivalent (blue circles represent N and white circles represent Br).

Figure 7.20 shows D2B data for ND_4FeBr_3 at 12 K, over the same range of *d*-spacing as the data sets in Figure 7.18., with reflections marked for a $\sqrt{3}a$ x $\sqrt{3}a$ x c hexagonal unit cell, $\sqrt{3}a$ x a x c orthorhombic unit cell and a $\sqrt{3}a$ x $3a$ x c orthorhombic unit cell. There appears to be no real evidence in these data to suggest the $\sqrt{3}a$ x $3a$ x c orthorhombic unit cell is actually adopted by the structure.

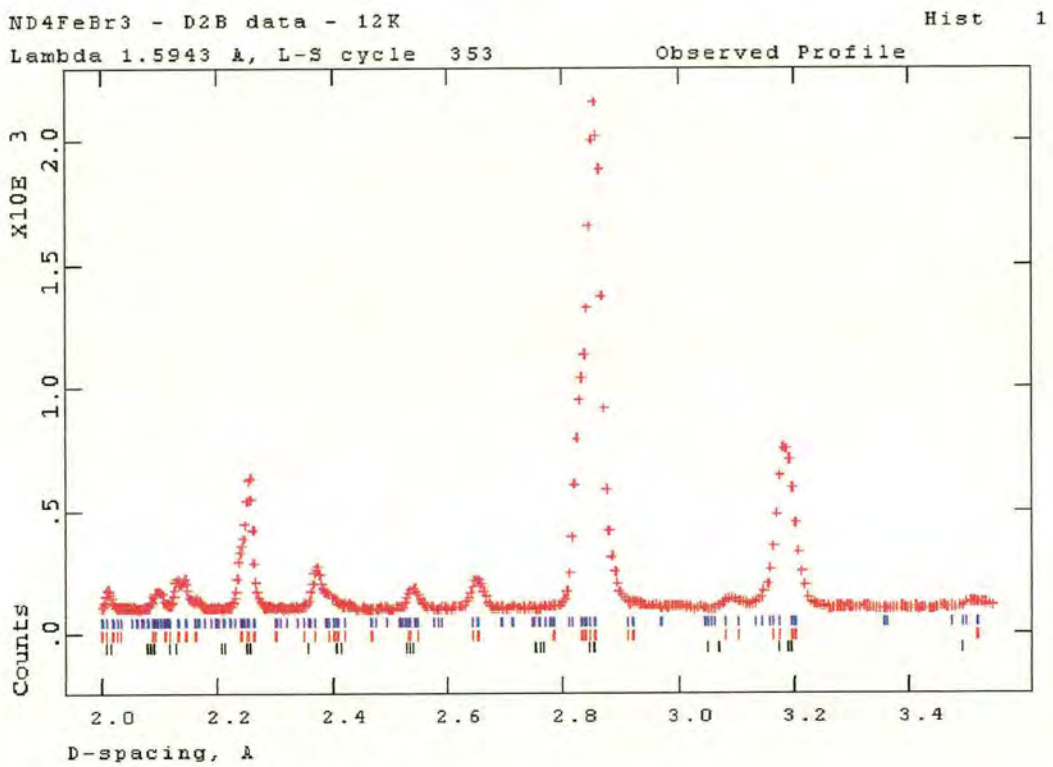

Figure 7.20. Data collected on D2B below the second transition in ND_4FeBr_3 can be indexed on a $\sqrt{3}a$ x a x c orthorhombic unit cell, for which reflections are indicated by red markers (central). $\sqrt{3}a$ x $\sqrt{3}a$ x c hexagonal unit cell (black markers, bottom) and $\sqrt{3}a$ x $3a$ x c orthorhombic unit cell (blue markers, top) are shown for comparison.

7.3.2. Powder neutron diffraction using diffractometer D1B

Data were collected on diffractometer D1B at ILL on a powder sample of ND_4FeBr_3 to investigate the long-range magnetic ordering. Several scans were taken at 5 minute intervals over the temperature range 1.5 - 10K; and are displayed in Figure 7.21. Two new reflections can be seen to emerge at 4.76 and 8.38 Å, and reflections at 5.67 and 6.35 Å significantly change intensity in this region. The intensities over these regions were then summed and are displayed as a function of temperature in Figure 7.22.

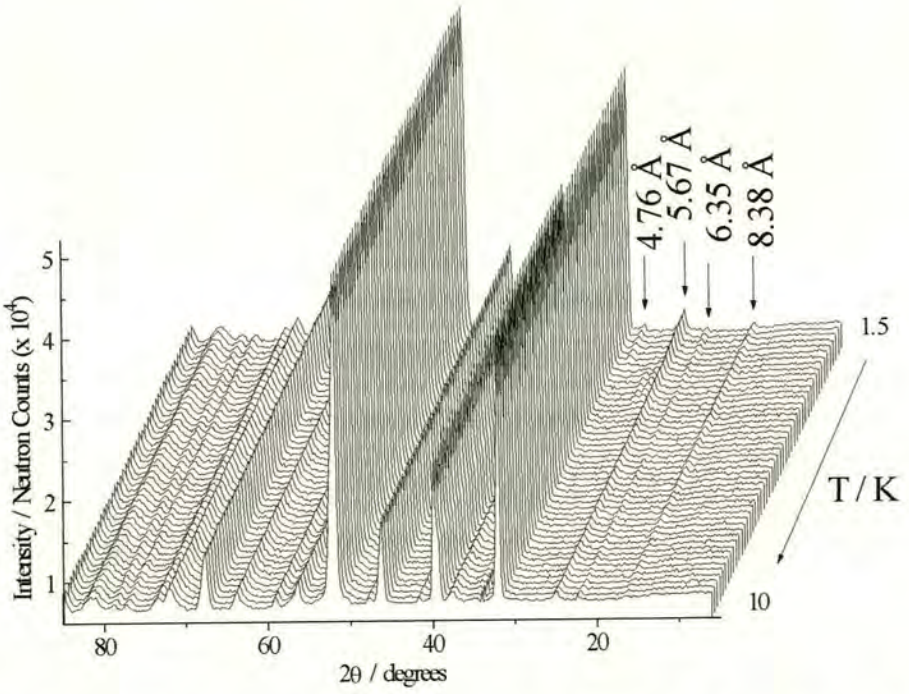

Figure 7.21. D1B data collected on a sample of ND_4FeBr_3 between 10 and 1.5 K shows a two new reflections at 4.76 and 8.38 Å and two further regions of changing intensity at 5.67 and 6.35 Å.

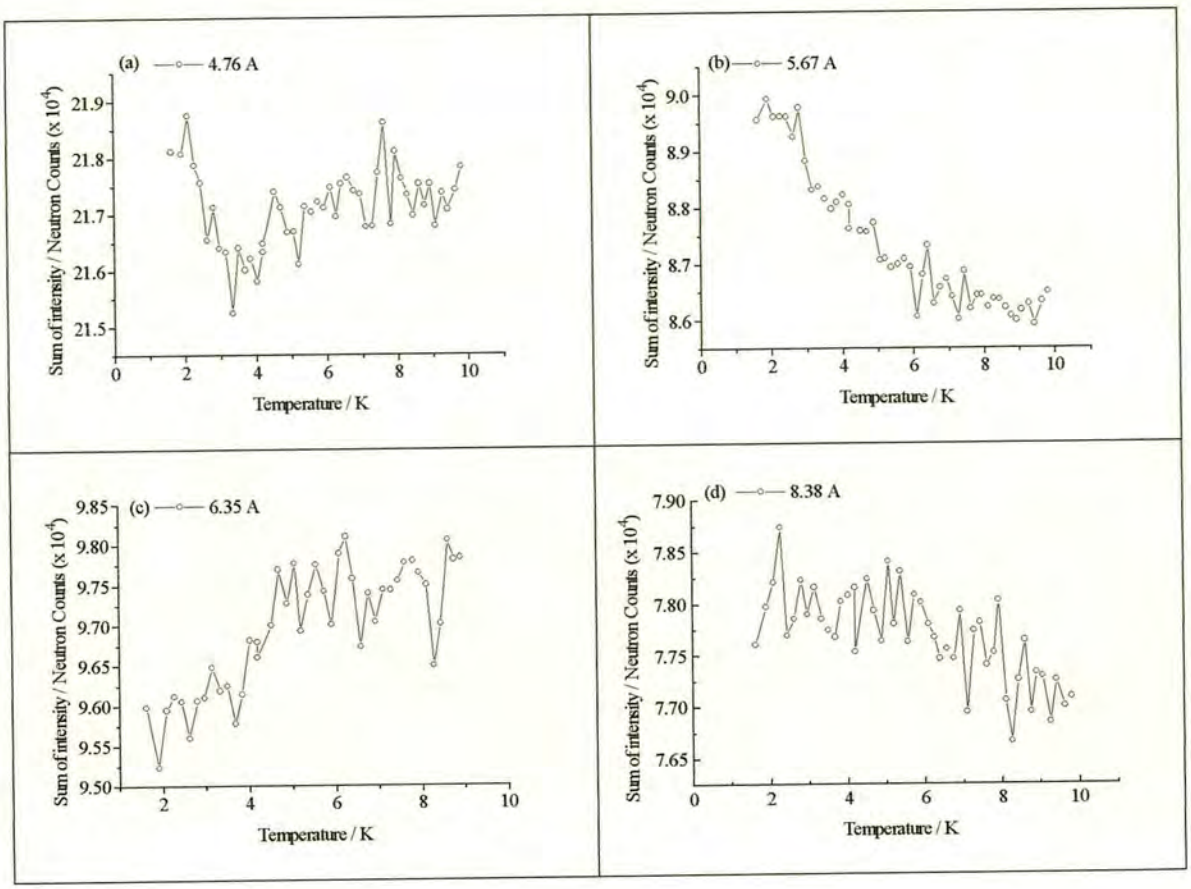

Figure 7.22. The summed intensities over the regions indicated in Figure 7.21 above. Reflections at (a) 4.76 Å, (b) 5.67 Å, (c) 6.35 Å and (d) 8.38 Å.

The intensity of the reflection at 8.38 Å changes gradually with temperature and shows no abrupt change near either of the temperatures at which magnetic transitions are believed to occur in ND_4FeBr_3. The reflection at 5.67 Å does change significantly near 6.0 K and indexes as (1 0 1) using an orthorhombic cell of dimension $\sqrt{3}a$ x na x c, thus it is not possible to discriminate between various possible orthorhombic cells on the basis of this reflection. There is a modest change around 4.0 K in the intensity o the reflection at 6.35 Å which indexes as (0 0 1); this suggests magnetic correlations which

are antiferromagnetic along *c*, and each (*ab*) plane must have some net component of moment. There is a weakly allowed nuclear component at this position so it is not possible to decide whether or not the lower-temperature magnetic structures contributes to this reflection. Finally, the reflection at 4.76 Å shows an abrupt transition at approximately 3.5 K. This reflection indexes close to (2 *k* 0) for an orthorhombic $\sqrt{3}a$ x k*a* x *c* cell; however, the D1B data indicates that the reflection is not quite commensurate with the lattice, the commensurate *d*-spacing being 4.68 Å. These observations will be discussed later in the light of magnetic susceptibility data reported in Chapter 8. However, at this stage it is clear that the correlations along *c* are antiferromagnetic, while in the (*ab*) plane they are compatible with the nuclear cell discussed in Section 7.3.1.3. The structural distortion from the simple $\sqrt{3}a$ x $\sqrt{3}a$ x *c* magnetic cells observed in undistorted ABX_3 antiferromagnets [25]. In some cases this imbalance may produce an incommensurate magnetic structure [89].

A data set collected at 1.54 K was selected from the data shown above, collected on D1B on ND_4FeBr_3. This was refined in GSAS on a $\sqrt{3}a$ x 3*a* x *c* orthorhombic cell using *P*1 symmetry, by employing the Le Bail extraction method, the refinement is illustrated in Figure 7.23. The new reflection at 8.38 Å can be indexed on this cell.

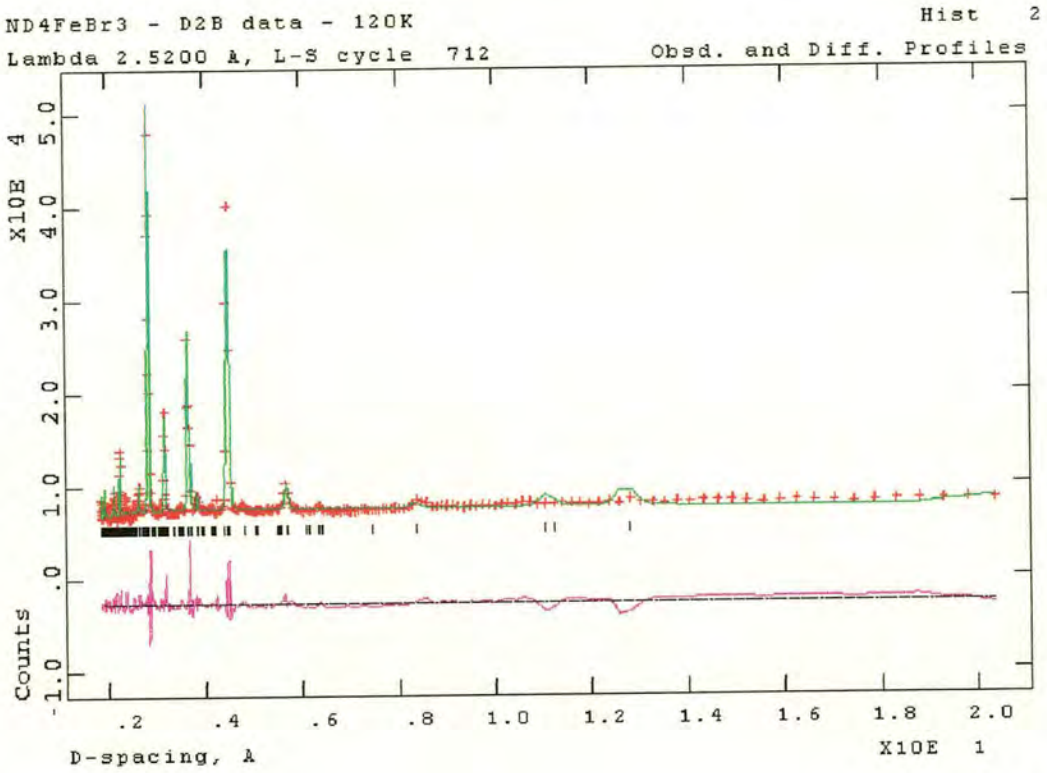

Figure 7.23. Le Bail extraction Rietveld refinement of a 1.54 K D1B data set; the reflection at 8.38 Å can be indexed on a $\sqrt{3}a$ x $3a$ x c orthorhombic unit cell.

7.4. Single crystal x-ray diffraction

Data were collected on a single crystal of NH_4FeBr_3 using the SMART diffractometer in Durham at 120 K and 60 K. It was not possible to collect data at above 200K as the oil protecting the crystal from air melts above 200K. A severe problem with the cryostat was experienced during this experiment with the result that the data are not sufficient to allow a complete refinement at either temperature, the problem encountered also means that the temperature may not have remained reliably at 60 K during the collection of the

second data set. At 120 K the structure observed was consistent with a $\sqrt{3}a$ x $\sqrt{3}a$ x c unit cell with $P6_3$ symmetry and lattice parameters a = 12.751(1) Å and c = 6.306(1) Å. A structural phase transitions was observed at 85-100K, as expected. At 60 K a preliminary refinement suggests a unit cell with orthorhombic symmetry in which one of the cell parameters is still $\sqrt{3}a$ and the other is a multiple of a. It is difficult to make a direct comparison between the powder and single crystal data as the temperatures of data collection are not comparable. It is hoped that a further experiment, scheduled in the very near future, will shed some light on this problem.

7.5. Summary

In summary, ND_4FeBr_3 has been refined successfully using a primitive a x a x c unit cell in space group $P6_3/mmc$ at temperatures above 270(10) K (BM16 data on ND_4FeBr_3 (291 K) and D2B data on $ND_4FeBr_3$470, 380 and 300 K). Data collected in the region 270(10) K to 90(10) K has suggests the material adopts a second structure, in which the $FeBr_3$ chain twist and slip relative to one another, all data sets in this temperature range (BM16 data on NH_4FeBr_3 (120 K) and D2B data on ND_4FeBr_3 at 200 and 120 K were successfully refined using a $\sqrt{3}a$ x $\sqrt{3}a$ x c unit cell in space group $P6_3$. Below 90(10) K the structure was observed to adopt a third structure, this appears to correspond to a $\sqrt{3}a$ x $3a$ x c orthorhombic unit cell.

8. Magnetic Susceptibility Measurements

8.1. Introduction

This chapter describes the measurement and interpretation of magnetic susceptibility data taken from powders and oriented crystals of the pure halides NH_4FeCl_3, ND_4FeCl_3, NH_4FeBr_3 and ND_4FeBr_3 and also of $Rb_{(1-x)}Cs_xFeBr_3$. A number of models are used to treat high and low-temperature susceptibility to assess which is the most appropriate, and to extract magnetic exchange and ligand field parameters. The low temperature magnetic phase diagram of these materials was studied as a function of applied magnetic field up to 1 T and as a function of temperature down to 1.8 K, to map out boundaries between ordered magnetic phases and compare them with the predictions of phase behaviour for these various frustrated, hexagonal antiferromagnets. Finally, the response of $Rb_{(1-x)}Cs_xFeBr_3$ to applied magnetic fields was investigated in order to test the hypothesis that the influence of the dopant on the host, producing local structural distortions and consequently reducing the local moment, could be reversed by the field. Further, it was anticipated that this material would show glassy magnetic behaviour, the response to the applied field being very dependent on whether the sample was cooled in a field, and therefore cooled into a homogenous magnetic phase, or cooled in zero field so that magnetic disorder froze in.

8.2. Experimental Details

The instrument used to measure the magnetic susceptibility was a Quantum Design Magnetic Property Measurement System (MPMS) model 1802 (Digital R/G Bridge).

The maximum field that can applied to the sample is 1 Tesla with error ±0.5 mT, which is largely due to remanence in the field when it is cycled between maximum and minimum values. The base temperature of the instrument is 1.7 K, produced by filling an inner reservoir with helium and pumping on it; this has a hold time typically of 30 – 60 minutes, so measurements below 4.2 K have a relatively small time window if it is important that the sample does not make an excursion above 4.2 K in order to complete low-temperature measurements. The maximum operating temperature of the instrument is 340 K. Data are first produced in the form of the voltage of the SQUID detector versus sample position, and this is automatically transformed by the instrumental software to the magnetisation of the sample. A standard sample is run every six months to ensure the instrumental calibration has not drifted. For this purpose a variety of paramagnetic salts are used, a common sample being Gd_2O_3, which may be obtained in high purity, and which contains ions with large, spin-only moments.

The usual method of mounting the sample involves grinding it into a fine power and placing it in a container with a small magnetic response; for all our measurements, a gelatine capsule with a small diamagnetic response served this purpose well. Such measurements provide an orientational average of the susceptibility and this is often sufficient for the purposes of locating ordering transitions, or mean exchange parameters, particularly for isotropic materials. In the present case, where the bulk magnetic susceptibility at both high and low temperatures may be quite anisotropic, it may be advantageous to measure oriented single crystals. This was possible for the materials prepared here; the small needles that could be found in the sample ampoules were sufficiently large and susceptible to give a good signal – indeed the limiting factor was generally the measurement of their mass in calculating molar quantities.

All the crystals studied were very air sensitive, so the majority of handling was carried out inside an argon glove box. The crystals were aligned by eye either perpendicular or parallel to the magnetic field that was applied during the measurement. This was done by attaching them to the inner wall of a drinking straw, in the glove box, using a small amount of Dow Corning vacuum grease; this grease has negligible magnetic signal compared with that of the sample. In addition the grease did not seem to react with the crystals and the layer of grease acted as a barrier against the air during the minute or so it took to remove the straw from the glove box and get it safely into the vacuum inside the magnetometer (also during the reorientation of the crystal). Great care was taken to ensure that the orientation of each crystal was as close as possible to ideally parallel and perpendicular; small deviations are inevitable but this should not have a significant impact on the data.

8.3. Susceptibility measurements as a function of temperature

8.3.1. ND_4FeCl_3 and NH_4FeCl_3

The susceptibility of ND_4FeCl_3 and NH_4FeCl_3 was measured on both powder and single crystal samples over a range of 1.8 to 300 K in a field of 0.1 T. A summary of the various samples used is given in Tables 8.1 and 8.2. It was felt necessary to rerun some of these samples because of their sensitivity to air, which in turn may influence their magnetic properties, so it appeared sensible to ensure all measurements should be repeated on fresh samples. In some cases the sample was too small relative to the sensitivity of the balance for us to determine the mass with any confidence, and this is indicated in the Tables.

Table 8.1. Details of ND_4FeCl_3 samples used in susceptibility measurements.

Powder (P) or crystal (C)	mass / mg	Fields / mT
C	~ 0.1	100
C	1.7	100
P	48.3	100

Table 8.2. Details of NH_4FeCl_3 samples used in susceptibility measurements. The sample whose mass is not stated was too small to be measured.

Powder (P) or crystal (C)	mass / mg	Fields / mT
C	-	100
C	2.7	100
C	31.4	10 - 1000
C	~ 1.2	100 - 1000
P	23.5	100
P	106.6	100

The data were corrected for the diamagnetic contribution of the sample and are displayed for the full temperatures range in Figure 8.1. This reveals clearly the anisotropic nature of the susceptibility.

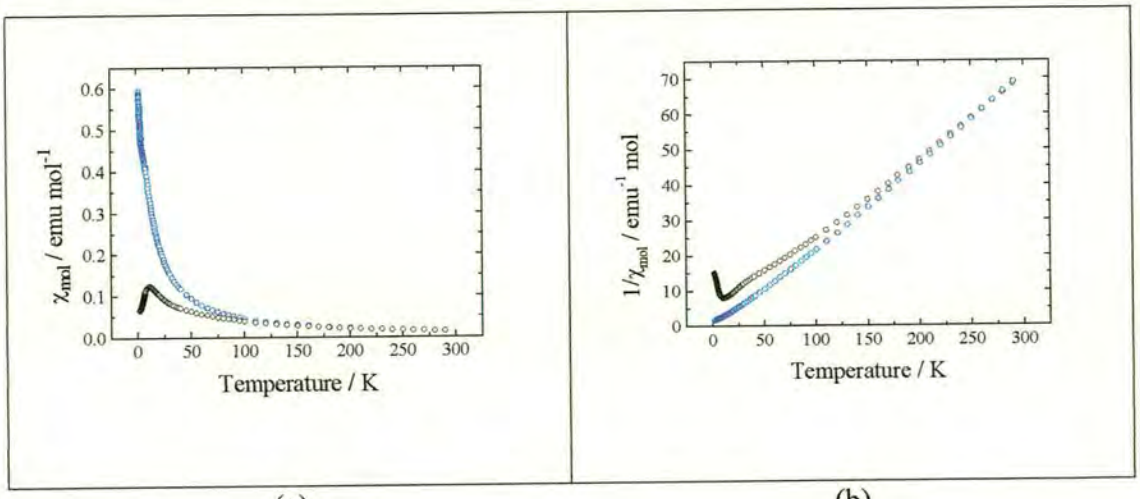

(a) (b)

Figure 8.1. Susceptibility (a) and inverse susceptibility (b) of an NH_4FeCl_3 needle crystal oriented parallel (black circles) and perpendicular(blue circles) to the applied field of 0.1T.

The susceptibility data for the deuterated analogue appeared very similar at all but the lowest temperatures so is not reproduced here for the full temperature range. The most distinctive features in the data for both the hydrogenous and the deuterated chloride samples are the broad maximum in the parallel susceptibility centred around 10 K, and a change in gradient of both the parallel and perpendicular data at 3.5-4 K. These regions of the susceptibility data are expanded in Figures 8.2-8.4. The feature at 3.5-4 K is consistent with the onset of the magnetic superlattice reflections observed in ND_4FeCl_3 on diffractometer D1B, outlined in section 5.1.4.2; the parallel and perpendicular susceptibility measurements for NH_4FeCl_3 and ND_4FeCl_3 reveal transitions at similar temperatures in (Figures 8.3 and 8.4).

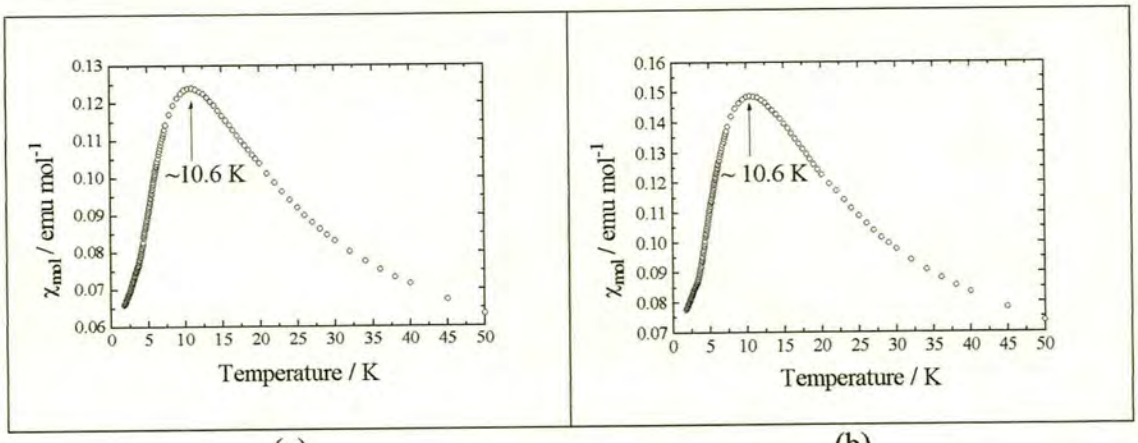

(a) (b)

Figure 8.2. Cusp in susceptibility of (a) NH_4FeCl_3 and (b) ND_4FeCl_3 with the field applied parallel to the c-axis

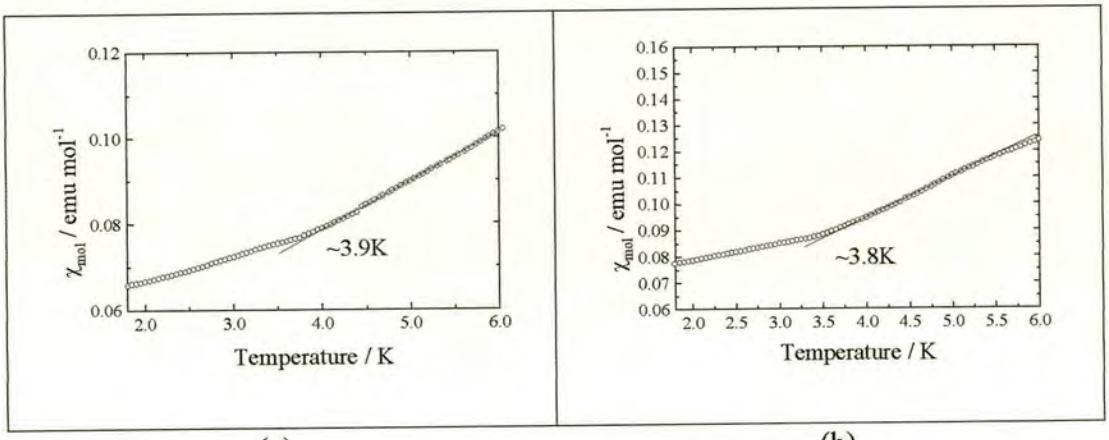

(a) (b)

Figure 8.3. Low-temperature susceptibility of (a) NH_4FeCl_3 and (b) ND_4FeCl_3 with the field applied parallel to the c-axis.

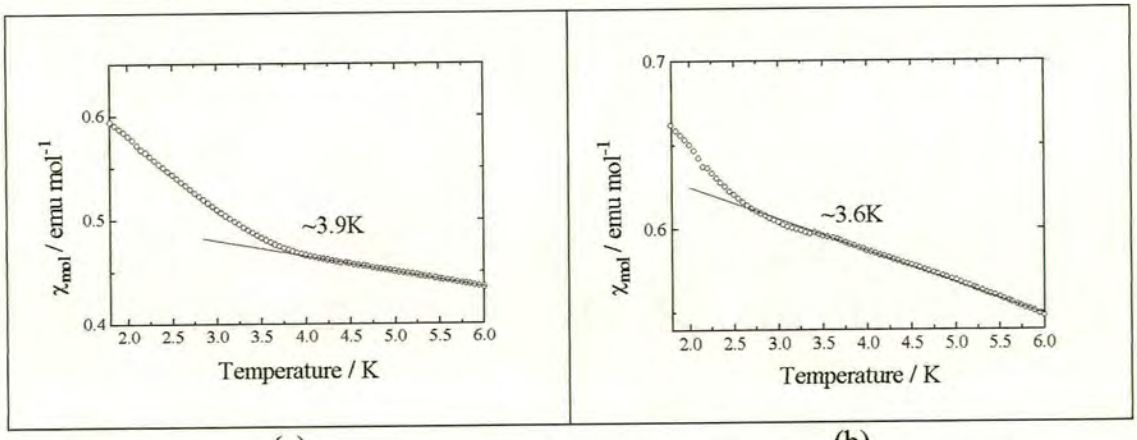

(a) (b)

Figure 8.4. Low-temperature susceptibility of (a) NH_4FeCl_3 and (b) ND_4FeCl_3 with the field applied perpendicular to the c-axis.

As expected the suceptibility of the powder samples can be clearly seen to be a combination of both the parallel and perpendicular components, Figure 8.5.

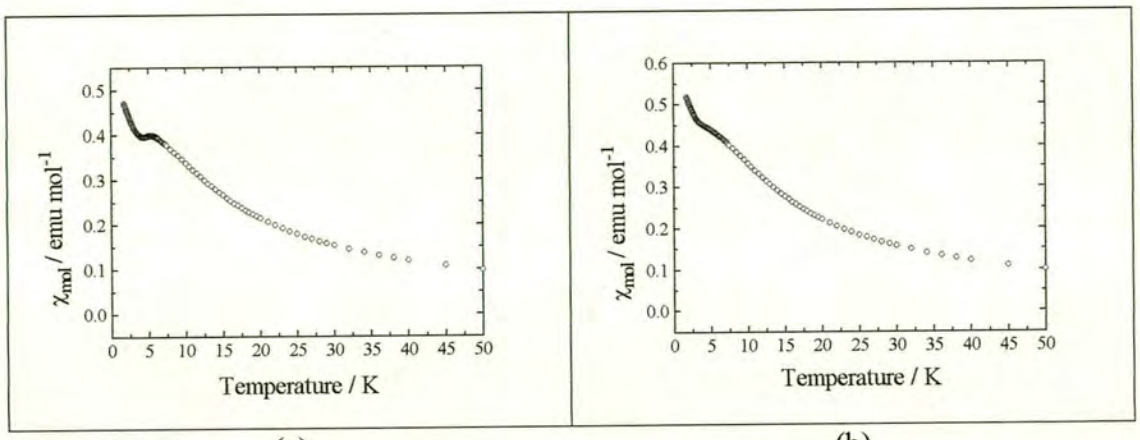

Figure 8.5. The suceptibilities of powder samples of (a) NH_4FeCl_3 and (b) ND_4FeCl_3.

The data can be observed more closely by taking the derivative of the susceptibility data with respect to temperature. These plots are shown in Figure 8.6 and clearly show a transition, in the form of a downward spike, in the region of 2 K in the perpendicular and powder data but this is almost completely absent in the parallel data.

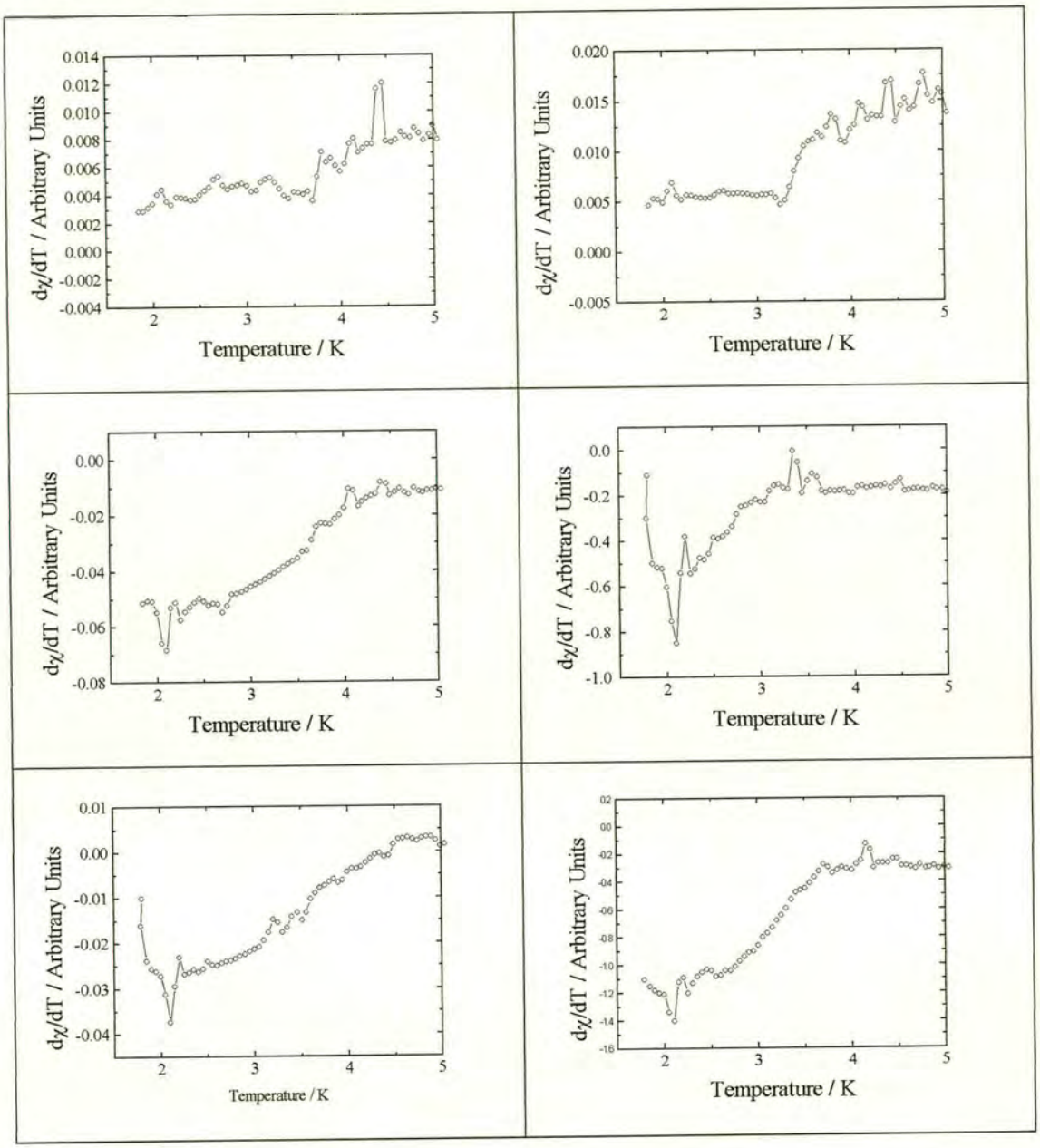

Figure 8.6. The derivative susceptibility with respect to temperature are shown for NH_4FeCl_3 (left) and ND_4FeCl_3 (right). The top plots are data from single crystals orientated parallel to the applied field of 0.1 T, the middle from crystals oriented perpendicular and the bottom plots are from powder samples.

8.3.2. NH_4FeBr_3 and ND_4FeBr_3

The susceptibility of NH_4FeBr_3 and ND_4FeBr_3 in the form of powders and single crystals was measured from 1.8 to 340 K in a field of 0.1 T. A summary of the various samples used is given in Tables 8.3 and 8.4. As was the case for the chloride sample, it was felt necessary to rerun some of these samples because of their sensitivity to air, which in turn may influence their magnetic properties, so that several measurements were repeated on fresh samples. In some cases the sample was too small relative to the sensitivity of the balance for us to determine the mass with any confidence, and this is indicated in the Tables.

Table 8.3. Details of NH_4FeBr_3 samples used in susceptibility measurements. The sample whose mass is not stated was too small to be measured.

Powder (P) or crystal (C)	mass / mg	Fields / mT
C	-	100
C	0.5	100
P	92.2	100
P	24.1	10 - 1000

Table 8.4. Details of ND_4FeBr_3 samples used in susceptibility measurements. The sample whose mass is not stated was too small to be measured.

Powder (P) or crystal (C)	mass / mg	Fields / mT
C	-	100
C	2.0	100
P	203.4	100

The form of the susceptibility as a function of temperature is illustrated in Figure 8.7 for oriented crystals of NH_4FeBr_3 and ND_4FeBr_3 respectively. This resembles the data for the chlorides at first sight, with a cusp in the region of 10 K, but on closer inspection it can be seen that the perpendicular component of the susceptibility is consistently lower than that for the chloride (Figure 8.1), which is consistent with the conclusions of the low-temperature neutron measurements that the bromide has antiferromagnetic intrachain interactions. A low-temperature discontinuity associated with a long-range ordering transition is found in the region of 6 K.

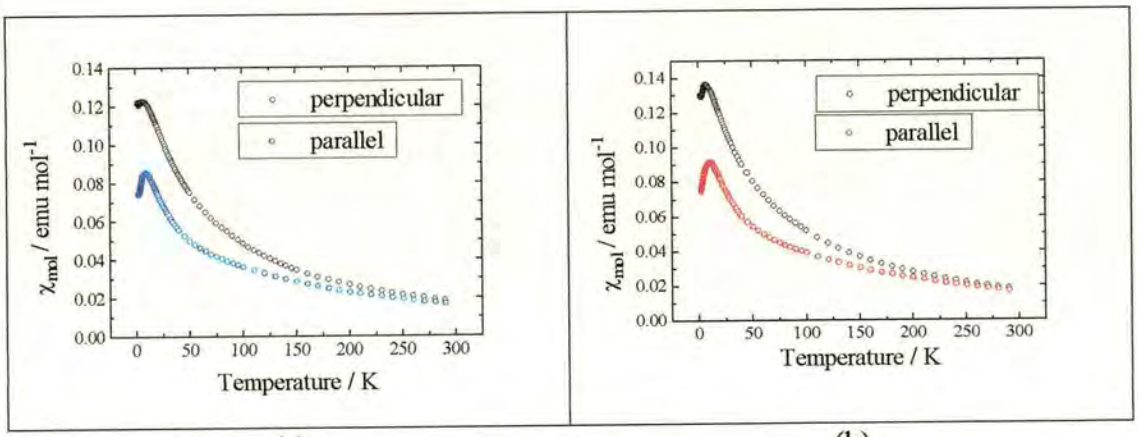

(a) (b)

Figure 8.7. Susceptibility of a crystal of NH_4FeBr_3 oriented perpendicular and parallel to the field (a) and similarly ND_4FeBr_3 (b).

A transition is clearly observed at approximately 6.2 K in the NH_4FeBr_3 data (with needle crystal parallel to the field) but surprisingly is not evident in the deuterated sample (Figure 8.8). Data taken with crystals oriented perpendicular to the applied field and powder samples are shown in Figures 8.9 and 8.10 respectively. Also evident in these samples is an upward turn in the susceptibility at around 2 K. This may be due to a small amount of paramagnetic impurity, possibly introduced when the crystal was reoriented to lie perpendicular to the applied field. The sample may have been briefly exposed to air during the reorientation. This effect can clearly be seen,

for both the H and D compounds, producing an increased inflection at 2 K; thus hydration may also be a factor in the form of the susceptibility.

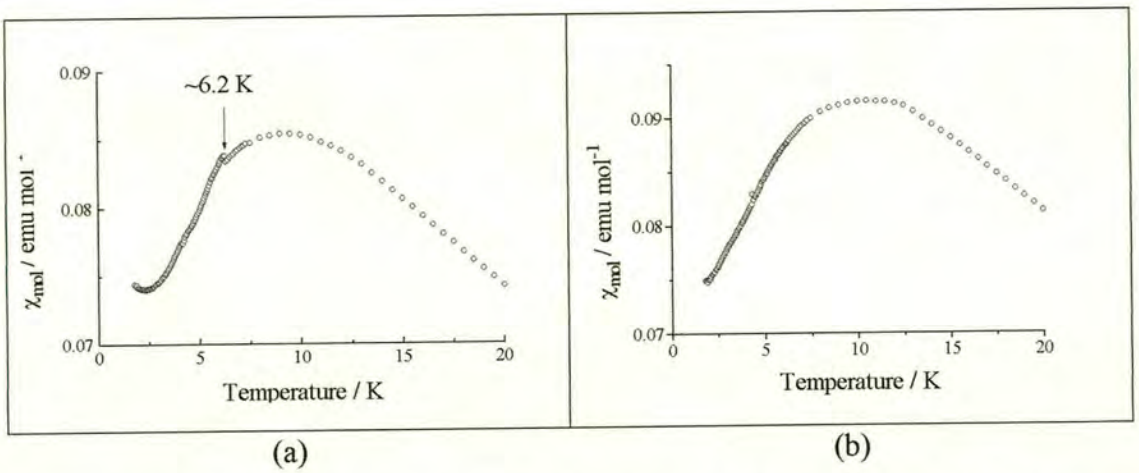

Figure 8.8. Low-temperature susceptibility of (a) NH_4FeBr_3 and (b) ND_4FeBr_3 with the field applied parallel to the c-axis.

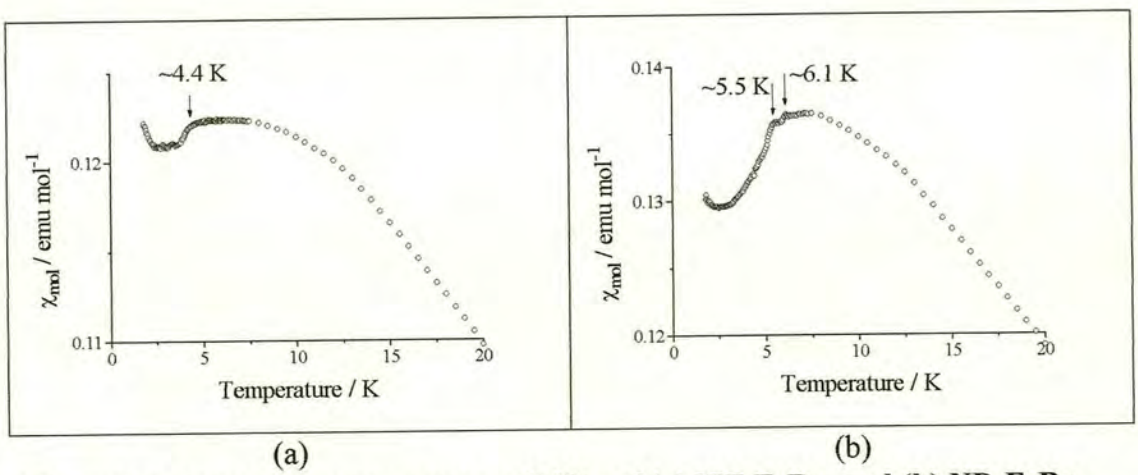

Figure 8.9. Low-temperature susceptibility of (a) NH_4FeBr_3 and (b) ND_4FeBr_3 with the field applied perpendicular to the *c*-axis.

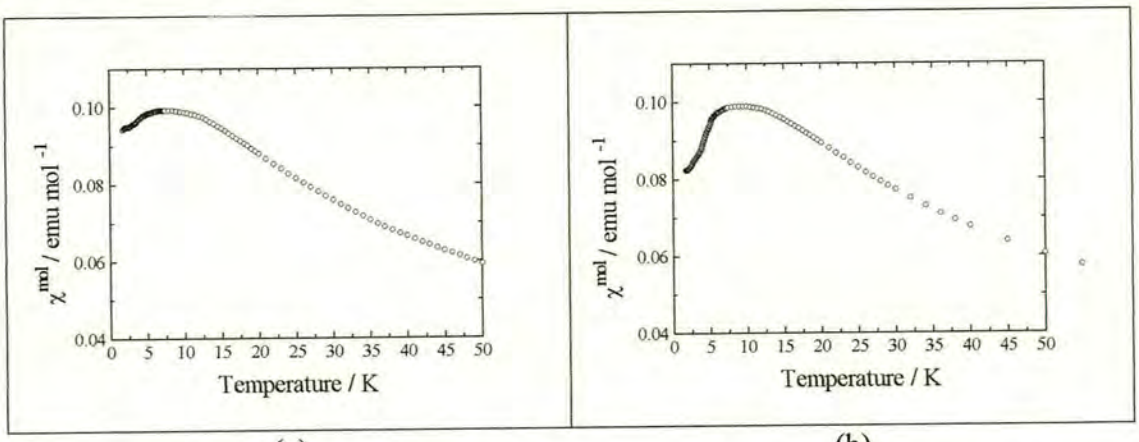

Figure 8.10. The suceptibilities of powder samples of (a) NH_4FeBr_3 and (b) ND_4FeBr_3. The apparent differences are probably due to a slight disparity in the degree of grinding of the samples.

Magnetic transitions sometimes appear more distinct when the derivative is taken of the data with respect to either temperature or applied field. The former case is shown in Figure 8.11 for both field orientations for the hydrogenated and the deuterated samples respectively. Unfortunately, there are several regions in the data sets where the temperature was not particularly stable, having made an excursion to a higher temperature and back as the inner helium reservoir ran out and was refilled. These regions are highlighted in Figure 8.11. There appears to be a distinct transition in the parallel susceptibility data of the NH_4FeBr_3 sample in the region of 6.3 K, which ties in well with the transition observed by diffraction (Fig. 7.22). It is harder to see much distinct evidence of an ordering transition at lower temperatures, though in the case of NH_4FeBr_3, it could be imagined from Figure 8.11(a) that there are transitions at one or both of 2.9 and 3.4 K, comparable with the growth of intensity in the powder neutron diffraction pattern at approximately 3.0 K (Figure 7.22).

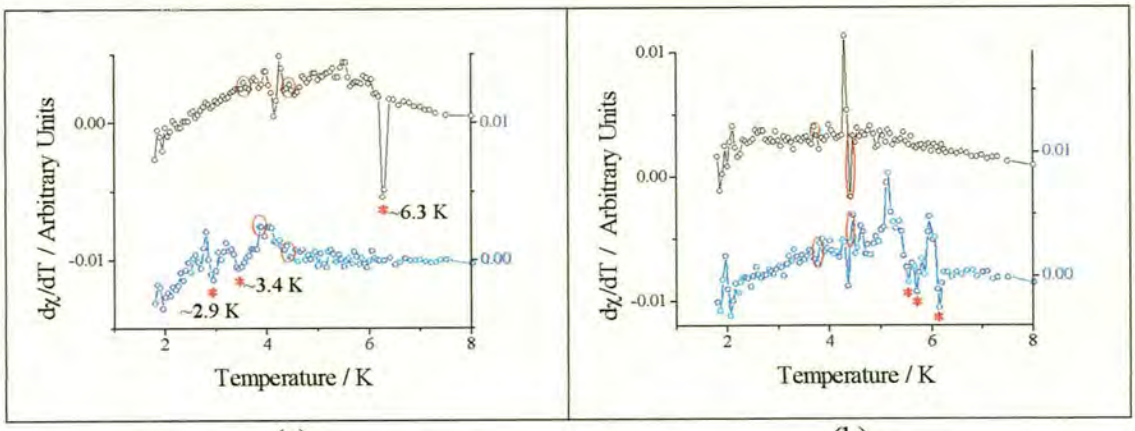

Figure 8.11. The derivative of the susceptibility with respect to temperature for data collected on a sample of (a) NH_4FeBr_3 and (b) ND_4FeBr_3 oriented parallel (black) and perpendicular (blue) to the applied field of 0.1 T. Regions where the temperature was unstable are circled in red. Regions where a magnetic transition may occur are highlighted with red asterisks.

8.4. Modelling the temperature-dependent susceptibility

8.4.1. Curie-Weiss treatment

At high temperatures the magnetic behaviour may be modelled successfully using the Curie Weiss equation, deviating from this behaviour below about 150 K; this was apparent in Figure 8.1 as the inverse susceptibility of a needle sample of NX_4FeCl_3, oriented perpendicular to the applied field deviated from linearity at about this temperature. Susceptibility data collected on powder and oriented single crystal samples of NH_4FeCl_3 and NH_4FeBr_3 and their deuterated analogues taken between 150 and 290 K were fitted using the Curie-Weiss expression, and optimised values for g and θ are given in Table 8.5, and a typical fit is shown in Figure 8.12. Values of g were calculated assuming that $S = 1$. The susceptibility was corrected for the diamagnetic response of the constituent atoms in each sample and a background

parameter was included to account for the temperature independent paramagnetism (TIP) that may arise from the mixing of electronic states into the ground state; this is known to attribute up to 25% to the susceptibility in these materials, but without detailed spectroscopic data it was not possible to calculate this with any confidence.

Table 8.5. Magnetic parameters derived from susceptibility data for powder and oriented single crystal samples of ammonium iron halides using the Curie-Weiss Equation

Sample	Type	g	θ/K
NH_4FeCl_3	powder	4.54(2)	2.3(4)
NH_4FeCl_3	$\perp$	4.15(5)	8.8(10)
NH_4FeCl_3	//	4.52(10)	-21.9(24)
ND_4FeCl_3	powder	4.51(4)	3.7(9)
ND_4FeCl_3	$\perp$	4.76(5)	5.7(10)
ND_4FeCl_3	//	4.69(7)	-12.2(16)
NH_4FeBr_3	powder	4.80(4)	-39.6(10)
NH_4FeBr_3	$\perp$	5.41(16)	-43.6(36)
NH_4FeBr_3	//	5.72(25)	-103.3(69)
ND_4FeBr_3	powder	4.88(4)	-41.6(11)
ND_4FeBr_3	$\perp$	4.06(21)	-66.0(72)
ND_4FeBr_3	//	5.03(44)	-191.0(176)

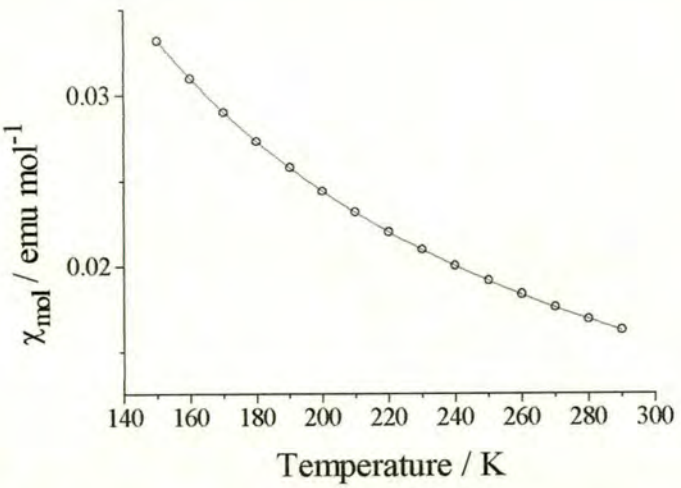

Figure 8.12. Example of a fit of the Curie-Weiss expression to the susceptibility of a powder sample of NH_4FeCl_3 over the temperature range 150-290K.

8.4.1.1. Fitting Using the MFA Anisotropic Single Ion Susceptibility Model

The data were fitted to a model in which the single-ion anisotropy was taken into account, as discussed in section 2.2; it is expected that this expression will not fit the data well close to and below the long-range ordering temperature, and also that it will not provide a good approximation to our data at and above temperatures where the population of the $J = 2$ state becomes appreciable. First the expression that does not incorporate short-range magnetic correlations was employed – this is essentially a molecular field approximation (MFA) plus the effect of the ligand field: expression 2.24 (with q, ω and α set equal to zero, also the susceptibility calculated using this expression must be multiplied by a factor of $N_A g^2/k_B$ to convert to molar susceptiblity) was least-squared fitted to the data taken between 6 and 80 K using MicroCal Origin (Version 5.0). It was possible to fit the parallel and perpendicular data simultaneously and link the optimised parameters in the fitting routine – for instance to set the value of the single-ion anisotropy D to be the same in each case. The results of these fits

are displayed for the chlorides in Figure 8.13 and optimised parameters in Table 8.6. It can be seen that there are significant deviations between fit and data; it also proved very difficult to keep the value of the exchange constant stable in the fit and there are significant uncertainties associated with these parameters.

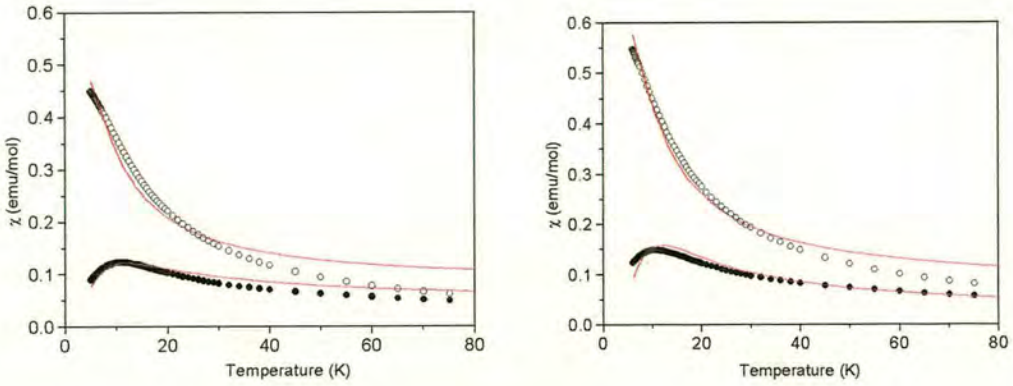

(a) (b)

Figure 8.13. Least-squares fit of the MFA model with single-ion anisotropy to data for (a) NH_4FeCl_3 and (b) ND_4FeCl_3

Table 8.6. Optimised values for magnetic parameters for NH_4FeCl_3 and ND_4FeCl_3 obtained from a least-squares fit of the MFA model to magnetic susceptibility data.

	NH_4FeCl_3	ND_4FeCl_3
D (K)	18.0(1)	17.6(5)
$J^{\perp}$ *(K)*	2.10(110)	2.17(22)
$J^{//}$ *(K)*	1.05(40)	0.62(20)
$g^{\perp}$	2.64(10)	2.63(10)
$g^{//}$	3.16(127)	3.23(74)

Optimised fits for the bromides and corresponding tables of parameters are reproduced in Figure 8.14 and Table 8.7 respectively.

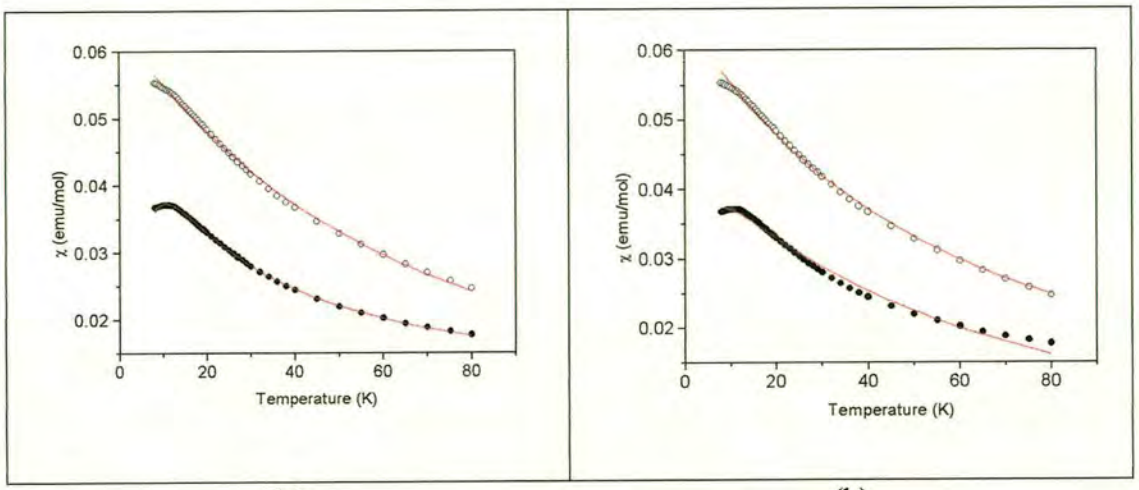

Figure 8.14. Least-squares fit of the MFA model with single-ion anisotropy to data for (a) NH_4FeBr_3 and (b) ND_4FeBr_3

Table 8.7. Optimised values for magnetic parameters for NH_4FeBr_3 and ND_4FeBr_3 obtained from a least-squares fit of the MFA model to magnetic susceptibility data.

	NH_4FeBr_3	ND_4FeBr_3
D (K)	6.41(12)	15.26(20)
$J^{\perp}$ (K)	-37(4)	-49(2)
$J^{//}$ (K)	-6.9(12)	-8.2(13)
$g^{\perp}$	3.20(13)	3.10 (12)
$g^{//}$	2.48(12)	2.34(16)

The value for $J^{\perp}$ for the bromide appears extremely high, both in comparison to $J^{//}$ for the bromide, and exchange parameters for the chloride. Attempts to fit $\chi^{\perp}$ for the

bromides with smaller values of $J^{\perp}$ yielded much higher values of $\chi^{\perp}$ than were observed. This discrepancy may be due to our neglect of the antiferromagnetic *inter*chain exchange, which will suppress $\chi^{\perp}$.

8.4.1.2. The DCEFA model

The effect of magnetic correlations was taken into account using the DCEFA model, noting that the limitations of the uncorrelated model with regard to the valid temperature range will also apply. Initial estimates for the parameters D and J were taken from the fits to the uncorrelated model and then used to obtain an estimate of the correlation parameter α using Equation 2.24. This was solved numerically with the aid of a program which divided the sum over the cell in Equation 2.20 into a box of side N, where N was typically 10, and then evaluated both sides of the expression using a set of values for D, J and α, α was then changed slightly and the inequality calculated again. This revealed whether α had been changed in the correct sense, and the process repeated iteratively until a satisfactory convergence was achieved. This refined value for α was then fed into the expression for susceptibility, 2.20, and compared with the data. The whole process was repeated until an optimised set of values for J, D and α were obtained, with α being recalculated at each step of the refinement. This program is reproduced in Appendix C.

The *appearance* of the fit did not differ from those of the previous section in which α was set to 0; however, the values of the optimised parameters did change and these are summarised in Table 8.8 for the chlorides and 8.9 for the bromides.

Table 8.8. Optimised values for magnetic parameters for NH_4FeCl_3 and ND_4FeCl_3 obtained from a least-squares fit of the DCEFA model to magnetic susceptibility data.

	NH_4FeCl_3	ND_4FeCl_3
D (K)	11.6(4)	11.1(3)
$J^{\perp}$ *(K)*	2.20(120)	2.13(21)
$J^{//}$ *(K)*	1.11(32)	0.71(21)
$g^{\perp}$	2.52(23)	2.51(12)
$g^{//}$	3.08(10)	3.23(52)

Table 8.9. Optimised values for magnetic parameters for NH_4FeBr_3 and ND_4FeBr_3 obtained from a least-squares fit of the DCEFA model to magnetic susceptibility data.

	NH_4FeBr_3	ND_4FeBr_3
D (K)	9.91(37)	9.41(40)
$J^{\perp}$*(K)*	-26(3)	-35(4)
$J^{//}$*(K)*	-5.2(11)	-6.1(10)
$g^{\perp}$	3.17(14)	3.21(16)
$g^{//}$	2.24(14)	2.20(18)

Thus, although the inclusion of the single-ion anisotropy, either with or without account taken of nearest-neighbour magnetic correlation, represents a considerable improvement over models which ignore it, there are still appreciable discrepancies between the data and the model. This could be due to inadequacies in the

approximations used to describe the effect of neighbouring correlations (which will be particularly significant close to T_N), or due to the approximations in the description of the electronic ground state and low-lying states that are considered to circumscribe the set of states required to give a full description of the magnetic properties of these materials; this second approximation may be poor at higher temperatures.

8.5. Magnetic (*B*,*T*) phase diagram for NH_4FeCl_3

The dependence of the magnetic phase diagram of hexagonal antiferromagnets as a function of applied magnetic field and temperature has been the subject of considerable theoretical work in recent years as it reveals much about the phase behaviour of frustrated systems [25,90]. The susceptibility of NH_4FeCl_3 was examined as a function of temperature and applied field to see if any phase boundaries could be mapped out. First, susceptibility data were collected for the NH_4FeCl_3 crystal as a function of temperature in different applied fields between 0.1 and 1 T, orientated both perpendicular parallel to the crystal c-axis. Fig. 8.15(a) shows data taken with the field applied perpendicular to the c-axis and normalised by dividing by the applied field. There is an abrupt change in the slope of these curves in the region of 0.2 T and 3 K which is seen more clearly in the derivative of these curves with respect to temperature which is reproduced in Figure 8.15(b).

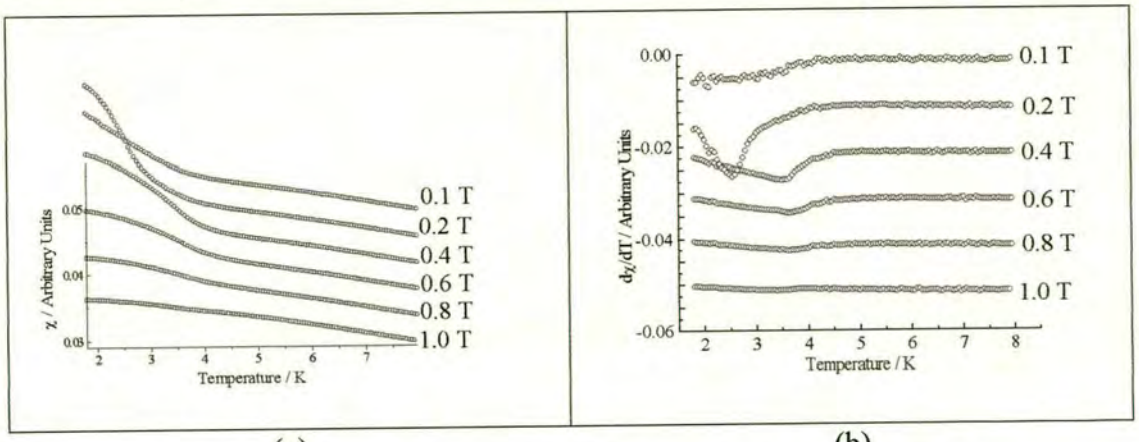

(a) (b)

Figure 8.15. (a) Dependence of magnetisation of NH_4FeCl_3 on temperature in various fields applied perpendicular to the c-axis and (b) Derivative of data shown in (a) with respect to temperature.

Data taken with the field oriented parallel to the c-axis showed no indication of such a transition (Figure 8.16(a)) – indeed between the limits of the measurement (0 – 1 T and above 1.8 K) no evidence for further magnetic transitions could be seen in these data or their derivative with respect to temperature (Fig. 8.16(b))

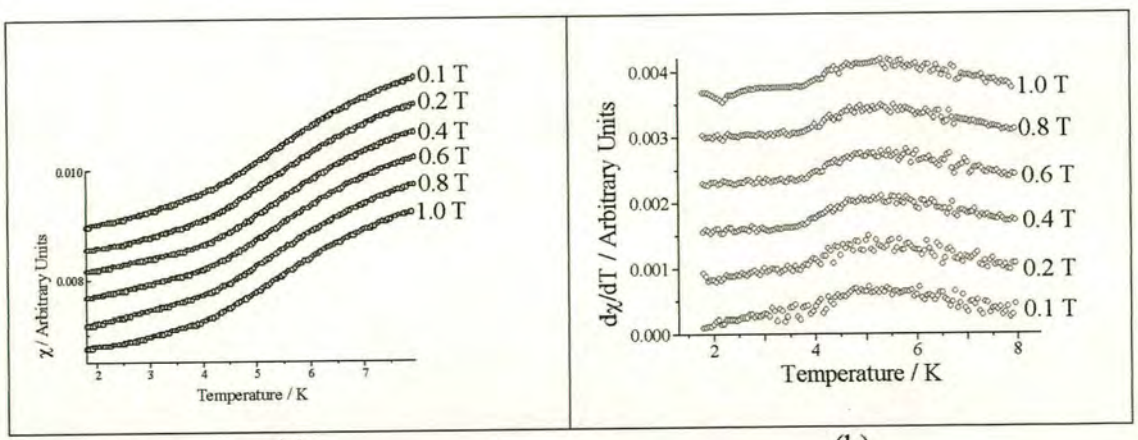

(a) (b)

Figure 8.16. (a) Dependence of magnetisation of NH_4FeCl_3 on temperature in various fields applied parallel to the c-axis and (b) Derivative of data shown in (a) with respect to temperature.

Very similar behaviour is seen for ND_4FeCl_3 though there are slight differences in the precise transition temperature as illustrated for a comparable measurement on the two materials shown in Figure 8.17.

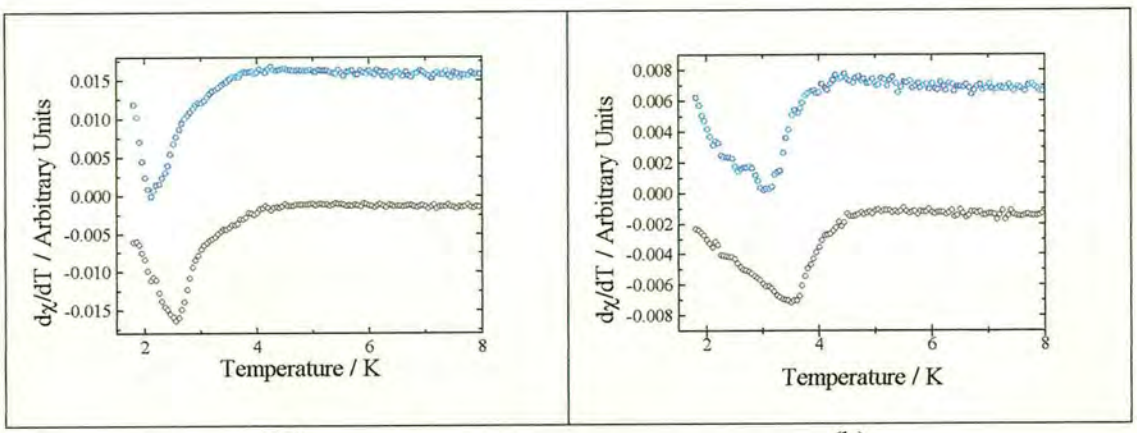

(a) (b)

Figure 8.17. A comparison of the derivative susceptibilities of crystals of NH_4FeCl_3 (black circles) and ND_4FeCl_3 (blue circles) exposes slight differences, the data is considered in a field of (a) 0.2 T and (b) 0.4 T applied perpendicular to the crystal c-axis.

Further measurements were made on the deuterated compound as these may be compared directly with the neutron scattering data. Figure 8.18(a) and (b) show the derivatives of the susceptibility with respect to temperature in various fields applied perpendicular and parallel to the c-axis respectively. The deuterated compound was studied in greater detail in the transition region, using finer steps in applied field (Figure 8.19).

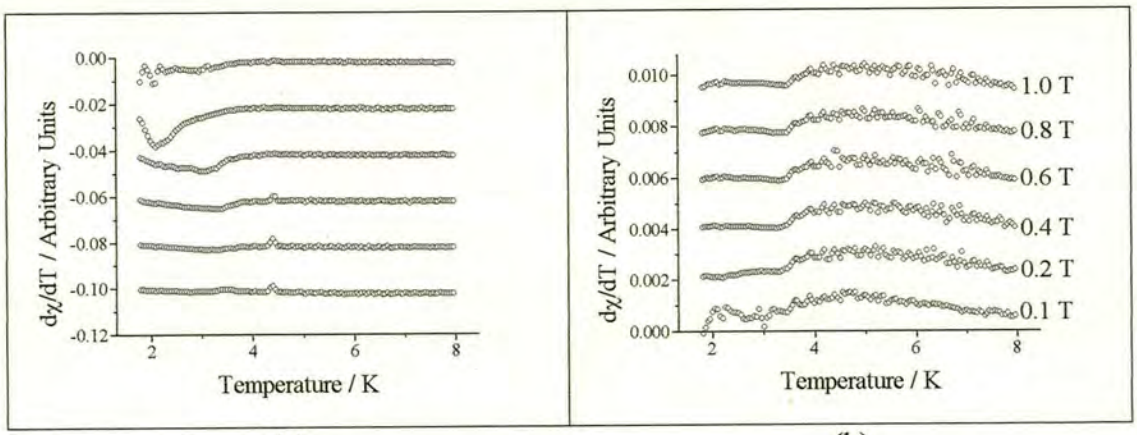

Figure 8.18. Derivatives plots, with respect to temperature, of data collected on a needle sample of ND_4FeCl_3 with a magnetic field applied (a)perpendicular to the c-axis (*cf.* Figure 8.15) and (b) parallel to the c-axis (*cf.* Figure 8.16), note that the scale of the y-axis is left in arbitrary units due to the uncertainty in the mass of the sample.

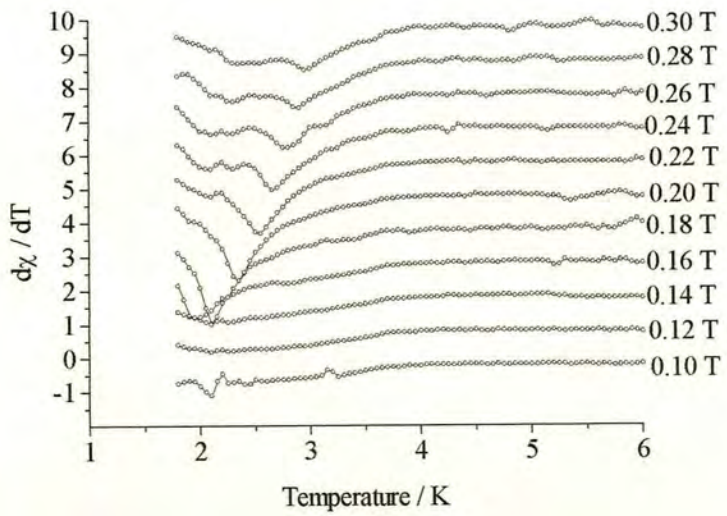

Figure 8.19. Magnetic phase boundaries in ND_4FeCl_3 with a field applied perpendicular to the crystal c-axis as revealed in the derivative of the susceptibility with respect to temperature

The transition region was then scanned in applied field at various set temperatures, and the results are summarised in Figure 8.20, together with the derivative of these data sets with respect to applied field in Figure 8.21.

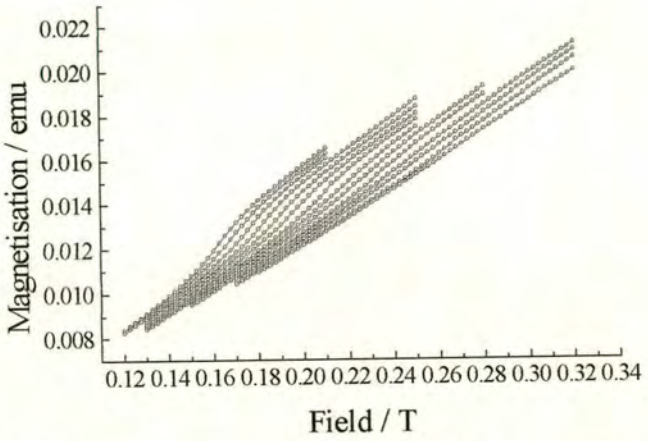

Figure 8.20. Variation of magnetisation with applied magnetic field perpendicular to the *c*-axis of ND_4FeCl_3 as a function of sample temperature. Data taken in 0.1 K steps from 1.8 K (top) to 3.1 K (bottom).

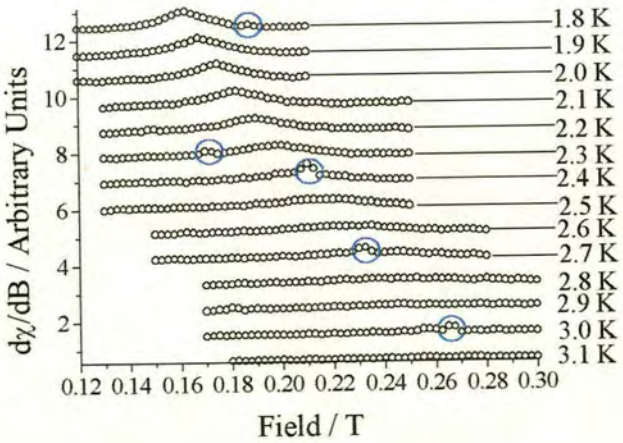

Figure 8.21 Derivatives with respect to field of data sets of Figure 8.20

Although the derivative scans highlight the transition more clearly, they also amplify artefacts such as the discontinuity that arises when the SQUID magnetometer makes

an excursion in temperature beyond the limits within which it was programmed. This is a common occurrence as the temperature rises through the boiling point of helium and overshoots.

Taking all the data measured as a function of temperature and field together results in a (B,T) phase diagram for ND_4FeCl_3 measured perpendicular to the crystal c-axis which is reproduced in Figure 8.22. This may be compared with the phase diagram for $RbFeCl_3$, which is reproduced schematically in Figure 8.23 [147] and also with the results of our neutron scattering measurements. It appears that ND_4FeCl_3 displays an incommensurate magnetic structure below $T_N = 3.7(2)$ K, significantly higher than that for $RbFeCl_3$. Furthermore, in low applied magnetic field there is no indication of further magnetic transitions down to 1.8 K, so the range of stability of the incommensurate phase is much broader in the ammonium salt. The structures and therefore the dipolar interactions of the rubidium and ammonium salts are comparable, so this influence on the stability of incommensurate structures will be comparable; however, a reliable comparison also requires a knowledge of the interchain exchange J', and it is not possible to extract comparative values of this parameter from the susceptibility data, nor to infer it from structural differences, and a proper treatment requires a determination of the spin-wave dispersion from inelastic neutron scattering measurements. However, our observations are compatible with the suggestion that the form of structural distortion observed at low temperatures in the ammonium salt may stabilise an incommensurate magnetic phase.

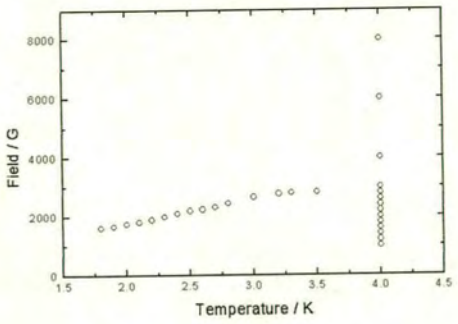

Figure 8.22. (*B*,*T*) magnetic phase diagram for ND_4FeCl_3 with the field applied perpendicular to the crystal *c*-axis.

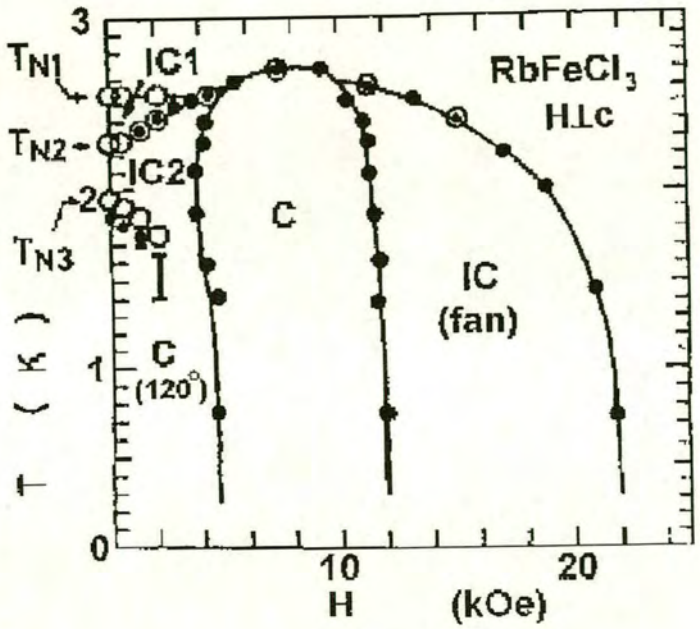

Figure 8.23. Schematic (*B*,*T*) phase diagram for $RbFeCl_3$ with the field applied perpendicular to the crystal *c*-axis, displaying boundaries between commensurate (C), incommensurate (IC_1, IC_2) and canted commensurate (C') or incommensurate (IC') phases [147].

In the past few years the co-operative behaviour of frustrated antiferromagnets has been given a new twist through the introduction of lattice distortions which reduce the symmetry of the exchange interactions and lead to modified triangular antiferromagnetic arrays [25,76,90,156]. Some of the inspiration for the theoretical work was provided by the growth of interest in layered frustrated antiferromagnets in relation to understanding the properties of high-T_c superconductors; this was reinforced by experimental work demonstrating that distorted ABX_3 hexagonal perovskites could be used to provide experimental models to test the theory. Thus, the so-called 'row model', illustrated in Figure 8.24(a) [85, 157], was inspired by work on $RbMnBr_3$, though a better basis to test this model experimentally is probably the anhydrous alum $KTi(SO_4)_2$ [92]. The 'centred honeycomb' model was prompted by the observation of the structural distortion in $RbFeBr_3$ from an a x a x c primitive cell of space group $P6_3/mmc$ to an $a\sqrt{3}$ x a $\sqrt{3}$ x c cell of space group $P6_3cm$ through movement of 1/3 of the magnetic chains along the c-axis relative to the others [158,159] and this led to the exchange geometry outlined in Figure 8.24(b) [85,89]. Finally, the 'staggered row' model, [160], illustrated in Figure 8.24(c) been modelled and shown to have a rich variety of magnetic phases depending on the relative values of the different nearest-neighbour in-plane exchange constants [89].

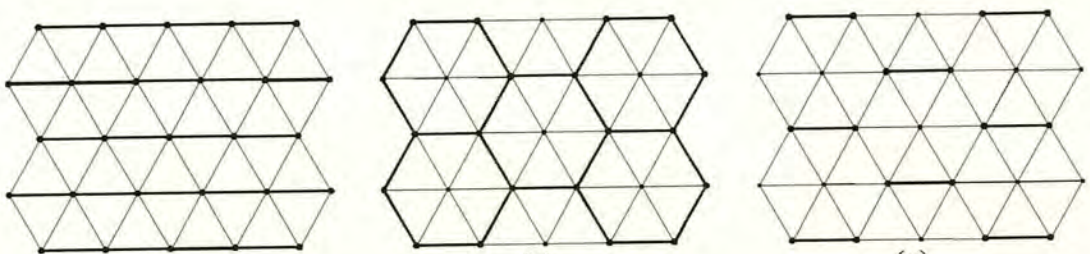

Figure 8.24. Distorted triangular lattices with inequivalent nearest-neighbour in-plane exchange J_1, J_2. The thickness of the bonds joining lattice points merely denotes inequivalence, and models exist in which thick lines may represent either stronger or weaker exchange: (a) is the 'row model', (b) the 'centred honeycomb' model and (c) the 'staggered row' model.

The co-operative behaviour of these modified triangular or hexagonal lattices has been calculated by various techniques to produce rich magnetic phase diagrams, generally expressed as a function of T and the ratio of the in-plane exchange constants - though also as a function of B and T for given values of exchange interactions.

The exchange geometry in ND_4FeCl_3 that arises from the structural distortion may be represented in the same fashion in Fig. 8.25(a). The structural distortion that moves ¼ of the $FeCl_3$ chains along the c-axis relative to the others produces a Kagome lattice of ¾ of the chains, and an expanded triangular lattice of the remaining ¼. We are not aware of a suitable theoretical model to treat the co-operative magnetic behaviour of such a lattice. Likewise, the structural distortion that produces the lowest temperature structure of ND_4FeBr_3 is also to produce a different lattice from those displayed in Figures 8.24(a)-(c). There is greater uncertainty about the geometry of the exchange lattice in this second case. Our various diffraction measurements suggest that the lowest temperature structure of ND_4FeBr_3 is derived from a $\sqrt{3}a$ x $\sqrt{3}a$ x c cell of space group $P6_3$, and that it is most likely to have an orthorhombic cell of dimensions ah x na x c, where n is likely to be greater than or equal to 2, and h is close to $\sqrt{3}$ (in the case that $h = \sqrt{3}$, the cell is hexagonal). Auto-indexing this cell gave a value of $h = 1.7025$ (*c.f* $\sqrt{3} = 1.7321\ldots$) for the orthorhombic multiplier. Thus, if Figure 8.24(b) is taken as a starting point and the effect of the structural distortion is considered, compressing the lattice along the cell edge of length ah, a tentative model for the geometry of the magnetic exchange, depicted in Figure 8.25(b), may be suggested. The more complex distortion leads to four different 'nearest-neighbour' distances which are assigned exchange constants J_1 to J_4 in order of increasing separation, and these are given in the key; it has been assumed

that the positions of the iron atoms along the c-axis is the same as in the $a\sqrt{3}$ x a $\sqrt{3}$ x c cell.

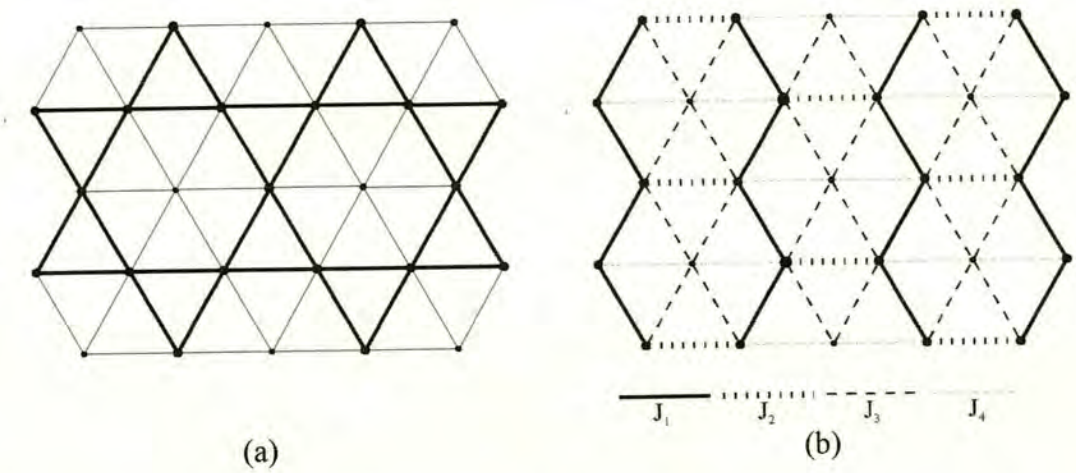

Figure 8.25. Magnetic lattice believed to be found in NH_4FeCl_3 and NH_4FeBr_3. The thick and thin lines in (a) denote stronger and weaker exchange, assigned purely on nearest-neighbour separation of the magnetic ions while in (b) the more complex pattern of exchange pathways is given in the key.

We are not aware of any theoretical model that represents either form of magnetic lattice shown in Figures 8.25(a) and (b) there is little to be gained by speculating in detail about the relation between the proposed lattices and the nature of the magnetic correlations observed in the powder neutron data. However, it is clear that for the chloride the temperature range over which an incommensurate magnetic structure is stable is greater than for the corresponding rubidium salt. In the case of the bromide, the magnetic cell in both low-temperature magnetic phases is commensurate with the nuclear cell along the cell edge of length *ah*, and indeed this edge of the magnetic cell is probably the same size as that of the nuclear cell. It is not possible to say anything definite about the size of the magnetic cell along *b*, other than that it appears to be incommensurate below approximately 3.5 K; incommensurate structures have been

observed in a number of distorted ABX_3 hexagonal perovskites, most notably in $RbMnBr_3$ [161,162,163} and rationalised using the relatively simple models outlined above with appropriate values of J_1 and J_2 [85,89].

8.6. Susceptibility of $Rb_{1-x}Cs_xFeBr_3$

Samples of pure $RbFeBr_3$ and $Rb_{(1-x)}Cs_xFeBr_3$ with x = 0.05 and 0.10 were loaded into gelatine capsules and preliminary measurements of their susceptibility measured both in zero applied magnetic field, and a field of 5 T applied parallel or perpendicular to the crystal c-axis using an Oxford Instruments MagLab VSM (vibrating sample magnetometer) in the Department of Physics at the University of Warwick.. The samples were first cooled to 1.9 K in an applied magnetic field of 5 T and then the field was switched off; the remanent field under these conditions is believed to be 3 mT.

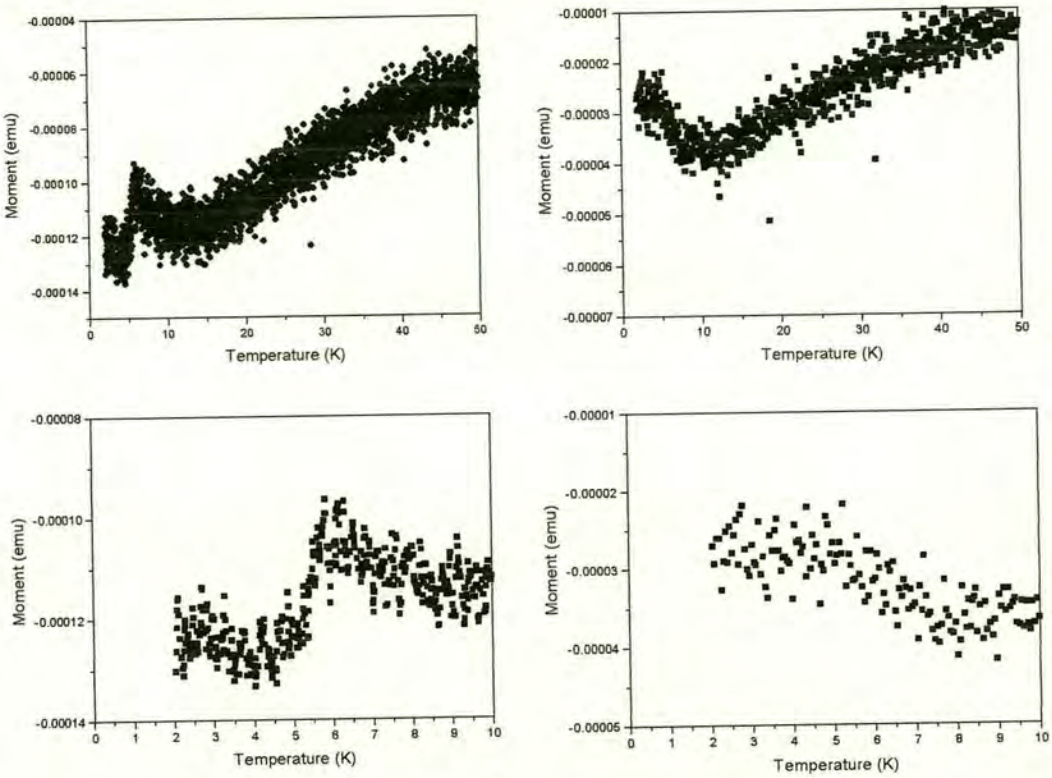

Figure 8.26. The magnetisation of (left) $RbFeBr_3$ and (right) $Rb_{0.9}Cs_{0.1}FeBr_3$ measured parallel to the c-axis in zero applied field.

Figure 8.26 shows the magnetisation of $RbFeBr_3$ and $Rb_{0.9}Cs_{0.1}FeBr_3$ measured parallel to the *c*-axis in zero applied field, revealing a distinct transition near 6.0K, but nothing distinct in the dilute sample. The sample of $Rb_{0.95}Cs_{0.05}FeBr_3$ was exposed to the air in the process of loading the sample and there was no opportunity to repeat measurements on this sample. When a field of 5 T was applied to both samples and the susceptibility measured in either orientation, the transition near 6.0 K could still be observed in the pure sample, but was less distinct in the sample of $Rb_{0.9}Cs_{0.1}FeBr_3$. In Figure 8.27, measurements on $RbFeBr_3$ measured parallel to the crystal *c*-axis also show a transition in region of 3 – 3.5 K, and this together with the transition at 6.0 K are highlighted in the plot of the derivative of the susceptibility with respect to

temperature.

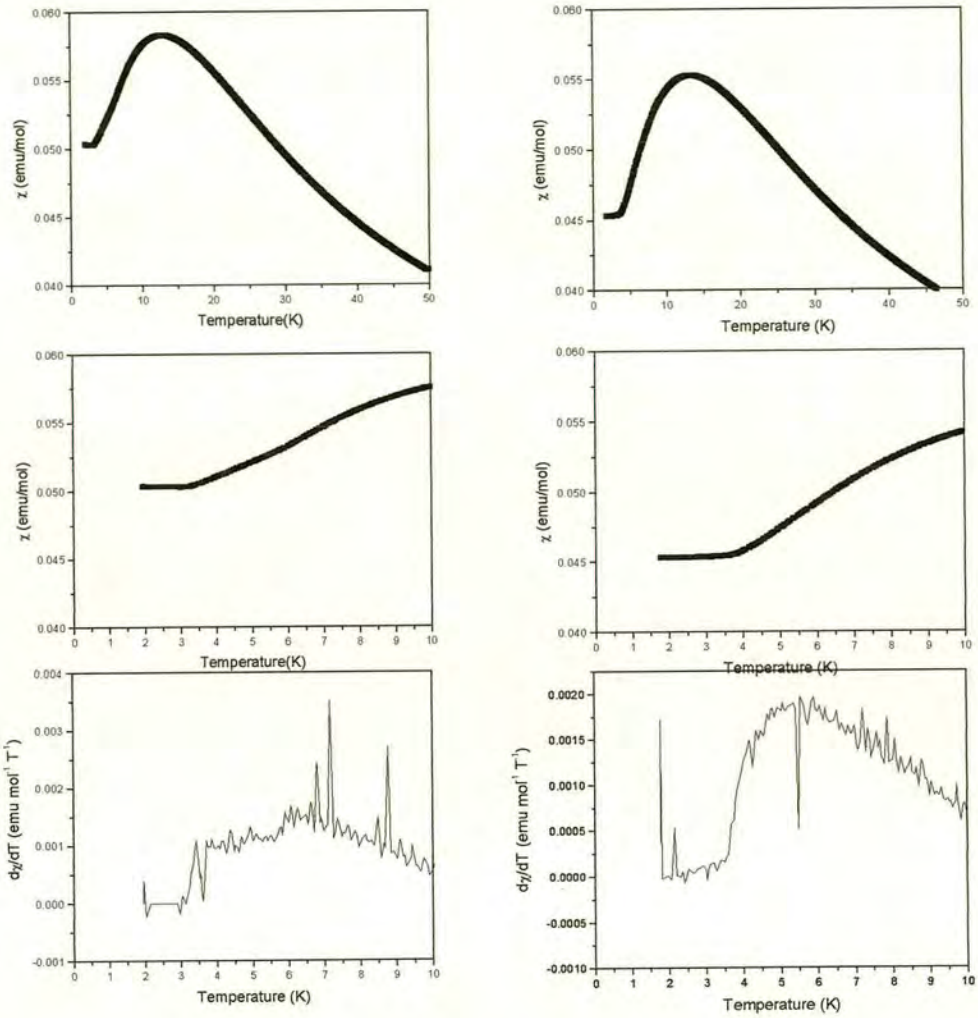

Figure 8.27. The susceptibility of (left) $RbFeBr_3$ and (right) $Rb_{0.9}Cs_{0.1}FeBr_3$ measured parallel to the c-axis in 5T applied field; the lowest plot on both sides is the derivative of the middle plot with respect to temperature.

The same measurements performed on the doped sample show a less abrupt transition – indeed it is really not clear that this sample has a transition corresponding to the 6.0 K transition of the pure compound . In Figure 8.27 the derivative plot for this sample has a feature at approximately 4.5 K that resembles the shape of the transition at

6.0 K in the pure compound, but it would require neutron diffraction measurements or Mössbauer or perhaps ac susceptibility measurements to clarify this; in contrast, there is a distinct transition in the dilute sample at 3.5-4.0 K that resembles very closely the transition at 3 – 3.5 K in $RbFeBr_3$. Thus, it would appear that doping $RbFeBr_3$ with 10% $CsFeBr_3$ destroys long-range magnetic order and this may be restored to some extent by applying a magnetic field.

What is particularly unusual about the dilute compound is that the susceptibility relaxes with time after is cooled in zero field to 1.9 K and then the field of 5 T of applied.

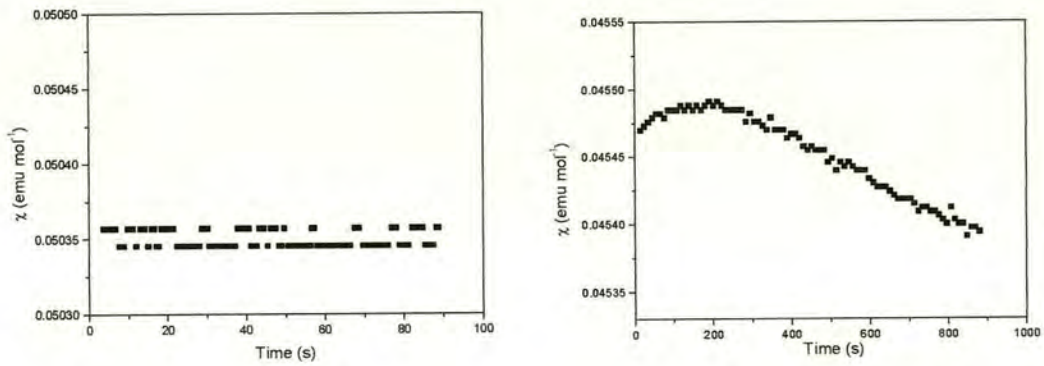

(a) (b)

Figure 8.28. Susceptibility of (a) $RbFeBr_3$ and (b) $Rb_{0.9}Cs_{0.1}FeBr_3$ measured as a function of time parallel to the *c*-axis in 5 T applied field at 1.9 K after cooling to 1.9 K in zero field. The scale of the y-axis is the same for both plots.

Figure 8.28 shows the variation of the susceptibility of both the pure and the 10% doped compound; the response of the former is invariant with time under these conditions, indicating that thermal equilibration has occurred and that there is no relaxation of the magnetisation over this time-scale which is entirely in keeping with the expected behaviour of a homogenous magnet; in contrast there is a modest change

in the susceptibility of the doped compound. Furthermore, this relaxation is not just in the direction of increasing susceptibility, but rather passes through a broad maximum. We are not aware of any precedent for this kind of behaviour and unfortunately were unable to repeat the measurements on this sample to ensure that the data were reliable because this instrument was not available for further measurements. It was, however, possible to attempt to study this phenomenon at the lower applied field of 1 T using the instrument at The University of Edinburgh. Data for the sample of $Rb_{0.9}Cs_{0.1}FeBr_3$ are displayed in Figure 8.29 and 8.30, measuring the relaxation of the magnetisation with time after cooling the sample in no magnetic field to a particular temperature then applying 1 T field parallel to the *c*-axis and measuring the susceptibility in that direction for times up to 7500 s; similar measurements on a sample of $Rb_{0.95}Cs_{0.05}FeBr_3$ are shown in Figure 8.31, while data for an undoped sample of $RbFeBr_3$ revealed no relaxation of magnetisation under similar conditions.

There is a problem with the measurement of the magnetisation below 4.2 K for prolonged periods with this instrument, as illustrated in all of these Figures: the hold-time of the inner reservoir of helium when it is pumped to reduce the temperature is not very long, and decreases as the set temperature decreases. Thus, it is not possible to sustain 1.8 K for very long – indeed any temperature below about 2.5 K could not be held for longer than 2500 s, so these measurements only serve to indicate trends in behaviour.

It is quite clear that in both doped materials there is some relaxation of the magnetisation with time and temperature and that the more heavily doped material is slower to relax at 1.8 K – indeed it only relaxes appreciably after the sample has made an excursion to higher temperatures.

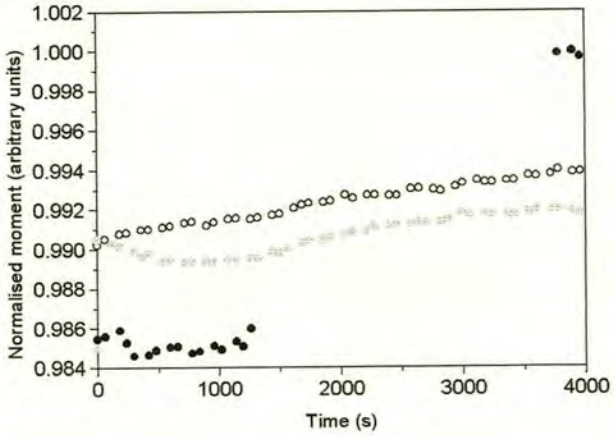

Figure 8.29. Time dependence of the susceptibility of $Rb_{0.9}Cs_{0.1}FeBr_3$ parallel to the crystal c-axis after cooling in zero applied magnetic field then applying 1 T at 1.8 K (filled black circles), 3.0 K (open black circles) and 3.5 K (gray circles). Data have all been normalised to the strongest response observed over the measurement period.

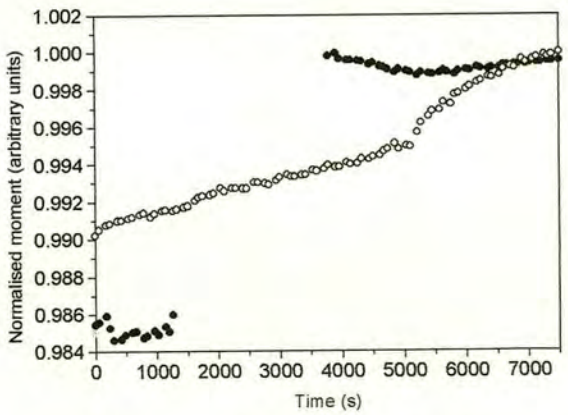

Figure 8.30. Data that were shown in Figure 8.29 taken over a longer time-scale and displaying the time dependence of the susceptibility of $Rb_{0.9}Cs_{0.1}FeBr_3$ at 1.8 K (filled black circles) and 3.0 K (open black circles. Data have all been normalised to the strongest response observed over the measurement period.

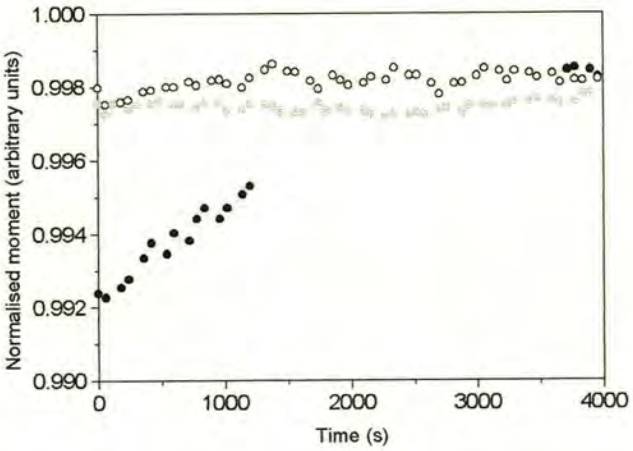

Figure 8.31. Time dependence of the susceptibility of $Rb_{0.95}Cs_{0.05}FeBr_3$ measured parallel to the crystal *c*-axis after cooling in zero applied magnetic field then applying 1T at 1.8 K (filled black circles), 3.0 K (open black circles) and 3.5 K (gray circles). Data have all been normalised to the strongest response observed over the measurement period which occurs at about 7000 s.

Thus, although these measurements essentially only provide a preliminary indication of the behaviour of $Rb_{1-x}Cs_xFeBr_3$ it is clear that this system has great potential as a model for the study of inhomogenous magnets. These measurements indicate that the effect of magnetic dilution may be countered to some extent by the application of a magnetic field, and that the system shows some form of glassy relaxation when cooled in zero field then subjected to an applied field. The temperature scale at which such phenomena may be observed in relatively accessible, requiring only pumped helium apparatus (though preferably apparatus that does not require regular recycling above 4.2 K to maintain at lower temperatures). Thus, $Rb_{1-x}Cs_xFeBr_3$ may represent an advance beyond $Rb_{1-x}Cs_xFeCl_3$ which has been previously studied as a model material of this sort [97]; in that case appreciable relaxation and reversal of the effect of dilution through the application of magnetic fields up to 5 T required temperatures of the order of 1 K.

It is not clear why the relaxation observed in an applied field of 1 T should differ from that in 5 T, as is clear from a comparison of Figures 8.28 and 8.29-8.31; the maximum that the susceptibility passes through at 5 T and 1.9 K could possibly arise from the relaxation of the magnet to produce regions of correlated moments of increasing size, sweeping up uncorrelated moments as they grow, and eventually giving rise to a reduction in the susceptibility. It is conceivable that this effect would be more significant as the applied field increases. It is, however, dangerous to speculate on the basis of a few measurements and further studies, using powder neutron scattering as well as more detailed susceptibility measurements to probe the growth of any regions of correlated moments.

8.7. Conclusions

Variable temperature magnetic susceptibility data taken from samples of NH_4FeCl_3, ND_4FeCl_3, NH_4FeBr_3 and ND_4FeBr_3 reveal similar behaviour that is rationalised well with the DCEFA model, to provide estimates of the intrachain exchange and single-ion anisotropy. Both chlorides have ferromagnetic J, while both bromides have antiferromagnetic J, in keeping with the conclusions of neutron scattering measurements. There is no appreciable difference in the values of J and D for the hydrogenated and deuterated samples, indicating that to a first approximation differences in hydrogen bonding has little influence on the ligand field and intrachain exchange geometry. However, there are measurable differences between hydrogenated and deuterated samples when the long-ordering transitions are studied, indicating that small differences in interchain exchange are introduced.

The mixed singlet-magnetic ground state material $Rb_{1-x}Cs_xFeBr_3$ shows potential as a model system whose magnetic disorder may be continuously tuned through the application of an external magnetic field.

9. Summary and Conclusions

The structure of $N(H/D)_4FeCl_3$ has been determined by X-ray and neutron diffraction in each of three structural phases. The room temperatures hexagonal primitive cell of dimensions *a x a x c* and space group $P6_3/mmc$ distorts on cooling to 181 K to a $P6_3$ cell with approximately the same dimensions, as the $FeCl_3$ chains undergo rotations. On cooling further to 19 K in the hydrogenated material, and 21-22.K in the deuterated material the cell expands to dimensions *2a x 2a x c* due to slippage of $FeCl_3$ chains parallel to the c-axis; the space group of this lowest temperature structural phase refines well in neutron and X-ray data sets but higher resolution synchrotron data suggest that there is a small distortion to a lower symmetry. The *2a x 2a x c* is unprecedented in this class of compound, and produces a new form of distorted hexagonal lattice. Powder neutron data taken at low temperatures reveal a long-range magnetic ordering transition at 3.5K to a structure with ferromagnetic correlations parallel to the crystal *c*-axis, and an incommensurate array within the *ab* plane; this is similar to one of the ordered magnetic phases of $RbFeCl_3$ and has been attributed to a competition between nearest-neighbour antiferromagnetic exchange, and a dipole-dipole interaction, which is significant because the intrachain correlations cause the moments within each chain to act in concert as a giant dipole. There is, however, a difference between the ammonium and rubidium iron chloride in that the region of stability of the incommensurate phase is much broader for the ammonium salt, suggesting that a second factor could stabilise incommensurate in-plane correlations, and this could arise from an imbalance in in-plane exchange in different directions.

The bromide salts also undergo successive phase transitions on cooling. The room temperature P63/mmc a x a x c distorts on cooling through 277K to an expanded cell

of dimensions $\sqrt{3}a$ x $\sqrt{3}a$ x c and space group $P6_3$; this undergoes a further transition on cooling to 80- 100K. The structure of this lowest temperature phase has not yet been determined unambiguously, though there is evidence to suggest an orthorhombic cell of dimensions $\sqrt{3}a$ x na x c. In such a case, a new form of distorted magnetic lattice would be produced, and indeed powder neutron data show successive magnetic long-range ordering transitions at 5 and 2K to a $\sqrt{3}a$ x $3a$ x c magnetic cell, corresponding to antiferromagnetic correlations parallel to the crystal c axis, and new form of a canted magnetic structure in the ab plane.

Further low-temperature X-ray diffraction measurement are required to determine the low-temperature structures of both the chloride and bromide unambiguously, and are planned for the near future on the Fddd diffractometer at Durham. This time a search will be made for specific supercell reflections with the benefit of the results of refinement of the powder diffraction data. Once a firm structural basis has been established, it would be desirable to look at the magnetic structure and phase diagram of the bromide and relate it by suitable modelling to the lattice and hence exchange geometry. The modelling of the susceptibility of these low-dimensional, induced moment magnets is clearly not an ideal way to extract exchange and ligand field parameters. The form of the temperature dependant susceptibility may be fitted to a realtively wide range of values of D and J, these two variables being strongly correlated. A more satisfactory appraoch would be to model the spin-wave dispersion, which provides a far more incisive probe of J and D, and will also give a good estimate of the interchain exchange. This in turn requires suitable, single-crystal samples, which require expertise in Bridgeman growth using suitable, sealed containers.

The incorporation of non-spherical, hydrogen-bonding molecules in the A-cation site of hexagonal perovskites could be developed further by attempting to insert other,

larger or less symmetric groups. Our attempts to put asymmetric amines in this position failed because of their thermal fragility, but it is possible that the tetramethylammonium cation could be placed in this position because it may be incorporated through the action of heat in related lattices.

Preliminary measurements on the mixed singlet-magnetic ground state magnet $Rb_{1-x}Cs_xFeBr_3$ suggest that it may be a suitable model disordered magnet in which the degree of magnetic homogeneity may be tuned continuously with an applied magnetic field. However, magnetic susceptibility is a blunt instrument to probe these properties, and a better method of following the evolution of magnetic correlations would be through neutron scattering as a function of temperature, time and history [93].

10. Bibliography

[1] D. C. Mattis, *The theory of magnetism I. Statics and dynamics;* Springer: Berlin, Vol. 17 (1988)

[2] J.B Porta, Natural Magick (Napes, 1589), reprint of 1st English Edition (Basic Books, New York, 1958)

[3] B. N. Figgis, M. Gerloch, and R. Mason, *Acta Cryst*, **17** 506 (1964)

[4] B. N. Figgis, R. Mason, A. R. P. Smith and G. A. Williams, *Acta Cryst.*, **B36** 509 (1980)

[5] G. A. Williams, B. N. Figgis and F. H. Moore, *Acta Cryst.*, **B36** 2893 (1980)

[6] P. A. Reynolds, B. N. Figgis and A. H. White, *Acta Cryst,* **B37** 508 (1981)

[7] B. N. Figgis and P. A. Reynolds, *Aust. J. Chem.*, **34** 2495 (1981)

[8] F. Mazzi, *Acta Cryst*, **8** 137 (1955)

[9] J. J. Fritz and H. L. Pinch, *J. Am. Chem. Soc.*, **79** 3644 (1957)

[10] J. C. Eisenstein, *J. Chem. Phys.*, **28** 323 (1958)

[11] T. Watanabe and T. Haseda, *Chem. Phys.*, **29** 1429 (1958)

[12] T. Haseda and A. R. Meidema, *Physica,* **27** 1102 (1961)

[13] L. J. De Jongh, A. C. Botterman, F. R. De Boer, and A. R. Meidema, *J. Appl. Phys.*, **40** 1363 (1969)

[14] F. Barendregt and H. Schenk, *Physica*, **49** 465 (1970)

[15] P. Bloembergen, K. G. Tan, F. H. J. Lefèvre and A. H. M. Bleyendaal, *Proc. Int. Conf. Magn.,* Grenoble *J. Phys.*, **32** suppl. C-1, p.879 (1970)

[16] L. J. De Jongh and W. D. Van Amstel, *Proc. Int. Conf. Magn.*, Grenoble *J. Phys.*, **32** suppl. C-1, p.880 (1970)

[17] H. E. Stanley, *Introduction to Phase Transitions and Critical Phenomena*, Oxford University Press (1971)

[18] R. B. Griffith, *Phys. Rev Lett.* **24** (1970) 1958

[19] R. B. Griffith and J. C. Wheeler, *Phys. Rev A* **2** (1970) 1047

[20] L. P. Kadanoff, (1971) *Proc. 1970 Varenna Summer School on Critical Phenomena* (M. S. Green, Ed.) pp. 100-117. New York: Academic Press

[21] E. Ising, *Z, f. Physik,* **31** 253 (1925)

[22] L. Onsager, *Phys. Rev,* **65** 117 (1944)

[23] L. de Jongh and A. R. Miedema, *Adv. Phys.* **23**,1 (1974)

[24] N. Suziki and M. Shirai, *Physica,* **136B** 364 (1986)

[25] M. F. Collins and O. A. Petrenko, *Can J. Phys.,* **75** 605 (1997)

[26] O. Muller and R. Roy, *Crystal Chemistry of Non-Metallic Materials 4: The Major Ternary Structural Familes,* Springer Verlag (1974)

[27] S. Jin, T. H. Tiefel, M. McCormack, R. A. Fastnacht, R. Ramesh and L. H. Chen, Science, **264** 413 (1994)

[28] M. Glazer, *Acta Cryst.*, B **28** 3384 (1972)

[29] J. M. Longo and J. A. Kafalas, *J. Solid State Chem.,* **1** 103 (1969)

[30] H. W. Zandbergen, PhD thesis, university of Leiden (1981)

[31] J. F. Ackerman, G. M. Cole and S. L. Holt, *Inorg. Chim. Acta,* **8** 323 (1974)

[32] R. D. Shannon, *Acta Cryst.* **A32** 751 (1976)

[33] N. Achiwa, *J. Phys. Soc. Japan.*, **27**, 561 (1969)

[34] D. Visser (1996), private comm.

[35] E. Grey and P. W. Smith, *Chem. Comm.*, 1525 (1968)

[36] H. J. Seifert and P. Ehrlich, *Z. anorg. u. allgem. Chem,*. **302** 284 (1959)

[37] J. Garcia, J. Bartolomé, D. Gonzalez, R. Navarro and W. J. Crama, *J. Chem. Thermo.,* **15** 1109 (1983)

[38] W. J. Crama, W. J. A. Maaskant and G. C. Verschoor, *Acta Cryst,* **B34** 1973 (1978)

[39] W. J. Crama, M. Bakker, G. C. Verschoor and W. J. A. Maaskant, *Acta Cryst*, **B35** 1973 (1978)

[40] C. Bellito, G. Dessy, V Fares, D. Fiorani and S. Viticoli, *J. Phys. Chem. Solids*, **45** 1129 (1984)

[41] C. Bellito, V Fares, D. Fiorani and S. Viticoli, *Inorg. Chem.* **24** 1939 (1985)

[42] G. N. Kwawer, R. A. Auerbach, G. L. McPherson, *Chem. Phys.* **121** 299 (1988)

[43] T. I. Li, G. D. Stucky and G. L. McPherson, *Acta Cryst.*, **B29** 330 (1973)

[44] J. D. Tornero, F. H. Cano, J. Fayos and M. Martínez-Ripoll, *Ferroelectrics*, **19** 123 (1978)

[45] P. S. Peercy, B. Morosin and G. A. Samara, *Phys.iRev B* **8** 3378 (1973)

[46] M. N. Braud, M. Couzi, N. B. Chanh, A. Meresse, C. Hauw and A. Gomez-Cuevas, *Ferroelectrics*, **104** 367 (1990)

[47] B. Morosin and E. J. Graeber, *Acta Cryst.*, **23** 766 (1967)

[48] H. J. Seifert and K. Klatyk, *Z. anorg. u. allgem. Chem*,. **342** 1 (1966)

[49] H. T. Witteveen and J. A. R. van Veen, *J. Chem. Phys.* **58** 186 (1973)

[50] A. Harrison and H. Greatorex, unpublished results, 1998.

[51] Engberg and H. Soling, *Acta Chem. Scand*, **21** 168 (1967)

[52] H. Soling, *Acta Chem. Scand.*, **22** 2793 (1968)

[53] J. P. Boucher, L. P. Regnault, J. Rossat-Mignod, Y. Henry, J. Bouillot, W. G. Stirling, *Phys Rev B, Condes Matter* **31** 3015 (1985)

[54] R. W. Asmussen, T. Kindt Larsen and H. Soling, *Acta Chem. Scand.*, **23** 2055 (1969)

[55] G. N. Tischenko, *Tn. Inst. Kristallogr., Akad. Nauk SSSR*, **11** 93 (1955)

[56] G. D. Stucky, *Acta Cryst.*, B **24** 330 (1968)

[57] W. J. Crama, H. W. Zandbergen, *Acta Cryst.*, **B37** 1027 (1981)

[58] R. D. Willett, C. Dwiggins, R. F. Kruh, R. E. Rundle, *J. Chem. Phys.* **38** 2429 (1963)

[59] R. D. Willett, *Transition Metal Chem.*, **12**, 410 (1987)

[60] H. Brasseur, L. Pauling, *J. Am. Chem. Soc.*, **60** 2886 (1938)

[61] G. D. Stucky, S. D. Agostino and J. McPherson, *J. Am. Chem. Soc.*, **88** 4828 (1966)

[62] J. Goodyear and D. J. Kennedy, *Acta Cryst.*, **B28** 1640 (1972)

[63] H. D. Megaw Crystallography, McGraw-Hill New York (1968)

[64] D. Visser and G. McIntyre, (1989), *Physica B*, **156** 259 (1989)

[65] A. Harrison and D. Visser, *Phys. Letters B*, **137** 79 (1989)

[66] T. Mitsui, K. Machida, T. Kato and K. Iio, *J. Phys. Soc. Japan*, **63** 839 (1994)

[67] D. Visser, B. Dorner, U Steigenberger, K. Kakurai, M Steiner, *Zeitschrift fur Physik B Condensed Matter*, **72** 487 (1988)

[68] A. Harrison, C. V. Stager and D. Visser, *J. Appl. Phys.* **69** (8) 5998 (1991)

[69] D. E. Cox, W. Yelon and M. Eibshutz, *Phys. Rev. B*, **12** 5007 (1975)

[70] J. Natarajean and J. Iyer, *J Solid State Chem*, 37, 6969 (1977)

[71] H. D. Hardt and F. Pazan, *Z. Allgem. Anorg. Chem.* **380** 16 (1971)

[72] P. Vanek, *J Solid State Chem*, 50 2001(1990)

[73] H. A. Kramers, *Physica* **1** 182 (1934)

[74] K. P. Sinha and N. Kumar, *Interactions of Magnetically Ordered Solids*, Oxford University Press, Oxford (1980)

[75] P. Ramirez, *Ann. Rev. Mat. Sci.*, **24**, 453 (1994)

[76] H.Kawamura, *J.Appl. Phys.* **61** 3590 (1987)

[77] B. Harris, C. Kallin and A. J. Berlinsky, *Phys. Rev. B*, **45**, 2899 (1992)

[78] J. T. Chalker, P. C. W. Holdsworth and E. F. Shender, *Phys. Rev. Lett.*, **65**, 855 (1992)

[79] A. S. Wills and A. Harrison, *J. Chem. Soc., Faraday Trans.*, **92**, 2161 (1996)

[80] A. S. Wills, A. Harrison, S. A. M. Mentink, T. E. Mason and Z. Tun, *Europhys. Lett. (submitted)*, (1998)

[81] A. S. Wills, PhD Thesis, The University of Edinburgh, (1997)

[82] M. E. Lines and M. Eibschütz, *Phys. Rev. B* **11**, 4583 (1975)

[83] M. Eibschütz, M. E. Lines and R. C. Sherwood, *Phys. Rev. B* **11** 4595 (1975)

[84] H. T. Witteveen and J. A. R. van Veen, *J. Chem. Phys.* **58** 186 (1973)

[85] H. Kawamura, *Prog. Theor. Phys. Suppl.*, **101** 545 (1990)

[86] M. L. Plumer , A. Caille and H. Kawamura, *Phys. Rev. B*, **44** 4461 (1991)

[87] G. Parker, W. M. Saslow and M. Gabay, *Phys. Rev. B*, **45** 11285 (1991)

[88] T. Kato, K. Iio, T. Hoshino, T. Mitsui and H. Tanaka, *J. Phys. Soc. Japan*, **61** 275 (1992)

[89] W. M. Zhang, W. M. Saslow, M. Gabay, M. Benakli, *Phys. Rev. B*, **48** 10204 (1993)

[90] M. L. Plumer, A. Caille, A. Mailhot and H.T. Diep, in '*Magnetic Systems with Competing Interactions*', (World Scientific, Singapore), Ed. H.T. Diep (1994)

[91] H. Tanaka and K. Kakurai, *J.Phys. Soc. Japan*, **63** 3412 (1994)

[92] S. T. Bramwell, S. G. Carling, C. J. Harding, K. D. M. Harris, B. M. Kariuki, L. Nixon and I. P. Parkin, *J.Phys.:Cond.Matt.*, **8** L123 (1996)

[93] A. Harrison, D. Visser, P. Day, W. Knop and M. Steiner, *J. Phys. C: Solid State Phys.*, **19** 6811 (1986)

[94] T. I. Quickenden and R. C. Marshall, *J. Chem. Educ.*, **49** 114 (1972)

[95] J. Crangle and M. Gibbs, *Physics World*, November, 31 (1994)

[96] *Solid State Magnetism*, J. Crangle (Edward Arnold, London, 1996)

[97] J. Clarke, *Sci. Am* **271** 36 (1994)

[98] P. Weiss, *J. Phys. Radium*, Paris **6** 667 (1907)

[99] R. L. Carlin, *Magnetochemistry,* Springer-Verlag (1986)

[100] M. E. Fisher, *J. Math. Phys.* **4** 124 (1963)

[101] M. E. Fisher, *Am. J.Phys.*, 32 343 (1964)

[102] N. Suzuki, *J. Phys. Soc. Japan*, **50** 2931 (1981)

[103] N. Suzuki, *J. Phys. Soc. Japan*, **52** 1002 (1983)

[104] N. Suzuki, *J. Phys. Soc. Japan*, **52** 1009 (1983)

[105] N. Suzuki, T. Isu and K. Motizuki, **23** 319 (1977)

[106] A. Harrison and D. Visser, *J. Phys.: Cond. Matt.*, **4** 6977 (1992)

[107] S. M. Putnik, *J Solid State Chem,* **36** 1011 (1976)

[108] *MPMS2 User Manual*, Quantum Design (Quantum Design, San Diego, 1991)

[109] M. E. Lines, *Phys. Rev B* **9** 3927 (1974)

[110] M. E. Lines, *Phys. Rev B* **11** 1134 (1975)

[111] N. Suzuki, *J. Phys. Soc. Japan*, **45** (6) 1791 (1978)

[112] H. Stout and L. H. Jensen, *X-ray Structure Determination: A practical guide*, 2nd edition, OUP, Oxford, (1985)

[113] P. Glusker, M. Lewis and M. Rossi, *Crystal Structure Analysis for Chemists and Biologists*, 1st Edition, VCH, New York, (1994)

[114] P. Glusker and K. N. Trueblood, *Crystal Structure Analysis – A Primer*, Oxford University Press (1985)

[115] Pictures obtained from htttp://www.esrf.fr.html

[116] S. W. Lovesey, *Theory of Neutron Scattering from Condensed Matter* Vols. **1** and **2**, Clarendon Press, Oxford (1984)

[117] M. F. Collins, *Magnetic Critical Scattering*, OUP, Oxford, (1989)

[118] M. Rietveld, *Acta Cryst.* **22** (1967) 151

[119] R. A. Young, *The Rietveld Method,* Oxford University Press (1993)

[120] H. M. Rietveld, *Acta Cryst.* **20** (1966) 508

[121] H. M. Rietveld, *J. Appl. Cryst.* **2** (1969) 65

[122] G. Caglioti, A. Paoletti and F. P. Ficci, *Nucl. Instrum. Methods*, **35** 223 (1958)

[123] J. Howard, *J. Appl. Cryst.* **15** 615 (1982)

[124] W. Finger, D. E. Cox and A. P. Jephcoat, *J. Appl. Cryst.*, **27** 892 (1994)

[125] W. Finger, *J. Appl. Cryst.*, **31** 111 (1998)

[126] A. Le Bail, H. Duroy and J. L. Fourquet, *Mater. Res. Bull.* **23** 447 (1988)

[127] A web site is dedicated to this problem. http://bragg.ing.unitn.it/sizestrain/

[128] A. Harrison and D. Visser, private communication.

[129] An extensive diffraction analysis software list is maintained at http://www.iucr.ac.uk/ccp14

[130] C. Larson and R. B. von Dreele, *The General Structure Analysis System* (GSAS) (1985)

[131] G. M. Sheldrick, SHELXL93. Program for crystal structure refinement. University of Göttingen, Germany

[132] R. C. B. Copley, A. E. Goeta, C. W. Lehmann, J. C. Cole, D. S. Yufit, J. A. K. Howard and J. M. Archer, *J. Appl. Cryst.* **30** (1997) 413

[133] Smart and Saint area detector control and integration software. Siemens Analytical X-ray Instruments Inc., Madison, Wi., USA;

[134] http://www.esrf.fr/exp/facilities/bl15/handbook/handbook.html

[135] http://www.ill.fr/YellowBook/D2B/main.html

[136] http://www.ill.fr/ YellowBook/D1B/main.html

[137] http://www.isis.rl.ac.uk/punchmanual/irislhtml; (b) C. J. Carlile and M. A. Adams, *Physica B* 182 (1992) 431

[138] J. Rubin, J. Bartolome, A. Magerl, D. Visser, G. J. Kearley and L. A. de Graaf, *Physica B* 156&157 (1989) 353

[139] D. Visser, G. J. McIntyre, W. G. Haije and W. J. A. Maaskant, *Physica B* **156&157** (1989) 254

[140] A. G. Aranda, E. R. Losilla, A. Cabeza and S. Bruque, *J. Appl. Cryst.* **31** 1 16 (1998)

[141] See http://www.iucr.ac.uk/iucr-top/comm/cpd/ for details of Treor 90 and other autoindexing software.

[142] S. A. Spittle, Part II Thesis, University of Oxford (1991)

[143] A.I. Laing, Part II Thesis, University of Oxford (1993)

[144] W. S. Howells, *RAL Technical Report*, RAL-TR-96-006, January (1996)

[145] J. Rubin, J. Bartolome, A. Magerl, D. Visser, G. J. Kearley and L. A. de Graaf, *Physica B* 156&157 (1989) 353

[146] N. Wada, K. Ubukoshi and K. Hirakawa, *J. Phys. Soc, Japan* **51** 9 2833 (1982)

[147] N. Wada, K. Sumiyoshi, T. Watanabe and K. Amaya, *J. Phys. Soc, Japan* **52** 6 1893 (1983)

[148] A. Harrison, D. Visser, P. Day, W. Knop and M. Steiner, *J. Phys. C: Solid State Phys.*, **19** 6811 (1986)

[149] N. G. Parsonage and L. A. K. Staveley, *Disorder in Crystals (The international series of monographs on chemistry)*, Oxford University Press (1978)

[150] W. Press, *Single-Particle Rotations in Molecular Crystals*, Springer Tracts in Modern Physics 92, Springer-Verlag Berlin Heidelberg (1981)

[151] M. Prager, W. press, B. Alefield and A. Huller, *J. Chem. Phys.*, **67** 5126 (1977)

[152] A. Huller and D.M. Kroll, *J.Chem. Phys.*, **63** 4495 (1975)

[153] W. S. Howells, *RAL Technical Report*, RAL-TR-96-006, January (1996)

[154] M. Prager and A. Heidemann, *Chem. Rev.*, **97** 2933 (1997)

[155] Z. W. Hendrikse and W. J. A. Maaskant, *Physica B* **233** 139 (1997)

[156] M.L.Plumer and A.Caille, *J.Appl. Phys.* **70** 5961 (1991)

[157] W. M. Zhang, W. M. Saslow and M. Gabay, *Phys. Rev. B* **44** 5129 (1991)

[158] M. Eibschutz, G. R. Davidson and D. E. Cox, *AIP Conf. Proc.* **18** 386 (1973)

[159] A. Harrison and D.Visser, *J.Phys.: Cond. Mat.* **1** 733 (1989)

[160] G.Parker, W.M. Saslow and M,.Gabay, *Phys. Rev. B* **23** 11285 (1991)

[161] C.J. Glinka, V.J. Minkiewicz, D.E. Cox and C.P. Khattak, *AIP Conf. Proc. On Magnetism and Magnetic Materials* (AIP, New York) 659 (1973)

[162] T.Kato, T.Ishii, Y.Ajiro, T. Asano and S.Kawano, J.*Phys. Soc. Japan* **62** 3384 (1993)

[163] L. Heeller, M. F. Collins, Y. S. Yang and B. Collier, *Phys. Rev. B* **49** 1104 (1994)

Appendix A

NH_4FeCl_3 and ND_4FeCl_3

A.1. Rietveld refinements of data collected on diffractometer BM16 at the ESRF, Grenoble

The Rietveld refinements of the neutron diffraction data collected on diffractometer BM16 at the ESRF, Grenoble on powder samples of NH_4FeCl_3 and ND_4FeCl_3 were carried out using the refinement package GSAS [9]. The fits are shown below.

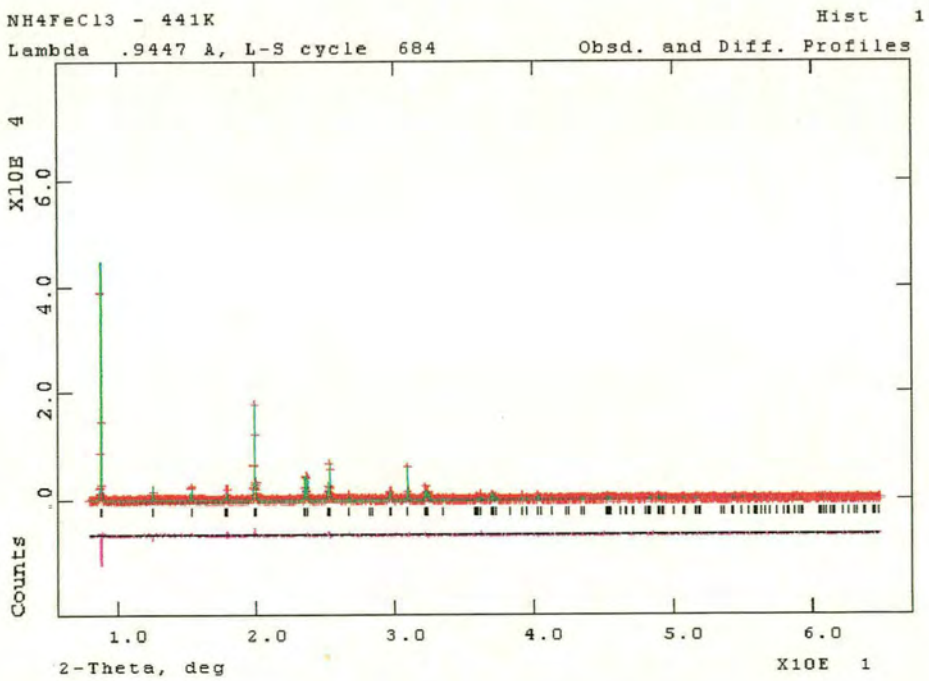

Figure A.1. Rietveld refinement of BM16 data collected on NH_4FeCl_3 at 441 K

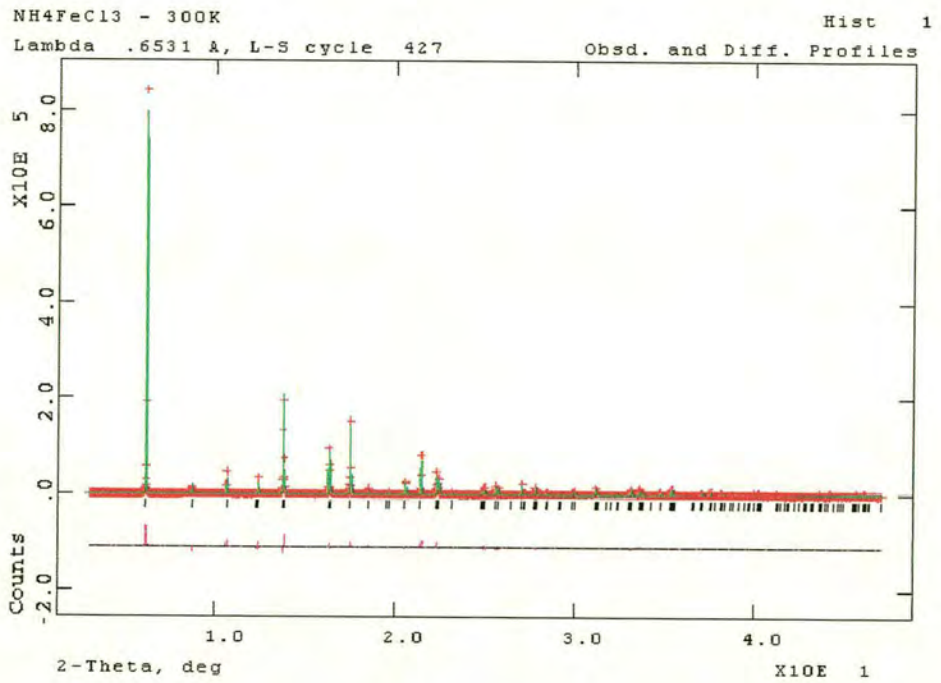

Figure A.2. Rietveld refinement of BM16 data collected on NH_4FeCl_3 at 300 K

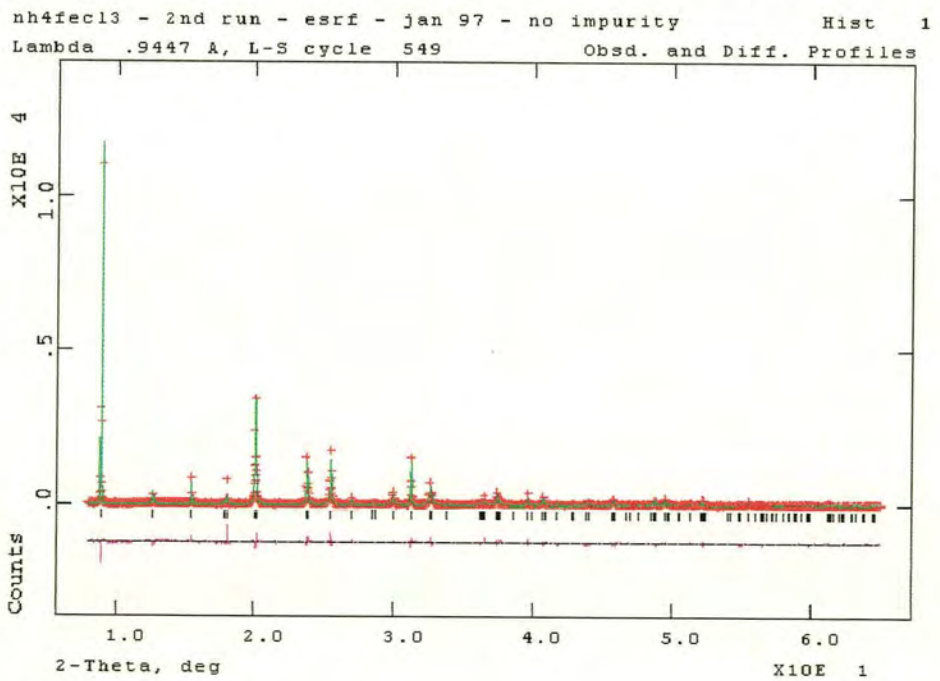

Figure A.3. Rietveld refinement of BM16 data collected on NH_4FeCl_3 at 291 K

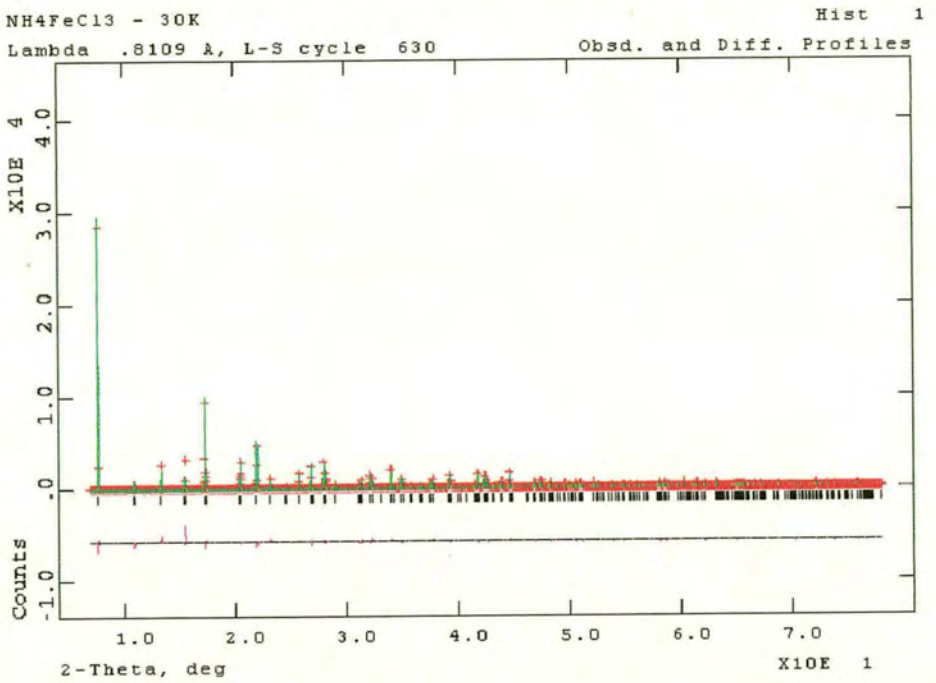

Figure A.4. Rietveld refinement of BM16 data collected on NH_4FeCl_3 at 30 K

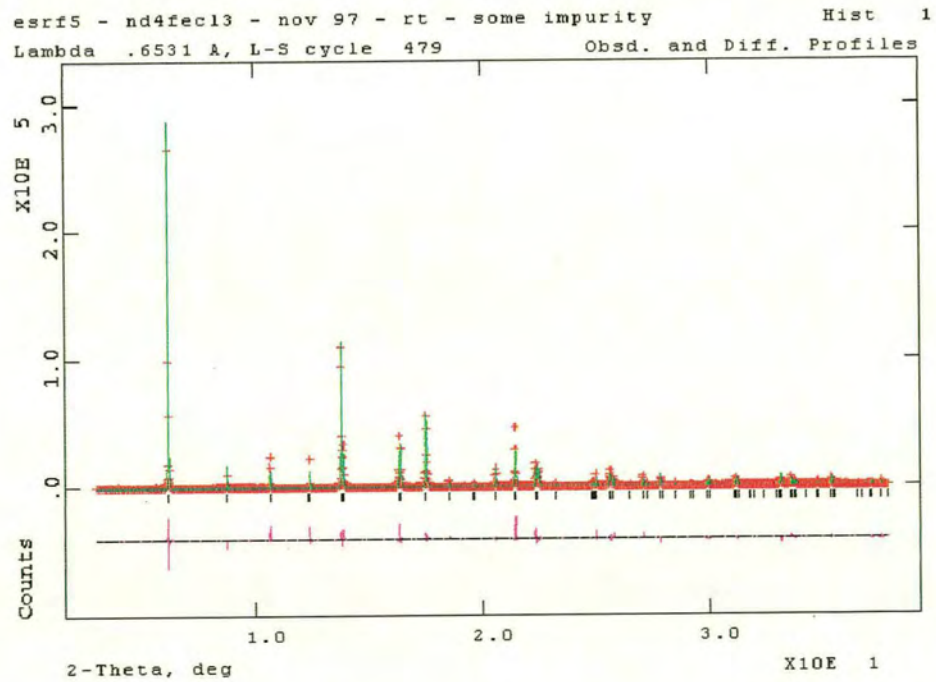

Figure A.5. Rietveld refinement of BM16 data collected on ND_4FeCl_3 at 300 K

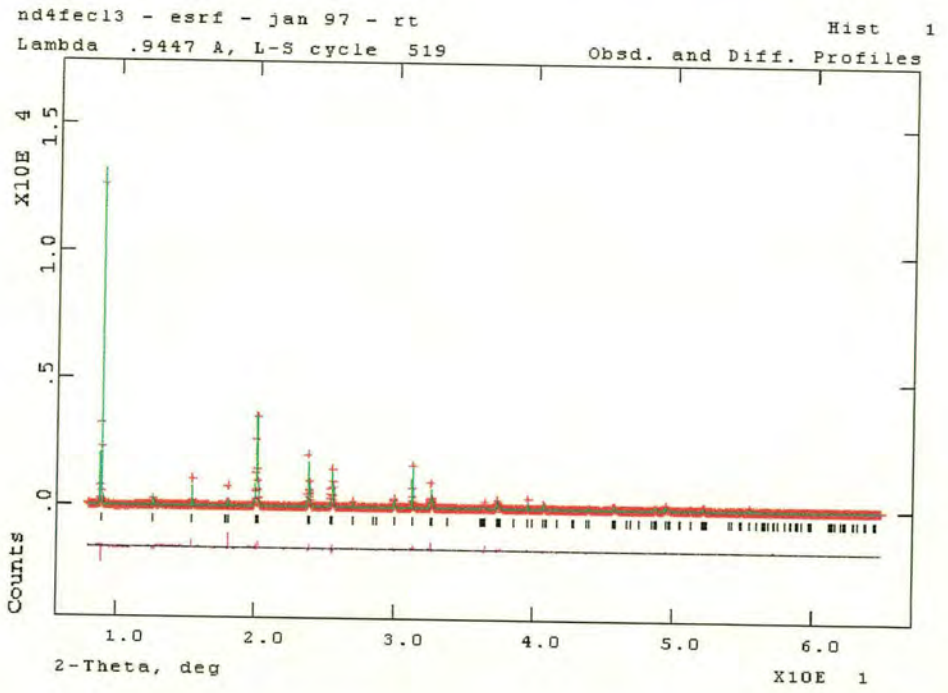

Figure A.6. Rietveld refinement of BM16 data collected on ND_4FeCl_3 at 291 K

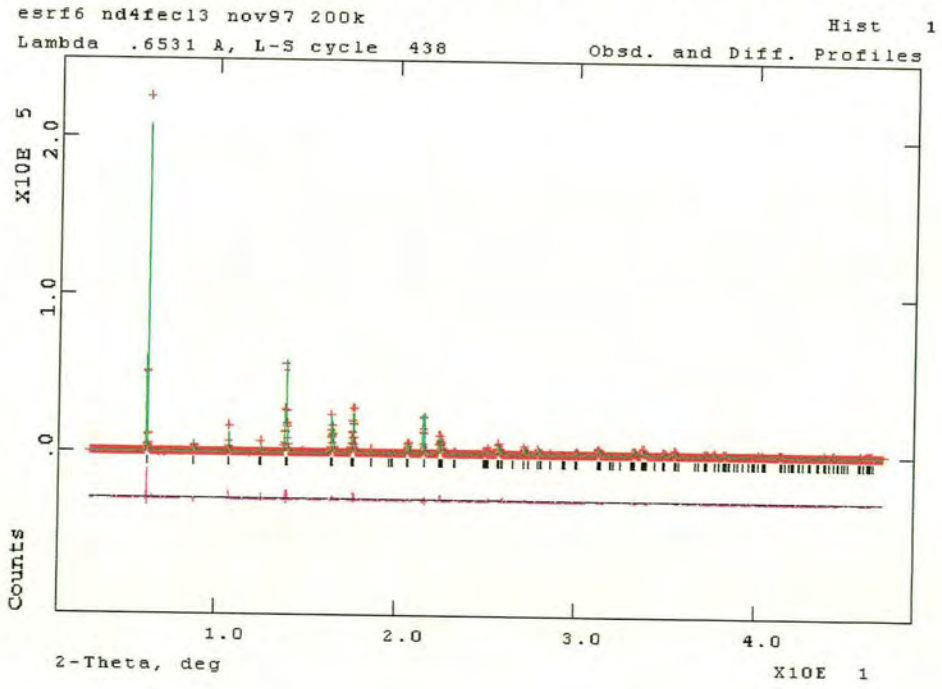

Figure A.7. Rietveld refinement of BM16 data collected on ND_4FeCl_3 at 200 K

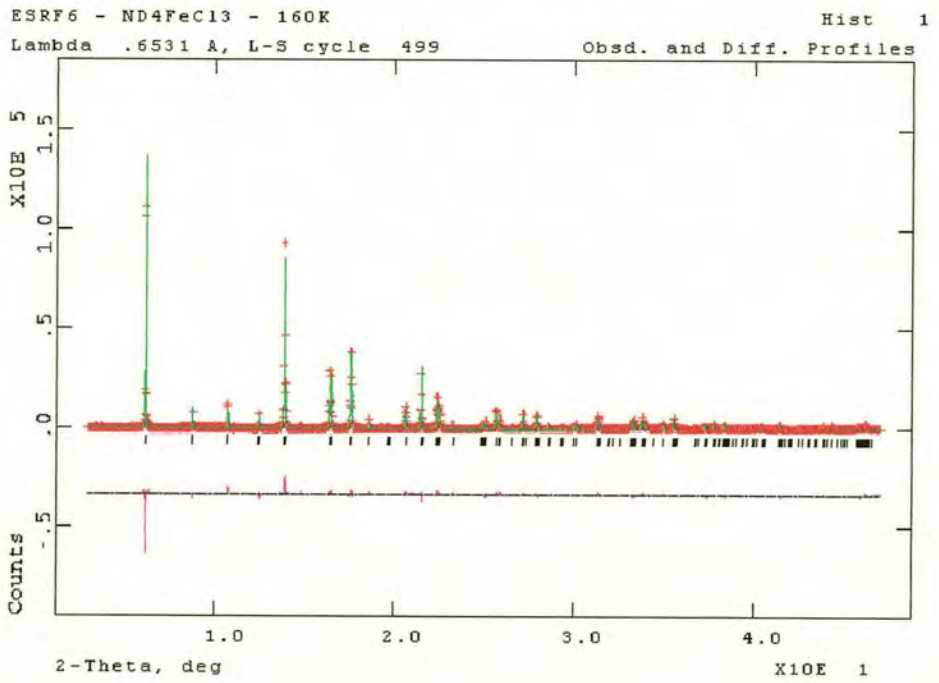

Figure A.8. Rietveld refinement of BM16 data collected on ND_4FeCl_3 at 160 K

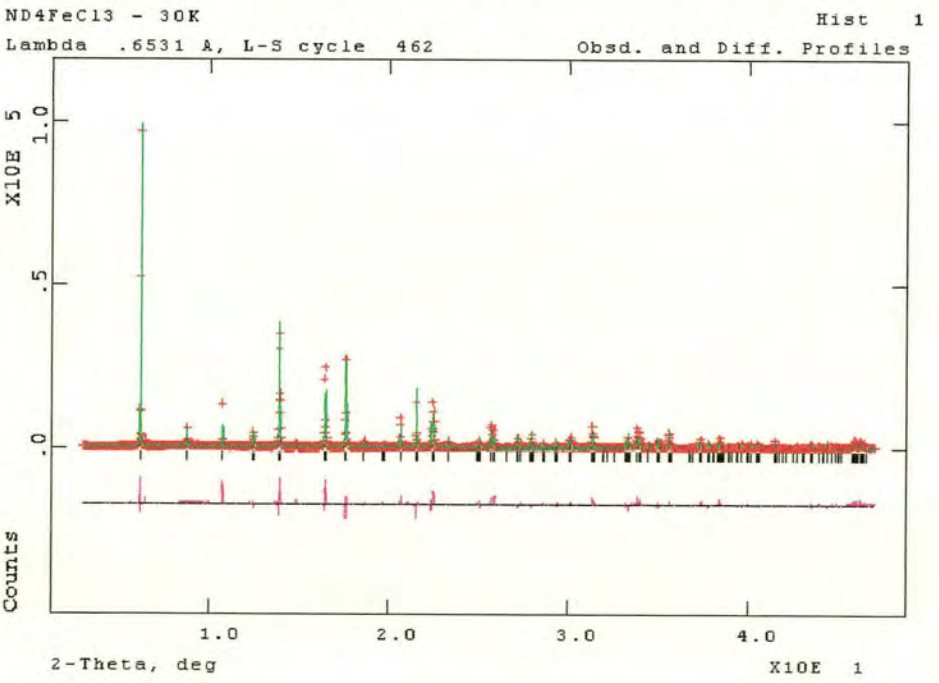

Figure A.9. Rietveld refinement of BM16 data collected on ND_4FeCl_3 at 30 K

Table A.1 The X-ray wavelengths for each data set collected using diffractometer BM16.

Sample	Temperature / K	Wavelength / λ
NH_4FeCl_3	423	0.944680
NH_4FeCl_3	300	0.653133
NH_4FeCl_3	291	0.944680
NH_4FeCl_3	30	0.810855
ND_4FeCl_3	300	0.653133
ND_4FeCl_3	291	0.944680
ND_4FeCl_3	200	0.653133
ND_4FeCl_3	160	0.653133
ND_4FeCl_3	30	0.653133

A.2. Rietveld refinements of data collected on diffractometer D2B at the ILL, Grenoble

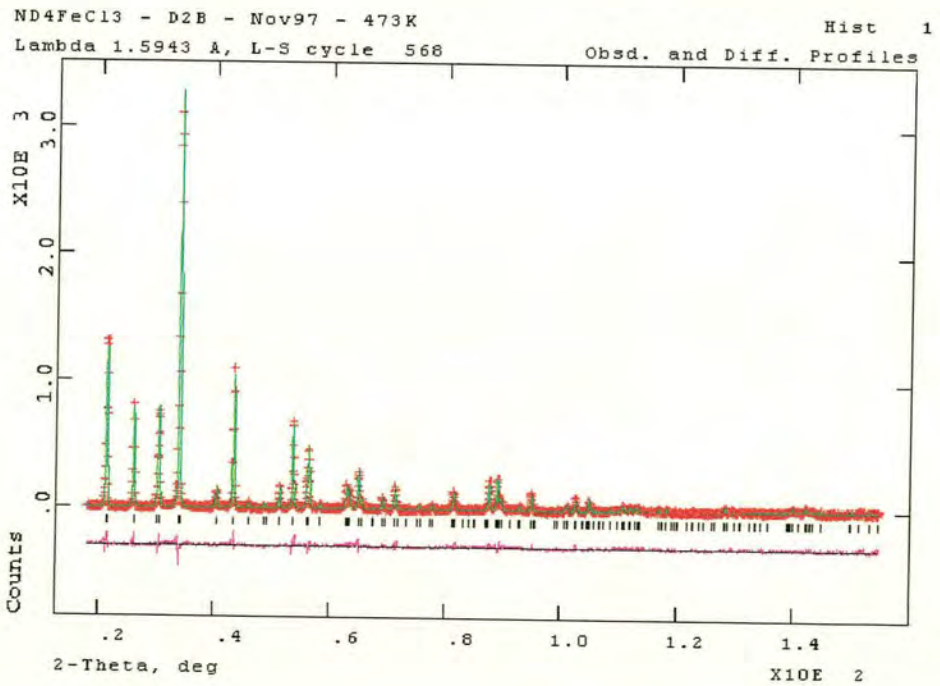

Figure A.10. Rietveld refinement of D2B data collected on ND_4FeCl_3 at 473 K

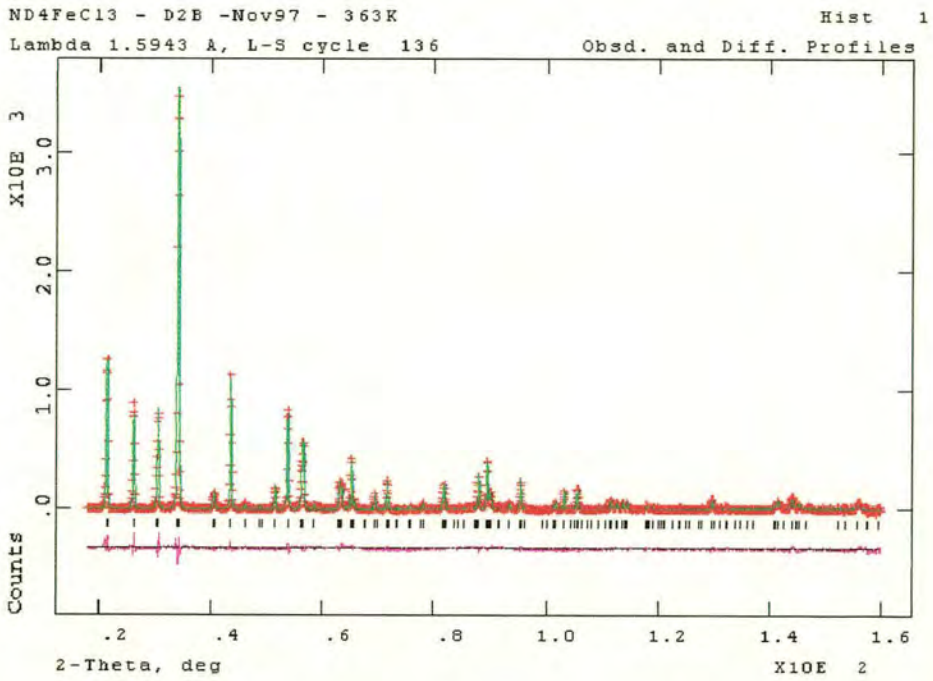

Figure A.11. Rietveld refinement of D2B data collected on ND_4FeCl_3 at 363 K

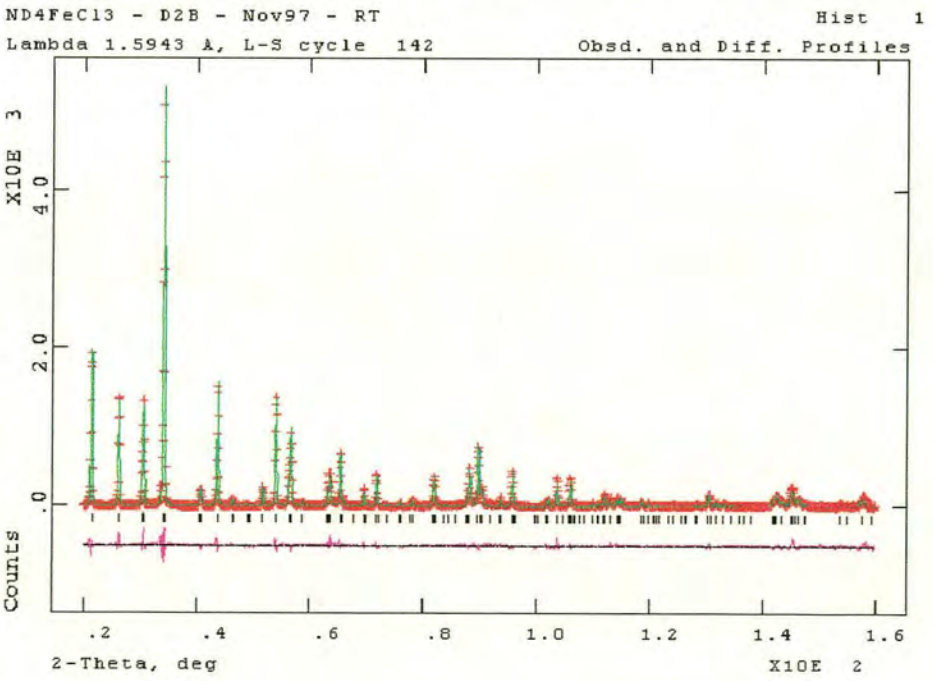

Figure A.12. Rietveld refinement of D2B data collected on ND_4FeCl_3 at 290 K

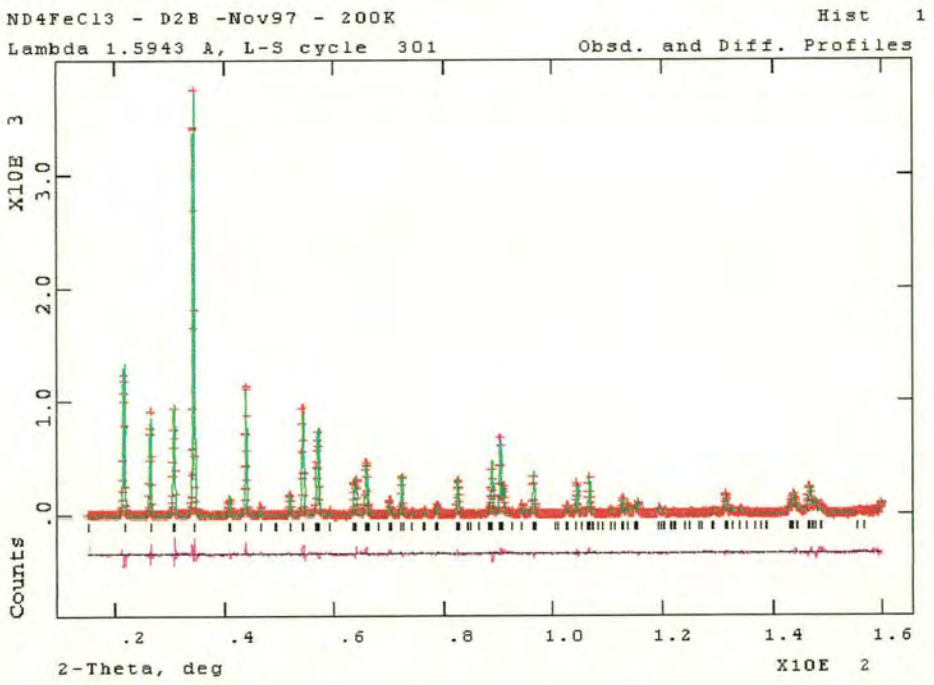

Figure A.13. Rietveld refinement of D2B data collected on ND_4FeCl_3 at 200 K

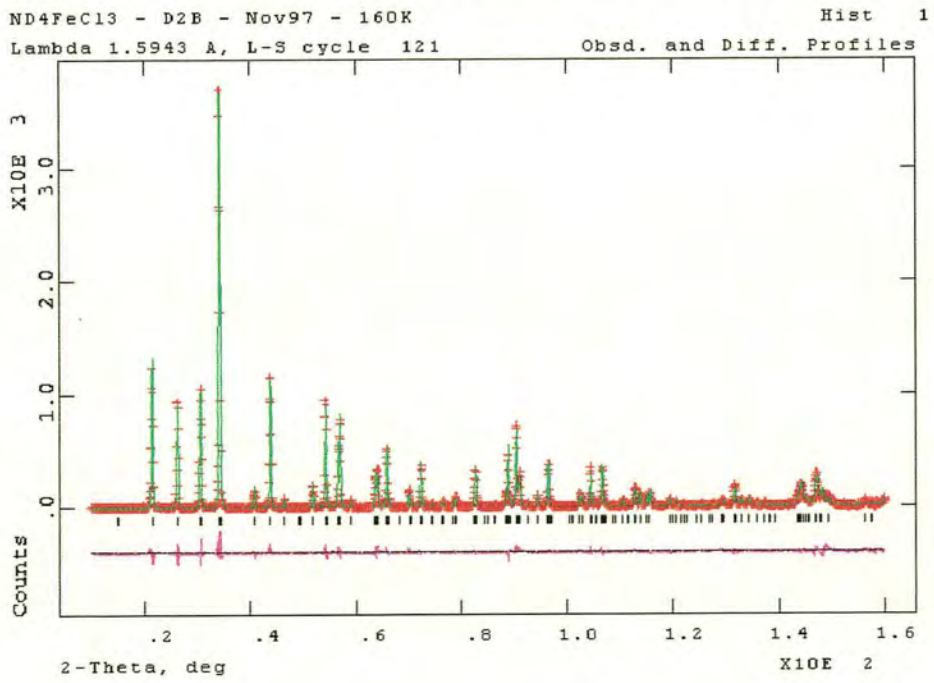

Figure A.14. Rietveld refinement of D2B data collected on ND_4FeCl_3 at 160 K

A.3. Selected bond lengths and angles obtained from Rietveld refinements of powder diffraction data

Figure A.15 illustrates the Cl-Cl distances (x), the Fe-Fe distances (y), Fe-Cl-Fe in chain bond angle (θ), and the intra chain Fe-Cl-Cl angles ϕ^1 and ϕ^2 (where ϕ^2 is not listed it is equal to ϕ^1). Table A.2 lists the values of θ, $\phi 1$, $\phi 2$, x and y obtained in all refinements carried out on data collected for NH_4FeCl_3 and ND_4FeCl_3 on diffractometers BM16 at ESRF and D2B at ILL.

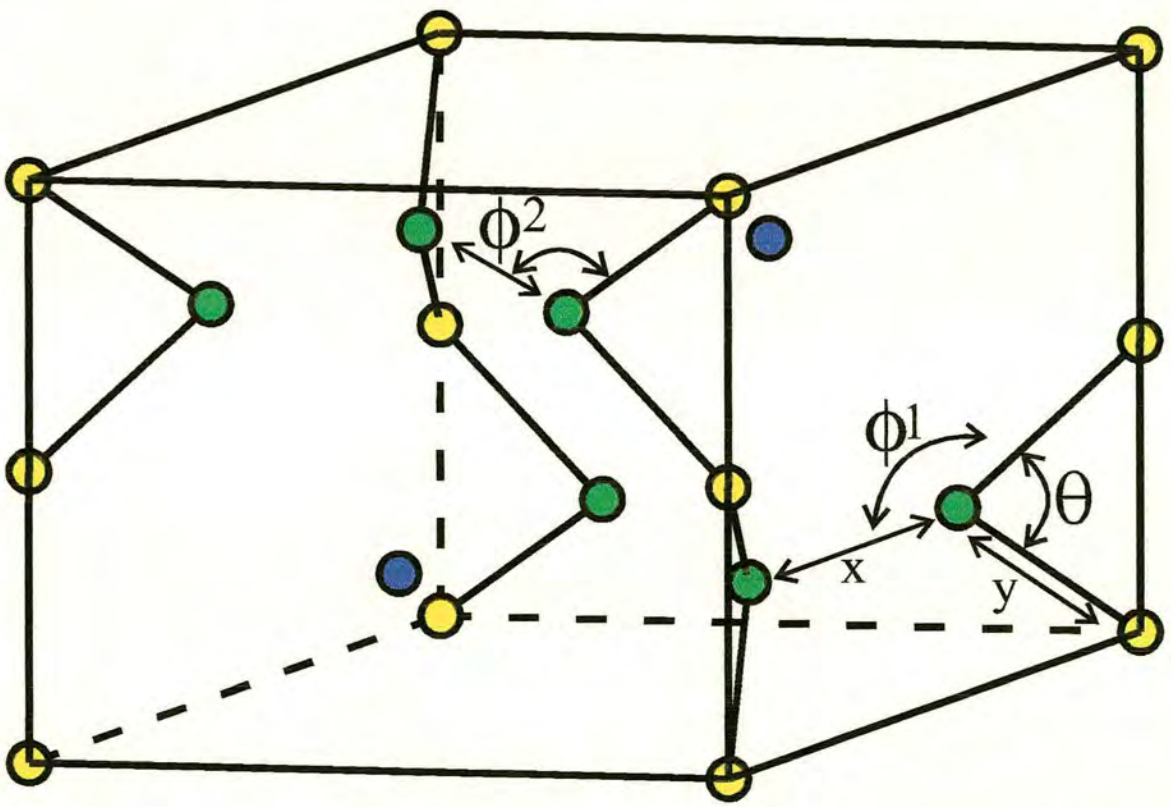

Figure A.15: The unit cell of NH_4FeCl_3 is depicted, showing the Fe-Cl-Fe bond angle (θ), the Fe-Cl-Cl bond angles (ϕ^1 and ϕ^2), the Cl-Cl distance (x), and the Fe-Cl distance (y).

Table A.2: Selected bond angles and distances obtained from refinement of data collected on NH_4FeCl_3 and ND_4FeCl_3 over a range of temperatures.

Sample	Temp.	diffract-ometer	θ	ϕ^1	ϕ^2	x	y
NH_4FeCl_3	423	BM16	74.28(7)	133.66(13)		3.6109(29)	2.5216(20)
NH_4FeCl_3	300	BM16	74.82(2)	133.46(4)		3.6054(9)	2.4849(6)
NH_4FeCl_3	291	BM16	74.38(5)	133.62(9)		3.5747(20)	2.4964(14)
NH_4FeCl_3	30	BM16	74.43(2)	138.01(4)	128.27(3)	3.5819(7)	2.4804(5)
ND_4FeCl_3	300	BM16	74.13(3)	133.71(5)		3.5637(13)	2.5044(9)
ND_4FeCl_3	291	BM16	74.56(5)	133.56(9)		3.5855(20)	2.4915(14)
ND_4FeCl_3	200	BM16	74.52(3)	133.57(5)		3.5749(11)	2.4836(8)
ND_4FeCl_3	160	BM16	74.65(3)	136.21(5)	130.52(5)	3.5850(10)	2.4778(7)
ND_4FeCl_3	30	BM16	74.33(4)	138.90(2)	126.97(2)	3.5847(17)	2.4868(12)
ND_4FeCl_3	473	D2B	75.67(1)	133.15(2)		3.6928(1)	2.4800(1)
ND_4FeCl_3	363	D2B	75.42(1)	133.25(2)		3.6570(1)	2.4756(1)
ND_4FeCl_3	300	D2B	75.12(8)	133.31(14)		3.6318(1)	2.4776(1)
ND_4FeCl_3	200	D2B	74.75(17)	133.49(30)		3.5841(20)	2.4805(14)
ND_4FeCl_3	160	D2B	74.60(14)	136.03(26)	130.79(25)	3.5809(20)	2.4817(14)

A.4. Bond lengths and angles obtained from refinement of single crystal data collected on NH_4FeCl_3

A.4.1. Edinburgh

A.4.1.1. 220 K

Table A.3. Atomic coordinates (x 10^4) and equivalent isotropic displacement parameters ($Å^2$ x 10^3) for 220 K. U(eq) is defined as one third of the trace of the orthogonalised U^{ij} tensor.

	x	*y*	*z*	*U(eq)*
Fe	0	10000	10000	23(1)
Cl	-1624(1)	-3249(1)	7500	29(1)
N	3333	6667	7500	37(1)

Table A.4. Bond lengths [Å] and angles [°] for 220k.

Fe-Cl#1	2.4784(3)
Cl-Fe-Cl#1	180.0
Cl-Fe-Cl#2	93.047(7)
Cl#1-Fe-Cl#2	86.953(7)
Fe-Cl-Fe#6	74.784(10)

Symmetry transformations used to generate equivalent atoms

#1 -x,-y,-z+2	#2 x-y,x,-z+2	#3 -y,x-y,z
#4 x+y,-x,z	#5 Y,-x+y,-z+2	#6 -x,-y,z-1/2

Table A.5. Anisotropic displacement parameters ($Å^2$ x 10^3) for 220 K. The anisotropic displacement factor exponent takes the form:

$-2\pi^2[h^2 a^{*2} U^{11} + ... + 2 h k a^* b^* U^{12}]$

	U^{11}	U^{22}	U^{33}	U^{23}	U^{13}	U^{12}
Fe	18(1)	18(1)	35(1)	0	0	9(1)
Cl	26(1)	15(1)	43(1)	0	0	8(1)
N	28(1)	28(1)	54(1)	0	0	14(1)

Table A.6. Hydrogen coordinates (x 10^4) and isotropic displacement parameters ($Å^2$ x 10^3) for 220 K.

	x	*y*	*z*	*U(eq)*
H(1)	3333	6667	6087(39)	55
H(2)	4015(20)	-1971(39)	7832(73)	55
H(3)	2649(20)	-2649(20)	7827(73)	55

A.4.1.2. 120 K

Table A.7. Atomic coordinates (x 10^4) and equivalent isotropic displacement parameters ($Å^2$ x 10^3) for 120 K. U(eq) is defined as one third of the trace of the orthogonalised U^{ij} tensor.

	x	*y*	*z*	*U(eq)*
Fe	0	10000	10000	14(1)
Cl	-1435(1)	6752(1)	7500	17(1)
N	3333	6667	7500	26(1)

Table A.8. Bond lengths [Å] and angles [°] for 120k.

Fe-C1# 1	2.4765(2)
Cl-Fe-Cl#1	180.0
Cl-Fe-Cl#2	92.907(7)
Cl#l-Fe-Cl#2	87.093(7)
Fe-Cl-Fe#6	74.590(10)

Symmetry transformations used to generate equivalent atoms:
#l -x1-y+2,-z+2 #2 x-y+l,x+l,-z+2 #3 x+y-l,-x+l,z
#4 y+1,x-y+2,z #5 y-1,-x+y,-z+2 #6 x,-y+2,z-l/2

Table A.9. Anisotropic displacement parameters ($Å^2$ x 10^3) for 120 K. The anisotropic displacement factor exponent takes the form:

$-2\pi^2[\, h^2 a^{*2} U^{11} + \ldots + 2\, h\, k\, a^*\, b^*\, U^{12}\,]$

	U^{11}	U^{22}	U^{33}	U^{23}	U^{13}	U^{12}
Fe	10(1)	10(1)	21(1)	0	0	5(1)
Cl	15(1)	10(1)	26(1)	0	0	5(1)
N	17(1)	17(1)	45(1)	0	0	8(1)

Table A.10. Hydrogen coordinates (x 10^4) and isotropic displacement parameters ($Å^2$ x 10^3) for 120 K.

	x	*y*	*z*	*U(eq)*
H(l)	3333	6667	8989(26)	81(15)
H(2)	2100(25)	6591(37)	7047(20)	51(7)

A.4.2. Durham

A.4.2.1. 291 K

Table A.11 Atomic coordinates (x 10^4) and equivalent isotropic displacement parameters ($Å^2$ x 10^3) for 291k. U(eq) is defined as one third of the trace of the orthogonalized U^{ij} tensor.

	x	y	z	U(eq)
Fe(1)	0	0	-7	31(1)
Cl(2)	-1621(1)	-3241(1)	2492(8)	38(1)
N(3)	3333	-3333	2503(81)	51(1)

Table A.12. Bond lengths [Å] and angles [°] for 291k.

Fe(1)-Cl(2)#1	2.483(3)
Cl(2)#1-Fe(1)-Cl(2)	86.87(14)
Cl(2)#1-Fe(1)-Cl(2)#3	93.150(12)
Cl(2)-Fe(1)-Cl(2)#3	93.148(12)
Cl(2)#2-Fe(1)-Cl(2)#3	179.98(9)
Cl(2)#1-Fe(1)-Cl(2)#4	93.150(13)
Cl(2)-Fe(1)-Cl(2)#4	179.98(8)
Cl(2)#3-Fe(1)-Cl(2)#4	86.84(14)
Cl(2)-Fe(1)-Cl(2)#5	93.149(13)
Cl(2)#2-Fe(1)-Cl(2)#5	93.148(13)
Fe(1)-Cl(2)-Fe(1)#6	74.92(2)

Symmetry transformations used to generate equivalent atoms:

#1 -x+y,-x,z #2 -y,x-y,z #3 y,-x+y,z-1/2

#4 -x,-y,z-1/2 #5 x-y,x,z-1/2 #6 -x,-y,z+1/2

Table A.13. Anisotropic displacement parameters ($Å^2 x\ 10^3$) for 291k. The anisotropic displacement factor exponent takes the form:

$-2\pi^2[\ h^2\ a^{*2}U^{11} + ... + 2\ h\ k\ a^*\ b^*\ U^{12}\ ]$

	U^{11}	U^{22}	U^{33}	U^{23}	U^{13}	U^{12}
Fe(1)	23(1)	23(1)	47(1)	0	0	12(1)
Cl(2)	33(1)	20(1)	56(1)	-2(1)	-3(1)	10(1)
N(3)	39(1)	39(1)	76(2)	0	0	19(1)

A.4.2.2. 120 K

Table A.14. Atomic coordinates (x 10^4) and equivalent isotropic displacement parameters ($Å^2$x 10^3) for 120k. U(eq) is defined as one third of the trace of the orthogonalized U^{ij} tensor.

	x	*y*	*z*	*U(eq)*
Fe(1)	0	0	8(4)	16(1)
Cl(2)	-1429(1)	-3248(1)	2493(7)	19(1)
N(3)	3333	-3333	2432(61)	28(2)

Table A.15. Bond lengths [Å] and angles [°] for 120k.

Fe(1)-Cl(2)#1	2.474(3)
Fe(1)-Cl(2)#3	2.485(3)
Cl(2)#1-Fe(1)-Cl(2)#2	87.32(13)
Cl(2)#1-Fe(1)-Cl(2)#3	92.920(13)
Cl(2)-Fe(1)-Cl(2)#3	179.7(2)
Cl(2)#2-Fe(1)-Cl(2)#4	92.920(13)
Cl(2)-Fe(1)-Cl(2)#4	92.919(13)
Cl(2)#3-Fe(1)-Cl(2)#4	86.84(13)
Fe(1)-Cl(2)-Fe(1)#6	74.61(2)

Symmetry transformations used to generate equivalent atoms:

#1 -y,x-y,z #2 -x+y,-x,z #3 -x,-y,z-1/2

#4 y,-x+y,z-1/2 #5 x-y,x,z-1/2 #6 -x,-y,z+1/2

Table A.16. Anisotropic displacement parameters ($Å^2 x\ 10^3$) for 120k. The anisotropic displacement factor exponent takes the form:

$-2\pi^2[\ h^2\ a^{*2}U^{11} + ... + 2\ h\ k\ a^*\ b^*\ U^{12}\ ]$

	U^{11}	U^{22}	U^{33}	U^{23}	U^{13}	U^{12}
Fe(1)	10(1)	10(1)	26(1)	0	0	5(1)
Cl(2)	15(1)	9(1)	31(1)	0(1)	-6(1)	5(1)
N(3)	19(1)	19(1)	47(4)	0	0	9(1)

A.4.2.3. 30 K

Table A.17. Atomic coordinates (x 10^4) and equivalent isotropic displacement parameters ($Å^2 x\ 10^3$) for 30k. U(eq) is defined as one third of the trace of the orthogonalized U^{ij} tensor.

	x	y	z	U(eq)	
Fe(1)	0	0	7(3)		7(1)
Cl(2)	-1395(1)	-3247(1)	2488(12)		9(1)
N(3)	3333	-3333	2465(95)		23(1)

Table A.18. Bond lengths [Å] and angles [°] for 30k.

Fe(1)-Cl(2)#1	2.471(4)
Fe(1)-Cl(2)#3	2.485(4)
Fe(1)-Cl(2)#4	2.486(4)
Cl(2)-Fe(1)-Cl(2)#1	87.4(2)
Cl(2)-Fe(1)-Cl(2)#3	179.6(2)
Cl(2)#1-Fe(1)-Cl(2)#3	92.91(2)
Cl(2)#2-Fe(1)-Cl(2)#4	179.6(2)
Cl(2)#3-Fe(1)-Cl(2)#4	86.8(2)
Fe(1)-Cl(2)-Fe(1)#6	74.60(2)

Symmetry transformations used to generate equivalent atoms:

#1 -x+y,-x,z #2 -y,x-y,z #3 -x,-y,z-1/2

#4 y,-x+y,z-1/2 #5 x-y,x,z-1/2 #6 -x,-y,z+1/2

Table A.19. Anisotropic displacement parameters ($Å^2 x\ 10^3$) for 30k. The anisotropic displacement factor exponent takes the form:

$-2\pi^2[\ h^2\ a^{*2}U^{11} + ... + 2\ h\ k\ a^*\ b^*\ U^{12}\ ]$

	U^{11}	U^{22}	U^{33}	U^{23}	U^{13}	U^{12}
Fe(1)	5(1)	5(1)	11(1)	0	0	2(1)
Cl(2)	7(1)	4(1)	13(1)	-1(2)	-7(2)	2(1)
N(3)	11(2)	11(2)	47(4)	0	0	6(1)

A.4.2.4. 10 K

Table A.20. Atomic coordinates ($x\ 10^4$) and equivalent isotropic displacement parameters ($Å^2 x\ 10^3$)for 10k. U(eq) is defined as one third of the trace of the orthogonalized U^{ij} tensor.

Atom	*x*	*y*	*z*	*U(eq)*
Fe(1)	0	0	-256(3)	4(1)
Cl(1)	695(2)	1621(2)	2235(2)	5(1)
Fe(2)	10(1)	5005(1)	-36(3)	7(1)
Cl(2)	-1624(2)	4076(2)	2452(2)	10(1)
Cl(3)	692(2)	6623(2)	2467(3)	8(1)
Cl(4)	926(2)	4301(2)	2485(3)	8(1)
N(1)	3333	6667	1933(19)	50(5)
N(2)	-1697(6)	1627(6)	2678(10)	7(1)

Table A.21. Bond lengths [Å] and angles [°] for 10k.

Fe(1)-Cl(1)#1	2.473(3)
Fe(1)-Cl(1)#3	2.479(2)
Fe(2)-Cl(2)#7	2.474(3)
Fe(2)-Cl(3)	2.476(3)
Fe(2)-Cl(4)#7	2.478(3)
Fe(2)-Cl(3)#7	2.481(3)
Fe(2)-Cl(4)	2.483(3)
Fe(2)-Cl(2)	2.484(3)
Cl(1)#1-Fe(1)-Cl(1)	87.16(9)
Cl(1)#1-Fe(1)-Cl(1)#3	179.81(11)
Cl(1)-Fe(1)-Cl(1)#3	92.98(5)
Cl(1)#3-Fe(1)-Cl(1)#4	86.88(9)
Fe(1)-Cl(1)-Fe(1)#6	74.70(6)
Cl(2)#7-Fe(2)-Cl(3)	93.54(7)
Cl(2)#7-Fe(2)-Cl(4)#7	87.31(10)
Cl(3)-Fe(2)-Cl(4)#7	92.58(9)
Cl(2)#7-Fe(2)-Cl(3)#7	86.95(10)
Cl(3)-Fe(2)-Cl(3)#7	179.48(5)
Cl(4)#7-Fe(2)-Cl(3)#7	87.24(10)
Cl(2)#7-Fe(2)-Cl(4)	93.46(7)
Cl(3)-Fe(2)-Cl(4)	87.25(10)
Cl(4)#7-Fe(2)-Cl(4)	179.22(10)
Cl(3)#7-Fe(2)-Cl(4)	92.92(7)
Cl(2)#7-Fe(2)-Cl(2)	179.42(11)
Cl(3)-Fe(2)-Cl(2)	86.86(10)
Cl(4)#7-Fe(2)-Cl(2)	92.24(6)
Cl(3)#7-Fe(2)-Cl(2)	92.66(7)
Cl(4)-Fe(2)-Cl(2)	86.99(10)
Fe(2)#8-Cl(2)-Fe(2)	74.60(8)
Fe(2)#8-Cl(4)-Fe(2)	74.54(9)

Symmetry transformations used to generate equivalent atoms:
#1 -x+y,-x,z #2 -y,x-y,z #3 x-y,x,z-1/2 #4 y,-x+y,z-1/2

#5 -x,-y,z-1/2 #6 -x,-y,z+1/2 #7 -x,-y+1,z-1/2 #8 -x,-y+1,z+1/2

Table A.22. Anisotropic displacement parameters ($Å^2 x\ 10^3$) for 10k. The anisotropic displacement factor exponent takes the form:

$-2\pi^2[\ h^2\ a^{*2} U^{11} + ... + 2\ h\ k\ a^*\ b^*\ U^{12}\ ]$

	U^{11}	U^{22}	U^{33}	U^{23}	U^{13}	U^{12}
Fe(1)	5(1)	5(1)	4(1)	0	0	2(1)
Cl(1)	6(1)	3(1)	5(1)	2(1)	-2(1)	1(1)
Fe(2)	4(1)	5(1)	12(1)	-1(1)	-1(1)	2(1)
Cl(2)	5(1)	6(1)	19(1)	-3(1)	-1(1)	2(1)
Cl(3)	7(1)	5(1)	12(1)	2(1)	0(1)	2(1)
Cl(4)	7(1)	8(1)	12(1)	1(1)	2(1)	5(1)
N(1)	4(4)	4(4)	140(15)	0	0	2(2)
N(2)	12(4)	17(4)	0(3)	8(3)	6(2)	13(3)

Appendix B

NH_4FeBr_3 and ND_4FeBr_3

B.1. Rietveld refinements of data collected on diffractometer BM16 at the ESRF, Grenoble

The Rietveld refinements of the neutron diffraction data collected on diffractometer BM16 at the ESRF, Grenoble on powder samples of NH_4FeBr_3 and ND_4FeBr_3 were carried out using the refinement package GSAS [130]. The fits are shown below.

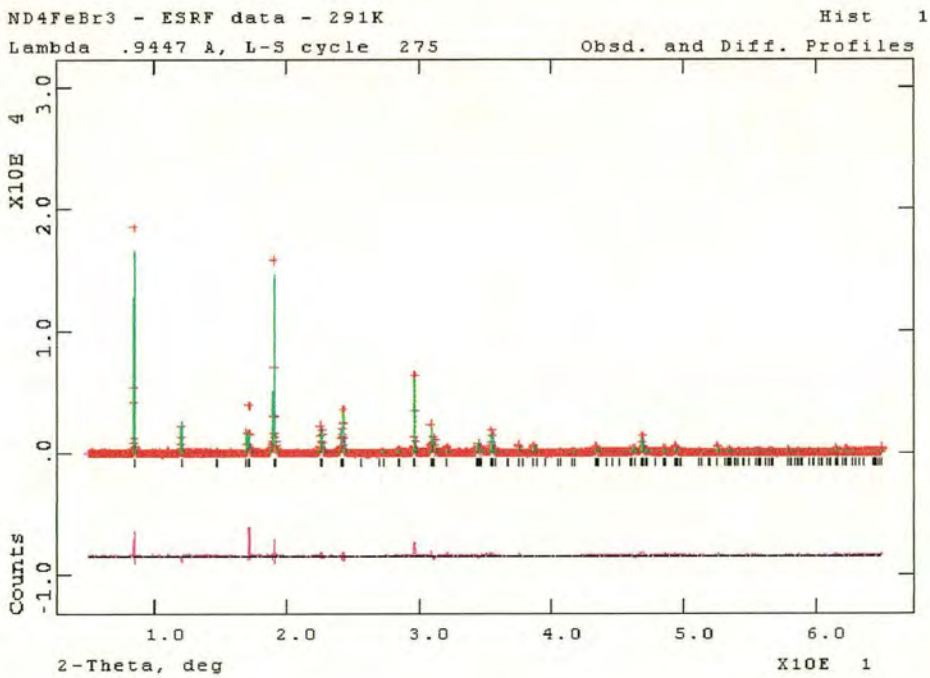

Figure B.1. Rietveld refinement of BM16 data collected on NH_4FeBr_3 at 291 K

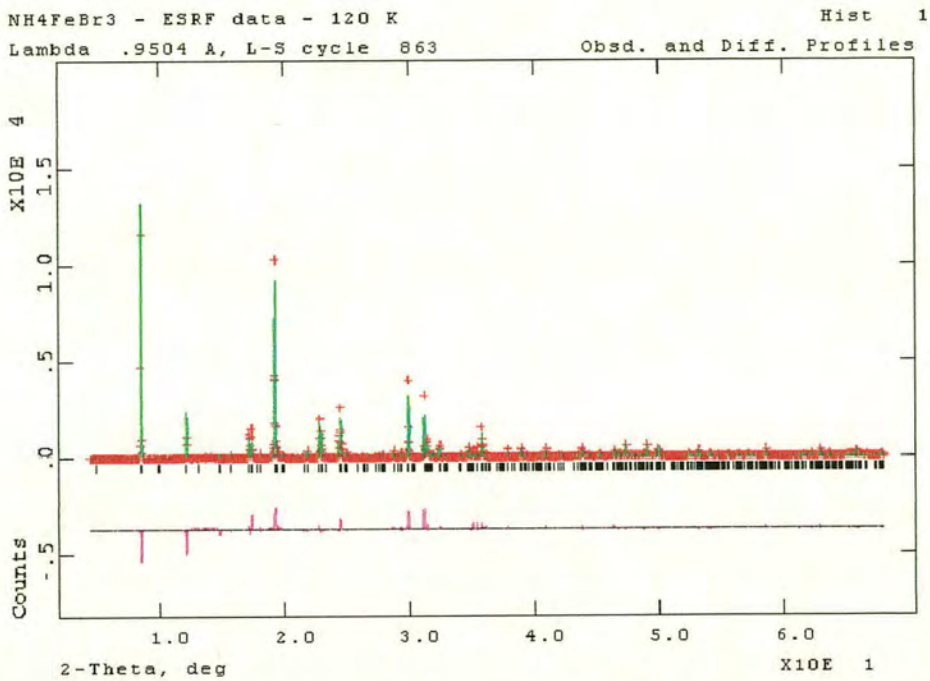

Figure B.2. Rietveld refinement of BM16 data collected on NH_4FeBr_3 at 120 K

Table B.1 The X-ray wavelengths for each data set collected using diffractometer BM16.

Sample	Temperature / K	Wavelength / λ
ND_4FeBr_3	291	0.944680
NH_4FeBr_3	120	0.950436

B.2. Rietveld refinements of data collected on diffractometer D2B at the ILL, Grenoble

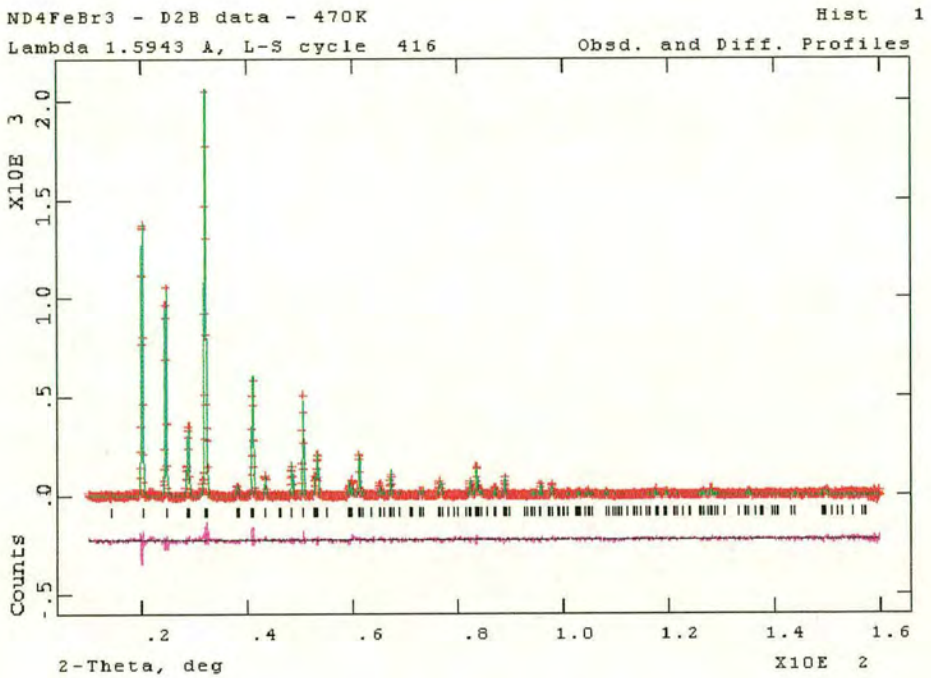

Figure B.3. Rietveld refinement of D2B data collected on ND_4FeBr_3 at 470 K

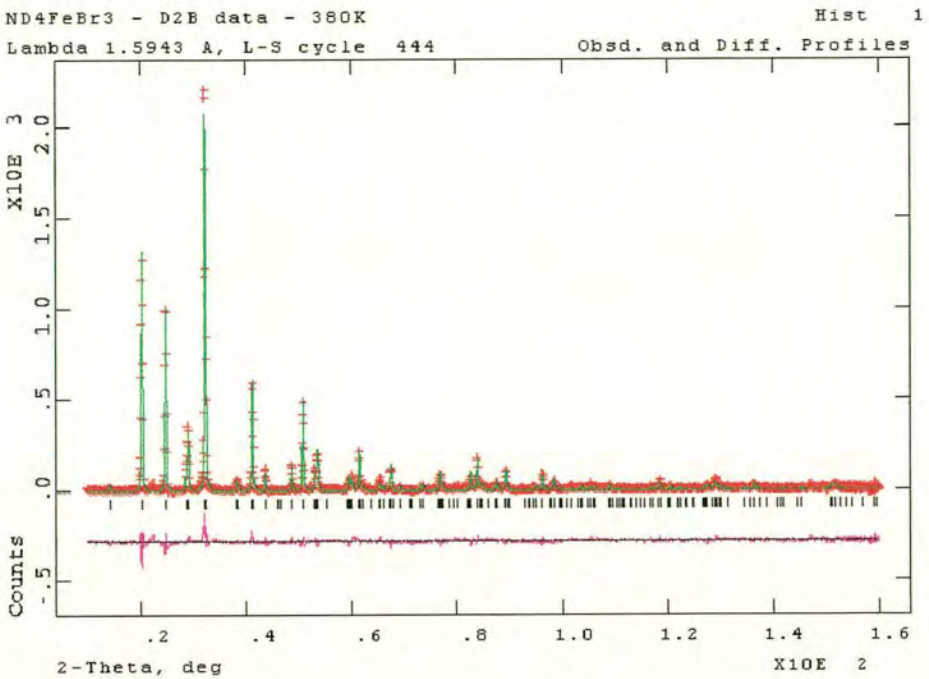

Figure B.4. Rietveld refinement of D2B data collected on ND_4FeBr_3 at 380 K

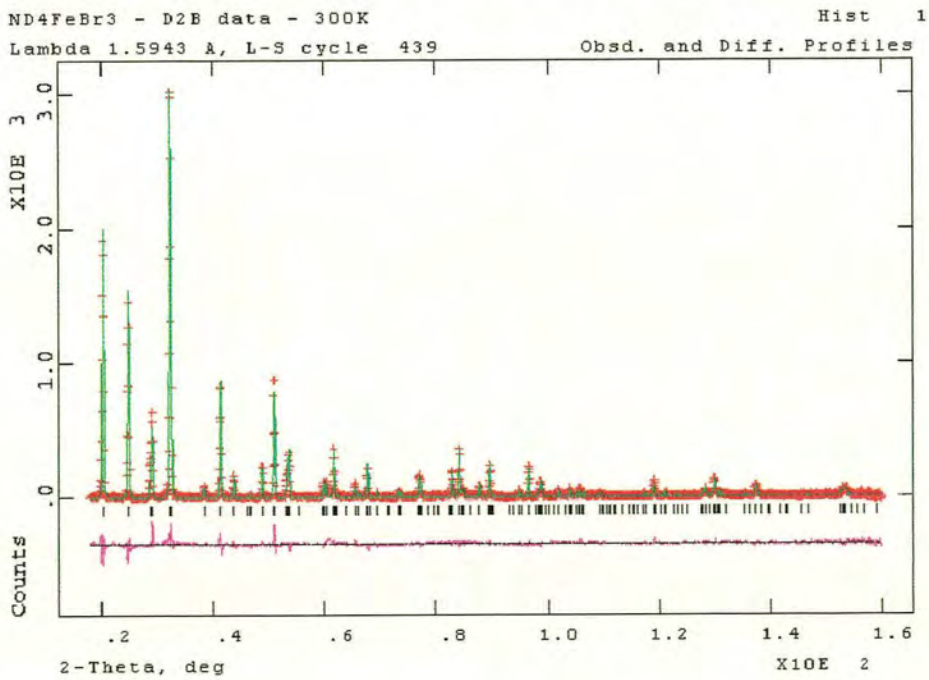

Figure B.5. Rietveld refinement of D2B data collected on ND_4FeBr_3 at 300 K

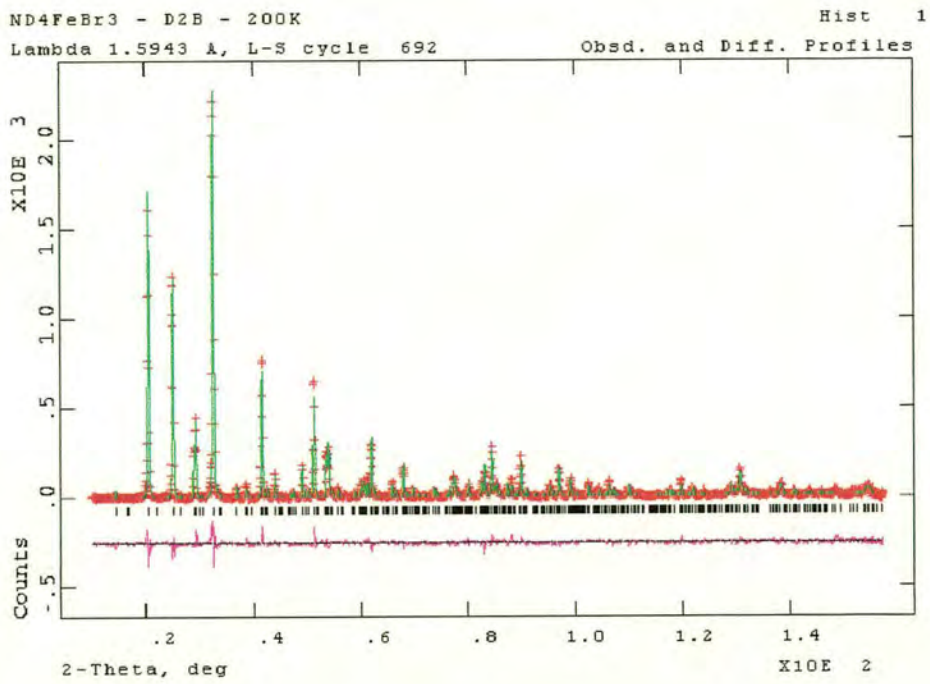

Figure B.6. Rietveld refinement of D2B data collected on ND_4FeBr_3 at 200 K

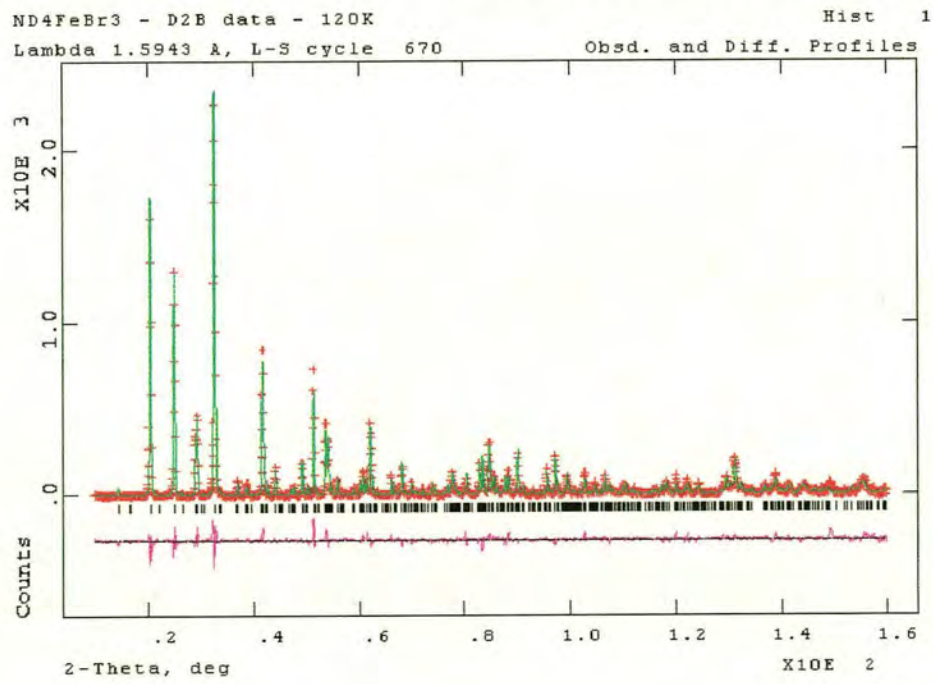

Figure B.7. Rietveld refinement of D2B data collected on ND_4FeBr_3 at 120 K

B.3. Selected bond lengths and angles obtained from Rietveld refinements of powder diffraction data

Figure B.15 illustrates the Br-Br distances (x), the Fe-Fe distances (y), Fe-Br-Fe in chain bond angle (θ), and the intra chain Fe-Br-Br angles ϕ^1 and ϕ^2 (where ϕ^2 is not listed it is equal to ϕ^1). Table B.2 lists the values of θ, $\phi 1$, $\phi 2$, x and y obtained in all refinements carried out on data collected for NH_4FeBr_3 and ND_4FeBr_3 on diffractometers BM16 at ESRF and D2B at ILL, at temperatures where the unit cell is primitive hexagonal.

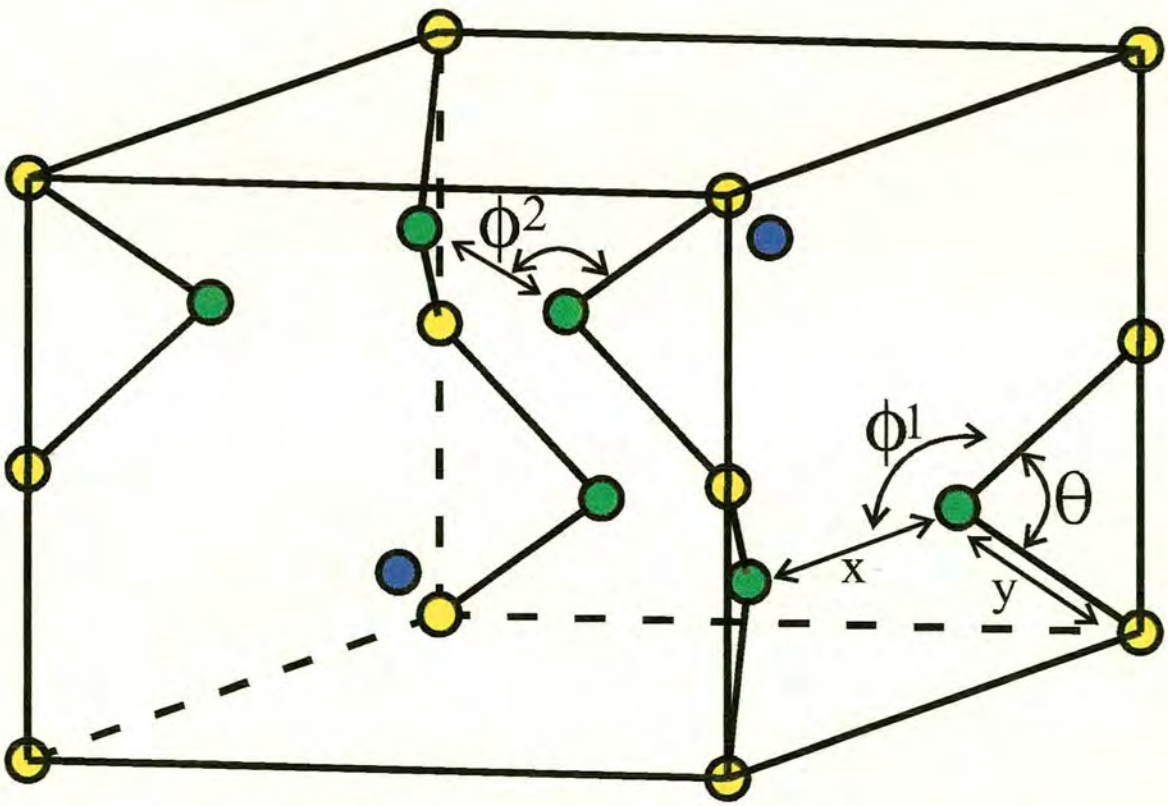

Figure B.15: The unit cell of NH_4FeBr_3 is depicted, showing the Fe-Br-Fe bond angle (θ), the Fe-Br-Br bond angles (ϕ^1 and ϕ^2), the Br-Br distance (x), and the Fe-Br distance (y).

Table B.2: Selected bond angles and distances obtained from refinement of data collected on NH_4FeBr_3 and ND_4FeBr_3 over a range of temperatures.

Sample	Temp	diffract-ometer	θ	ϕ^1	ϕ^2	x	y
NH_4FeBr_3	291	BM16	74.33(4)	133.64(7)	-	3.7702(17)	2.6244(12)
ND_4FeBr_3	470	D2B	74.17(8)	133.70(14)	-	3.8024(36)	2.6498(25)
ND_4FeBr_3	380	D2B	73.54(10)	133.92(18)	-	3.7421(42)	2.6585(30)
ND_4FeBr_3	300	D2B	73.73(8)	133.86(15)	-	3.7348(35)	2.6446(25)

B.4. Calculated and observed reflection listings for data autoindexed using Treor 90 [141]

B.4.1. NH_4FeBr_3 data collected on BM16 at 120 K

A = 12.754430 .001667 A ALFA = 90.000000 .000000 DEG
B = 12.754430 .001667 A BETA = 90.000000 .000000 °
C = 6.304298 .000980 A GAMMA =120.000000 .000000 °
UNIT CELL VOLUME = 888.16 Å^3

H	K	L	SST-OBS	SST-CALC	DELTA	2TH-OBS	2TH-CALC	D-OBS
1	1	0	.014586	.014590	-.000004	13.874	13.875	6.3780
1	1	1	.029538	.029520	.000018	19.793	19.786	4.4820
2	1	1	.048968	.048973	-.000005	25.569	25.571	3.4810
2	2	0	.058346	.058360	-.000014	27.956	27.959	3.1890
3	0	1	.058677	.058700	-.000023	28.037	28.042	3.1800
0	0	2	.059724	.059718	.000006	28.291	28.290	3.1520
1	0	2	.064630	.064581	.000049	29.455	29.444	3.0300
2	2	1	.073308	.073290	.000019	31.418	31.414	2.8450
1	1	2	.074245	.074308	-.000063	31.624	31.637	2.8270
4	0	0		.077814			32.395	
3	1	1	.078176	.078153	.000023	32.473	32.468	2.7550
2	1	2	.093734	.093761	-.000027	35.656	35.661	2.5160
4	1	0	.102076	.102130	-.000054	37.265	37.275	2.4110
3	0	2	.103445	.103488	-.000044	37.523	37.531	2.3950
4	1	1	.117103	.117060	.000043	40.022	40.015	2.2510
2	2	2	.118150	.118078	.000072	40.209	40.196	2.2410
3	1	2	.122930	.122941	-.000011	41.050	41.052	2.1970

NUMBER OF OBS. LINES = 16
NUMBER OF CALC. LINES = 17
M(16)= 71 AV.EPS.= .0000297
F 16 = 89.(.006261, 29)
M CF. J.APPL.CRYST. 1(1968)108

F CF. J.APPL.CRYST. 12(1979)60
0 LINES ARE UNINDEXED
M-TEST= 71 UNINDEXED IN THE TEST= 0

B.4.2. ND_4FeBr_3 data collected on BM16 at 4.2 K

A = 12.587890 .000833 A ALFA = 90.000000 .000000°
B = 7.394723 .000587 A BETA = 90.000000 .000000°
C = 6.345552 .000574 A GAMMA = 90.000000 .000000°
UNIT CELL VOLUME = 590.67 Å^3

H	K	L	SST-OBS	SST-CALC	DELTA	2TH-OBS	2TH-CALC	D-OBS
1	1	0	.014532	.014596	-.000064	13.847	13.878	6.3900
2	0	0	.014978	.014979	.000000	14.060	14.060	6.2940
1	1	1	.029328	.029332	-.000004	19.721	19.723	4.4980
2	0	1	.029723	.029715	.000008	19.855	19.852	4.4680
2	1	1	.040577	.040566	.000011	23.242	23.239	3.8240
3	0	1	.048410	.048438	-.000028	25.421	25.428	3.5010
			.048521			25.450		3.4970
0	2	1	.058127	.058141	-.000014	27.902	27.906	3.1950
2	2	0	.058382	.058383	-.000001	27.965	27.965	3.1880
0	0	2	.058936	.058944	-.000008	28.100	28.102	3.1730
3	1	1	.059309	.059289	.000020	28.190	28.186	3.1630
4	0	0	.059914	.059915	-.000001	28.337	28.337	3.1470
1	2	1	.061904	.061885	.000019	28.814	28.809	3.0960
1	0	2	.062711	.062689	.000023	29.005	29.000	3.0760
2	2	1	.073154	.073119	.000035	31.384	31.377	2.8480
1	1	2		.073540			31.469	
4	0	1	.074667	.074651	.000016	31.716	31.712	2.8190
2	1	2	.084814	.084774	.000040	33.863	33.855	2.6450
4	1	1	.085459	.085502	-.000043	33.995	34.004	2.6350
3	2	1	.091826	.091843	-.000016	35.279	35.282	2.5420
3	0	2	.092626	.092646	-.000020	35.438	35.442	2.5310
1	3	0	.101402	.101405	-.000003	37.137	37.137	2.4190
0	2	2	.102331	.102349	-.000018	37.313	37.316	2.4080
4	2	0		.103319			37.499	
3	1	2	.103445	.103497	-.000053	37.523	37.533	2.3950
5	1	0	.104489	.104468	.000021	37.719	37.715	2.3830
1	2	2	.106086	.106093	-.000008	38.017	38.018	2.3650
5	0	1	.108365	.108353	.000012	38.439	38.437	2.3400
1	3	1	.116172	.116141	.000031	39.856	39.851	2.2600
2	2	2	.117311	.117327	-.000016	40.059	40.062	2.2490
4	2	1	.118045	.118055	-.000010	40.190	40.192	2.2420
4	0	2	.118892	.118859	.000033	40.340	40.334	2.2340
5	1	1	.119105	.119204	-.000099	40.378	40.395	2.2320
4	1	2	.129687	.129710	-.000023	42.215	42.219	2.1390
3	2	2	.136100	.136051	.000049	43.298	43.289	2.0880
1	0	3		.136369			43.343	
5	0	2	.152583	.152561	.000022	45.986	45.982	1.9720

NUMBEROFOBS.LINES= 34
NUMBEROFCALC.LINES= 36

M(20)= 72 AV.EPS.= .0000195
F20=114.(.005343, 33)
M(30)= 61 AV.EPS.= .0000198
F30=128.(.004794, 49)
M(34)= 50 AV.EPS.= .0000233
F34= 99.(.005214, 66)
1 LINESAREUNINDEXED
M-TEST= 72UNINDEXEDINTHETEST= 1

Appendix C

Program to calculate the susceptibility in an induced moment paramagnet using the DCEFA model

The following program was used in this project to calculate the susceptibility and subsequently the ligand field and exchange parameters in NH_4FeCl_3 and NH_4FeBr_3 and their deuterated analogues. The theory involved is discussed in chapter 2 and the results obtained are given in Chapter 8.

```
C. PROGRAM TO CALCULATE SUSCEPTIBILITY IN PARAMAGNETIC REGIME FOR
C. DCEFA MAGNET.
C. SUZUKI J.PHYS.SOC.JAPAN 45 (1979) 1794
C.
C.
C. SUZUKI DCEFA MODEL FOR PARAMAGNETIC PHASE, BOTH AS POWDER AND IN
C. SINGLE CRYSTAL (PARA AND PERP) FORMS
C.
C.  ALSO CALCULATES BONNER-FISHER EXPRESSION, AND CEF EXPRESSIONS
C.
C.
      REAL Q1,Q2,Q3,AX,SX
      REAL BOLTZ,PI,EX(4),ANISO,CORR,QC,T,JZERO,JQ,E,EEE,BETA,
     1RO,QQJ,WQ1,TEMP(100),X(3),SELF,SELFD,CORRD,DA,Q(50,3),TK(200)
      INTEGER IFAIL,NOM,NOQ,ZERO,ICYCLE,CYC
      COMMON/USE/ICYCLE,CYC,NUP,Z1,Z2,Z3,Z4,Z5
      REAL SUSCPRP,SUSCPOW,SUSCPAR,RO1,JZPAR,JZPRP
C.
C.
      COMMON/SPACE2/EX,ANISO,QC
      COMMON/SPACE3/POP,T,BOLTZ
C.
      open(unit=4,file='c.inp')
      open(unit=6,file='out.doc')
      open(unit=7,file='1.dat')
      open(unit=8,file='2.dat')
      open(unit=9,file='3.dat')
      PI=3.14159266
      BOLTZ=0.0861708
      N1=10
      N2=N1
      N3=N1
C.
      READ(4,*) EX(1),EX(2),EX(3),EX(4)
```

```
      READ(4,*) ANISO
      READ(4,*) CORR
      READ(4,*) NOT
      READ(4,*) (TK(I),I=1,NOT)
      QC=0.5
      WRITE(6,3030) EX(1),EX(2),EX(3),EX(4),ANISO
3030  FORMAT(' EX1,EX2,EX3,EX4,ANISO ',5F9.4)
      WRITE(6,3040)
3040  FORMAT('          ')
      write(6,3045)
3045  FORMAT('      T       CORR      CEFPRP      CEFPAR
     1     CEFPOW ')
      write(6,3040)
C.
      BOLTZ=0.0861708
C.
C. SUBROUTINE ITERAT TO SELF-CONSISTENTLY CALCULATE SX,ALPHA
C.
C.
      DO 10000 I=1,NOT
      T=TK(I)
C.
      DA=0.005
      KKK=0
      CALL TSUM(SELF,CORR)
      WRITE(9,1000) CORR,SX,SELF
      SELFD=SELF
      CORR=CORR+DA
      CALL TSUM(SELF,CORR)
      WRITE(9,1000) CORR,SX,SELF
      IF(SELF/SELFD.LT.0) GOTO 2000
      IF(SELF/SELFD.EQ.0) GOTO 2100
      IF(ABS(SELF)-ABS(SELFD).LT.0) GOTO 2200
      DA=-DA
2200  IND=0
2300  SELFD=SELF
      CORRD=CORR
      SXD=SX
      CORR=CORR+DA
      CALL TSUM(SELF,CORR)
9300  WRITE(9,1000) CORR,SX,SELF
      IF(SELF/SELFD.LT.0)GOTO 2000
      IF(SELF/SELFD.EQ.0)GOTO 2100
      IND=IND+1
      IF(IND.GT.100)GOTO 7000
      GOTO 2300
2000  KKK=KKK+1
      IF(KKK.GE.2) GOTO 2400
      DA=-0.5*DA
      GOTO 2200
C.
C.
2400  AA=ABS(SELF/(ABS(SELF)+ABS(SELFD)))
      CORR=CORR*(1.0-AA)+CORRD*AA
2100  CONTINUE
      WRITE(9,2500) CORR
C.
C.
```

```
1000  FORMAT(' CORR,SX,SELF',3F12.4)
2500  FORMAT(' FINAL VALUE OF CORR IS ',F12.4)
      GOTO 8000
7000  WRITE(7,3001)
3001  FORMAT(' NO MINIMUM SEEN ')
8000  JZERO=2*EX(2)+6*EX(1)
C.
      JZPRP=2*EX(2)+6*EX(1)
      JZPAR=2*EX(4)+6*EX(3)

3333  CONTINUE
C.
C.    corrx=0.0
      EEE=ANISO+CORR*(2*(EX(2)-EX(4))+6*(EX(1)-EX(3)))
      BETA=EEE/(T*BOLTZ)
      RO=(EXP(BETA)-1)/(EXP(BETA)+2)
      RO1=1/(EXP(BETA)+2)
C.
      SUSCPRP=4*RO/(EEE-4*RO*JZPRP*(1-CORR))
      SUSCPAR=2*RO1/(BOLTZ*T-4*RO1*JZPAR*(1-CORR))
      SUSCPOW=(2*SUSCPRP+SUSCPAR)/3
C.    WRITE(6,55566) CORR,JZPRP,JZPAR,RO,RO1
C.5566 FORMAT(' CORR, JZPRP, JZPAR, RO,RO1 ',5F12.4)
C.
C.
C.    y=3.0*boltz*t/(8.0*ex(2))
C.    u=1.0/(tanh(3.0/(2.0*y)))-2.0*y/3.0
C.    fishrec=ex(2)*y*(1.0-u)/(1.0+u)
C.    fish=1.0/fishrec
C.    cefrec1=ex(2)*(-1.0+(sqrt(1+y**2.0)))
C.    cefrec2=ex(2)*(-1.0-(sqrt(1+y**2.0)))
C.    cef1=1.0/(cefrec1)
C.    cef2=1.0/(cefrec2)
      WRITE(6,3050) T,CORR,SUSCPRP,SUSCPAR,SUSCPOW
      WRITE(8,3051) T,CORR,SUSCPRP,SUSCPAR,SUSCPOW
3051  FORMAT(F8.4)
3050  FORMAT(5F12.4)
C.
10000 CONTINUE
C.
      STOP
      END
C.
C. SUBROUTINE TSUM TO SUM CHI(2,2) OVER BRILLOUIN ZONE
C.
C.
      SUBROUTINE TSUM(SELF,CORR)
      COMMON/SPACE2/EX,ANISO,QC,JPLUS,JMINUS,JPARA,JZERO
      COMMON/SPACE3/POP,T,BOLTZ
      COMMON/GRID/N1,N2,N3
      REAL PI,ANISO,EN(3),SELF,SX,X(4),ALPHA,BETA,GAMMA,WQ1,
     1WQ2,DQ1,DQ2,DQ3,DENST,CHI,RO,JQ,JZERO,
     2JQQ,POP,T,BOLTZ,EX(4),QC,EEE
C.
      PI=3.14159266
      BOLTZ=0.0861708
      JZERO=2*EX(2)+6*EX(1)
      EEE=ANISO+CORR*(2*(EX(2)-EX(4))+6*(EX(1)-EX(3)))
```

```
      BETA=EEE/(T*BOLTZ)
      RO=(EXP(BETA)-1)/(EXP(BETA)+2)
C.
C.
      N1=10
      N2=N1
      N3=N1
C.
      SELF=0.0
      DENST=1.0/(N1*N2*N3)
      DQ1=1.0/(2*N1)
      DQ2=0.5/(2*N2)
      DQ3=0.5/(2*N3)
      SELF=0.0
C.
C.
      DO 1000 I1=1,N1
      X(1)=DQ1*(2*I1-1)
       DO 1000 I2=1,N2
       X(2)=DQ2*(2*I2-1)
        DO 1000 I3=1,N3
        X(3)=DQ3*(2*I3-1)
      JQ=2*EX(2)*COS(2*PI*X(3))+2*EX(1)*(COS(2*PI*X(1))+
     1COS(2*PI*X(2))+COS(2*PI*(X(1)+X(2))))
C.    WRITE(6,55555) RO,EEE,JQQ,JQ,EX(1),EX(2)
55555 FORMAT(' RO, EEE, JQQ ',6F12.4)
      JQQ=JQ-CORR*JZERO
      WQ1=EEE**2-4*RO*EEE*JQQ
C.    WRITE(6,55556) JQQ,WQ1
55556 FORMAT(' JQQ, WQ1 ',2F12.4)
      WQ1=SQRT(WQ1)
      CHI=1/(TANH(WQ1/(2*T*BOLTZ))*WQ1)
       SELF=SELF+CHI
C.
1000  CONTINUE
      SELF=SELF*DENST*2*EEE*RO
      SELF=SELF-(2+2*EXP(BETA))/(2+EXP(BETA))
      RETURN
      END
```